THE UNIVERSITY *of* EDINBURGH

Pitching paddles, hydraulic PTOs and shallow water waves: The development of a coupled non-linear modelling approach for WEC design

CAITLIN WORDEN HODGE

This thesis is submitted in partial fulfilment of the requirements for the award of:

Engineering Doctorate (Eng.D.)

This degree is jointly awarded by the University of Edinburgh, University of Exeter and University of Strathclyde. The work presented has been conducted under the industrial supervision of Zyba Ltd as a project within the Industrial Doctoral Centre for Offshore Renewable Energy.

April 2020

Declaration

I declare that this thesis has been composed solely by myself and that it has not been submitted in part or in full in any previous application for a degree. Except where stated otherwise by reference or acknowledgement, the work presented is entirely my own.

Signed: _____ Date: 18/04/2020

Caitlin Worden Hodge

Abstract

Investor confidence in the wave energy industry has been eroded by the collapse of forerunners who went “too big too quickly” and relied on models that were developed primarily for other industries such as Oil & Gas. The underlying assumptions of linear wave theory may be valid for the analysis of large static structures but it proves inaccurate when investigating the behaviour of small dynamic systems, particularly those with geometrical asymmetry and deployments in shallow water. CFD is able to deal with these complex fluid-structure interactions by solving the governing equations of the dynamics of the fluid.

However, it is difficult for a developer to justify the additional computational expense and expertise required to accurately implement CFD unless its power and value are fully exploited. In this thesis OpenFOAM is used to develop a numerical wave tank, along with a fully integrated non-linear PTO model, to allow investigation of the whole CCell system, including the coupled behaviour of the hydrodynamics and PTO system. In a comparative exercise evaluating hydrodynamic coefficients, the CNWT demonstrated the information that would be overlooked if a linear model, such as NEMOH, was instead adopted. An increased understanding of the wave-structure interaction is provided by the CNWT, allowing interrogation of CCell’s defining parameters, which lead to the pilot deployment design increasing its CWR in predominant wave conditions by 69.8% in comparison to an equivalent flat paddle. Furthermore, conveyance of the pressure distribution from extreme loading scenarios facilitates the structural design of the composite WEC through FEA software analysis. The coupled PTO model also provides representative operational flow rates through the hydraulic system, which allows better characterisation of the PTO system in dry testing.

Combination and adaptation of these different numerical tools can provide an efficient modelling strategy for the development of a WEC, yielding a more accurate understanding of the system dynamics and overall performance than commonly used linear codes. Increased confidence in these model outputs accelerates the design process for developers and ensures that the concept is more thoroughly tested and de-risked prior to expensive prototype demonstrations. Adoption and extension of the numerical strategy as detailed within this work could lead to renewed credence and, more importantly, investment to the industry as a whole.

Word count for the main body of this thesis: **68,600**

Acknowledgments

I owe a considerable gratitude to Henry Weller for the initial development of OpenFOAM and the continued work from CFD Direct and the contributing community. Without your software and the decision to keep it open-source, my work would not have been possible.

I would like to thank my academic supervisors: Dr Zhiming Yuan, Prof Tom Bruce and Prof Philipp Thies. Our areas of interest may not always have aligned but thank you for your guidance and for providing both kind words and necessary criticism of my work.

This thesis would be nothing without the tireless efforts of my industrial supervisor Dr Will Bateman to develop CCell. Your willingness to teach and your belief in my ability have unearthed my love of coding, for which I am eternally grateful.

To all my wonderful Zyba colleagues, both past and present, you have been an absolute pleasure to work with and learn from. Your common desire to engineer solutions to help the world is inspiring. Special mention must go to Tara Massoudi for brightening my days and keeping me in check.

My family and friends have been nothing but encouraging throughout this process and I am truly thankful for your friendship. To my twin sister Mackenzie, your humour will get me through most things but without the competitive spirit I developed growing up alongside you I probably wouldn't have attempted this. To my parents, Cathy and Brian, thanks for allowing that competitiveness to flourish along with an inquiring mind so that I could actually achieve what I set out to do.

Finally, Kiran, thank you for seeing through me and recognising when I do and don't actually need a break, without you this would have taken a lot longer. You may not have read beyond the introduction, but your unwavering love and support have helped me finish every sentence, paragraph and chapter (and you taught me to drive a golf ball 210 yards in the process).

This research was funded by the Energy Technologies Institute and the RCUK Energy Programme through the Industrial Doctoral Centre for Offshore Renewable Energy (Grant number EP/J500847/1) and is gratefully acknowledged.

Confidentiality

agents cannot be held liable for the use of and reliance of the opinions, estimates, forecasts and findings in this document.

Contents

List of Figures

List of Tables

Abbreviations

6DoF	Six degrees of motion solver.
ALS	Accidental Limit State.
AMI	Arbitrary Mesh Interfaces.
BEM	Boundary Element Method.
CAD	Computer Aided Design.
CCP-WSI	Collaborative Computational Project in Wave Structure Interaction.
CFD	Computational Fluid Dynamics to simulate fluid-structure interactions.
CfD	Contracts for Difference.
CNWT	CFD Numerical Wave Tank.
CWR	Capture Width Ratio.
DB	Dynamic Boundary.
DDPM	Digital Displacement Pump-Motor.
FLS	Fatigue Limit State.
FDM	Finite Difference Method.
FEM	Finite Element Modelling, usually applied to structural analysis.
FMEA	Failure Mode and Effects Analysis.
FMECA	Failure Mode, Effects and Criticality Analysis.
FOT	Forced Oscillation Tests.
FVM	Finite Volume Method.
HPA	Heaving Point Absorber.
IS	Impulse Source.
JONSWAP	Joint North Sea Wave Project representative wave energy spectra.
KHL	Kelvin Hydrodynamics Laboratory, University of Strathclyde.
LCOE	Levelised Cost of Energy.
MAEP	Mean Annual Energy Production.
NOAA	US National Oceanic and Atmospheric Administration.
O&M	Operations and Maintenance.
OpenFOAM	Open-source Field Operation And Manipulation. An open-source CFD tool box.
OWC	Oscillating Water Column.
OWSC	Oscillating Wave Surge Converter.

PISO Pressure Implicit with Splitting of Operator.

PRM Power Regulation Module.

PTO Power Take Off system to convert extracted energy into a useful form.

PWT Physical Wave Tank.

RAO Response Amplitude Operator, used to express a response relative to a unit wave height at each frequency.

RANS Reynolds Averaged Navier-Stokes Equations.

RIRF Radiation Impulse Response Function.

ROCs Renewable Obligation Certificates.

RPM Revolutions per Minute.

RZ Relaxation Zone.

SB Static Boundary.

SLS Servicable Limit State.

SPH Smoothed Particle Hydrodynamics.

STL Stereolithography file format. Used by CAD software to represent 3D Systems.

SWL Still Water Level. The mean water level in the absence of waves.

TRL Technology Readiness Levels.

TPL Technology Performance Levels.

ULS Ultimate Limit State.

VoF Volume of Fluid methodology.

WEC Wave Energy Converter.

WES Wave Energy Scotland.

Nomenclature

Below is a list of commonly used symbols and their meanings and units unless otherwise explicitly stated in the text. For symbols that have multiple meanings, their use in different applications should be distinct enough that it is clear which meaning is implied.

a_b	Acceleration of a body (m/s^2)
a_i	Amplitude of wave frequency component in irregular seas (m)
ak	Wave steepness
A	Area (m^2)
A_{CR}	Crest amplitude (m)
A_{cy}	Cross sectional area of a piston (m^2)
B_{ij}	Component of radiation damping matrix ($i = j = 5$ indicates Pitch in Nms/rad)
B_{PTO}	PTO angular damping coefficient (Nms/rad)
C	Hydrostatic stiffness (for pitch this is in Nm/rad)
C_a	Coefficient of added mass ($\rho C_a A = M_{ij}$)
C_D	Coefficient of Drag
C_M	Inertia coefficient ($C_M = 1 + C_a$)
C_p	Phase velocity, or celerity (m/s)
C_g	Group celerity (m/s)
C_G	Generator Damping (Nms/rad)
$\underline{d}$	Distance vector between two cell centres
D	Diameter of a cylinder (m)
D	Motor Displacement (m^3)
E	Average energy per unit surface area of the wave (Jm^{-2})
f	Wave Frequency (Hz)
F	Water surface function
F_e	Excitation Force (N)
F_R	Froude Number
$\underline{F}$	Force tensor for a body in the six modes of motion $\underline{F} = (F_x, F_y, F_z, M_x, M_y, M_z)$
g	Acceleration due to gravity (9.81ms^{-2})
h	Water Depth (m)

H	Individual zero up-crossing wave height (m)
H_max	Maximum wave height (m) in a given number of waves N_R
H_s	Significant wave height (m)
I	Moment of inertia (kgm^2)
I	Electrical Current (A)
J	Energy flux of a wave (W/m)
k	Wavenumber, $k = 2\pi/\lambda$ (rad/m)
k	Turbulent kinetic energy (J)
K_C	Keulegan Carpenter number
L	Characteristic length of the device (m)
L_V	Vertical extent (or Height) of body (m)
M	Mass (kg)
M_A	Added mass (kg)
M_{ij}	Component of Added mass matrix ($i = j = 5$ indicates pitch in Nms^2/rad)
$\underline{n}$	Unit vector normal to the surface
p	Pressure (N/m^2)
p_{atm}	Atmospheric pressure (N/m^2)
p_D	Dynamic pressure (N/m^2)
p_0	Stagnation pressure (N/m^2)
P	Absorbed wave power (W)
P	Hydraulic oil Pressure (N/m^2)
Q	Generic flow variable field
Q_i	Volumetric flow rate into a control volume (m^3/s)
Q_o	Volumetric flow rate out of a control volume (m^3/s)
R	Ratio between velocities at two cell layer elevations
R	Electrical Resistance (Ω)
Re	Reynolds Number
s_{max}	Maximum stroke length $(^o)$
S	Control surface
$S_n(\omega)$	Variance density spectrum (m^2/Hz)
S_Q	Source of generic flow variable field
t	Time (s)
T	Wave Period (s)
T_G	Generator Torque (Nm)
T_m	Motor Torque (Nm)
T_p	Peak wave period (s)
$\underline{U}$	Velocity tensor for a body in the six modes of motion
	$\underline{U} = (U_x, U_y, U_z, \Omega_x, \Omega_y, \Omega_z)$
U_0	Amplitude of velocity oscillation (m/s)
U_R	Ursell Number
V	Volume (m^3)

V	Voltage (V)
x, y, z	Cartesian coordinates
$\dot{x}$	Linear velocity (m/s)
$\ddot{x}$	Linear acceleration (m/s^2)
X_o	Amplitude of displacement (m)
$\underline{u}$	Velocity vector $\underline{u} = (u, v, w)$
α	Phase fraction, $\alpha = 1$ is water and $\alpha = 0$ is air
α_R	Acceleration relaxation factor
β	Blending function used in wave relaxation zones
δ	Logarithmic decrement
ϵ	Rate of dissipation of turbulence energy (m^2/s^3)
η	Surface elevation (m)
η_v	Volumetric efficiency
η_{mech}	Mechanical efficiency
γ	Blended differencing coefficient
λ	Wave length (m)
κ	Bulk Modulus
ν	Kinematic viscosity (m^2/s)
ω	Shaft rotational speed (rad/s)
ω_{nom}	Nominal shaft rotational speed (rad/s)
ω	Circular wave frequency, $\omega = 2\pi/T$ (rad/s)
ω	Specific turbulence dissipation (s^{-1})
ω_n	Natural frequency (rad/s)
ϕ	Velocity potential
ϕ_f	Mass flux ($kgs^{-1}m^{-2}$)
ϕ_I	Incident velocity potential
ϕ_D	Diffracted velocity potential
ϕ_R	Radiated velocity potential
ψ	Stream function
φ_i	Phase of wave component in irregular seas
ρ	Density. For seawater this is taken as 1025kgm^3
τ_{fric}	Frictional torque (Nm)
τ_{noload}	No load motor torque (Nm)
θ_{no}	Measure of non-orthogonality of cells
θ	Pitch of the paddle
$\dot{\theta}$	Angular velocity of the paddle (s^{-1})
$\ddot{\theta}$	Angular acceleration of the paddle (s^{-2})
Θ_o	Amplitude of angular displacement
ζ	Damping ratio describing decay of oscillations in a system after a disturbance

When discussing the shape of the paddle or its motion particular terminology will be used. The “shoreward” motion is defined as “forwards”, and the two terms will be used interchangeably. Similarly the terms “seawards” motion and “backwards” motion are equivalent. The front face of the paddle is that which faces the incident wave, and is also the concave face of the curved paddle.

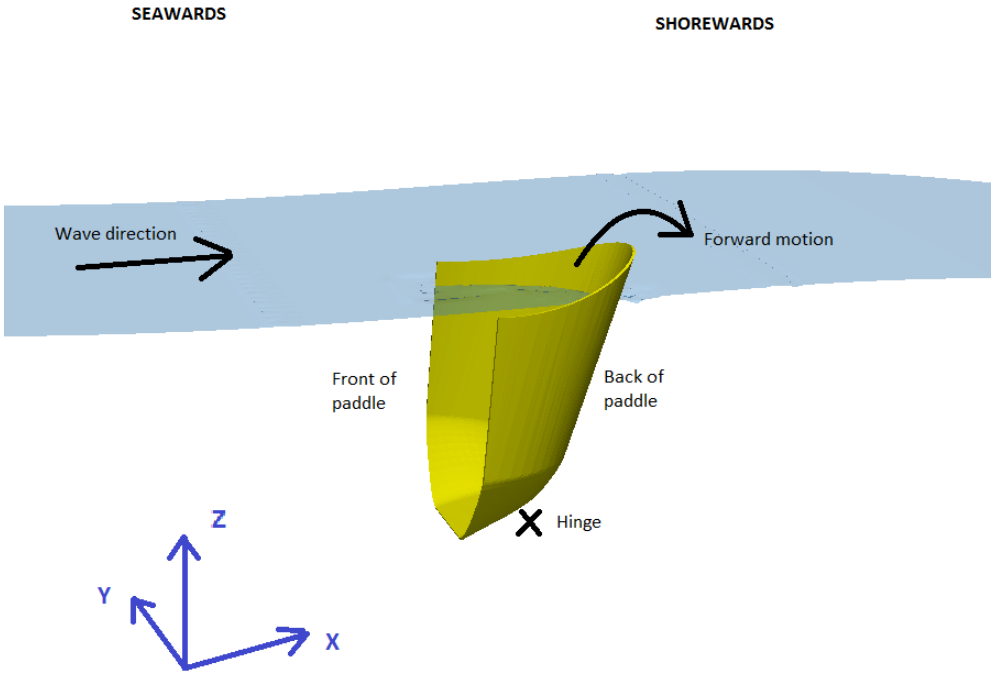

Part I

Background of Research

Chapter 1

Introduction

1.1 Current State of the Wave Energy Industry

In July 2017 the £10 million Saltire Prize passed without any winners, or even real contenders. It was open to any team that could demonstrate a commercially viable wave or tidal stream technology by providing a minimum 100GWh of electrical output in a continuous 2 year period. In light of this disappointment, First Minister Nicola Sturgeon acknowledged that for marine energy, the path to commercialisation was longer and more difficult than initially anticipated. The prize was originally announced in 2008, the same year that three Pelamis devices were preparing to be towed off the Portuguese coast to create the first wave farm and nearly £50m of UK public funding was spent on marine energy infrastructure (EMEC, Flowave, Wavehub and NAREC)(Carcas, Davies, and Edge 2017). Industry confidence was high, but unfortunately short-lived.

Technical Challenges

Technical failures have led to the eventual demise of a number of wave energy projects, and the collapse of both Pelamis and Aquamarine in 2014 and 2015 respectively. Some failures may have been down to bad luck or extenuating circumstances but most have been due to the lack of understanding of the key challenges of the wave environment. Earlier players in the industry fell victim to the assumption that components used in other industries like oil and gas would be sufficient for use within Wave Energy Converters ("WECs"). However, the design cases are quite distinct: a large stationary oil platform behaves very differently in waves in comparison to a relatively small and dynamic WEC. Even in operational conditions a WEC will experience variable loading characterised by slow moving components under significant forces. This is coupled with the usual issues from a harsh salt water environment: corrosion, biofouling and ingress of sediment, which can impact the lifetime of the device by weakening materials or causing critical components, such as bearings, to seize. Key componentry that would be far beneath the water surface in an oil and gas installation operates close to, or at, the air-water interface in a WEC where highly oxygenated water accelerates the corrosion process. Furthermore, marine growth can alter the device hydrodynamics and prevent seals working correctly, both of which affect the buoyancy of the device. Failure of watertight fittings

was considered to be the reason behind the sinking of Finavera Renewables' AquaBuOY 2.0 in 2007 (Page 2007) and is also the likely reason why Wello's Penguin WEC has recently sunk at EMEC's Billia Croo wave test site (The Orcadian 2019).

A WEC must contend with extreme waves in stormy conditions, which can be an order of magnitude larger than the forces experienced in usual operation. Large waves can increase the amplitude of motion resulting in impact loadings from interaction with mechanical end stops or in the case of moored devices detachment from their moorings, as happened with the Oceanlinx device in 2010 (Arnold 2010) and the CETO 4 device in 2014 (Parkinson 2014).

Industry Failings

With such a litany of technical failures and ensuing bad press for the wave energy industry, it is hard to believe that the blame lies solely with the engineers and technology developers. External pressures to follow a particular development path or strategy have led to the omission of basic testing and have restricted the flexibility needed to truly innovate and resolve fundamental issues. These commercial and political failures have stemmed from a lack of understanding between developers and investors or governmental bodies. For example, timelines driven solely by investors led to the premature installation of the Oyster device, without full quality control checks or dry testing of the pressurised system. In lieu of these land based tests, the device underwent critical commissioning assessments subsea where access and maintenance are risky, expensive and inhibited by the challenging environment.

This hasty drive for full scale deployments was also encouraged by a number of government schemes. Inappropriately targeted funding put a premium on full scale devices, and even arrays, rather than demonstrating feasibility at less capitally intensive scales. Like the Saltire prize, vast amounts of this funding went unclaimed (Hannon, Diemen, and Skea 2017): in 2007 the Department of Trade and Industry's £42m Marine Renewable Deployment Fund was completely untouched as no full scale demonstrator was able to continuously operate for 3 months; in 2009 only £9.6m of the £22.5m Marine Renewables Proving Fund was awarded; and in 2012 the Marine Energy Array Demonstrator, requiring an array of three devices with combined capacity of 3MW to generate at least 7GWh, unsurprisingly was not allocated.In addition, as Hannon et al point out, these unrealistic expectations were self-defeating as developers over-promised their technological progress in order to bid for funding and then subsequently under-delivered.

The government also made a number of amendments to policy regarding first the Renewable Obligation Certificates ("ROCs") and later the Contracts for Difference ("CfD"), which dampened the investment climate. Most recently the government has removed the ring-fenced subsidy for marine energy, forcing wave and tidal project developers to unsuccessfully contend for CfD against bids from offshore wind (DBEIS 2017). But maybe the government is learning from past mistakes. Schemes like CfDs are directed at technology that is already operating reliably but needs help in making further incremental changes; they offer little support to early stage innovation (Kingston 2017). Making these CfDs practically unattainable to the wave energy industry perhaps removes the temptation to go too big too quickly.

Without an established market for their devices, a number of WEC developers have used

patents to protect the value of their technology. But the value of patents is dubious in this industry. Firstly, patents registered in the early 2000's will likely lapse before any device is properly commercialised. It is also unlikely that the real value for a device will come from the overall shape. A much bigger determining factor for the success of a device will be internal subsystems and how they are controlled, which would be better kept as trade secrets. Secondly, patents have sometimes prevented innovation or any real deviation from the original concept, due to fear of moving outside the claim's scope. Furthermore, this desire to protect intellectual property has prevented collaboration within the industry and as a result has led to a failure to learn from previous errors or naiveties.

Successes & Potential

There have, however, been successes. In the decade that the Saltire prize was in existence there was a flurry of activity in the wave energy industry and some major steps forward have been made. The total production may be a lot less than the minimum criteria of the prize but it is not trivial either: the 800kW Oyster device installed at EMEC in June 2012 allegedly generated 1MWh in 5 hours (Renzi, Doherty, et al. 2014); the two 750kW Pelamis P2 devices produced 250MWh over 2-3 years; and the Mutriku plant, which was the next iteration of the shore-based OWC LIMPET device (493MWh from 2006-2013 (Carcas, Davies, and Edge 2017)), successfully operated between 2011 and 2018 supplying 1.6GWh to the grid (Tethys 2018). Furthermore, the developers of WaveRoller, an OWSC, operated three 100kW prototypes between 2012-2014 providing enough data for Lloyd's Register to award the first Technology Qualification certificate for an ocean energy device (AW Energy 2018).

It is true that devices have been built at large or full scale, they have been installed and they have been operational. The behaviours and outputs have also been close to those estimated by wave-to-wire models, providing confidence in the tools used by the industry. The only problem is that the devices have not been operational for very long. Although the industry may not have met the predictions of earlier road maps[1], marine energy will undoubtedly play an important role in the future in resolving the energy trilemma and ultimately combating climate change. The wave energy resource is massive; some more idealistic studies estimate it to be 29,500TWh/yr (Kempener and Neumann 2014). Though this is much lower when pragmatic constraints such as technical feasibility, geography and economics have been enforced, there is still a significant potential. Recoverable energy from the US coastline is estimated as 1170 TWh/yr (Jacobson, Hagerman, and Scott 2011), whilst in the UK estimates vary between 50 - 69 TWh/yr (The Carbon Trust 2011),(The Crown Estate 2012), though the wide variation in published resource estimates hints at the high level of uncertainty in their calculation.

Industry Progress

So what are the missing pieces of this complex wave energy puzzle? What is still hindering the industry and how are these shortcomings being addressed allowing the sector's potential to be realised?

Two major remaining challenges are the lack of corroborated data that indisputably prove the

[1] even in 2016, after the collapse of the big contenders of wave energy, some reports still believed the installation of a further 610MW of ocean energy was achievable by 2021(Ocean Energy Forum 2016)

worth of a particular device and the lack of incentives for investors due to the absence of clear signals from government or demonstrable revenue streams.

The first challenge requires more open reporting of performance figures and further testing both at larger scales and in conditions outside the normal operating envelope. Initiatives like Wave Energy Scotland ("WES"), a 100% funded wave-focused programme, provide a rigorous process to reduce both technical and commercial risks to developers, offering them the opportunity to innovate and assess their technology pragmatically. As part of their stage-gated back-to-basics approach, WES stipulates the development route, requiring demonstration of realistic performance at increasing scales as well as device survival in extremes. But as WES's funding is determined by Holyrood, it is currently only guaranteed until 2021. This imposes tight deadlines on their programme and they may be at risk of inducing the same external pressures they were trying to alleviate.

The lack of corroborated data can also be addressed through higher fidelity numerical modelling and increased confidence in model outputs. A clearer indication of realistic Mean Annual Energy Production ("MAEP") can attract investors. Similarly, a better understanding of device loading accelerates the design and manufacture process where previous uncertainty had led to indecision and abstention from cutting steel. These models are essential in progressing the performance of the technology and reducing risks before developers incur the immense, and historically destabilising, cost of full scale prototypes.

Increased numerical modelling capabilities, however, may not have helped prevent the failures experienced by the former industry leaders. The roots of the problem were not necessarily components that would have been de-risked through numerical modelling. When one of the cylinder modules of the Oyster device catastrophically failed, fracturing a 2" thick steel casing and destroying the cylinder rod, the cause was found to be an isolation valve that through vibration or turbulence had spun itself closed. The build up of pressure within the system should have been alleviated through a pressure relief valve, however that also malfunctioned and allowed pressure to rise to an estimated 5 times the design value (Anonymous 2019). The only method that could have predicted this sort of failure is a comprehensive Failure Mode, Effects and Criticality Analysis ("FMECA") and full understanding of the differences between the normal use and reliability of a component and its operation in a WEC.

Overcoming the second challenge of a lack of investor incentives will largely depend on successful lobbying by the industry as well as the favourable outcome of initiatives like WES; but developers also have a part to play. Targeting smaller or more niche markets and layering services, like aquaculture, coastal protection or data collection, can demonstrate the commercial value of wave energy beyond grid scale. Meanwhile, developers can test their concepts in lower energy sites closer to shore and accumulate operational data that could direct further innovation and lead to Technology Qualification. Demonstration of a robust device with additional benefits and alternative revenue streams will only help to improve investor confidence.

The industry is still a number of steps away from achieving a commercial wave farm. Currently the WES estimate that the earliest deployment of multiple devices is 2025. However, this is dependent on the successful outcome of their Stage 3 competition as well as a problem free pre-commercial demonstration beginning in 2021 and an encouraging investment climate. In order to provide a meaningful amount of electricity to the grid, with multiple deployments, it

is likely an additional decade is needed to set up supply chains and appropriate Operations and Maintenance ("O&M") infrastructure. What is needed is realism with regard to the state of the sector. Previous overly-optimistic evaluations and unattainable trajectories have achieved nothing save for undermining the legitimacy of the industry as a whole. With increased modelling capabilities, comprehensive de-risking methodologies and development of alternative markets, wave energy will begin to realize its potential.

1.2 Types of Wave Energy Converter

The underlying theory of waves, and the orbital path taken by water particles allows for a number of different approaches to the conversion of wave energy. The distinction between types of device is usually by the WEC's degree of freedom: pitch, heave or surge. Devices are further classified by their proximity to the shore, and whether they are floating or fixed to the seabed. However, common to all WECs are four main subsystems: the prime mover that converts wave energy into a usable mechanical motion; the PTO that converts the energy into electrical power; the control of the device to maximise power and avoid extreme loading; and the foundations or moorings against which the WEC reacts. Diagrams of the operation of the main types are shown in Figure 1.1, and are briefly explained below:

- **Point Absorbers** target the heave motion. They are characterised by a large float that sits on the surface of the water, much like a buoy. It converts the motion of the buoyant top, relative to the base, into electrical power. Notable examples: The Wavestar (Wavestar Energy 2011) which houses the PTO subsystems on a large platform out of the water or Carnegie's CETO device (Carnegie Clean Energy 2017) with a bottom mounted PTO.
- **Submerged Pressure Differential devices** appear similar to point absorbers but are deployed closer to shore in shallower water. They exploit changes in sub-sea water pressure from waves by converting the resulting motion to electricity with a direct-drive generator. Notable example: Archimedes Waveswing submerged wave power buoy (AWS Ocean Energy Ltd 2016).
- **Attenuators** generate power by the hinged motion between two surface bodies. The dynamic response of the different bodies due to wave action causes a relative motion about the hinge that drives a generator. They are generally located parallel to the direction of wave. Notable examples: Pelamis (The European Marine Energy Centre Ltd 2017) and more recently Mocean (McNatt 2017).
- **Oscillating Wave Surge Converters** target the surge motion of wave action. A paddle oscillates like a pendulum about a pivoted joint, which can be mounted on the sea bed or floating. In a near shore environment an OWSC benefits from the concentration of wave energy both in the surge motion and as a result of refraction. Notable example: Aquamarine's Oyster (The European Marine Energy Centre Ltd 2015) and, the subject of this research, Zyba's CCell (Bateman 2018).
- **Oscillating Water Columns** ("OWC")operate by forcing a column of air through a turbine as the water elevation changes within a partially submerged hollow container. These can

be floating offshore or built into the shoreline. Notable example: LIMPET (Land Installed Marine Powered Energy Transformer) (The Queen's University Belfast 2002).

- **Overtopping devices** operate like a hydro plant with a submerged turbine at its center. Waves are encouraged to overtop the perimeter of the reservoir from which the water then flows through the turbine to generate power. Notable example: Wave Dragon (Wave Dragon 2017).

Less common device types are:

- **Rotating Mass devices** like the Penguin being developed by Wello Oy (Wello Oy 2018). It generates power through the rotational motion of a large mass contained within an asymmetrical body, which is designed to maximise motion from the waves.
- **Bulge Wave devices** like Anaconda (Sustainable Energy Research Group 2012) consist of a rubber tube filled with water anchored at one end to be parallel with the wave direction. As waves pass over the top of the tube, the pressure variations along its length generate a bulge wave which progresses along the tube to the PTO.

Of all the ways to convert wave energy there has been, as of yet, no clear winner. Prototypes of all device architectures continue to be investigated, though some are purely in the interest of science and have less potential to be commercialised (Hannon, Diemen, and Skea 2017). Currently the innovation behind most of the individual subsystems is also being driven by WEC developers. A lack of consensus on design means that other actors in the supply chain have less confidence and are less likely to fund their own innovation. However, this supplier-led innovation was critical in the up-scaling of offshore wind. One of the largest challenges to delivering more power from wind was gearing, but there was a clear signal to the gearbox developers that their R&D effort would be recouped if they were successful. The WES programme has targeted this cross sector collaboration with funding calls not just for the novel WEC, but also for the power take off system; structural materials and manufacturing processes; and control systems (Wave Energy Scotland 2019). Going into the third stage of the novel WEC competition, a hinged raft and a fully-submerged point absorber are still in contention and there is finally evidence of this collaboration particularly with regards to the PTO and control.

However, it is less clear whether the WES programme has provided consensus on device type. The competition judges the team's ability to deliver the project, as much as the technology itself; in this nascent industry the two are very hard to decouple. Babarit created a database of WEC hydrodynamic performance by reviewing the reported Capture Width Ratio ("CWR") from 90 different WEC studies that considered an incoming wave resource of around 25kW/m (Babarit 2015), the outcome of which is summarised in Table 1.1. The classifications used in the study differ slightly to those described above but it is likely that both of WES's two finalists would be placed within the "Heaving Devices (plus variants)" category. It is interesting that this category performs second-worst, though self-admittedly WES backs projects that offer the biggest reward for the smallest risk, and heaving devices have historically been one of the most studied concepts. OWSCs take both extremities, with fixed concepts claiming the highest energy absorption per width of device and floating concepts offering least efficiency. Babarit does not mention specifically the location offshore of these devices, but the difference

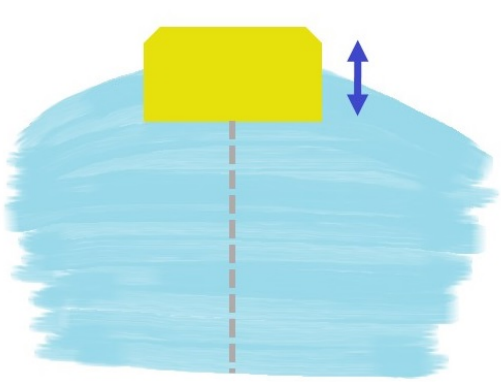

(a) Point Absorber

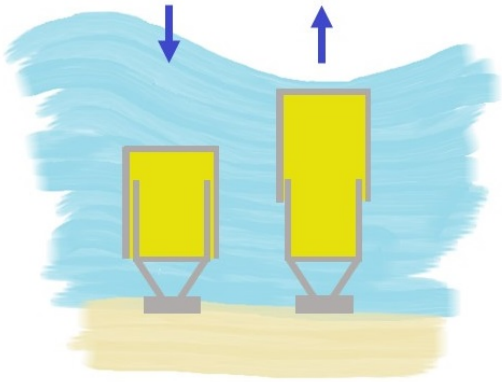

(b) Submerged Pressure Differential

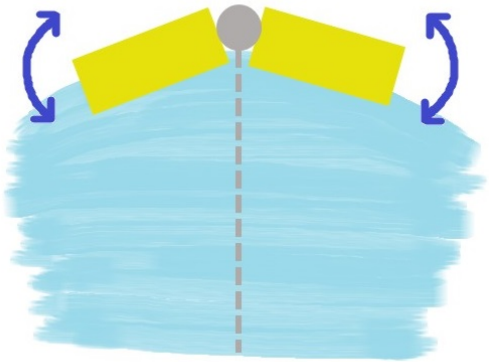

(c) Attenuator

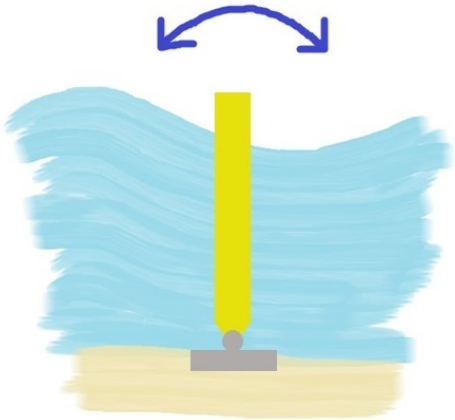

(d) Oscillating Wave Surge Converter

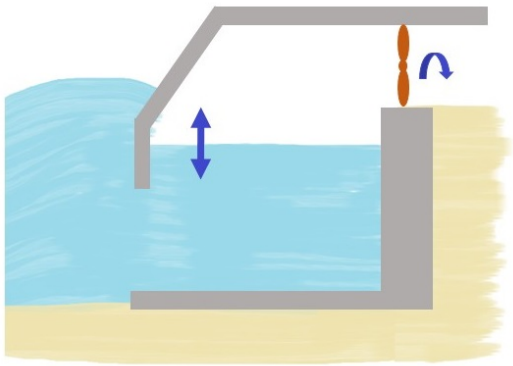

(e) Oscillating Water Column

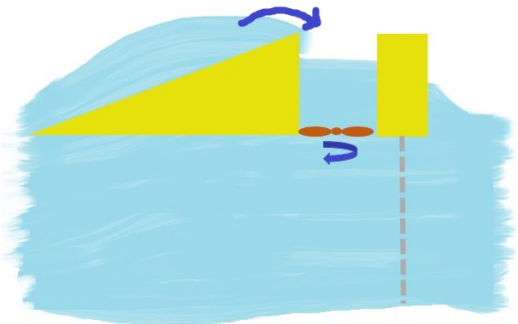

(f) Overtopping Device

Figure 1.1: Types of Wave energy Converter

in OWSC data may offer evidence of the benefits of shallow water effects to these surge converters.

Table 1.1: Mean and standard deviation of CWR and characteristic dimension for each WEC category. Reproduced from (Babarit 2015)

	Capture Width Ratio (%)		**Characteristic Dimension (m)**	
	Mean	**STD**	**Mean**	**STD**
OWCs	29	13	20	10
Overtopping Devices	17	8	124	107
Heaving Devices	16	10	12	7
Fixed OWSCs	37	20	18	14
Floating OWSCs	12	5	33	24

1.3 The CCell Concept

This project has been sponsored by Zyba Ltd, an engineering company with expertise in numerical modelling. Since 2014 the majority of Zyba's focus has been on the development and commercialisation of CCell, a curved OWSC. The curvature of the prime mover is designed to enhance the hydrodynamic performance of the device as well as provide additional structural strength and reduce the material requirements in construction. A time line of CCell's evolution and important milestones is depicted in Figure 1.2.

The idea of improving the efficiency of energy capture of an OWSC by curving the paddle was initially conceived in 2012, and following a convincing performance during initial laboratory testing at UCL, a patent application was made and awarded shortly after. Conceptual development continued throughout 2013 and 2014 with the integration of a controllable PTO for a secondary phase of physical testing at Plymouth University's COAST laboratory. The device was designed, like other OWSC concepts, to be fixed to the sea bed in shallower coastal waters where the horizontal motion of water particles is amplified due to shoaling effects (Folley, T. Whittaker, and Henry 2007). A larger scale version of the device was manufactured from steel and deployed near shore in 2015. The aim of this preliminary sea trial was to evaluate the manufacturability of the device and provide insight into basic offshore operations, including a suitable deployment strategy. A key learning from this work was the expense of manufacturing a curved structure in steel and the additional costs associated with transportation due to its weight. This issue aligned with the focus of the WES call for novel WEC devices, specifically focussing on the prime mover and their overall objective of reducing WEC costs by 50-75% in the medium term.

In 2016 work began on the WES project to optimise the design of a CCell paddle made from composites. Fibre reinforced composites were chosen as they provide increased geometrical freedom allowing complex shapes and areas of double curvature that could not otherwise be formed with conventional materials and manufacturing processes. Composites provide high strength to weight ratios as well as corrosion resistance leading to a lighter weight and more durable CCell device than the steel precursor.

As part of the evolution of CCell, in the WES project, a floating device was designed and tested. This design choice was made to overcome a limitation discovered in previous lab

testing: that when the top of the device was submerged by just 0.2m an estimated 26% of power was lost. A floating concept would maintain its draught and optimal operating position, thus accommodating changes in sea level due to the tidal cycle and expanding the number of potential sites for deployment.

In the competition guidelines WES stipulated the creation of hydrodynamic and performance models to corroborate analytical predictions, gain understanding of non-linearities and assess the impact of the device's leading dimensions. This doctoral research project began in June 2016, mid way through the WES project, with the initial focus of fulfilling the above modelling and optimisation criteria. Zyba had initiated the development of a Computational Fluid Dynamics ("CFD") model in OpenFOAM, however prior to the commencement of this EngD, it was limited in accuracy and restricted to simulations of a static device in a wave field.

Physical modelling provides valuable information on body motions, structural loads and hydrodynamic power capture efficiencies of the prime mover and was a key outcome of the WES project. A variety of different paddle shapes were considered and tested at 1:15 scale in multiple rounds of tank deployment allowing for device exploration and optimisation prior to the final mandatory performance assessment. These tests also provided key physical data with which to validate the Numerical Wave Tank ("NWT") developed in OpenFOAM.

At the completion of the WES project, consideration of Zyba's business model and the path to commercialisation for CCell dictated a return to a fixed base concept. A commercial application for a smaller device, targeting coastal protection and coral restoration rather than electricity export, was identified through work with the Global Coral Reef Alliance. Coupling CCell with an electrochemical process used to accumulate limestone around steel rebar produces the the required electricity at the point of use. The power requirement for this process is much smaller (2-10kW) allowing previously overlooked deployment sites with a lower wave resource to be considered. As a result, a pilot device was installed on the east coast of Mexico in the Carribean Sea in July 2018. The benefit of this approach is that the WEC is effectively being tested in a nursery site, providing operational data and experience that can be used in the future when provision of consumer electricity is deemed commercially viable.

As the priorities of the sponsor company have changed, the modelling rationale and optimisation parameters have also adjusted. As such, there is work detailed within this thesis that is directed to either the "Floating" concept evaluated in the WES lab testing, Figure 1.3, or the "Fixed-base" pilot deployment concept, Figure 1.4. Where relevant, it will be made clear which device is being discussed using this terminology.

Figure 1.2: History of the development of Zyba Ltd's wave energy converter CCell. Images within figure are courtesy of Zyba Ltd.

Figure 1.3: Artistic impression of Floating CCell Concept, developed during the WES project. Image courtesy of Zyba Ltd.

Figure 1.4: Artistic impression of Fixed-based CCell concept for coastal protection. Image courtesy of Zyba Ltd.

1.4 The Present Study

Considering the evaluation of the current state of the wave energy industry there are two areas that appear central to the future success of the industry. These are the accurate prediction of power performance and the integration of suitable survivability measures. Crucially, these are needed earlier in the development process before stakes, and costs, get too high.

Numerical codes adopted from the Oil & Gas industry do not fully reflect the operation and hydrodynamics of a WEC. However, the barriers to entry and feasibility of a fully non-linear design process result in developers relying on these linear codes for performance predictions. The intention of this study is firstly to showcase where and when these linear codes can

be used and when more complex modelling techniques are necessary. Secondly, this work aims to present an appropriate methodology and develop an extended set of tools for a WEC developer to analyse both the power output and expected loadings with higher fidelity.

Of the four main subsystems of a WEC this present study is focused initially on the hydrodynamics and primary wave absorption system that exploits the wave power. The power take-off ("PTO") subsystem is also then considered in both the determination of its design and effective representation integrated within the hydrodynamic modelling.

Detailed electrical design of the control and instrumentation system was provided by other affiliates of Zyba, however, the software development, integration and testing of this system has formed a secondary focus of the period of research at Zyba. Construction of the PTO system and manufacture of the telemetry system for dry-testing, provided the opportunity to evaluate the accuracy of the innovative coupled non-linear modelling approach.

The breadth of topics covered in the study reflect the varied work carried out at Zyba both in numerical modelling and development of software, as well as physically building and testing different components.

1.4.1 Aims & Objectives

The overall aim of this project is to accelerate the development of a wave energy device through an appropriate numerical modelling strategy. The underlying objectives are to:

- Model WECs in Operational Conditions through:
  - Assessment of suitability and limitations of modelling techniques available to a wave energy developer at different stages of the design process.
  - Simulation of the entire CCell WEC including the coupled behaviour of hydrodynamics and PTO system.
- Evaluate and Enhance WEC Survivability by developing a tool kit for the engineering team to evaluate design suitability in specific extreme loading scenarios
- Develop a recommended strategy for use of the CNWT with appropriate methods to optimise the design work flow.

1.4.2 Contribution to Knowledge

This work is an original investigation of the hydrodynamic performance of wave energy converters, in particular the CCell OWSC, through use of a variety of numerical modelling tools. The contribution of knowledge to the industrial sponsor consists of the development of suitable methodologies and work flows for the assessment of different WEC designs, which was used extensively in the design of the pilot device. Listed below are the main contributions to knowledge:

- Evaluation of numerical techniques currently available to wave energy developers and a better understanding of their limits of accuracy particularly when considering an asymmetrical device.
- Development of a CFD NWT ("CNWT") that can efficiently model a fixed bottom OWSC.

This also included the development of a work flow for the industrial partner and definition of suitable metrics to evaluate a WEC design.

- Coupling of a more accurate PTO model with CFD simulation that encompasses realistic system losses and dynamics of the hydraulic PTO system. This provides a better understanding of the behaviour of the PTO and its interaction with the moving wave paddle.
- Software and hardware development of telemetry system for low power pilot deployment which prioritised low cost.
- Extension of the CNWT to provide insight into design load cases such as shallow water extremes or directional waves. This also included the coupling of the CFD output with FEM.

Although focused on the development of CCell, it provides knowledge that contributes to both the industrial partner company and the wider wave energy industry, as elements of the work are easily adapted to consider alternative WEC concepts. For example, the PTO model is in effect a plug-in for OpenFOAM and needs only the current time step and expected angular velocity of the prime mover, it could be used for any WEC with an hydraulic PTO.

Publications

Worden Hodge, C., Bateman, W., Zhiming, Y., Thies, P. R., Bruce, T. (2018). “Coupled Modelling of a Non-Linear Wave Energy Converter and Hydraulic PTO”, in Proceedings of the 28th International Ocean and Polar Engineering Conference, 10-15 June, Sapporo, Japan.

Worden Hodge, C., Bateman, W., Zhiming, Y., Thies, P. R., Bruce, T. (2017). “Performance analysis of the CCell wave energy device”, in Proceedings of the Twelfth European Wave and Tidal Energy Conference, 28-31 August, Cork, Ireland.

1.4.3 Outline of Thesis

The thesis is arranged into four distinct parts, as demonstrated by the mind map in Figure 1.5, showing the relationship of each chapter to the relevant part. The first part focuses on the background of the research, beginning with an assessment of the current state of the wave industry and the challenges that have hindered the progression of the sector, Chapter 1. This is followed by a description of the development journey undergone by the sponsor company and how this research fits into the timeline of events along with the works objectives and main contributions to knowledge. The second chapter of the background research section, Chapter 2, contains a brief overview of the theory behind numerical modelling of WECs. It is written as a reference for the following chapters to prevent excessive mathematical formulae interrupting the narrative.

The second part is titled “Selection and Implementation of Modelling Framework” and is again split into two chapters. The first, Chapter 3, is essentially a literature review of previously used techniques and their fallibilities particularly due to assumptions of linearity. It concludes with the recommendation of using CFD for the modelling of CCell. Chapter 4, then discusses the methodology behind the development of a CFD test bed including choice of solvers, verification and validation from initial tank testing of the floating CCell concept. The chapter then continues with a comparison of the results from forced oscillation tests in CFD against

the hydrodynamic coefficients calculated by a BEM solver commonly used in industry, as an evaluation of the applicability of linear theory for devices that are asymmetrical with respect to their fluid-structure interaction.

The third part contains the “Numerical Investigations” conducted in the CNWT to evaluate three separate concepts: design of the prime mover, realistic representation of the PTO system, and creation of extreme load cases. The first, contained in Chapter 5, evaluates the parameter space of the CCell concept, providing understanding and rationale for certain design decisions as well as considering power absorption estimates. Chapter 6 details the development of a non-linear PTO model and its coupling with OpenFOAM to provide a better understanding of the interaction between the device’s hydrodynamics and PTO system. The PTO system for the pilot deployment is then used as a test bed to investigate the validity of the coupled solution. The concept of extreme loads is then considered in Chapter 7, beginning with a discussion of device failure and how numerical modelling can be used to de-risk the structural design of a WEC. The effect of wave slam, directional waves and steep waves are then investigated through the development of suitable modifications to the CNWT and knowledge gained from laboratory testing of the floating CCell device.

The final part of the thesis, Chapter 8, offers final remarks drawing together a discussion of the main findings and conclusions, as well as identifying areas for further development and investigation.

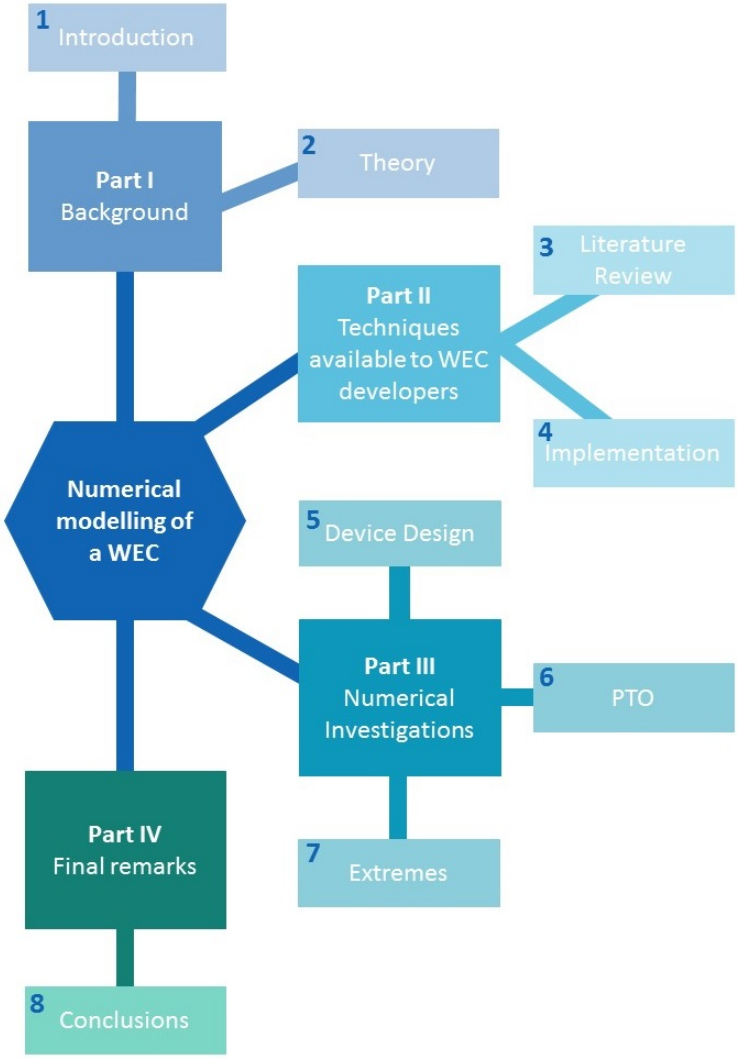

Figure 1.5: Thesis structure and content

Chapter 2

Numerical Principles

The purpose of this chapter is to provide the background theory required in the subsequent chapters. It is presented in a condensed manner to highlight the importance of the concepts introduced to the wider application in WEC development. The intention is that this chapter is only required for reference, and prevents the excessive use of equations in the main text of the thesis. For a more involved derivation or discussion of the following "textbook" material a number of references are suggested at the top of each section. The topics covered are:

- Founding principles of fluid dynamics, including simplifications to potential flow.
- The solution of Laplace's equation to provide a linear mathematical representation of water waves.
- Terminology regarding hydrodynamics and the forces acting on WECs.
- Solution strategy and underlying discretisation required for CFD, including a discussion of turbulence modelling.

2.1 Governing Equations of Fluid Dynamics

Much of the theory in this section is drawn from the author's undergraduate Engineering lecture notes as well as the textbook "Fluid Mechanics" (Douglas et al. 2011).

The underlying principles of fluid dynamics can be contained in just two equations [1], which together are deemed sufficient to fully describe the flow of any Newtonian fluid. These expressions are:

- **The continuity equation:** mass must be conserved such that the rate of increase of mass in a fluid element equals the net rate of mass flow into the element.

$$\frac{\partial \rho}{\partial t} = -\left(\frac{\partial \rho u}{\partial x} + \frac{\partial \rho v}{\partial y} + \frac{\partial \rho w}{\partial z}\right) = - \bigtriangledown \cdot (\rho \underline{u}) \tag{2.1}$$

- **Navier-Stokes equation:** momentum must be conserved such that a body's rate of

[1] The complete governing equations contain the conservation of energy as a third equation which equates the rate of change of energy to the net flux of heat plus rate of work done on the fluid element

change in momentum is equal to the net force acting on it (i.e. Newton's second law)

$$\frac{\partial \underline{u}}{\partial t} + (\underline{u} \cdot \bigtriangledown)\, \underline{u} = -\frac{1}{\rho} \bigtriangledown p + \nu \bigtriangledown^2 \underline{u} \tag{2.2}$$

How these equations are formulated is dependent on the perspective taken, though all methods utilise a Control Volume ("CV") to help conceptualise (Bakker 2006). For example the frame of reference could be moving with the fluid (Lagrangian), or more commonly at a fixed location with fluid moving through the CV which is termed the conservative form (or Eulerian). The size of the CV also influences the formulation. For an arbitrarily sized CV the integral form is used, whereas if considering an infinitesimally small fluid element, the differential form is more appropriate. Taking the continuity equation as an example it was first shown in differential form, Equation (2.1), and is shown now in integral form:

$$\frac{\partial}{\partial t} \int_V \rho \delta V + \int_S \rho \underline{u} \cdot \delta S = 0 \tag{2.3}$$

Potential Flow

Simplifications are often made to these governing equations (Kersale 2018), such as:

- **Incompressible:** in incompressible flows the density of the fluid is assumed constant. This is equivalent to stating that the divergence of the flow velocity is zero. It reduces the continuity equation to:

$$\bigtriangledown \cdot \underline{u} = 0 \tag{2.4}$$

- **Inviscid:** in invsicid flows, the viscosity is assumed to be zero. This equates to perfect slip at a boundary, thus inviscid flows are unable to predict boundary layers or their separation and subsequent drag effect. Considering a flow as inviscid reduces the Navier Stokes equation, Equation (2.2), to the Euler equation, Equation (2.5). All fluids have a finite viscosity, thus the solution is idealised and can be unphysical such as D'Alembert's paradox. However, it can be useful in providing an approximate solution for the pressure distribution of the outer flow region which can then be coupled with a boundary layer approximation to build a full solution.

$$-\bigtriangledown p = \rho \left(\frac{\partial \underline{u}}{\partial t} + (\underline{u} \cdot \bigtriangledown)\, \underline{u} \right) \tag{2.5}$$

  The integrated form of the Euler equation provides a relationship between the pressure and velocity of the flow, more commonly known as Bernoulli's equation:

$$-\frac{\partial \phi}{\partial t} + \frac{1}{2} \left(|\bigtriangledown \underline{u}| \right)^2 + \frac{p}{\rho} + gz = C(t) \tag{2.6}$$

- **Irrotational:** in irrotational flow fluid elements do not rotate relative to their own centre of gravity, (a simple physical analogy is the pods on a ferris wheel). A principle cause of rotation in a fluid is torque from shear forces, thus inviscid flows are often also irrotational.

In irrotational flows the vorticity is zero:

$$\bigtriangledown \times \underline{u} = 0 \tag{2.7}$$

If we adhere to the governing principles of fluid dynamics but apply the above simplifications (incompressible, inviscid and irrotational), we arrive at potential flow theory. From vector calculus it is easy to show that for any scalar, ϕ,

$$\bigtriangledown \times \bigtriangledown \phi = 0 \tag{2.8}$$

thus for irrotational flow, the following must be true:

$$\underline{u} = \bigtriangledown \phi \tag{2.9}$$

where $\phi = \phi(x, y, z, t)$ is a continuous function and is called the velocity potential function. This is significant as in any point in the fluid, the derivative of this function in a particular direction provides the velocity component of a fluid particle at that point i.e:

$$u = \frac{\partial \phi}{\partial x}, v = \frac{\partial \phi}{\partial y} \text{ and } w = \frac{\partial \phi}{\partial z} \tag{2.10}$$

Now substituting the velocity potential into the continuity equation reduces the problem further and the underlying flow can be described by Laplace's equation:

$$\bigtriangledown^2 \phi = 0 \tag{2.11}$$

The strength of this approach is that the Laplace equation is linear, and therefore allows superposition. This means that known solutions can be combined through addition and subtraction to build up suitable solutions for different problems, i.e. if ϕ_1 and ϕ_2 both independently satisfy Laplace then $\phi_3 = A\phi_1 + B\phi_2$ is also a valid solution.

2.2 Water Waves

The full derivation of the linear equations for water waves is described in "Water Wave Mechanics for Engineers and Scientists" (R. Dean and Dalrymple 1993), which has been a frequent reference throughout this doctoral programme along with the lecture notes provided during the taught component.

Waves are the conduit for energy passing through a body of water. They transmit energy in orbitals, not the water itself, and are characterised by the fluctuations in the elevation of the water surface as gravity attempts to restore equilibrium to the displaced fluid. The initial acting force may differ but most commonly water waves originate from wind acting on the surface (wind-driven or surface waves). Other types (in increasing length of period) include: storm surge from atmospheric pressure changes, tsunami waves from underwater disturbances such as earth quakes, and tides from the gravitational pull of the Sun and Moon.

Water waves can in some cases be well approximated considering potential theory. It is

reasonable to assume that water is incompressible and viscous effects are concentrated at the sea bed and surface, thus much of the main body of fluid is effectively irrotational. Thus for the mathematical analysis of waves, Laplace's equation is an appropriate starting point.

2.2.1 Boundary Conditions

In order to obtain a unique solution to the Laplace equation, Equation (2.11), that is representative of the physical situation, suitable boundary conditions must be established. The most obvious boundary condition is that fluid cannot flow through an impermeable surface (e.g. a solid structure or the sea bed) or any interface such as the water's surface itself. If the surface is expressed as $F(x, y, z, t) = 0$ then the mathematical representation of this **kinematic boundary condition** is

$$\underline{u} \cdot \underline{n} = -\frac{\partial F/\partial t}{|\bigtriangledown F|} \tag{2.12}$$

where $\underline{n}$ is the unit vector normal to the surface.

The **dynamic free surface boundary condition** encapsulates the fact that a free surface cannot support a pressure variation across the interface, thus the pressure must be uniform along the wave form. This is satisfied by applying the Bernoulli equation, Equation (2.6) with a constant pressure at the surface. When this is evaluated at $z = 0$ and linearised this provides:

$$\eta = \frac{1}{g}\frac{\partial \phi}{\partial t} \tag{2.13}$$

2.2.2 Linear Theory

To facilitate the solution of the Laplace equation, Equation (2.11), and get an initial estimate of the characteristics of a wave field, Linear wave theory (or Airy wave theory) also assumes that the water is of uniform depth. The relevant surfaces are defined as:

- sea bed: $z = -h$
- free surface: $z = \eta(x, y, t)$ where η is the vertical displacement of the free surface about the horizontal plane $z = 0$ and for a progressive wave of a single frequency can be defined as:

$$\eta = \frac{H}{2} cos(kx - \omega t) \tag{2.14}$$

By first considering the kinematic boundary condition at the sea bed in conjunction with the dynamic free surface boundary condition it can be shown that a valid solution for the Laplace equation is:

$$\phi = \frac{\omega}{k}\frac{H}{2}\frac{cosh(k(z+h))}{sinh(kh))} sin(kx - \omega t)) \tag{2.15}$$

In order to satisfy the kinematic free surface boundary equation and have non-zero amplitude waves then another functional relationship is identified: the frequency dispersion relation, Equation (2.16).

$$\omega^2 = gktanh(kh) \tag{2.16}$$

Dependent on the water depth further approximations can be made to this relation, in particular with regards to $tanh(kh)$. When the argument of the hyperbolic tangent becomes large (as in deep water where the relative depth is $h/\lambda > 1/2$) this approaches unity, and when the argument is small we arrive at the shallow water ($h/\lambda < 1/20$) approximation where $tanh(kh \approx kh)$. Between these water depths (intermediate water depths) no simplification is made.

Equation (2.16) describes how a wave field of many different frequencies would "disperse" due to the various frequency components travelling at different celerities, or phase velocities, determined by $C_p = \lambda/T$ or ω/k. For wave energy, group velocity C_g is more important as it is the speed at which energy is transmitted. This is calculated by differentiating the dispersion equation with respect to the wave number, which produces Equation (2.17). Once this is evaluated it can be shown that n asymptotes to $1/2$ in deep water and 1 in shallow water. The phase speed of shallow water waves is less influenced by wave frequency (i.e frequency dispersion does not occur), thus individual components in a group better maintain their position as they all travel at a value close to the group celerity. This means that the wave energy and wave profile travel at the same speed, whereas in deep water the energy is transmitted at only half the speed.

$$C_g = \underbrace{\frac{1}{2}\left(1 + \frac{2kh}{sinh2kh}\right)}_{n} C_p \tag{2.17}$$

2.2.3 Energy in a Wave

The energy contained within a wave is made up of two constituents: the potential energy from the displacement of the free surface from its equilibrium position and the kinetic energy from the motion of the water particles. The total average energy per unit surface area of the wave available for energy extraction is therefore:

$$E = KE + PE = \frac{1}{8}\rho g H^2 \tag{2.18}$$

The average rate at which the energy is transferred over a wave cycle is called the energy flux of the wave, and is the product of the dynamic pressure and horizontal water particle velocity, averaged over a wave period:

$$J = \frac{1}{T}\int_0^T \int_{-h}^{\eta} \frac{\partial \phi}{\partial t} u \, dz \, dt \tag{2.19}$$

When the integration is completed up to the free surface this becomes:

$$J = EC_g \tag{2.20}$$

The Capture Width Ratio (CWR) is a metric related to the hydrodynamic efficiency of a device. It is defined as the ratio of absorbed wave power, P (in kW), to the wave resource, J (in kW/m), per the characteristic length of the device, L (in m), which is often taken as the device width.

$$CWR = \frac{P}{JL} \tag{2.21}$$

2.2.4 Irregular Waves

A monochromatic wave is an unrealistic representation of the actual ocean surface which comprises a seemingly random variation in surface elevation. However a record of this variation over a particular length of time can be described mathematically as the sum of a large number, N, of individual waves, with amplitudes a_i, frequencies ω_i and phases φ_i:

$$\eta = \sum_{i=1}^{N} a_i cos(\omega_i t + \varphi_i) \tag{2.22}$$

Different spectra can then be plotted by considering a particular variable against the frequency component. Of most use to a WEC developer is the continuous variance spectrum ($S_n(\omega)$ measured in m^2/Hz) as wave energy is proportional to this variance and therefore the total energy E_T of the spectrum can be calculated through simple integration with respect to wave frequencies, Equation (2.24).

$$S_n(\omega) = \lim_{\triangle\omega \to 0} \frac{1}{\triangle\omega} 0.5a^2 \tag{2.23}$$

$$E_T = \rho g \int_0^\infty S_n(\omega) d\omega \tag{2.24}$$

Many spectra exist that characterise the waves in particular areas, the simplest being the Pierson-Moskowitz spectrum developed from data in the North Atlantic, and the JONSWAP spectrum, which modified this to provide a better approximation for fetch limited seas like the North sea. In addition to having a frequency and amplitude, each individual wave component is also characterised by a direction as wave patterns from different wind events combine.

2.3 WEC Hydrodynamics

The main texts that have been referred to in this section are "Marine Hydrodynamics" (Newman 2018) and "Handbook of Ocean Wave Energy" (Todalshaug 2017), supplemented with the lecture series "Marine Hydrodynamics (13.021)" (Techet 2005).

An understanding of the interaction of structures and fluids and the forces acting on WECs or exerted by WECs on fluids is critical in WEC design and evaluation. When discussing the motion of a WEC the mode of motion is also important. There are six modes of oscillatory motion of a body: three translational motions in the direction of x, y and z and three rotational about each of the axes, as shown in Table 2.1.

Table 2.1: Modes of motion for a body with associated components of velocity and force.

Mode	**1**	**2**	**3**	**4**	**5**	**6**
Motion	Surge	Sway	Heave	Roll	Pitch	Yaw
Component $\underline{U}$	U_x *(m/s)*	U_y *(m/s)*	U_z *(m/s)*	Ω_x *(rad/s)*	Ω_y *(rad/s)*	Ω_z *(rad/s)*
Component $\underline{F}$	F_x *(N)*	F_y *(N)*	F_z *(N)*	M_x *(Nm)*	M_y *(Nm)*	M_z *(Nm)*

The rules of physics are equally applicable offshore as they are on dry land. Newton's second law, requiring that all forces acting on a body are balanced by the body's inertial force, is in particular used as a first port of call for numerical modelling and design of WECs. Loads

on a WEC originate from a long list of sources: gravity, buoyancy, PTO, wave excitation, wave radiation, drag and mooring configurations and can generally be categorised into fluid or external forces.

2.3.1 Fluid Forces

Assuming linearity, the wave field around a WEC can be described as the superposition of the incident wave ϕ_I, diffracted wave ϕ_D (interaction between the incident wave and a motionless body) and radiated wave ϕ_R (wave produced by the body oscillating in calm waters). The principal fluid forces are shown in Fig 2.1.

$$\phi = \phi_I + \phi_D + \phi_R \tag{2.25}$$

2.3.1.1 Hydrostatic

The hydrostatic force is the restoring force from the balance of gravity and buoyancy. When the amplitudes of motion are small the force can be linearised and a hydrostatic stiffness coefficient is used based on the water plane area of the body. The hydrostatic stiffness is affected by two things: changes in the submerged volume and moment arm effects from the off-neutral positioning of the centre of gravity and centre of buoyancy. Clearly, the hydrostatic stiffness must only be specified for heave, roll and pitch; the components for surge, sway and yaw are all zero as the hydrostatic load does not change for displacements in these directions.

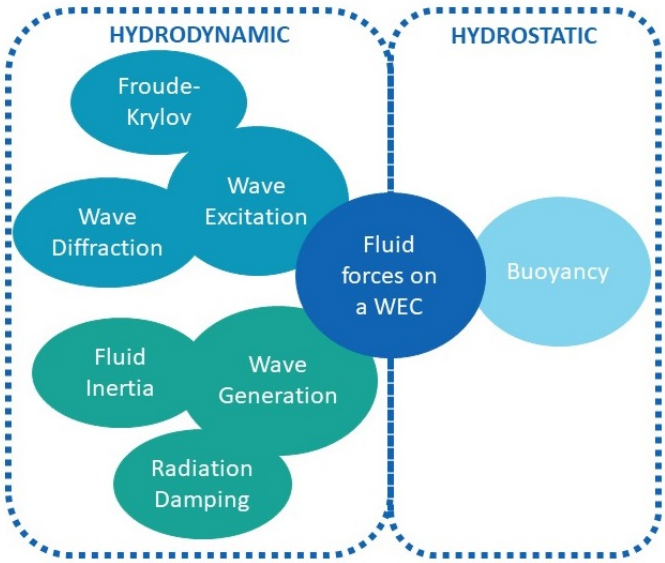

Figure 2.1: Fluid forces on a WEC and their origin

2.3.1.2 Froude-Krylov

The Froude-Krylov force on a structure originates from the unsteady pressure field generated by the undisturbed incident wave field. It is calculated with no knowledge of the effect the stationary structure's presence may have on the wave field. By equating the linearised version of the Bernoulli equation (assuming $\bigtriangledown \underline{u}$ is small and therefore higher power terms can

be neglected) at any depth z with that at the free surface, the pressure variation beneath the waves surface is shown to have three contributing factors: atmospheric, hydrostatic and dynamic.

$$p(x, y, z, t) = p_{atm} - \rho g z - \rho \frac{\partial \phi}{\partial t} \tag{2.26}$$

Taking just this dynamic pressure term and knowledge of the body's geometry the Froude-Krylov force can be calculated:

$$\underline{F}_{FK} = -\rho \int_S (\frac{\partial \phi_I}{\partial t} + gz) \underline{dS} \tag{2.27}$$

2.3.1.3 Diffraction

Even if the body is stationary the wave field will be scattered through diffraction and reflection in order to satisfy the kinematic boundary condition (i.e. the body is solid and water cannot pass through). This is illustrated in Fig 2.2a. The overall force from the wave diffraction potential is:

$$\underline{F}_D = -\rho \int_S \frac{\partial \phi_D}{\partial t} \underline{dS} \tag{2.28}$$

2.3.1.4 Radiation

When a body moves in fluid, the fluid must also move to accommodate this motion, thus a moving structure creates waves in a body of fluid, Fig. 2.2b. The force on the body due to this radiation potential is separated into two parts as one is in phase with the body's acceleration and the other is in phase with the body's velocity:

$$\underline{F}_R = -\rho \int_S \frac{\partial \phi_R}{\partial t} \underline{dS} = -M_{ij} \underline{\dot{U}}_j - B_{ij} \underline{U}_j \tag{2.29}$$

- **Added mass (M_{ij}):** when a body accelerates the fluid also accelerates and this requires an additional inertial force. The added mass is not a physical amount of water, the mass is distributed throughout the body of fluid that is moved by the body. Therefore, as the kinetic energy of the fluid changes with time so does the magnitude of the added mass. For translational modes of motion the units are kg, and for rotational modes it is kgm^2 or equivalently Nms^2/rad
- **Radiation damping (B_{ij}):** a moving body in fluid generates outgoing waves in phase with the velocity of the body. For translational modes the units of damping are Ns/m and for rotational they are Nms/rad.

2.3.2 Equations of Motion

Newton's second law for a pitching body under the action of gravity (M_g), waves (M_w) and a PTO system (M_{PTO}) is encapsulated in Equation (2.30).

$$I\ddot{\theta} = M_g + M_w + M_{PTO} \tag{2.30}$$

Considering the components of the moment induced by the wave as the wave excitation, buoyancy and radiation, with the PTO approximated as a linear damper $M_{PTO} = -B_{PTO}\dot{\theta}$,

this becomes:

$$(I + M_A)\ddot{\theta} + (B + B_{PTO})\dot{\theta} + C\theta = M_{exc} \tag{2.31}$$

where I is the body's inertia, M_A is the added mass, B is the radiation damping and C is the hydrostatic stiffness.

2.3.3 Morison Equation

Applying potential flow theory's ideal flow about a circular cylinder reveals that the pressure force is made up of a steady term that is proportional to $U^2(t)$ and an unsteady term that is due to $\frac{dU(t)}{dt}$. The magnitude of the steady term, or drag force, is dependent on the point at which the flow separates and the pressure in the wake, both of which vary with the Reynolds number of the flow. Thus the drag force can be calculated as:

$$dF_D = C_D \rho \frac{AU^2(t)}{2} \tag{2.32}$$

where C_D is the drag coefficient. Wake effects in steady flow have been studied extensively providing a wealth of empirical data on the drag coefficient. However the values of drag coefficient determined in time-independent flow will not necessarily correspond to those in oscillatory flow.

A similar expression is proposed for the unsteady, or inertial, term Equation (2.33). The inertia coefficient can be broken down further to $C_M = 1 + C_a$, where the unity term is equivalent to the dynamic pressure of the undisturbed oscillatory field (i.e. the Froude-Krylov force in waves). C_a is due to the object's shape and the disturbance it causes, or alternatively it can be thought as the force necessary to accelerate the flow around the cylinder. Experimental values of C_M are between 1 and 2 for slender cylinders dependent on the flow characteristics. Even in potential flow theory $C_M = 2$ thus there is a force term due to the fluid accelerating past the cylinder even in the absence of friction. By considering the kinetic energy of both a stationary body in an oscillating flow field and an oscillating body in a stationary flow, it can be shown that $\rho C_a A = M_{ij}$ as used in Equation (2.29).

$$dF_I = C_M \rho V \frac{dU}{dt} \tag{2.33}$$

In an oscillatory flow $U(t)$, the Morison equation gives the inline force parallel to the flow direction, eg the force on a vertical pile is:

$$F_T = \int_{-h}^{\eta} \frac{1}{2} \rho C_D D \left| U_x \right| U_x dz + \int_{-h}^{\eta} \rho C_M A \dot{U_x} dz \tag{2.34}$$

If the body is oscillating with velocity $V_x(t)$ as well as the flow, then the Morison equation becomes:

$$F_T = \int_{-h}^{\eta} \frac{1}{2} \rho C_D D \left| U_x - V_x \right| (U_x - V_x) dz + \int_{-h}^{\eta} \rho C_a A (\dot{U_x} - \dot{V_x}) dz + \int_{-h}^{\eta} \rho A \dot{U_x} dz \tag{2.35}$$

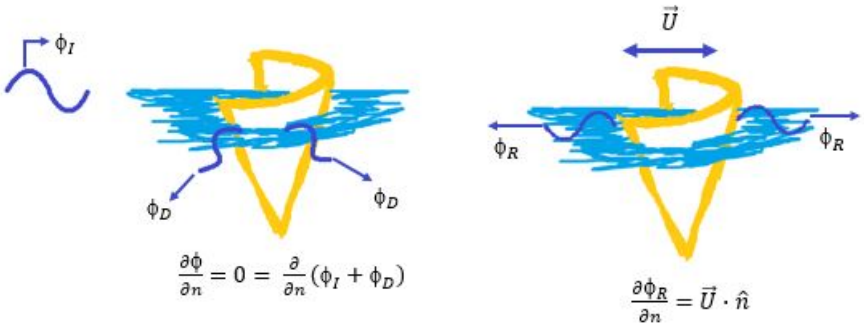

(a) Wave Diffraction **(b)** Wave Radiation

Figure 2.2: Illustrations of wave field potentials

2.3.4 Keulegan Carpenter Number

The Keulegan-Carpenter number, or period number K_C, is a useful dimensionless quantity when considering bluff bodies in an oscillatory flow such as a wave field or an oscillating body in a stationary fluid. It indicates whether drag or inertial forces dominate. For a small K_C number inertia forces are more important whereas a large K_C number suggests that drag and turbulence are more significant. For a cylinder in oscillatory flow, the contribution from the two force components is approximately equal when the K_C number is in the range of 15-20. In different flow situations it can be shown that as long as the K_C is constant then C_a and C_D are also constant.

The K_C is defined in Equation (2.36), as the ratio between the distance travelled in one period of oscillation T (derived from the amplitude of the flow velocity oscillation, U_0, or the amplitude of the object's velocity, in case of an oscillating object), to the characteristic length scale of the object L (for instance the diameter for a cylinder under wave loading)

$$K_C = \frac{U_0 T}{L} \tag{2.36}$$

The KC number can be used to justify the negation of different terms of the Morisons equation. The general rules of thumb for offshore engineering (Journee and Massie 2001) concerning slender cylinders ($\frac{D}{\lambda} < 0.2$) are if $K_C < 3$ then the inertia is dominant and drag can be neglected as the flow does not travel far enough for much of a boundary layer to be created. Potential flow theory is considered applicable for flows within this range. For $3 < K_C < 15$ it is acceptable to linearise the drag. For $15 < K_C < 45$ both components are important and the full Morison equation must be evaluated. As $K_C \to \infty$ approximates a constant current, above $K_C = 45$ the drag force dominates and significant vortex shedding is expected, thus inertial effects can be ignored.

2.4 Computational Fluid Dynamics

Concepts covered in this section were largely drawn from the author's undergraduate lecture notes and notes from CFD direct's OpenFOAM training course "Applied CFD". For a general discussion of CFD and its implementation "An Introduction to Computational Fluid Dynamics:

The Finite Volume Method" (Versteeg and Malalasekera 2007) was also used along with the lecture series presented on-line by Lars Davidson of Chalmers University "Numerical Methods for Turbulent Flow" (L. Davidson 2005).

The complexity of fluid problems, particularly turbulent flows, prevents the governing equations being solved directly and in their entirety. Instead numerical modelling methods have been developed to approximate the equations and problem in order to generate a solution that is meaningful.

2.4.1 Discretisation

To calculate unknown flow variables, e.g. a velocity component, the governing equations can be rewritten as a generalised transport equation that forms the basis for numerical methods in CFD. For a generic field Q the standard transport equation is:

$$\underbrace{\frac{\partial p\underline{Q}}{\partial t}}_{Rate of Change} + \underbrace{\nabla \cdot (\rho \underline{U} \underline{Q})}_{Advection} - \underbrace{\nabla \cdot (\Gamma \nabla \underline{Q})}_{Diffusion} = \underbrace{S_Q}_{Sources} \tag{2.37}$$

All CFD simulation requires some discretisation, as it involves taking the above differential equations and continuous fields and approximating the problem by a system of discrete values and matrix equations that can be solved. Achieving the desired accuracy of the solution at the minimal computational expense is the ultimate goal of any discretisation scheme. For spatial discretisation the solution domain is defined by a number of nodes and smaller discrete cells that make up the computational mesh on which the PDEs are subsequently discretised. The two most commonly used methods that employ this meshing technique (meshless techniques do exist but are less mature) are the Finite Difference Method ("FDM") and the Finite Volume Method ("FVM"). The principal difference between these methods is the choice of either the differential or integral form of the base equations. When employing the simplifications of potential flow theory a third type of spatial discretisation is available, the Boundary Element Method ("BEM").

2.4.1.1 Finite Difference Method

The PDE is converted to its discrete version by replacing each partial derivative term by a difference term using forward, backward or central differencing in time and space. Therefore it is approximated by an algebraic equation dependent only on the value of the variable at that node and neighbouring nodes. The error between the exact and numerical solution is dependent on the order of the truncation error of this modified equation. Even-order derivatives of the truncation error, e.g. from first order upwind method, causes numerical dissipation which has an effect much like viscosity, while numerical dispersion is the result of odd-order derivatives. FDM is conceptually simple but the conservation principle is not inherently enforced and it is only effective on structured grids thus is restricted to simpler geometries.

2.4.1.2 Finite Volume Method

By instead considering the integral form of the governing equations, and applying Gauss's divergence theorem (the outward flux of a tensor field through a closed surface is equal

to the volume integral of the divergence over the region inside the surface) Equation (2.37) becomes:

$$\underbrace{\frac{\partial}{\partial t}\left(\int_V \rho Q \delta V\right)}_{Rate of Change} + \underbrace{\int_S \underline{dS} \cdot (\rho \underline{U} Q)}_{Advection} - \underbrace{\int_S \underline{dS} \cdot \Gamma \nabla Q}_{Diffusion} = \underbrace{\int_V S_Q dV}_{Sources} \tag{2.38}$$

This results in exact adherence to the conservation of fluid variables at the cell centres as FVM integrates over each CV. FVM is therefore able to handle more complex grid structures and geometries as long as cells are contiguous and each pair of neighbouring cells only have one common face. However, this is at the expense of computational effort as approximation requires interpolation, differentiation and integration. For example, taking the diffusion term, in the first step Gauss's theorem is applied, this is then approximated with face values found through interpolation schemes and the face gradient is discretised:

$$\int_V \nabla \cdot (\Gamma \nabla Q)\, dV = \int_S \underline{dS} \cdot (\Gamma \nabla Q) \approx \sum_f \Gamma_f \underline{S_f} \cdot (\nabla Q)_f = \sum_f \Gamma_f \left|\underline{S_f}\right| (\partial Q / \partial n)_f \tag{2.39}$$

For each term in the transport equation a suitable quadrature formula is chosen to approximate the integral. A brief summary of the treatment of the diffusion and advection terms and issues that arise with FVM is presented below.

Diffusion Diffusion is the net movement of particles from high concentration to low concentration. In the numerical solution this is represented between two cells A and B as:

$$\underline{S_f} \cdot (\nabla Q)_f = |S_f| \frac{Q_A - Q_B}{|\underline{d}|} \tag{2.40}$$

Figure 2.3 demonstrates the problem encountered when the geometry of the mesh results in the vector between the centre of one cell and its neighbour being non-orthogonal to the plane of the face. For example, when integrating the pressure field over a volume, the normal gradient is required i.e. $(\frac{\partial p}{\partial n})_f$. If the pressure gradient is calculated between cell A and cell B, it uses p_B and p_A which are matrix coefficients evaluated at cell centres, but this is not normal to the face as the face is non-orthogonal i.e $\theta_{no} \neq 0$. In these cases a correction term is calculated (the transverse gradient) $(\frac{\partial p}{\partial k})_f$ and added as an explicit source. The bigger this corrective term however, the more unstable the simulation becomes.

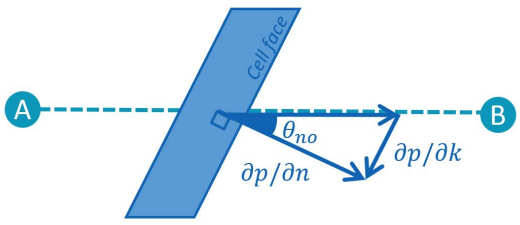

Figure 2.3: Issues in discretisation with non-orthogonal cells

A good level of mesh non-orthogonality is critical in a stable simulation, with $\theta_{no} > 90°$ being totally unacceptable and $\theta_{no} < 60°$ considered reasonable. To improve stability, numerical

strategy can be employed that limits the size of the allowable transverse gradient, though at the expense of accuracy.

Advection Advection is the motion of particles along with the bulk flow.[2] Like the diffusion term, it is integrated over a control volume and linearised, as demonstrated below using the turbulent kinetic energy field k.

$$\int_V \nabla \cdot (\rho \underline{U} k)\, dV = \int_S d\underline{S} \cdot (\rho \underline{U} k) \approx \sum_f \underline{S_f} \cdot (\rho \underline{U})_f = \sum_f \phi_f k_f \tag{2.41}$$

In the final step of the approximation, the mass flux ϕ_f is defined as a new variable, exploiting the fact that it is often needed in multiple terms. The key issue in this discretisation is the interpolation of the advected field, which is calculated at the cell centres, to the cell faces.

There are a number of possible advection schemes which are based on: central differencing or upwind methods. The upwind method uses only the upwind cell to determine the value on the face, i.e. it is equivalent to it. This method leads to a very stable solution as the value at the face and never become unbounded, however, it is also very inaccurate.

$$(k_f)_{UD} = \begin{cases} k_a & \text{for } \phi_f \geq 0 \\ k_b & \text{for } \phi_f < 0 \end{cases} \tag{2.42}$$

The central differencing method interpolates between the upwind and downwind cell to calculate the value on the face, providing a reasonably accurate solution. However it can be unstable or unrealistic as the value may go beyond the permissible bounds e.g if temperature could only be between $1°C - 4°C$ you may end up with values outside these limits such as $0.8°C$ or $4.2°C$.

$$(k_f)_{CD} = \frac{\left|\underline{d_{af}}\right|}{\left|\underline{d_{ab}}\right|} k_a + \left(1 - \frac{\left|\underline{d_{af}}\right|}{\left|\underline{d_{ab}}\right|}\right) k_b \tag{2.43}$$

where $|\underline{d_{af}}|$ is the distance between the cell centre and the cell face, and $|\underline{d_{ab}}|$ is the distance between neighbouring cell centres.

Blended Differencing methods amalgamates both approaches leading to moderate unboundedness.

$$(k_f)_{BD} = (1 - \gamma)(k_f)_{UD} + \gamma (k_f)_{CD} \tag{2.44}$$

[2] In general convection is reserved for vertical movement and advection for horizontal

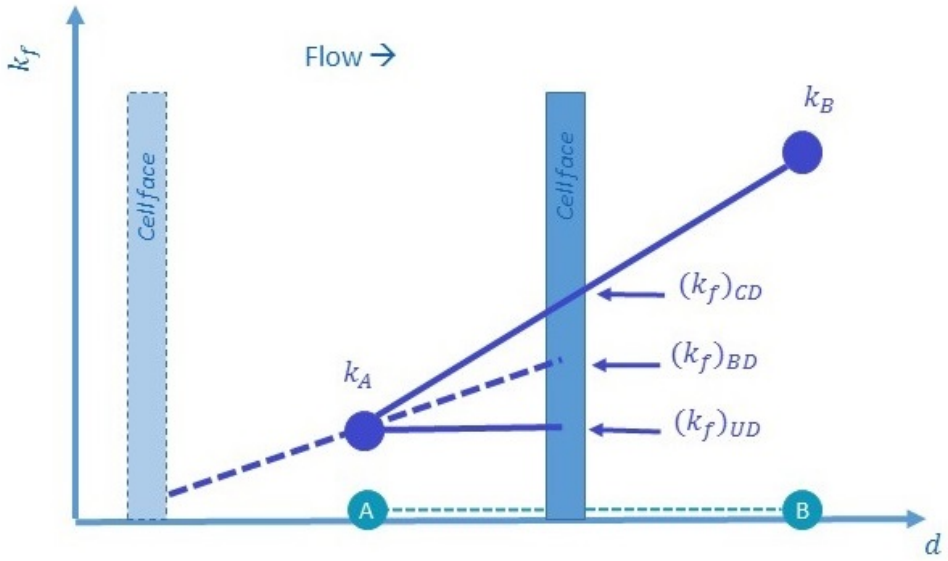

Figure 2.4: Explanation of different advection schemes where CD = Central Differencing, BD = Blended Differencing and UD = Upwind method.

2.4.1.3 Boundary Element Method

The boundary element method employs the boundary conditions to evaluate boundary values that satisfy the governing equations in the integral form(Hinch 2017), (Edwards 2018). It exploits the ability of Green's identities to represent velocity potentials by distributions of sources and sinks. In the case of marine engineering Green's theorem is used to derive integral equations for the velocity potentials on the wetted surface of the body boundary. The boundary is then discretised in to a number of panels leading to a fully populated matrix form of the integral equations. A solution is sought for the strength of each source and sink assuming that they are constant on each panel and that the potential is evaluated at its centroid and is equal to the normal incident potential. BEM can be advantageous as only the boundary needs to be represented as a mesh, not the actual fluid domain. However, its reliance on known and simple Greens functions result in it only being applicable to linear problems, thus it is limited to considering potential flow.

2.4.1.4 Temporal Discretisation

For time-varying, or transient problems, such as experienced in water waves the solution is time dependent. Unlike in spatial discretisation where impacts of the flow could be experienced in any direction, for temporal discretisation the solution 'marches' on, as only the future time step can be influenced. The solution is advanced step by step from an initial value. Considering a generic time-dependent problem and integrating with respect to time over a single time step, the following is obtained:

$$\int_t^{t+\triangle t} \frac{\partial \phi}{\partial t} dt = \int_t^{t+\triangle t} f(t, \phi(t)) dt \tag{2.45}$$

A choice can then be made to approximate the integral using the value of the integrand evaluated at the initial time or the final time, or even a combination of the two. This is

mathematically expressed as:

$$\frac{\phi^{(n+1)} - \phi^{(}n)}{\triangle t} = \beta \cdot f(t, \phi^{(n)}) + (1 - \beta) \cdot f(t + \triangle t, \phi^{(n+1)}) \tag{2.46}$$

- If $\beta > 1$ then it is the fully explicit Euler method as direct computation is possible from known quantities only.
- If $\beta \leq 1$ then the computation depends on other unknown variables and the method is termed implicit. Implicit numerical methods require an iterative technique to obtain the solution.
  - $\beta = 1$ is the fully implicit Euler method.
  - $\beta = 0.5$ denotes the Crank Nicolson scheme, which uses the trapezoid rule to discretise.

Temporal discretisation approaches impact both the accuracy and stability of the solution. Explicit methods require a sufficiently small time step to remain bounded and stable. The stability criteria is defined by the Courant-Friedrichs-Lewy ("CFL") Condition in Equation (2.47) which requires the time step to be less than the time required for information to propagate across the cell. Implicit schemes are more complex to program and require an increased computational effort for the iterative techniques but they do allow larger time steps to be used as they are unconditionally stable(Craft 2018). Though to preserve accuracy the time step should also be limited in transient solutions in accordance with the CFL condition, as a larger time step presents itself as increased damping and introduces inaccuracies.

$$\frac{U \triangle t}{\triangle x} < 1 \tag{2.47}$$

2.4.2 Pressure Coupling

The Navier Stokes equations provide a relation for the conservation of momentum for each spatial dimension (x, y, z), therefore along with the continuity equation there are four equations to solve four variables: u, v, w, p. However, these equations are intertwined, as all velocity components appear in every equation and to solve for the velocity the pressure must be known. But the pressure field cannot be evaluated without first knowing the velocity[3]. This results in a coupled algorithm that iterates through the momentum equations and continuity equations using successive corrections to the assumed pressure field until convergence is attained and the resulting velocity field satisfies both the continuity and momentum equations.

A number of iterative solution strategies have been developed, the best known example is Semi-Implicit method for pressure-linked equations ("SIMPLE") which is aimed at steady state problems. A similar strategy for transient solutions exists, the Pressure implicit and Splitting of Operators ("PISO") algorithm . PISO is an extension of the SIMPLE algorithm that incorporates an additional correction step, thus steps below describe the SIMPLE regime but are common to both. In these strategies the actual pressure and velocities are considered as a guessed value ($p*$) plus a correction(p'). ie $p = p^* + p'$. The first step is to use the guessed pressure

[3]In compressible flows this is not the case as the continuity equation and energy equation provide transport equations for density and temperature respectively allowing pressure to be calculated from the equation of state $p = p(\rho, T)$

value (the value from the previous time step) in the discretised momentum equation, where H is a discretisation operator, [4] to provide an initial guess for the velocities with the momentum predictor.

$$U^* = \frac{1}{A}H(U^*) - \frac{1}{A}\nabla p^* \tag{2.48}$$

Then by considering the continuity equation, Equation (2.49) and making the assumption that $\nabla \cdot \frac{1}{A}H(U') = 0$ the corrected pressure value can be calculated with the pressure equation, Equation (2.50).

$$\nabla \cdot (U^* + U') = \nabla \cdot \frac{1}{A}H(U^*) + \nabla \cdot \frac{1}{A}H(U') - \nabla \cdot \frac{1}{A}\nabla p^* - \nabla \cdot \frac{1}{A}\nabla p' = 0 \tag{2.49}$$

$$\nabla \cdot \frac{1}{A}H(U^*) = \nabla \cdot \frac{1}{A}\nabla p \tag{2.50}$$

Finally, the new velocity can be calculated with the momentum corrector equation (2.51).

$$U = U^* + U' = \frac{1}{A}H(U*) - \frac{1}{A}\nabla p \tag{2.51}$$

For a steady state solution, steps in "time" have no impact, thus the "time" can be advanced and the whole process iterated until the solution converges. For a transient solution, convergence must be achieved at each time step. Thus the PISO regime has a number of corrector loops to re-evaluate the pressure equation based on an improved U. Figure 2.5 shows the solution steps.

An under-relaxation scheme is used to prevent divergence of the pressure correction term.

$$p^{new} = p^* + \alpha p' \tag{2.52}$$

If $\alpha = 1$ then there is a chance that the solution becomes unstable and may oscillate between iterations, where as a very small α would take a much longer time to converge.

[4] Another issue in solving the Navier Stokes is the decision of where to "store" variables. If velocities and pressures are collocated then it may lead to unrealistic behaviour as in the classic "checker board" pressure example which calculates a pressure gradient of zero. To overcome this a "staggered" grid is used, so that the velocities are stored on the cell faces, which negates any interpolation as this is where they are needed in the transport equations. Another method of overcoming this without staggering the velocity variables, is the Rhie Chow interpolation. (L. Davidson 2005)

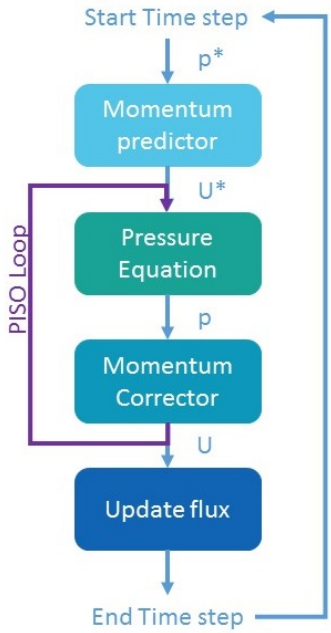

Figure 2.5: Calculation steps involved for the SIMPLE pressure coupling strategy, with the extension for the PISO regime highlighted in purple. Based on (Versteeg and Malalasekera 2007)

2.4.3 Boundary Conditions

To fully define the problem, flow conditions must be supplied at the boundaries, to close the equations. For transient flow the initial values of all flow variables are also required and must satisfy the governing equations.

Boundary conditions generally fall into two categories: Dirichlet conditions which specifies a value at each point on the boundary, and Neumann conditions which specify the normal gradient at each point. Clearly not every boundary can be specified with a Neumann condition as this would allow an infinite number of solutions, the value needs to be specified somewhere to pin the solution. For example the pressure field as calculated by the pressure coupling regimes above, only gives a reference pressure, without a defined boundary condition an absolute pressure value cannot be given.

2.4.4 Turbulence

Turbulence is characterised by fluctuations in time and disorder in space over a range of timescales, with large scale eddies determined by geometry and smaller scales determined by viscosity. The smallest eddies have a high associated velocity gradient and therefore dissipate a lot of energy. However, they also require a lot of information to be fully described and if the eddy size is larger than the mesh cell size, these losses are not resolved. Therefore approximations can be used with models to reduce the computational cost. There are many different incompressible Reynolds Averaged Navier-Stokes (“RANS”) based turbulence models

however, each is at some point based on empirical data and is therefore fallible, especially if for a very different application from the one used to experimentally define the values.

Reynolds number, Re, is a dimensionless number used to inform about the state of the flow in different fluid flows.

$$Re = \frac{U \cdot L}{\nu} \tag{2.53}$$

where L is the characteristic length and ν is the kinematic viscosity.

Most simply it is a ratio of the largest to smallest eddies in the flow, or can be thought of as the ratio between inertial and viscous forces such that strong viscous effects exist at low Re whereas at high Re inertial effects dominate. It also suggests the importance of turbulence to the solution of the flow as at low Re the flow is laminar. As the Reynolds number increases, perturbations grow chaotically instead of being damped by viscous forces, these fluctuations in time and disorder in space over a range of timescales being the hallmarks of turbulence.

Low Re flows limit the choice of turbulence model as many, such as the $k - \epsilon$ model (Launder and Spalding 1974), were derived for aeronautical applications in high speed flows where the turbulence is more isotropic. It generally performs poorly where large pressure gradients and significant streamline curvature is present. The $k - \epsilon$ model is also not valid all the way to the wall, as the ϵ equation becomes singular when it is integrated through the viscous sublayer, thus wall functions must be used.

One of the most common turbulence models is the $k - \omega$ model, which performs better in low Re and adverse pressure gradient regions and reliably predicts the law of the wall though requires a very fine mesh close to the wall (Wilcox, David C 1998).

$k-\omega SST$ is another suitable model which combines the robust nature of $k-\epsilon$ in the free stream though uses $k - \omega$ near walls. This is a higher fidelity model capable of predicting separation in regions of adverse pressure gradient more accurately than the other two models mentioned (Menter 1993).

Part II

Selection and Implementation of Modelling framework

Chapter 3

Review of Numerical Modelling Strategies

This chapter comprises a review of existing literature discussing different modelling options available to WEC developers. The line of interrogation sequentially asks Why, What, When and How to elicit an informed decision about the most appropriate methodology for the optimisation of the CCell WEC. The structure of this chapter is detailed below:

- **Why** is numerical modelling required? A comparison of physical and numerical modelling.
- **What** numerical models are available? An explanation of frequency and time domain models and their associated limitations
- **When** is a particular modelling strategy most applicable? A discussion of appropriate simplifications for both different WEC types and modelling objectives in progressive levels of technology readiness.
- **How** should CCell be modelled and optimised? The summary of the chapter, explaining the modelling methodology adopted and reasons behind this decision.

3.1 Why is numerical modelling required?

The first empirical study using scale models is attributed to William Froude in the 1860's and his investigation of ship design. It is from this work that he established the Froude Number, defined in Equation (3.1) as the ratio between inertial and gravitational forces, which is used in naval architecture to determine the resistance of an object moving through water.

$$F_R = \frac{u}{\sqrt{gL}} \tag{3.1}$$

Ship model basins and towing tanks have since been used to gain an understanding of the hydrodynamics, resistance and sea keeping of ships. With the advent of offshore renewable energy projects, there has been a renewed focus on tank testing and the provision of a scaled wave field to test devices. Stephen Salter's development of his famous Duck device included

the construction of the first multi-paddle absorbing wave tank for prototype testing in 1976 (Edinburgh Designs 2016). Wave tanks have since evolved from simple channels or flumes to circular tanks capable of omnidirectional wave and current generation to simulate any sea conditions around the British Isles (The University of Edinburgh 2018).

Physical model testing provides a method of evaluating and de-risking a design in repeatable and controlled conditions and most importantly at a reduced cost to the developer. As identified in the Equimar Protocols (McCombes, Johnstone, and Grant 2011) there are a number of objectives that developers may wish to satisfy through Physical Wave Tank ("PWT") testing programme:

- Characterisation of the device with key performance parameters to confirm operation and calibrate analytical models and software;
- Investigate impact of different configurations and dimensions to understand key aspects of the design and parametric sensitivities within analytical models;
- Evaluate technical feasibility including identification of any "show-stoppers";
- Device optimisation and screening of different configurations.

In addition, scale model testing may aid the developer in securing further funding through demonstration of manufacturability and development of key components.

However, there are a number of limitations inherent to tank testing primarily because of the scaling involved. The scaling of a WEC is not simple due to a variety of different scaling laws of the physical phenomena that govern its behaviour. The practicalities of manufacturing or sourcing some of the intricate componentry at a reduced scale, for example the PTO, is also problematic. Furthermore, experimentation is only capable of measuring information at discrete points governed by, for example, the location of pressure and strain sensors and wave gauges. By contrast, numerical models provide a comprehensive understanding of the entire fluid domain at any scale. Mirroring the progression from wind tunnels to aeronautical codes, research has been conducted on numerical wave tanks to reproduce flows around marine structures. This follows on from the pioneering work from Longuet-Higgins and Cokelet on mixed Eulerian and Lagrangian methods in the late 1970's to compute fully nonlinear free surface motions in the time domain (Longuet-Higgins and Cokelet 1976). These methods improve the fundamental understanding of the coupled interactions between ocean waves and the dynamic motion of the device, including stresses and strains across the structure.

Similitude between the model and real application is achieved when they are geometrically similar (all linear dimensions share same scale ratio), and share kinematic similarity (velocities and fluid streamlines are similar) and dynamic similarity (ratios of all forces are constant).[1] Dynamic similitude is impossible to attain in the study of wave energy devices as the scaling of gravity effects, and hence water waves, are ensured through equality of Froude number, whereas viscous forces including friction require equality of Reynolds number. Equating the two scaling parameters, it is clear that the only way these could both be true is by altering the kinematic viscosity of the fluid, which is a measure of a fluid's resistance to flow (Steen 2014). But a 1:10 scale model would require 1% of the kinematic viscosity of the full scale and no such fluid exists. Proper scaling of mooring lines and cables is also difficult to attain as

[1] If the model is geometrically and kinematically similar then dynamic similarity is automatically achieved.

they are susceptible to viscous effects and their material properties, particularly stiffness, also scale differently to Froude. Numerical models are able to change the scale of the simulation with negligible added cost, thus can consider both NWTs to replicate physical model testing as well as full scale devices. A CNWT study of an OWSC (Pál Schmitt and Elsäßer 2017) maintained the same size domain but varied the viscosity of the fluid to obtain Froude and Reynolds similitude and better understand scaling effects in NWTs. This resulted in a 2% increase in angular displacement for the "full scale" in comparison to the scaled version. They also highlighted the importance of a much finer mesh to resolve boundary layer phenomena at the full scale.

Assessment of hydrodynamics in a scaled NWT should be considered carefully, as demonstrated in (Mundon, Rosenberg, and Rij 2017). Using StarCCM+, they investigated the dependence of hydrodynamic coefficients (added mass and drag) on the dimensionless numbers K_C and Re with forced oscillation tests of a submerged heave plate at various scales. In general they found that hydrodynamic coefficients tend to asymptote to a fixed value for a given K_C as Re increases. Furthermore, for high K_C the added mass and drag were almost invariant to Re number, but at lower K_C ($K_C \leq 2$) the drag was substantially overestimated, thus scaling coefficients for low K_C is less successful.

A significant additional benefit of numerical models is the ability to make rapid modifications to the WEC design without the additional manufacture and testing costs. However, numerical simulations can be slow to compute without adequate computer power and some simplifications must be introduced for efficiency. Complex effects, such as parametric roll and slamming due to large amplitude motions, are hard to accurately depict numerically with such linear simplifications. The developers of SEAREV discovered that their models completely failed to predict such phenomena, which were clearly observed in the tank (Babarit, Mouslim, et al. 2009). Such oversights can lead to significant over-prediction of system efficiency and subsequently has the potential to erode investor confidence. Therefore numerical and physical experiments should be conducted in parallel, acknowledging their inherent strengths and weaknesses. Development of a national NWT is currently under-way with the Collaborative Computational Project in Wave Structure Interaction ("CCP-WSI") that is fully complementary to existing physical modelling facilities. Their aim is to develop an opensource NWT within a central code repository that is tested and validated against experimental data and available for marine and coastal engineering research (CCP-WSI 2017).

However, there is still progress to be made in both types of modelling as currently neither approach adequately simulates survivability conditions. These strongly non-linear interactions are at the limit, or sometimes beyond, the capabilities of most numerical models (as will be explored in the next sections), or would take an inordinate amount of computational power to resolve. Wave tanks are limited by their physical dimensions and capabilities of the wavemakers restricting survivability tests to $\sim$1:50, which as discussed above prevents testing with a suitable PTO. Survivability tank testing recommendations from EMEC (Holmes 2009) state that it is 'highly recommended that the scenarios studied are conducted using a medium scale model' i.e at 1:10–25. Though it is unclear where this would be possible.

3.2 What numerical models are available?

Numerical modelling allows a greater understanding of a specific device's response, hence can be used in the optimisation of the WEC system by considering the loadings on the device, and the MAEP. A wide range of potential modelling techniques for WECs have been proposed since the first serious attempts at numerically understanding the response of a device in 1976, when Evans presented a theory for predicting the absorption of wave power by means of a "damped, oscillating, partly or completely submerged body"(Evans 1976). Like the WEC concepts themselves, the techniques are far ranging, attempting to capture the many different WEC operating principles at different stages of development.

Numerical models can be split into two main categories: frequency domain and time domain, with CFD belonging to the time domain but also considered as a distinct technique. A comparative analysis of these techniques, along with examples of how they have been used in WEC development, is presented below.

3.2.1 Frequency domain

In the frequency domain, the equations of motion are reduced to a system of linear algebraic equations. These rely on the linear concept of superposition, potential flow theory and boundary element methods for the necessary device hydrodynamic coefficients and response amplitude operators ("RAO") for floating or submerged bodies. This requires a linearization of the hydrodynamics and the response of the device; however, this assumes that motions are small and harmonic. These assumptions limit the applicability of the technique and introduce considerable inaccuracies when used to evaluate the scenarios in which viscous effects are important, such as extreme or breaking waves, or when the motions of the device become large and non-linear.

Boundary element methods (or panel methods), are used to determine the radiation and excitation loads on the structure by solving for the velocity potential on the mean wetted surface of the body. In particular BEM models provide estimates for the hydrodynamic coefficients such as added mass, damping and the force per unit wave amplitude incident on the WEC. The application of BEM has been successfully used within the offshore and ship building industry as a design tool for the last 30 years. However, the use of such codes for WEC optimisation, where energy production is related to amplitude of motion, is at odds with the linearity assumptions that are valid for classical sea-keeping studies. Indeed, some WEC devices are designed to align their natural frequency with that of the predominant wave conditions, which is the antithesis of the design philosophy for ships and offshore structures. The most commonly used frequency domain diffraction code is WAMIT developed by Dr. Chang-Ho Lee and Prof. J. Nicholas Newman since 1987 (Lee 1995) and is capable of analysing wave interactions with offshore platforms and other structures or vessels (WAMIT, Inc 2016). Other codes that compute first-order wave loads on offshore structures have subsequently been conceived: ANSYS AQWA, Moses and NEMOH.

The straightforward nature of this modelling technique makes for fast computation and these codes can rapidly provide insight into WEC response at the early stages of the design process, though their limitations to small amplitude linear motions must be well understood by the user.

It is used most effectively in the basic shape optimisation and general frequency response characteristics including identification of resonant frequencies. However, caution should be taken when evaluating device motions or prediction of energy production as the technique can significantly differ from experimental results. Furthermore, the full WEC system can only be appropriately modelled if the mooring system can be modelled by a linear spring and the PTO represented using either a linear damper or a linear spring-damper system, which can be easily characterised in the frequency domain.

From review of relevant literature, the success of using frequency domain models appears to depend on both the type of device considered and the focus of the study. A number of researchers compared the output from WAMIT to experimentally derived results:

- (Ko et al. 2018) considered their cylindrical WEC with different rotational axes and compared the pitch motion RAOs. This identified the importance of including viscous effects as configurations with the lowest viscous damping had closest agreement with the WAMIT results. Overall there was an observable difference in the results, attributed to the absence of nonlinear effects in WAMIT analysis.
- Investigating different configurations of their OWSC through evaluation of the wave torque and hydrodynamic coefficients in WAMIT, (Folley, T. Whittaker, and van't Hoff 2007) found a good agreement with the wave torque measured on a 20th scale model of the flap.
- Both (Penalba, Kelly, and J. Ringwood 2017) and (Crooks et al. 2016) set out to compare the output of the commercial BEM solver, WAMIT, and NEMOH, an open-source equivalent. Crooks, considering only an OWSC, used forced oscillation tests to evaluate the estimated hydrodynamic coefficients from the two solvers against experimental data. He found a good agreement between the codes, though found their calculations were only valid for small amplitude oscillations up to 0.3rad displacement. Penalba numerically investigated a wider range of devices including a submerged axisymmetric point absorber, a two-body point absorber, an OSWC, and a floating OWC. Overall a high level of agreement was achieved. However, he highlighted previously known limitations in the formulation of NEMOH, due to the presence of thin elements particularly in the damping plate of the two body point absorber and the OWC when not modelling as a full cylinder.
- Furthermore, in a review of modelling efforts, (Wolgamot and Fitzgerald 2015), it was found that although the free surface elevation of a fixed OWC was reasonably well predicted by WAMIT far from resonant conditions, near resonance the elevation was over predicted by a factor of 2.
- Acknowledging both the limitation of BEM methods to small motion amplitudes, and the benefit of using such a simple and efficient numerical solver, (Pál Schmitt et al. 2016) developed a novel application for NEMOH. Observing slamming events in experimental modelling of the Oyster OWSC they used NEMOH coupled with the FEA tool Code Aster to provide a vibrational analysis tool to investigate the high frequency impact from wave 'slam'.
- In (van't Hoff 2009) the motion and torque on an OWSC were studied using WAMIT and wave tank experiments finding that the accuracy of prediction is severely limited when

wave overtopping occurs. This is not unexpected due to the nonlinearities introduced by overtopping.

3.2.2 Time domain

Time-domain models are founded on the same principles as the previously described frequency domain approach assuming linearity, with the core hydrodynamic coefficients and forces typically derived from linear potential flow models. However, there are a number of benefits to time-domain models. Most significantly they are capable of dealing with the nonlinearities arising from the PTO and moorings, which can be included as an external force term. They also allow modelling of transient situations, such as faults or brake activation, whereas modelling in the frequency domain is limited to stationary processes. The fundamental approach is also flexible and can accommodate both simple and complex WECs, and due to the linearity assumption, it does not limit the number of degrees of freedom that can be modelled.

The Cummins equation (Cummins 1962) is the foundation for these time-domain models, and can be defined as a set of ordinary differential equations (ODEs) and solved numerically.

$$\sum_{j=1}^{6}((M_{ij}+A_{ij}^{\infty})\ddot{x_j} \; + \; \int_0^t K_{ij}(t-\tau)\dot{x_j}(\tau)d\tau \; + \; C_{ij}(x_j)) = F_i^{wave}(t) - F_i^{ext}(x,\dot{x},t) \qquad (3.2)$$

where:

M_{ij} = Mass matrix
C_{ij} = restoring coefficient matrix
A_{ij}^{∞} = added mass at infinite frequency
$K(t)$ = radiation impulse response function (“RIRF”) or memory function
F^{wave} = wave force
F^{ext} = external forces (e.g. PTO or mooring)

The convolution integral RIRF is included in the equations of motion to account for radiation forces; it is a "memory effect" as it presents the waves generated by the body after the initial wave force.

This time domain approach does have some drawbacks, one being that all forces must be described as a function of the state of the system or wave properties, thus it cannot handle the complex phenomena within extremes. Another problem with the time domain approach in general is that there must be a finite duration of the simulation. Therefore, for simulation of response in irregular waves (a random stochastic process) there will be a large variability in output dependent on input signal. According to (Saulnier et al. 2009), the uncertainty of the estimated response and expected power capture decreases with the square root of the simulation duration.

An extensive study conducted in (Babarit, Hals, et al. 2012) evaluated the performance of eight different WEC principles at five potential deployment locations using a custom built Wave-to-Wire time-domain model for each device based on Equation (3.2). This required the calculation of hydrodynamic coefficients using the BEM codes WAMIT or Aquaplus. Recognising the propensity of these devices to violate the linearity and irrotationality assumptions of potential

theory, a quadratic damping term similar to the drag term in the Morisons equation, Equation (2.34), was added to incorporate viscous effects and limit unrealistically large amplitudes of motion. However, as the estimation of suitable drag coefficients is a significant source of uncertainty, the authors performed a sensitivity analysis varying the coefficients from one quarter to twice their nominal values. It was noted that the influence of drag coefficient variation on the energy absorption was never found to be more than 30% for any device. Furthermore, Babarit et al. acknowledged that the numerical models were likely to deviate from real behaviour by overestimating the dynamic response, providing an upper estimate of device performance. They also believed that as the modelling approach was the same for all devices then the comparisons between device trends would still hold true even if exact numbers were not. Though as will be shown in Section 3.3.1, some device types are more susceptible to inaccuracies from linear assumptions than others.

3.2.3 CFD

An alternative to these linearised potential flows is CFD software that has been used extensively in aeronautical applications. The first published modelling of a WEC with CFD came in 2004. Breakthroughs in automatic surface capturing and boundary fitted mesh generation (Mingham et al. 2004), along with increasingly available computer power allowed the development of higher fidelity modelling in packages such as ANSYS Fluent and StarCCM+. It has also been accelerated by the availability of high quality open source software such as OpenFOAM (Greenshields 2016) and Code-Saturne. CFD is beneficial as it is able to deal with more complex fluid-structure interactions that cannot be computed with approaches that assume linearity. It has also been found that CFD offers a better prediction of hydrodynamic coefficients and overall WEC response in experimental testing compared to methods using linear potential flow theory (Luo et al. 2014).

The describing system of PDEs that govern the dynamics of fluid and encapsulate the conservation of mass, momentum and energy within a system cannot be solved analytically so approximate solutions are obtained via numerical algorithms. This involves discretising the computational domain into a mesh and using either the finite difference or finite volume method (though the finite volume method is preferred due to the geometric flexibility it offers along with the physically constant treatment of flow across cell boundaries). The aspect ratio and size of cells greatly impact the accuracy of CFD simulations and the first port of call in any CFD study is a mesh convergence study. Complex geometries and steep waves can significantly increase the number of cells and subsequently the computational effort to attain a solution. It is not unheard of to conduct 3D WEC studies with millions of cells: Palm et al. studied a point absorber using 8,320,000 cells which took 10 hours per wave period in the larger regular waves simulated (Palm et al. 2016).

In a comprehensive review of CFD-NWTs for WECs, (Windt, J. Davidson, and J. V. Ringwood 2018), it was found that 39% of such studies use OpenFOAM, an open source CFD software. Although requiring considerable learning times and lacking a user-friendly GUI, it is backed by a large online community. More critically it allows access to the source code for specific tailoring and avoids the purchasing of prohibitively expensive license fees.

OpenFOAM has been used to analyse a variety of WEC components as it has the advantage

of being able to solve the fully non-linear 3D Navier-Stokes equations and thus can handle more complex phenomena which are beyond the ability of BEM methods.

- (Iturrioz et al. 2015) aimed to validate an NWT for simulation of the complex dynamics involved in OWC problems with experimental data obtained for a fixed, detached OWC at the IH Cantabria wave flume. The model was found to successfully reproduce the inner free surface elevation and air pressure as well as the velocity through the top of the device.
- A study by (Majid et al. 2012) exploited the efficiency of linear theory and the accuracy of CFD to improve estimations of the energy production of an OWSC. The NWT, implemented in Flow3d, was used to provide drag coefficients that accounted for the viscous damping in the time domain wave-to-wire model.
- The performance of an OWSC (the WaveRoller device) was also investigated, (Loh et al. 2016) using a rotating mesh interface in OpenFOAM to allow body motion, and a linear damper to model the PTO mechanism. The damping value of the PTO was determined using a least square fit to experimental data. Both the 2D and 3D configurations of the model provided a good agreement with the 1:24 physical model data, with small discrepancies in torque values attributed to non-linearities of the PTO.

3.2.4 Future developments

With the upward trajectory of available computer power, there is clear room for improvement in the development of CFD models to more accurately portray WEC response and predict the MAEP. So far when discussing CFD methods only Eulerian formulations have been considered. An alternative Lagrangian method exists called Smoothed Particle Hydrodynamics (“SPH”), where particles are moving nodes advected with the fluid rather than fixed control volumes. Therefore SPH inherently conserves mass, perfectly handles advection and introduces no numerical dissipation. This makes it well suited to flows where convection and interface tracking are critical and, as it is meshless, it can handle complex dynamic geometries (Omidvar 2010). SPH’s one source of inaccuracy is from boundary conditions as they are much more difficult to implement, especially wall treatment and variable resolution. This results in SPH being unsuitable for problems that involve a wide range of scales. Furthermore, it is quite computationally expensive as neighbouring particles can be much more numerous than neighbouring cells in a discretized finite volume method. This has hindered its development since its first conception in 1977 (Gingold and Monaghan 1977), but with progress in computational parallelisation SPH is at an advantage as the algorithm is much simpler to parallelize than FVM.

Regarding the limitations of the modelling techniques there is also an opportunity to develop hybrid models that seek to combine the strengths of each approach. Some progress has already been made (Babarit, Folley, et al. 2013), though a key challenge remains in the design of a seamless transfer of information between sections of the hybrid model. This coupling could also be extended to the modelling of an array. CFD could be used to resolve the flow near the individual WECs, while another flow model could propagate the waves between the WECs, this would reduce the numerical diffusion errors that occur within CFD.

Alternative modelling approaches have also been suggested such as models from data: a

statistical technique based on measured data rather than modelling the complex physical processes (e.g. Artificial Neural Networks). Input data is required to make this approach feasible, and it is suggested that NWT simulations are advantageous for compiling these data sets due to the wealth of data available (Penalba, Giorgi, and J. V. Ringwood 2017). Accordingly, the performance and validity of such models is limited by the accuracy of the input data supplied.

3.2.5 Limitations

A considerable limitation in the non-linear modelling of WECs is available computational power, which is often central to the justification of using a simpler model. However, any assumptions made also limit the accuracy of the output and it is essential that the developer has a clear understanding of the implications of different assumptions. Potential flow theories can be extended with non-linear terms but their accuracy is still below that of a CFD simulation that solves the fully non-linear Navier-Stokes equations, as shown in Figure 3.1.

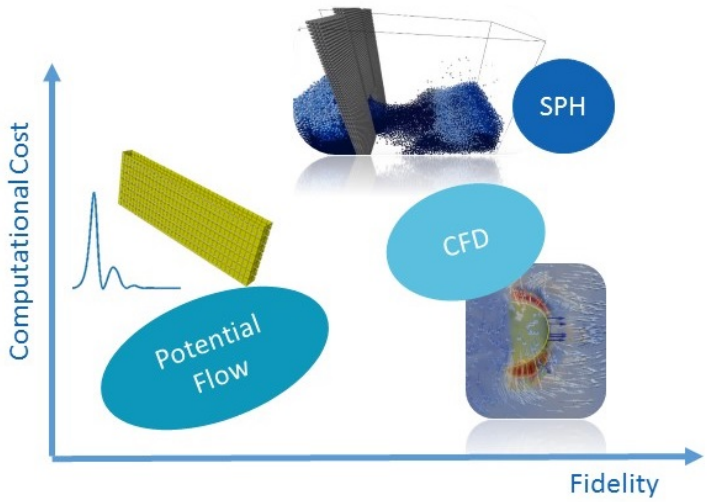

Figure 3.1: Compromise between Computational expense and fidelity of different modelling techniques. Diagram of SPH from (Guy 2015)

Common to all approaches discussed is the problem of model validation: very little data exists publicly about the performance of a WEC device from laboratory testing, and even less for real operational data. To ensure proper validation, carefully designed lab tests must be conducted, accepting and mitigating some of the limitations in creating perfect replication. A comparison of the limitations of each approach is demonstrated in Table 3.1.

Table 3.1: Comparison of limitations of each modelling approach

Frequency Domain	Time Domain	CFD
Assumes linearity, cannot simulate complex fluid-structure interactions	Assumes linearity, though some non-linear phenomena can be modelled	Numerical dissipation and/or dispersion inherent in discretisation techniques
Cannot model viscous effects	Cannot model viscous effects directly	Empirically defined turbulence models may have limited accuracy for specific application
Cannot simulate control as linear representation of PTO is not sufficiently accurate	More computationally expensive but not necessarily more accurate than frequency domain	Computationally exigent and correct construction is complex
Monochromatic frequency domain not an accurate representation of real waves	Requires a large number of simulations for accurate MAEP per sea state	Requires a large number of simulations for accurate MAEP per sea state

3.3 When is a modelling strategy most applicable?

Applicability of a model for a particular investigation is dependent on two things: (1) the device type: as the relevance of different non-linear dynamics differ between WEC types so do the modelling approaches that are recommended; (2) the reason for the modelling and desired output, which is often linked to the stage of development at which the modelling is conducted.

3.3.1 Sources of Non-linearity

WEC modelling has borrowed a number of techniques from the offshore engineering industry where non-linear behaviour is assumed to be important only during extreme conditions. However, in the wave energy industry large motions and associated non-linear dynamics are also the norm in power production mode. Linear approaches adopted from the oil and gas industry often fall short when modelling a WEC due to inaccuracies introduced from reduced relevance of assumptions. (Penalba, Giorgi, and J. V. Ringwood 2017) suggests the approach taken to modelling WECs should instead consider survival mode as operation in “highly non-linear region” while power production should consider the non-linear region and the linear region.

Non-linear effects originate from two different sources: those from the WEC device (wave structure interactions and external forces such as PTO system and moorings) and the wave resource itself (particularly due to wave steepness and water depth.)

3.3.1.1 Hydrodynamic forces

The source and impact of non-linearities in the formulation of the hydrodynamic forces (as introduced in Section 2.3.1) is discussed below:

- **Froude-Krylov:** Linear codes, such as NEMOH, use the mean wetted surface of the body in their computations and they require the body to be meshed only up to the Still Water Level ("SWL"). This loses accuracy when there are large relative motions between the free-surface and the device, as this results in a large variation in the wetted surface over time. A non-linear formulation would calculate over the instantaneous wetted surface at each time step.
- **Diffraction and Radiation:** If the body is very small in comparison to the wave length non-linear contributions from the radiation force are often ignored and the diffraction force is neglected completely. (Renzi, Doherty, et al. 2014) found that previous modelling theories relating to point absorbers and terminators neglected the diffracted wave field and hence poorly predicted the dynamics of Oyster. Using BEM modelling they determined a mathematical reference model to explain the mechanism of energy extraction and identified diffractive dynamics as the main contributor to Oyster's excitation torque.
- **Viscous:** For devices that are much larger than the wave amplitude, inertia forces dominate and viscous losses are not considered important. However if the flow past a vertical cylinder is considered then it is clear that for smaller bodies the inclusion of viscous effects is required for accurate determination of drag and inertia force components. As the wave crest approaches run-up occurs on the front of the cylinder and then, towards the mid point of the cross section, the flow separates and a wake develops behind the cylinder. When the trough approaches and the flow reverses, the existing wake is washed back past the cylinder, creating a new wake. This description clearly violates the assumption of irrotational flow. The same analysis can be used in surging converters, which develop strong turbulent vortices, or any WEC that includes a damping plate[2]. External incorporation of viscous losses is possible through use of the Morisons equation and an experimentally derived drag coefficient. Such a coefficient could be found through physical or numerical modelling, or alternatively deduced from existing data for similar structures, though a sensitivity analysis should be conducted to reflect the higher levels of uncertainty in this approach.

Two single-DoF devices exploiting different modes of oscillation: a heaving point absorber ("HPA") and an OWSC, were considered in (Giorgi and J. V. Ringwood 2018) and the relevance of different non-linear forces were assessed. For this study, the authors developed a parsimonious hydrodynamic model[3], by combining appropriate linear and non-linear forces in a BEM formulation. Non-linear Froude-Krylov terms and viscous drag terms are added to the linear diffraction and radiation terms and the controlled PTO force to calculate the total force on the device. To allow for a closer comparison, reactive control was applied by tuning the PTO stiffness and damping to maximise amplitude motion and power absorption, which was important in the study as it increases the relevance of non-linearities. Although they have not

[2] A damping plate changes the hydrodynamic properties of the WEC by introducing extra viscous damping and increasing the added mass

[3] A parsimonious model here was defined as one that only describes relevant non-linearities as a compromise between model fidelity and computational cost.

yet demonstrated validation of their model, analysis of results found that, as expected, different non-linear forces are dominant in devices with significantly different hydrodynamics. The HPA was affected almost exclusively by the non-linear FK forces (contributing 81–96% of the total hydrodynamic force), while the OWSC had important contributions from radiation, diffraction and viscous effects. Considering a range of different wave heights and periods of regular waves, the authors also concluded that the relative contribution of FK forces increased with wave period but was independent of the wave height. The viscous drag contribution showed little variation for the HPA except for a slight reduction in larger period waves. Conversely the OWSC exhibited a strong dependence on both parameters. In a fully linear system, the phase of each component would be independent of wave height. Therefore it was expected that the non-linearities would also significantly affect the phase of the different force components. For the OWSC in particular, it was suggested that hydrodynamic losses would be larger in waves of increased amplitude as the phase difference between the two dissipative terms (radiation and viscous drag) reduces producing a more constructive interaction.

Viscous losses due to flow separation and vortex shedding are thought to heavily influence the performance of OWSCs. As demonstrated in (Yanji Wei, Rafiee, et al. 2015), vortices are generated and shed at each half wave period at the edge of the flap locally. Finding a good comparison between the CFD model (ANSYS Fluent) and the experimental data at 1:25 scale, the authors then conducted a series of simulations of different configurations and scales to investigate viscous forces and scaling effects. There are two separate force components on marine structures due to waves, one that acts tangentially (shear stress) and one normally (pressure). Considering the issues of scaling, any differences in torque on the flap due to waves are a result of either the shear stress on the flap surface or the shed vortices. They conjectured that the contribution of the shear stress on the total torque can be neglected, sharing the conclusion from the CFD analysis of an OWSC in (Pál Schmitt, Bourdier, et al. 2012), which indicated shear forces contributed less than 1% of the total surge force. Wei et al. went on further to conclude that viscous scaling effects were insignificant in their study as vortices were short lived with only local impact, and comparisons of CFD simulations at different scales did not show remarkable differences. Though they did note that a lack of data prevented verification of their numerical results.

The diffraction parameter ($KL = \frac{2\pi L}{\lambda}$) is interpreted as a measure of the importance of diffraction and the amount of wave scatter from a structure. Diffractive effects are commonly ignored unless $KL \geq 1$. Introducing this non-dimensional parameter, along with the K_C number from Section 2.3.4 it is easier to develop some rules of thumb for the applicability of different hydrodynamic approximations, as shown in Figure 3.2. The regions A-C can be interpreted as:

- Regime **A**: The larger K_C numbers suggests viscous effects are important but the diffraction parameter is small, so Morisons equation is acceptable.
- Regime **B**: Body inertia and skin friction (rather than form drag) dominate. The body is small in comparison to the wave length therefore Froude-Krylov is valid.
- Regime **C**: Must take into consideration the diffraction and radiation effects, therefore Froude-Krylov approximation is not valid

The areas outside these regions require other non-linear effects to be included. The contours

of wave steepness show increasingly non-linear wave effects with the breaking of waves providing the extreme.

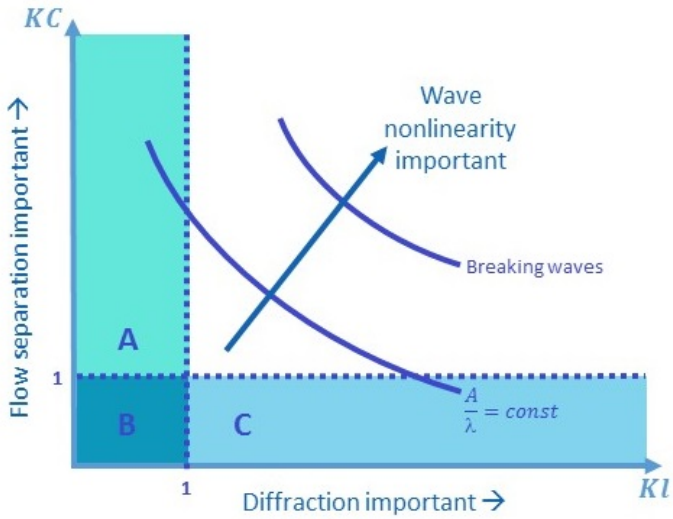

Figure 3.2: Limits of applicability for different hydrodynamic approximations. Reproduced from (Techet 2005)

Particular WEC designs are susceptible to more specific manifestations of non-linearities, for example:

- **Parametrically excited motions:** is the amplification of roll/pitch motions caused by non-linear coupling of at least two degrees of freedom. In literature it is also called the Mathieu-type instability. This instability is related to the geometrical characteristics of the device caused by dynamic variation of the metacentric height, and the relative positioning of the centre of gravity and centre of buoyancy (eg. if the metacentric height becomes negative then the object is unstable and the motion amplitudes may be much larger).
- **Slamming** (Henry et al. 2014) attempted to replicate and characterize an impact event experienced in real sea tests in both extremes and power production mode. The event was identified from an impulsive component on the load time history. Understanding of this loading was crucial to the structural design of both the prime mover and the foundations through which the load ultimately transmits. Similar impact events are apparent in static coastal structures and ship dynamics. However, through experimental investigations undertaken of an undamped OWSC at 1:25 scale, it was concluded that this was more of a water-entry problem than a classic wave impact event as the flap's velocity dominates the problem. Images from a high speed camera deduced that the event occurs when the flap "slams" into the oncoming wave. Travelling from a shoreward position, the flap's motion is little effected by water resistance, as the water level on the seaside is low, thus the restoring moment induces a high angular velocity at the point the device re-enters the water. A jet of water is ejected in front of the OWSC as the airgap in front of the flap is closed off from three sides. Slamming is highly non-linear, with the pressure magnitude and distribution, and duration of the event considered key variables. Henry et al, thus used fully non-linear methods (SPH and OpenFOAM) to

reproduce slamming in an NWT, finding a good agreement with measured device motion and pressure trace from a sensor positioned on the seaward side of the flap. A similar study (Yanji Wei, Abadie, et al. 2016) investigating slamming with an ANSYS Fluent model also found the flap motion and free surface evolution of such a phenomenon were well predicted by CFD.

An impressive list of papers concerning the modelling of WECs have been condensed, (Penalba, Giorgi, and J. V. Ringwood 2017), into a list of recommendations dependent on the device type and main source of non-linearities identified, as shown in Table 3.2.

Table 3.2: Comparative study of the impact of different non-linear effects on different WEC types. Recreated from (Penalba, Giorgi, and J. V. Ringwood 2017). Where H = High, L = Low, VL = Very Low and N/A = Not proven.

		Relevance of Non Linear effects			
WEC	**Characteristic Non Linear Behaviour**	*Froude-Krylov*	*Radiation/ Diffraction*	*Viscous*	**Modelling Recommendation**
OWC	Sloshing, Breaking waves (Coastal), Parametric Excitation	H	-	H	CFD
HPA	Parametric Excitation	H	VL	L	Partially nonlinear potential theory with viscous drag
OWSC	Slamming	L	N/A	H	CFD

3.3.1.2 Mooring forces

Another problem that has been poorly predicted by linear theory is the effect of mooring restraints, which is worsened in near-resonant conditions as amplitude of motions increase. As length of mooring lines increases the dynamic characteristics also become more profound and, slack moorings in particular, can introduce transient large snap tensions as they oscillate at their limit between taut and slack. Previous CFD analysis that used simplified linear spring equivalence to model the mooring dynamics was evolved in (Palm et al. 2016) to produce a fully coupled CFD-mooring model with OpenFOAM and their proprietary software MooDy. From experimental validation studies of a cylindrical buoy with three catenary mooring cables, a good overall agreement for buoy motions and mooring forces was demonstrated.

3.3.1.3 PTO

One common PTO system for WECs is high-pressure hydraulics as they are suited to the slow motions and large forces that are experienced in wave energy conversion. Such an hydraulic system includes pistons, valves, accumulators and motors, resulting in a highly non-linear operation. In most considerations of the PTO system in WEC modelling, the PTO is treated as a linear damper either alone or in parallel with a spring, thus avoiding any non-linear effects. Progress was made with the development of PTO-Sim (So, Simmons, et al. 2015) as it provides a fully modelled PTO but relies on BEM methods to obtain hydrodynamic coefficients for the device and hence there is no consideration for the coupled effect of the two systems (hydrodynamics and PTO restraint).

3.3.1.4 Wave resource

In the derivation of linear theory in Section 2.2.2 it was assumed that the sea bed was horizontal and the amplitude of the wave is small leading to its prediction of harmonic waves, symmetrical about the SWL with water particles moving in closed paths. However, in the real sea environment these conditions are often violated. The Ursell number is a dimensionless number that determines relevance of various wave theories based on the wavelength, wave height and water depth, Equation (3.3). A high Ursell number indicates large, finite amplitude waves for which linear wave theory is insufficient.

$$U_R = \frac{H\lambda^2}{h^3} \tag{3.3}$$

Nonlinear wave theories In deriving linear wave theory, the bottom boundary condition is exactly satisfied but an approximation for the dynamic free surface boundary condition is found, selecting only the linear terms. Stokes applied perturbation theory[4] to the fundamental linear theory to improve this approximation. Stokes developed it as a power series in terms of the wave steepness ka, with the naming convention following the number of harmonic components added, and the expectation that the solution would converge as more terms are considered. Thus far, the theory has been extended from Stokes first (equivalent to linear theory) to Stokes fifth, with each successive term steepening the crests and flattening the troughs of the initial sinusoidal profile (Fenton 1990). The distinguishing aspect of Stokes fifth is that it can account for open orbits of water particle. This aperiodic term in the expression for water particle displacement is Stokes drift: a net particle displacement in the direction of wave propagation. However, Stokes restricts wave heights in shallow water to $H_{max} \approx h/2$ thus is generally not applicable in coastal waters.

Cnoidal theory is another approach that computes the velocity potential from a given amplitude, wave length and water depth. It is characterised by sharper crests and flatter troughs than sinusoidal representation and it performs particularly well in shallow water as the underlying assumption of the theory is that the ratio of water depth to wave length is a small number. It spans the range between linear theory and solitary theory. Solitary theory being when a water depth approaching zero is considered and the wave lies entirely above the SWL with particles transferred in the direction of the wave propagation. In reality solitary waves are rarely observed, but the theory is most closely matched in tsunamis.

$$u = \frac{\partial\phi}{\partial x} = \frac{\partial\psi}{\partial y} \tag{3.4}$$

$$v = \frac{\partial\phi}{\partial y} = \frac{\partial\psi}{\partial x} \tag{3.5}$$

Through the Cauchy-Riemann equations, Equations (3.4 & 3.5) an equivalent to the velocity potential analysis derived in Section 2.2.2 is evident. A simple expression of this is: the potential lines describing constant velocity potential ϕ are perpendicular to the stream lines, which are tangent to the velocity and signify constant ψ, the stream function. Stream function theory is computationally simpler, with all corrections obtained simultaneously and has exact

[4] Perturbation theory splits a problem into a simpler problem that can be solved exactly and one that considers the effect of a small deformation

adherence to the dynamic boundary condition (R. G. Dean 1965). It is generally applicable as long as the wave height is below the breaking criterion.

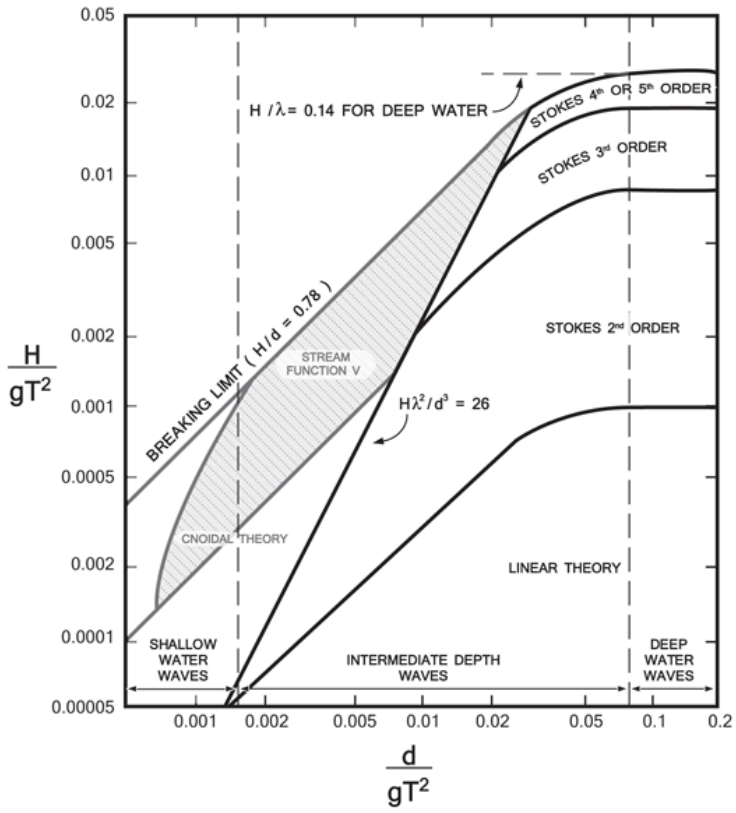

Figure 3.3: Ranges of applicability for different wave theories (US Army Corps of Engineers 2002)

Figure 3.3 denotes the applicability of each theory for waves of different height and period in different water depths. They have been evaluated in terms of how closely each theory adheres to the dynamic free surface boundary condition. In shallow water Cnoidal theory is most applicable, but in deeper water Stoke's theory dominates with varying order of perturbation theory dependent on the wave height. An Ursell number of 26 separates the Cnoidal and Stokes validity regions, though Stokes may become unstable for $Ur > 10$. Close to the breaking limit, stream function theory must be used for accurate representation of the free surface and associated dynamics. In his review of non-linear dynamics within the entire chain of a WEC development, Penalba et al found that there was little mention of the importance of modelling non-linear waves in the estimation of power production purposes. However, it was suggested by some researchers that over 90% of operational wave conditions can be considered as linear (Penalba, Giorgi, and J. V. Ringwood 2017).

Shallow water effects Studies of the coastal environment often necessitate the use of non-linear wave theories due to the increasingly non-linear characteristics of near shore waves. As waves enter into shallow water they become dispersive as the wave form undergoes deformation and their celerity, height and length are influenced by the water depth. According to the dispersion relation Equation (2.16) as a wave of a particular frequency enters shallower

water its wave length will decrease and subsequently the phase speed will also reduce. This is the basic premise of refraction and shoaling, two processes that occur in shallow water wave transformation.

Due to waves slowing down in shallow water, the direction of propagation of waves changes in the coastal environment. This phenomenon is called refraction and is observed in other wave types such as sound and light, thus it is a thoroughly investigated process and is well characterised by Snell's law. The result in water waves is that wave crests tend to become parallel to the coastline. In order to adhere to the principle of conservation of energy, the rate at which energy enters and leaves a control volume must be equivalent if no generation or dissipation occurs. In waves, no energy flux is permitted across wave rays, thus if b is the width between two wave rays, this can be expressed with the following.

$$(EC_p)_1 b_1 = (EC_p)_2 b_2 \tag{3.6}$$

Therefore, in shallower water with parallel wave rays, if there is a decrease in the wave phase speed C_p then there must be an increase in energy E per crest width, which requires an increase in wave height, as shown in Equation (2.18). Thus shoaling is the effect by which waves entering shallower water change amplitude (R. Dean and Dalrymple 1993).

The most physically complex process that affects water waves is wave breaking. This occurs when the height of the wave increases beyond a particular level and results in wave energy being transformed into turbulent kinetic energy. The increase in turbulent intensity near the sea bed is a key driver of near shore sediment transport and construction within the surf zone must consider these processes. There are numerous breaking criteria that have been suggested based on geometric, kinematic or dynamic considerations, but the first attempts to predict the onset of breaking still prevail as engineering rules of thumb. In 1893 Michell (Michell 1893), noted that waves first start to break when the angle of the wave crest exceeds 120^o, which is equivalent to $(\frac{H}{\lambda})_b = 0.142)$. This limiting steepness coincides with the velocity of the water particles in the crest moving at approximately the phase velocity. However, depth effects also influence the wave thus a secondary breaking criteria is often cited:

$$(\frac{H}{h})_b = 0.78 \tag{3.7}$$

However, the relevance of this second limit is restricted as the slope of the sea bed is not included. Conditions with a more gently sloped bed have been seen experimentally to allow wave heights up to $1.4h$ before breaking is initiated (Southgate 1988).

Wave breaking has been extensively investigated both numerically and experimentally. These simulations have two distinguished zones: the wave propagation zone and the surf zone, and it is the latter zone that requires a turbulence model as one of the governing processes is turbulence generation. The choice of turbulence model is key for a good agreement between NWT and PWT and has been the focus of much research. The $k-\epsilon$ model has been found to overestimate the turbulence at the breaking point leading to a suppression of the maximum height due to its damping effect. Although developed for a single phase flow in aerospace applications, the $k-\omega$ model has performed better in validation studies. Jacobsen et al (Jacobsen, Fuhrman, and Fredsøe 2012) used a $k-\omega$ model in the validation tests of their

wave generation toolbox for OpenFOAM, demonstrating that the aspect ratio (≈ 1) of the mesh is of key importance in obtaining a good representation of surface elevations and undertow profiles. More recent studies, (Devolder, Rauwoens, and Troch 2017) and (Devolder, Troch, and Rauwoens 2018), have produced and assessed the performance of $k-\omega SST$ model that explicitly includes the density in the turbulence transport equations through the introduction of a buoyancy term. This development addresses the issue of density variation across the water-air interface in two phase flows (particularly those represented by the VoF method), which results in excessive prediction of turbulent kinetic energy in that zone and can cause considerable wave damping in high steepness waves.

As turbulence modelling is equally relevant in flows with significant vortex shedding or when wave breaking occurs, these findings are relevant for WEC modelling even in regular waves far from the surf zone which otherwise have low levels of turbulence.

3.3.2 Relevance to technology development stages

At different stages of development the key metrics and purpose of modelling changes. Initially there are a large number of variables requiring a parametric survey and sensitivity analysis. Methods that require less computational expense are better suited to studies that investigate a large number of runs e.g. power production assessment and optimisation. Then as the WEC design is refined, a more specialised modelling of particular subsystems or device performance outside of the operational sea conditions is of more interest. As the development of the WEC progresses, increasingly high fidelity models are needed as they inform critical component design e.g. structural loading.

The wave industry has adopted the use of Technology Readiness Levels ("TRLs") that were originally developed by NASA, to benchmark the progression of technology and assess the development status. Table 3.3 demonstrates expected output and the modelling requirements at each TRL considering only TRL 1-6 as TRL 7-9 involve full-scale construction. At low levels, the focus is strategic research, with elementary modelling and small scale proof of concept to decide on the overall design and understand any limitations or constraints. Up to TRL 3 it is generally considered that linear frequency-domain models and potential flow solvers are sufficient to assess various concepts and inform the design process. For TRL 4-6 the main aim is technology validation with increasingly specialised modelling and integration of subsystems (Mooring, PTO, structural design) both numerically and in the laboratory environment at larger scales. For these stages time-domain models are required with appropriate incorporation of non-linearities and direct coupling of different subsystems. TRL 7-8 involves full scale demonstrations and deployments of the WEC to finalise the characterisation of performance harvesting wave power, assess survivability and address environmental and O&M considerations. A fully technologically ready WEC (TRL 9) is one with demonstrated utility scale deployments e.g. WEC farms.

Progression through the TRLs is also marked by the increase in investment required to satisfy each stage. The CAPEX and risk associated with full scale prototypes and deployments has pushed previous WEC developers over the edge financially.

Table 3.3: Interpretation of modelling requirements for TRLs.

TRL	Modelling	Outcome
1/2	Potential Flow modelling	WEC Type Chosen
3	Small scale lab testing	WEC basic design Validation of elementary models
4	Time Domain using hydro coeffs and simple PTO Initial control system modelling Medium scale lab testing	Design optimisation Power performance matrix
5	Survivability testing Full nonlinear simulations of integrated subsystems	Advanced component design Full scale structural design
6	Subsystem integration Large scale testing including telemetry	Full scale PTO characterised Control system optimised

Weber has demonstrated the use of a second metric to fully describe and quantify the status of a WEC technology (Weber 2012). Analogous to the TRLs, there are nine Technology Performance Levels ("TPLs"), indicating the techno-economic performance of a device. The initial 3 levels describe a system where the majority (TPL = 1) to the minority (TPL=3) of key performance indicators do not satisfy potential economic viability. TPL 4-6 outline the amount of key technology implementation and improvement are required to satisfy economics in favourable and distinct market conditions. Finally TRL 7-9 detail the amount of financial support required for the WEC to be competitive with other renewable devices.

Weber's proposed TPL-TRL matrix encapsulates the development of a WEC to maturity, with the aim of achieving both economic and commercial success with a clear split between research and demonstration activities. If the developer prioritises progression through TRL rather the TPL, they risk being inflexible to design changes. They could arrive at full scale and then attempt to implement performance improvements which are much more expensive, take a lot more time and may be impossible without fundamental changes in concept. It would also likely erode investor confidence. A strategy better suited to thorough de-risking is highlighted in Figure 3.4, and traverses the TPLs at a lower TRL and then only undergoes expensive prototype demonstration when sufficient confidence is gained in the concept. This requires a high-fidelity modelling strategy to be adopted that incorporates the full system (the hydrodynamics and the PTO) to evaluate the holistic performance of the WEC. However, at higher levels of TPL an increasingly accurate and thus computationally expensive model is required. This may explain why early drivers in the wave energy sector jumped to full scale prematurely, as either the requisite models or computational power were not available as an alternative.

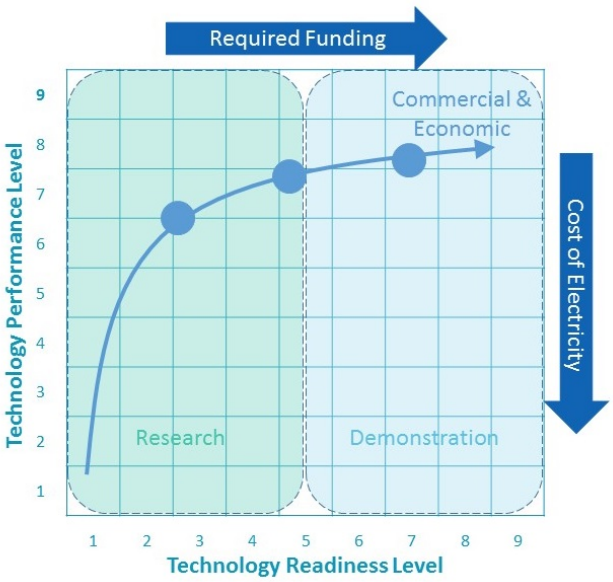

Figure 3.4: TRL and TPL matrix with the ideal development trajectory. Adapted from (Weber 2012)

3.4 How should CCell be modelled and optimised?

Numerical modelling has become a valuable toolbox for WEC developers as it allows rapid modifications to a WEC design without the additional manufacture and testing costs, or scaling issues. It can build up a picture of expected energy production and the load estimates on the device, which can aid design decisions and inform the required O&M procedures. However, numerical simulations can be slow to compute without adequate computer power and some simplifications must be introduced for efficiency, especially at earlier stages of development.

Figure 3.5: Example of the non-linear effects observed in tank testing of the CCell Floating WEC.

A wide range of numerical modelling techniques for WECS have been proposed to allow a greater understanding of a device's hydrodynamic response. However, like the WEC con-

cepts themselves, there is a lack of consensus among developers about the most appropriate methodology. “Cheaper” codes that are less time intensive have so far prevailed, with frequency domain diffraction codes used as the norm, particularly in the earlier stages of the design process. For latter stages of design and optimisation the time domain is used to include transient effect. However, their reliance on potential flow theory and boundary element methods (WAMIT, Inc 2016) produce some sizeable limitations meaning that they cannot account for: large relative motions between the free surface and the device motion, viscous losses or extreme loading events (Vyzikas 2014). However, all of these non-linearities are observed in the true response of a WEC in real seas, see for example the viscous effects pictured in Figure 3.5. If the device is to be deployed in shallow water, as is the case for CCell, depth effects such as shoaling and wave breaking are also more likely to occur. According to the ranges of validity of different wave theories, the Ursell number for the pilot deployment dictates that the Cnoidal theory ought to be used as Stokes theory is likely to become unstable. Therefore, the “cheaper” linear codes would only be capable of producing low to mid-fidelity estimates of the fluid-structure interaction.

Considering the limits of applicability for different hydrodynamic approximations and characteristic dimensions and wave conditions of CCell suggests that linear methods are suitable. It also predicts that diffraction is insignificant and hydrodynamic loading will be dominated by inertial effects. However, from review of existing literature, particularly that concerning OWSCs, the relevance of non-linear effects such as vortex shedding, over-topping, slamming events and pitching motions in excess of $0.3rad$, suggest that CFD is the only way to numerically model the device behaviour accurately.

It is clear that development through TRLs 4-6, which aims to de-risk and provide greater confidence in performance estimates, requires more advanced modelling techniques than linear theory can provide. The intention of the subsequent chapters is to develop an appropriate CFD modelling strategy and address the limitations of existing work such as the reliance on linear PTO models and modelling of extremes.

Chapter 4

Modelling Methodology Adopted for CCell Design

Following the analysis of the different modelling techniques available to developers, this chapter outlines the practicalities of implementing and validating the chosen CFD strategy. Initial analysis using the CNWT is then conducted to provide commentary on the legitimacy of linear codes for the design of an OWSC which is asymmetric with respect to its fluid-structure interaction. The chapter is divided into three sections:

- Creation of a CNWT and discussion of pertinent solver choices.
- Validation of CFD results through physical modelling of the floating CCell concept with targeted testing to isolate different system components.
- Applicability of linear codes for an OWSC through comparison of radiation coefficients derived from CFD forced oscillation tests and NEMOH.

4.1 CFD Modelling Methodology

CFD packages solve the Navier-Stokes equations that govern the dynamics of fluid and encapsulate the conservation of mass, momentum and energy within a system. Numerical solution of these equations is achieved by discretisation of time and space in order to form a set of linear algebraic equations and an iterative method, to resolve the pressure-velocity coupling, is used to reach a converged solution at each time step. There are a number of commercial packages available, however the cost of licensing fees and "black-box" treatment of the underlying code reduce its suitability for research projects. Open-source Field Operation And Manipulation ("OpenFOAM"), is an alternative open-source CFD toolbox, which has been used extensively both in academic and commercial spheres since its initial release in 2004. It is a collection of C++ libraries that cover most engineering and scientific applications for CFD that together provide a powerful and flexible platform. Development of the software in C++ with object-oriented programming, modularity of template classes and operator overloading has allowed users to customise code, and write bespoke solvers for more niche applications, with relative ease. In particular the syntax for mathematical operators and PDEs has created

an easily readable code, very similar to the underlying mathematical equations (CFD Direct 2017). OpenFOAM also provides a range of utilities for pre- and post-processing with tools for meshing (either from a user input file, or from an STL file for more complex and specific geometry) and data visualisation, through an interface with ParaView. Furthermore, the functionality for parallelization of simulations is provided as standard, through the third-party package OpenMPI. Therefore, as there are no license fees per core (as is often the case for commercial codes), there is no barrier for users to employ all computational resources available to them and investigate increasingly complex phenomena. This makes it suitable for investigation of wave-structure interactions and is the chosen CFD software for this research. The user input files for a simulation are structured into three main folders:

- **constant**: contains a full description of the case mesh (in polyMesh) and files specifying physical properties, such as gravity, the chosen turbulence model and details of the wave generation and absorption.
- **system**: provides the specfication of the parameters for the solution of the problem. The three main files are: controlDict, which specifies time step, start and end time, and controls data output; fvSchemes, where discretisation schemes are selected; and fvSolution in which tolerances and other required solver parameters are set. This folder is also where the controls for meshing and decomposition for parallel simulations are stated.
- **time directories**: stores data for particular fields in individual files. At the initiation of the simulation a 0 directory must be specified with the initial boundary conditions for each parameter.

4.1.1 Choice of Solvers

An underlying assumption of these multi-phase numerical simulations is that the fluid is incompressible, for which OpenFOAM provides a number of incompressible solvers to solve the RANS equations. For the current modelling, a transient multi-phase solver designed for two incompressible, isothermal immiscible fluids with optional mesh motion is chosen, called interFOAM[1]. interFOAM uses a merged PISO and SIMPLE algorithm, see Section 2.4.2. This sequentially solves the motion, the momentum and then the pressure equations with each iteration to reduce residual errors and improve convergence for a transient problem (Greenshields 2016). The strength of the merged ("PIMPLE") algorithm is that it conducts multiple PISO loops per time step to obtain convergence and overall can run with a larger time step. To reduce the overall execution time of these transient simulations whilst ensuring stability, adaptive time stepping is used. This automatically reduces the time step when velocities are larger to preserve the CFL condition, Equation 2.47, with a maximum Courant number specified as $maxCo = 0.5$.

The user has the ability to fully customise the solver for their application, prioritising accuracy, stability or boundedness. These options are specified in the fvSchemes and fvSolution files. A discussion of these inputs is provided below, and template files are provided in Appendix A, to show parameter choices made in this work.

[1] In earlier versions of OpenFOAM a distinction was made between solutions with dynamic bodies (interDyMFOAM) and static bodies (interFOAM), however, as of OFv6.0 interFOAM now handles both

fvSchemes Derivatives and interpolation of values from one point to another must be assigned an appropriate numerical scheme in fvSchemes. Generally standard Gaussian finite volume integration is used, which interpolates values from cell centres and then sums on cell faces. However, there is a large amount of choice available to the user, with some schemes being specifically designed for particular derivative terms. The terms requiring numerical schemes are split by the types of derivatives, e.g. time, gradient, divergence and Laplacian.

For most of the types of derivative it is sufficient to set a default for all variables, for example, linear interpolation is effective for gradient terms and used throughout. However, there are a significant number of options for divergence schemes as the treatment of advective terms is challenging. Again the schemes are based on Gauss integration with a selection of different interpolation schemes, e.g. linear (central differencing), upwind and linearUpwind (blended differencing). A discussion of the theory behind these main schemes is provided in Section 2.4.1.2. Additional options are: the limitedLinear scheme, which is linear except for in regions with rapidly changing gradient where it is limited to the upwind value; and vanLeer, which is similar but imposes weaker limits than limitedLinear. For vector fields designated "V-schemes" (limitedLinearV) are used, which calculate a single limiter value based on the component that has the most rapidly changing gradient and applies this to the other components. This method prioritises the stability of the solution over the accuracy, whereas in scalar fields, it is often boundedness that is prioritised.

Poor mesh quality, with non-orthogonal cells can cause instabilities due to the size of the non-orthogonal correction term. To improve stabilities, but reduce accuracy, the size of the correction term can be reduced. This can be specified as limited correctedψ, with ψ marking the level of correction. However, if none of the correction terms are used (i.e. uncorrected), then the user should consider re-meshing as this severely impacts accuracy of output.

fvSolution The options for the PIMPLE algorithm are specified in the fvSolution file. nCorrectors indicates the number of PISO loops (i.e. the number of times that the pressure equation and momentum corrector are calculated in each time step). nOuterCorrectors effectively specifies whether the solver is PISO or PIMPLE (multiple loops), as it enables looping over the entire system of equations within on time step. Additionally, in some simulations such as low Re and multiphase flows, the momentum predictor step (as shown in Figure 2.5) is turned off to allow for stability and convergence.

As well as the application solver interFOAM, which dictates the set of equations to be solved, each discretised equation has a linear-solver specified for the solution of it's matrix equation. These are marked by the variable they are solving, thus for interFOAM the phase fraction, velocity, pressure and the turbulence variables must be designated in fvSolution, and in dynamic cases cellDisplacement is also included. As equations may be solved multiple times within one time step, there is also an option to provide different settings for the final time it is solved. Generally smoothSolver and GAMG (generalised geometric-algebraic multi-grid) have been used in this study, based on tutorial examples provided by OpenFOAM developers.

The solvers are iterative and are based on reducing the equation residual over successive iterations. The residual is a measure of the error in the solution, thus the smaller it is, the more

accurate the solution. After each iteration the residual is re-evaluated and the solver stops if:

- the residual falls below the solver tolerance (tolerance), which is set at a value below which the solution is deemed "accurate enough"
- the ratio of current to initial residuals falls below the solver relative tolerance (relTol). However, this limits the relative improvement from initial to final solution, in transient simulations it is usual to set it to zero to force convergence to solver tolerance at each timestep.
- the number of iteration exceeds the maximum number of iterations allowed (maxIter).

Under-relaxation can be applied to particular fields or equations to limit the change in the variable's value between successive calculations. This functionality is used to improve convergence and avoid instabilities. However, as it slows the change between steps, a number of iterations would be required to accumulate the physical changes in a transient solution, which is costly. Therefore, for transient solutions it is best practice to turn off under-relaxation for all terms and instead reduce the time step.

Surface Representation

Simulating a moving fluid interface, such as in ocean waves, is problematic as the location of the boundary is continuously changing and must be calculated at each time step as it is not known in advance. It is particularly challenging when the interface is highly distorted either due to the waves themselves or the presence of a structure. Two possible methods are available, either surface tracking or surface capturing. In surface tracking, typically only the fluid region is modelled, with the free surface presented as a moving boundary. However, it is a mesh-based technique that requires remeshing at each time step. It also means that entrained air bubbles are not modelled, and phenomena like wave breaking, which significantly distort the surface, are not accurately predicted because of grid skewness and complexity of the mesh. Though they do perform well in simple cases. Alternatively, capturing methods use a fixed grid that extends over both the air and water regions, along with an additional fluid property to identify the interface. These methods are more robust than the tracking algorithms and can handle more distorted surfaces as well as viscous effects.

To capture the free surface, interFOAM uses a Volume of Fluid methodology ("VoF") with a phase-fraction (α) within each fluid volume that identifies the relative proportions of air and water. The momentum, and other fluid properties within each fluid volume are defined by the mixture, and a single momentum equation is solved. Multiphase systems can then be simulated using an advection equation for the phase fraction α.

$$\frac{\partial \alpha}{\partial t} \; + \; \nabla \cdot (U\alpha) \; = \; 0 \tag{4.1}$$

and when discretised this becomes:

$$(\alpha - \alpha^0)\frac{V}{\triangle t} \; + \; \sum_f \phi_f \alpha_f \; = 0 \tag{4.2}$$

The phase fraction is limited to be between 0 and 1, therefore boundedness[2] is critical and multiphase VOF simulations can often be hindered by diffusion at the free surface, where the boundary between air and water 'spreads' non-physically as the simulation progresses. Typically the only method to guarantee boundedness is to use the upwind implicit advection scheme, however this does not provide an accurate solution. This inaccuracy lead to the development of MULES (Multidimensional universal limited for explicit solution) for OpenFOAM:

$$(\alpha - \alpha^0)\frac{V}{\triangle t} \; + \; \sum_f \phi_f \alpha_U \; + \; \sum_f \lambda_f^+ \phi_f^+ (\alpha_H - \alpha_U) \; + \; \sum_f \lambda_f^- \phi_f^- (\alpha_H - \alpha_U) \; = 0 \tag{4.3}$$

where f refers to the "on the face" and

- α_H is high-order scheme evaluated from known values
- α_U is the upwind scheme evaluated from known values
- λ_f^- limiter when $\alpha_{max}(=1)$
- λ_f^+ limiter when $\alpha_{min}(=0)$
- ϕ_f^+ fluxes out of cells
- ϕ_f^0 fluxes in to cells

This method works by substituting the bounded values of α (0 and 1) separately into Equation (4.3) and solving to evaluate the limiters λ. These are then used within the MULES equation to advance the solution of α and guarantee boundedness. The MULES equation can be used explicitly, where sub-cycling is required [3], or semi-implicitly in a predictor-corrector method where first an upwind implicit solution of the phase fraction is calculated and then a high-order explicit MULES correction is applied. This latter method provides a significant speed-up of computation in comparison to the fully explicit method.

Body Motion Solver

A specialised motion solver is also required to simulate the wave structure interaction when the body has one or more degrees of freedom. However, the motion of the body is also part of the solution itself and is unknown beforehand. This six degree of freedom solver first sums the pressure (normal F_N) and viscous (tangential F_T) force contribution from each cell face on a surface. Then, taking into consideration any additional forces on the body due to specified restraints, the solver evaluates the motion of the body due to these forces, where a_b is the acceleration of the body about it's centre of mass.

$$F_N + F_T + F_{restraint} = ma_b \tag{4.4}$$

The use of different restraints is specified in the file dynamicMeshDist, along with the properties of the body such as mass, inertial matrix and relative position of the centre of mass to the origin of the body. Restraints supplied by OpenFOAM are linearDamper, linearSpring and linearAxialAngularSpring. A customisation by Zyba, allows for a bidirectional specification of

[2]Boundedness is achieved if the variable stays within a specified range, i.e. between the upper and lower bound.
[3]as otherwise a much smaller time step would be needed for the whole simulation for required accuracy

the damping in the linearAxialAngularSpring, such that damping coefficient, B_{PTO}, for seaward or shoreward motion can be prescribed separately. The torque for the PTO restraint for angular motion used in dynamic simulations in the CNWT is calculated by Equation (4.5).

$$M_{PTO} = -B_{PTO}\dot{\theta} \tag{4.5}$$

4.1.2 Boundary Conditions

Particularly in low speed, incompressible flows disturbances introduced at an outflow boundary can affect the entire computational region. The most commonly used condition is a continuative boundary that consists of zero normal derivatives for all quantities and is intended to represent a smooth continuation of the flow through the boundary. To provide a single solution this needs to be pinned to a particular value somewhere and as a rule in subsonic flow the inlet and wall are set to a `fixedValue`, whilst the outlet is a `zeroGradient` for all variables. The pressures, however, need to be of opposite type to the velocities with the inlet and walls specified as a `zeroGradient` and the outlet a `fixedValue`.

Entrainment BC An entrainment boundary condition, as described below, provides protection in case the inflow becomes an outflow at some point in the simulation and you were unaware of this occurring at initiation of the simulation. For example, 3D effects such as vortices may cause inflows or outflows depending on their direction. In the set up for this study, the entrainment boundary condition is used for the atmosphere boundary condition. If unsure about the boundary condition then set:

- Velocity (0/U): type `pressureInletOutletVelocity`

  value `uniform (0 0 0)`

  This sets the outflow to `zeroGradient`, the tangential inflow to zero and the normal inflow to `zeroGradient`. i.e. this forces the velocity to be normal to the boundary. But instability can arise if the pressure does not change accordingly.

- Pressure (0/p_rgh): type `totalPressure`

  p0 `uniform 0`

  Normally pressure would be set to a `fixedValue` but this could lead to instabilities. Therefore the total pressure is used to ensure that it is self-stabilising, such that when the velocity increases the static pressure reduces.

$$p = p0 - \frac{\rho |U|^2}{2} \tag{4.6}$$

fixedFluxPressure `fixedFluxPressure` is a substitute for `zeroGradient` where the normal gradient is not zero and is instead evaluated to balance body forces, e.g. gravity, surface tension or buoyancy. This is required in the 0/p_rgh file for all patches other than the atmosphere.

symmetryPlane In cases where there is some symmetry about the solution, computational expense can be reduced by meshing only half of the domain. In this study the CCell device is

symmetric about the x-z plane, thus only the positive y values are meshed, and the boundary at y=0 is set as a symmetry plane.

Wave Generation and Absorption

To investigate coastal and offshore engineering problems, the CNWT must be capable of producing an accurate wave field through some sort of numerical wave maker. This involves both wave generation and, as the domain is finite, wave absorption to prevent reflections within the "tank". There are a number of proposed methodologies to serve this purpose. For wave generation these range from a numerical representation of a physical wave tank with a moving wall, to additions of a source term to the underlying equations. The four most commonly used techniques are:

- **Static Boundary (SB)**: Imposes a Dirichlet boundary condition on the wave velocity and surface elevation provided from a suitable wave theory. This type of wave generation is beneficial as it requires the smallest domain size.
- **Dynamic Boundary (DB)**: A dynamic boundary is employed to act like a flap or piston wave maker. However, this requires the complexity of both the moving mesh and the control strategy for the wave maker. It is also prone to the same evanescent wave issues as a physical wave piston.
- **Relaxation Zone (RZ)**: In the relaxation zone (a region adjacent to the boundary) a weighting function is used to blend the target velocity potential to the computed potential within the simulation domain. The blending function uses a value of $\beta = 0$ at the boundary and $\beta = 1$ at the interface between the relaxation zone and the rest of the domain. Between these limits, β is smoothly varied to avoid any sudden discontinuities.

  $$F = \beta \cdot F_{calc} + (1 - \beta) F_{theory} \tag{4.7}$$

  The blending function is applied to the pressure, velocity and surface elevation fields at each time step to merge the desired theoretical solution at the boundaries of the domain, with those calculated by the numerical model. This requires a significant extension to the domain size to prevent reflections.
- **Impulse Source (IS)**: Alters the RANS equation by adding an impulse term with a coefficient that is equal to unity within the wave maker zone and zero everywhere else.

The relaxation zone, static boundary and dynamic boundary methods can also be used for wave absorption along with geometric sloping of the sea bed to dissipate wave energy, numerical beaches that include a dissipation term in the RANS equation and mesh stretching that utilises the inherent dissipation that comes from spatial discretisation. A study by Windt. et al (Windt, J. Davidson, Pál Schmitt, et al. 2019) compared the options available to OpenFOAM users: OpenFOAM's own functionality available in version 6.0 (SBM or Numerical Beach), olaFLOW (SB or DB methods) and waves2Foam (RZ),[4] evaluating the velocity profile and surface profile for different sea states. From their study it was found OpenFOAMs own SBM performed poorly with large and consistent errors, whereas waves2Foam's RZ method showed good overall performance and could accurately simulate shallow water, deep water and poly-

[4] they also compared their own IS method developed in-house

chromatic waves with a low reflection coefficient from the absorption zone and negligible re-reflections from the wave generation boundary. The drawback of the RZ method is the additional computational cost due to the increased domain size, and as the authors noted, for polychromatic seas there is an inexplicably dramatic increase in computation effort in comparison to the monochromatic waves. The computational penalty of the RZ method can be reduced by also employing mesh gradation to reduce the overall cell count whilst enhancing absorption. The SB method from the olaFlow tool box showed mixed results: throughout the study it required least computational effort and apart from the RZ method it was the only method that could model shallow water waves with Cnoidal theory (the DB method could not reproduce the nonlinearities), but its reflection coefficients were 25% for deep water and polychromatic seas.

However, the enhanced performance of the RZ method especially for short and steep waves, along with its ease of implementation and the ability to couple with external wave propagation models has lead to the choice of waves2Foam package (Jacobsen, Fuhrman, and Fredsøe 2012) for the CFD NWT used in this work.

For effective absorption of the waves, and to prevent reflections from the outlet, it has been found that the outlet relaxation zone must be in the region of one wave length long (G. Wei and Kirby 1995).

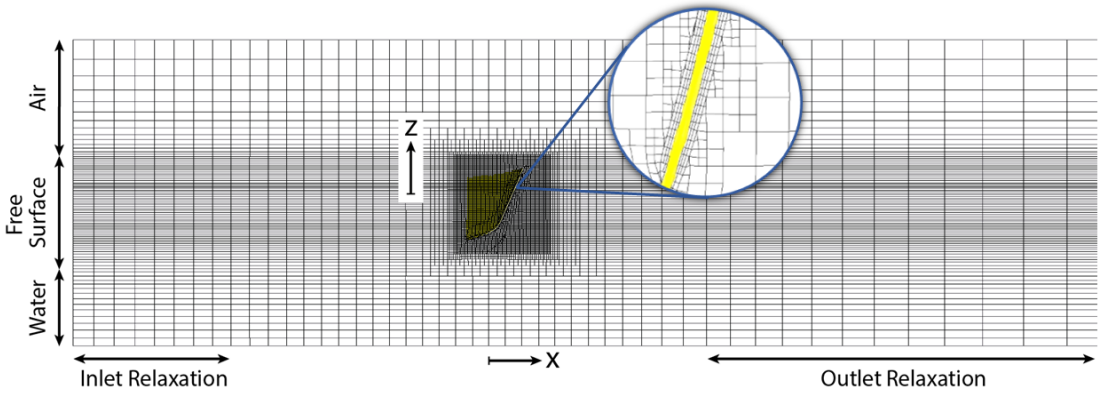

Figure 4.1: Mesh Design for Floating CCell modelling

4.1.3 Domain Meshing

The mesh can greatly affect the outcome of the numerical modelling, especially with regards to the rate of convergence, solution accuracy and CPU time required. A large number of cells give higher accuracy but it also greatly increases the memory and CPU requirements. This can partly be overcome by varying the cell size depending on placement within the flow. For instance cells adjacent to the structure should be fine enough to resolve boundary layer flow, whereas far from the structure, changes are less pronounced and a coarser mesh is adequate. The main measures of mesh quality are skewness, smoothness and non-orthogonality:

- Skewness: The optimal cell would be equilateral (skewness is zero), where as a degenerate cell, or sliver, is near coplanar. High skewness of cells can lead to instabilities and lower accuracy.

- Smoothness: The change in size between adjacent cells. If adjacent cells are very different in size then the numerical error will increase as the equations being solved have been developed assuming a gradual change in size.
- Non-orthogonality: The deviation from a regular grid where the vector from neighbouring cell centres is orthogonal to the face between the cells. In a regular grid this vector would be parallel to the face normal and $\theta_{no} = 0$. If cells have a non-orthogonality above $\approx \theta_{no} = 75^o$ re-meshing should be considered. This is covered in further detail in Section 2.4.1.2.

To maintain the integrity of the wave and the free surface, a suitable mesh density must be used across the domain, with a concentration of cells around areas with high flow velocities, as illustrated in Figure 4.1. Therefore when modelling surface water waves, the mesh density should be greatest at the free surface. However, the size of cells used in this region is inversely proportional to the number of cells required for the full domain, with a very high number of cells negatively influencing the computational time per simulation.

Cells both above and below the Free Surface layer are graduated, increasing in height the further they are from the free-surface. This graduation is merely used to concentrate cells around those areas with either the greatest mass-flux or greatest interest (i.e. around the modelled device) and to reduce total cells in the domain. Similarly, cells down-wave of the device are gradually increased in size to facilitate numerical dispersion within the relaxation zones. An example of the wave propagation within the numerical tank is shown in Figure 4.2.

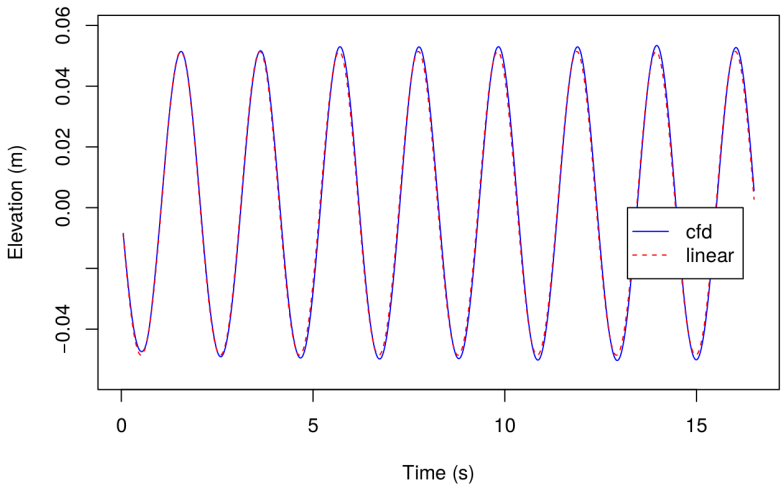

Figure 4.2: Surface elevation of wave propagated in numerical tank sampled at the middle of the domain compared to Airy's linear wave theory. H=1.5m, T=8s at 1:15 scale.

Around the paddle further refinement is added with three nested cell blocks. In each block an additional level of refinement is added in both the x and y directions, where one level of refinement splits the original cubic cell into four equal cells. These layers step the cell size down to a final boundary layer adjacent to the paddle at an appropriate resolution for the chosen turbulence model.

To determine the cell sizes within the free surface layer it is assumed that the horizontal mass

flux from one cell layer to the next should vary by less than 10%. Mathematically this is derived from a linear representation of the water waves, with the horizontal velocities defined by:

$$U_x(z,t) = a\omega \frac{cosh(k(z+h))}{sinh(kh)} e^{-i\omega t} \tag{4.8}$$

Thus the ratio, R, between velocities at two cell layer elevations, $z = z_a$ and $z = z_b$, respectively is

$$R = \frac{U_x(z_b,t)}{U_x(z_a,t)} = \frac{cosh(k(z_b+h))}{cosh(k(z_a+h))} \tag{4.9}$$

where $R < 1$. If (4.9) is rearranged, then

$$z_a = \frac{1}{k} \cdot acosh\left[\frac{cosh(k(z_b+h))}{R}\right] - h \tag{4.10}$$

alternatively

$$z_b = \frac{1}{k} \cdot acosh\left[R\, cosh(k(z_a+h))\right] - h \tag{4.11}$$

Thus at the Free-Surface, where $z_a = 0$ then from Equation (4.11) the cell height $(z_a - z_b)$ is

$$\Delta z|_{z=0} = -\frac{1}{k} \cdot acosh\left[R \cdot cosh(kd)\right] + d \tag{4.12}$$

At the surface $(z = 0)$ the cells should be approximately cuboid, such that $\Delta x \simeq \Delta y \simeq \Delta z$ in order to achieve a good quality mesh around the paddle.

The objective of an appropriate mesh is therefore to minimise the number of cells, while maintaining a sufficiently accurate solution. Grid convergence, or mesh independence, occurs when the solution is invariant to further grid refinement. In these tests a static simulation was repeated with a simple curved paddle, and the R ratio varied to assess grid independence of the solution. For these simulations, computational expense was saved by modelling only half of the domain, with symmetry along the x-axis at $y = 0$.

Another consideration regarding mesh size is that when using turbulence models such as the $k - \omega SST$ model or models with enhanced wall treatment, the non-dimensionalised Reynolds based distance to the wall $(y+)$, as defined in Equation (4.13) where U_τ is the shear velocity, must be $\approx O(1)$ to ensure effective capture of the viscous sub layer. Thus it is critical that the cell closest to the wall is sufficiently small.

$$y+ = \frac{\rho U_\tau \triangle y}{\mu} \tag{4.13}$$

It is clear from Figure 4.3 that the lower limit of the ratio between velocities at two cell layer elevations is 0.97 for an accurate result. However a higher ratio causes unnecessary penalties, as shown in Table 4.1, reducing the cell height from 0.022m (45 cells per metre of wave height at 1:15 scale) to 0.015m (67 cells per metre of wave height at 1:15 scale) increases the number of cells by 3.5 times and the execution time by more than tenfold.

Table 4.1: Comparison of Mesh design

	R Ratio			
	0.92	0.95	0.97	0.98
Wave Zone Cell height (m)	0.047	0.038	0.022	0.015
Total cells	19,522	35,478	148,137	515,734
Execution time (s)	623	785	2,042	23,329

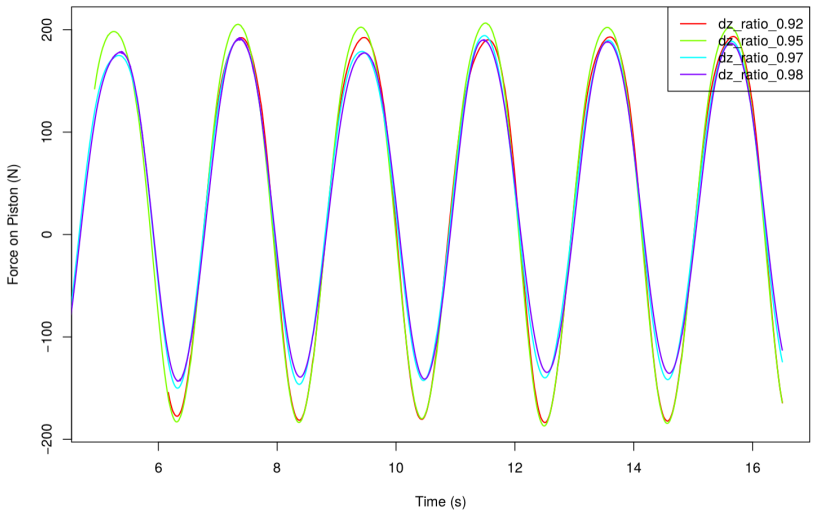

Figure 4.3: Effect of different Mesh Design and cell sizes by varying R ratio: 0.92, 0.95, 0.97 and 0.98

Dynamic Mesh

In dynamic simulations the computational grid must move or deform with the motion of the body. All, or part of, the domain can be re-meshed at each time step to ensure the quality of the grid, but this is computationally expensive and so mesh distortion is usually favoured. Mesh-distortion techniques in OpenFOAM are based on node repositioning calculated through spherical linear interpolation and the distance from the body. This is implemented such that smaller cells close to the body are locked to the body and undergo minimal deformation, where as cells at a set distance from the body remain stationary. As suggested by the name, mesh distortion can result in collapsed or distorted cells if not carefully considered. It is essential that the quality and geometric validity of the grid is maintained.

An alternative methodology to account for the mesh motion is to use Arbitrary Mesh Interfaces (“AMI”), that moves a cylindrical subset of the mesh with a sliding interface between the stationary and dynamic regions. However, in meshing the cylinder around the WEC body, discontinuities are introduced into the mesh, particularly in the x direction, which causes numerical dissipation. Additionally, the mesh must extend non-physically beneath the WEC to account for the fact that the WEC is hinged near the sea bed and the hinge must be at the centre of the rotating cylinder. To represent the sea bed, Schmitt et al (Pál Schmitt and Elsäßer

2015) used an additional dissipation parameter in all cells below the physical water depth to act as a negative source term and reduce flow velocity.

4.1.4 Dynamic Solution Stability

The staggered approach of the PIMPLE algorithm can be unstable for problems that involve fluid-structure interaction in incompressible flows. The instability manifests at the end of each stroke of the device motion, when the device changes direction. A recent study suggested that the impact of this instability is directly related to the relative magnitudes of the objects mass (M) and its associated added mass (M_A) (Devolder, Pál Schmitt, et al. 2015). Devolder concluded that if the added mass is much larger than the device, as is the case for the composite construction of CCell, then the instability will increase and the simulation will fail.

In order to stabilise the simulation, an acceleration relaxation factor α_R is used such that the acceleration at the current iteration of the time step is tempered by the acceleration calculated in the previous iteration, to prevent unrealistic spikes in the acceleration.

$$a^{n+1}_{relax_i+1} = \alpha \cdot a^{n+1}_{i+1} + (1 - \alpha_R) \cdot a^{n+1}_{i} \tag{4.14}$$

where

$$\alpha = \frac{M}{M + M_A} \tag{4.15}$$

For the curved CCell paddle, the added-mass is significant due to the large entrained volume within the concave face. As an initial calculation at laboratory scale, the CCell paddle has a mass of $M = 4.54kg$ and can be considered as a half-cylinder with diameter $D = 0.59m$ and length $L = 0.75m$. Thus,

$$M_A = \rho_{water} \tfrac{1}{2} \cdot \pi \frac{D^2}{4} \cdot L \tag{4.16}$$

This provides an added mass equal to $M_A = 102kg$, clearly within the instability region. Thus, from Equation (4.15) a stable solution requires $\alpha_R \approx 0.043$. In previous laboratory work undertaken in the Plymouth wave basin, estimates from calculations at the PTO suggested that the added mass was forty times the mass of the device itself. If this value is used, the acceleration relaxation reduces to $\alpha_R \approx 0.02$. The added mass of the device varies with frequency of excitation, and therefore should be considered in future simulations. A sensitivity analysis was conducted concerning the acceleration relaxation factor, as shown in Figure 4.4, in which a range of values from $0.02 < \alpha_R < 0.12$ were considered and which provided good agreement. Values above $\alpha_R = 0.2$ resulted in a failed simulation, with non-physical acceleration spikes and paddle motions.

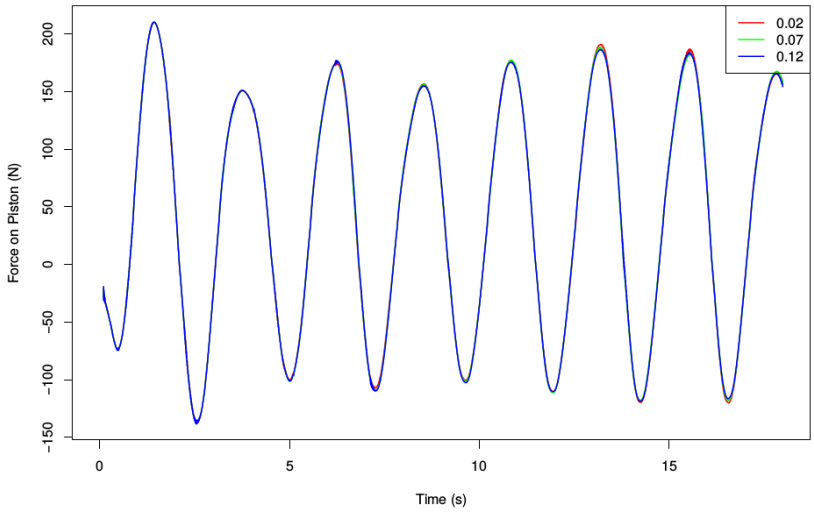

Figure 4.4: Sensitivity analysis of choice of acceleration relaxation factor on the calculated force on the piston.(Modelled at 1:15 scale. Equivalent full scale regular wave parameters: T=8s, H=1.5m)

4.1.5 Turbulence Modelling

For a typical, full-scale regular wave, the Reynolds number is $\sim 10^4$, using the major axis of the particle ellipse as the characteristic length. This suggests that the flow is low Reynolds. Considering the turbulence models available, and discussed in Section 2.4.4, it is clear that the $k-\epsilon$ model would not be suitable due to its derivation in high-speed flows. However, the $k-\omega$ and $k-\omega SST$ are candidate turbulence models for this application.

Choosing appropriate values for the turbulent kinetic energy, k, and specific turbulence dissipation, ω, is not obvious. Simplifications can be made to help in their selection. In particular, the calculation of the turbulence kinetic energy can be simplified using the turbulent intensity, I such that $k = 1.5(UI)^2$. The closer the turbulence intensity is to zero the less impact turbulence has on the flow. For an external flow, $0.05\% < I < 1\%$. Similarly the turbulent viscosity ratio β, can be used to determine the eddy viscosity: $\beta = \nu_t/\nu$ and for external flows this should fall within the range of $1 < \beta < 10$. This is then used to determine the turbulence dissipation parameter as $\omega = k/\nu_t$

A sensitivity analysis of these turbulent parameters, I and β was conducted within the range of expected values to provide confidence in the specification of the input parameters. It was found that as long as the initial estimate was within the correct order of magnitude the OpenFOAM solver converges to the same result.

A static simulation of floating CCell paddle at 1:15 scale was then repeated with different turbulence models selected, the results are presented in Figure 4.5. There is only a small difference in the values predicted by the two turbulent simulations. However, there is a more appreciable difference between the laminar and $k-\omega SST$ turbulent simulation with the laminar simulation over predicting the loads on the piston. Taking the root mean squared error between the laminar and $k-\omega SST$ signals and normalising it by the range in force values, this was evaluated at 3.5%. Although this error is of comparable magnitude to the expected error

between experimental and simulation values, it is still notable as the simulation investigated was static and with a relatively small wave. In larger waves where the device response is also larger, it is expected that the effect of turbulence will be more significant. The $k-\omega SST$ model is chosen as it is more robust in the free-stream flow whilst capable of handling adverse pressure gradients more accurately.

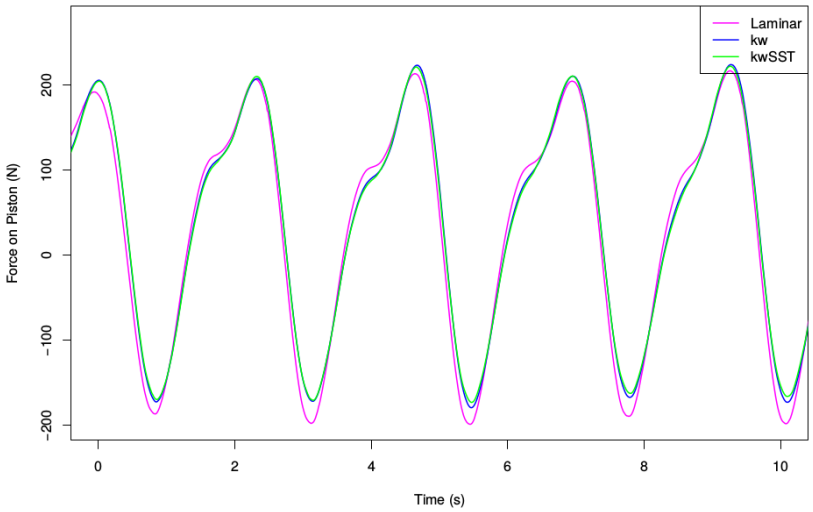

Figure 4.5: Effect of choice of turbulence model. (Modelled at 1:15 scale. Equivalent full scale regular wave parameters: T=8s, H=1.5m)

4.2 Validation of CFD

During the second half of 2016 the floating CCell device underwent an iterative design process with the development of the CFD models described above to evaluate the parameter space, and a series of laboratory tests. This culminated in a performance assessment of the optimised device in November 2016 consisting of tests in regular, irregular and directional seas. This also provided the opportunity to conduct particular tests to evaluate the performance of the CFD model.

4.2.1 Physical Modelling Set Up

Physical modelling was undertaken at 1:15 scale at the Kelvin Hydrodynamics Lab (KHL) 76m x 4.6m x 2.5m tank. Although a towing tank, this facility was sufficient for the testing conducted as the waves were unidirectional, the mooring footprint of the device could be accommodated and the water depth of 2m was representative of possible deployment locations (Holmes 2009). The tank contains a mounting point, approximately mid-way along its length, onto which a turntable is installed that allows the test apparatus to be rotated by 10^o and 30^o for directional testing of the device. The configuration of the tank is illustrated in Figure 4.6

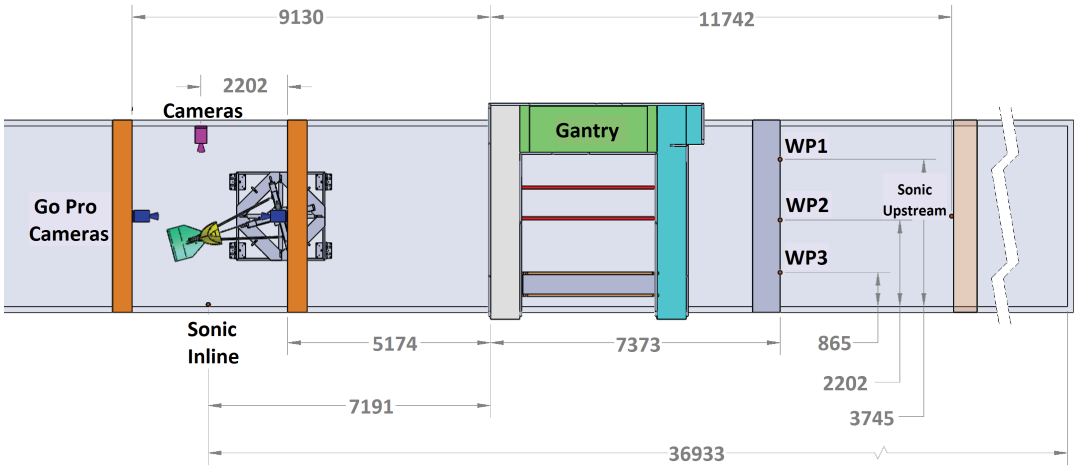

Figure 4.6: Wave tank set up for Performance and Validation testing at KHL in November 2016, shown with the CCell device oriented at 10^o to the incoming wave direction. Image courtesy of Zyba.

The tank has four adjustable depth wave makers with active absorption capable of generating waves with a period between 0.55-10s and up to 0.5m height. A 14.5m long, height adjustable passive beach is installed to absorb reflections and is reported by KHL to reduce reflections to less than 5% across the entire bandwidth. Between runs the tank was left to settle for around 3 - 5 minutes, which allows wave energy to be dissipated and absorbed by both the wave makers and beach. This settling was also aided by lane-markers, which were raised to the surface between tests and are particularly effective at reducing transverse waves.

A total of six wave probes were used to capture the wave field in the tank. Three custom made resistive probes using wave gauge amplifiers, were situated in a line across the tank upstream of the device. These probes allowed transverse variations in the surface elevations to be recorded. Three ultra-sonic probes recorded wave elevations upstream, downstream and inline with the device.

The motions of the system were measured using both Qualisys motion capture and a rotational sensor at the hinge point of the paddle. Qualisys measures all six degrees of motion (x,y,z, pitch, yaw, roll) for both the paddle and heave-plate using sets of reflective marker balls, as shown in Figure 4.8.

The force on the piston was calculated from the pressure difference across the piston from two pressure sensors installed at either end of the cylinder. However, this method of measuring the wave induced loading included the frictional forces experienced within the PTO circuit, which do not scale correctly with the rest of the device. Therefore, an additional load sensor was incorporated into the device at the connection of the piston to the paddle, to measure the load induced on the piston of the PTO directly.

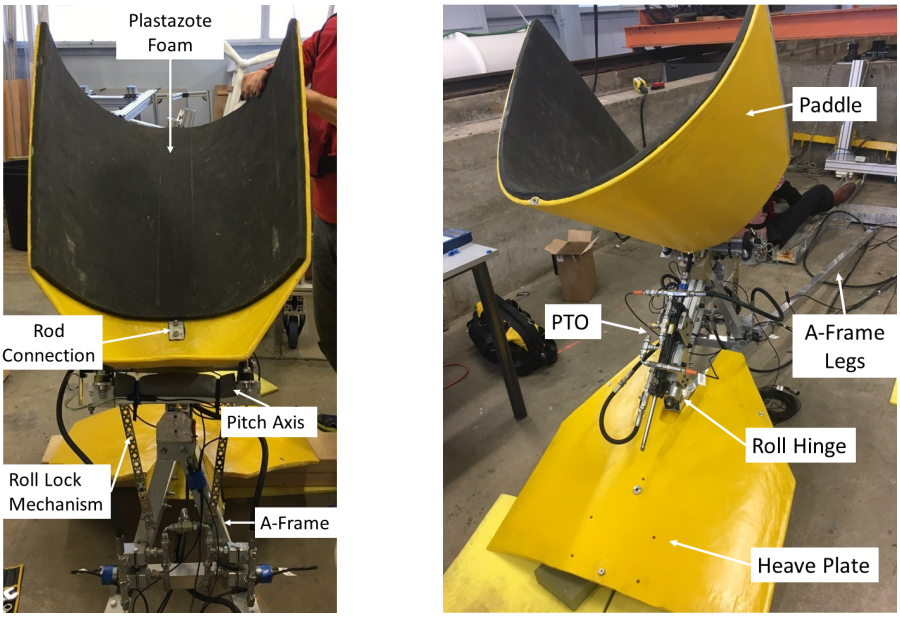

(a) Front view of the assembly

(b) Back view of the assembly

Figure 4.7: Assembly of 1:15 scale model of the floating CCell device

The device ultimately tested is shown in Figures 4.7a & 4.7b. Although the optimisation focused on the paddle shape, other relevant components of the system and their purpose are:

- The heave plate is designed to maintain the paddle in the optimal position in the water column as well as functioning as the mount for the PTO system, with the relative motion between the paddle and the heave plate driving the PTO piston. In larger seas, the asymmetry between crest and trough loads, leads to the heave plate sinking, which aids survivability of the device by causing the paddle to "duck" further beneath the water surface.
- The A-Frame works in conjunction with the heave plate to keep the paddle at the desired position in the water column and is the basis of the device's mooring.
- To increase survivability of the device, a roll capability was introduced into the design, such that if the device is hit by waves that differ significantly from the design incident direction, the lateral forces on the paddle and support structure are minimised. To test its effectiveness a locking mechanism was also incorporated to allow comparison with and without the additional degree of freedom.
- The PTO system at the laboratory scale shares as much of the architecture of a full-scale PTO as possible, in order to provide some confidence to the estimation of the efficiency of a scaled up system. Issues with sourcing suitable componentry and the scaling of frictional effects precluded the use of an hydraulic motor, but proportional valves were used to investigate damping effects. This subsystem was supplied by the University of Bath who were project partners for the WES project.

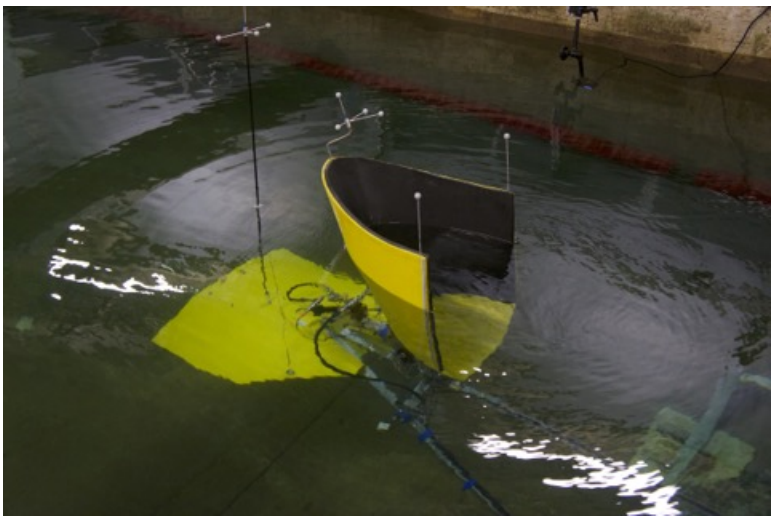

Figure 4.8: Floating CCell deployed in wave tank at Kelvin Hydrodynamics Lab. View from the seaward face of the device.

The centre of mass and centre of buoyancy positions, shown in Table 4.2, were calculated using a varying density SolidWorks model, with the origin located at the centre of the hinge. This was measured with the edge of the paddle wings vertical. The buoyancy values stated are those provided when the bottom hinge of the paddle is 0.56m below the surface, which is the designed optimal neutral position of the device. The system must be sufficiently buoyant to maintain the paddle hinge at the desired location. At full scale this would be achieved inherently within the system integration design, however for the lab testing the required additional buoyancy was provided by lining the seaward face of the paddle with 15mm of Plastazote foam (closed cell cross-linked polyethylene foam).

Table 4.2: Physical characteristics of the floating CCell paddle used in laboratory testing.

Mass of paddle (kg)	4.54
Buoyancy of paddle (kg)	11.92
Centre of mass x,y,z (m)	(0.042, 0, 0.425)
Centre of Buoyancy x,y,z (m)	(0.012, 0, 0.324)
Paddle Width (m)	0.59

One of the primary objectives of the tank testing was to collect data to be used to validate the CFD model. To aid the validation process a number of specialised tests which isolated particular subsystems were conducted. The initial CFD models simulated only the paddle with a linear damper representation of the PTO and assumed pitching about the paddle hinge as the only degree of freedom. This excluded the second pivot point at the seabed and any complexities introduced by the heave plate coupling. The numerical model outputs a moment about the hinge, thus the derived force on the paddle is always perpendicular to it. However, the PTO piston was not mounted in this way, thus a coefficient must be applied to accommodate the direction of the piston force, Figure 4.9.

$$F_{CFD} = \cos(\alpha)\frac{M_y}{\mathsf{a}} \tag{4.17}$$

where $\cos(\alpha)$ is the portion of the paddle force which is in line with the piston.

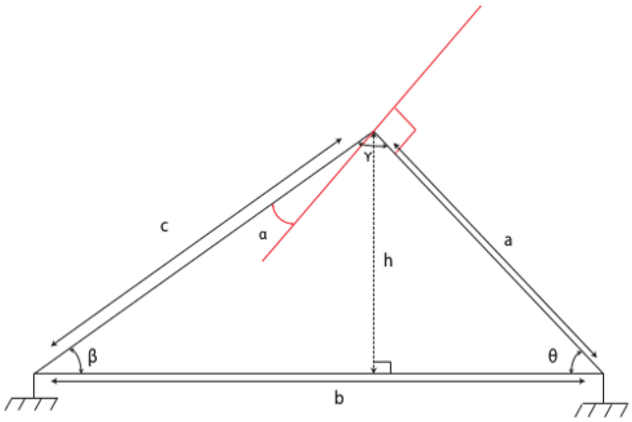

Figure 4.9: Derivation of coefficient required to derive force on piston from numerical modelling, where c represents the piston and the line of action of F_{CFD} is depicted by the red line

4.2.2 Static Tests

Static tests were replicated in the wave tank by locking the PTO piston and clamping the heave plate to a board that spanned the width of the tank, well above the water level, to prevent any pitching about the foundations. With the inclusion of the $k-\omega SST$ turbulence model the comparison is very close, Figure 4.10 with the normalised RMS error found to be 3.9%. The force profiles described by both the physical and numerical wave tanks are near identical, though the seawards force experienced in the wave trough has a flattened peak in the physical tank tests. This likely due to flexure within the physical system and reflections from the side walls, both of which were visible in the wave tank.

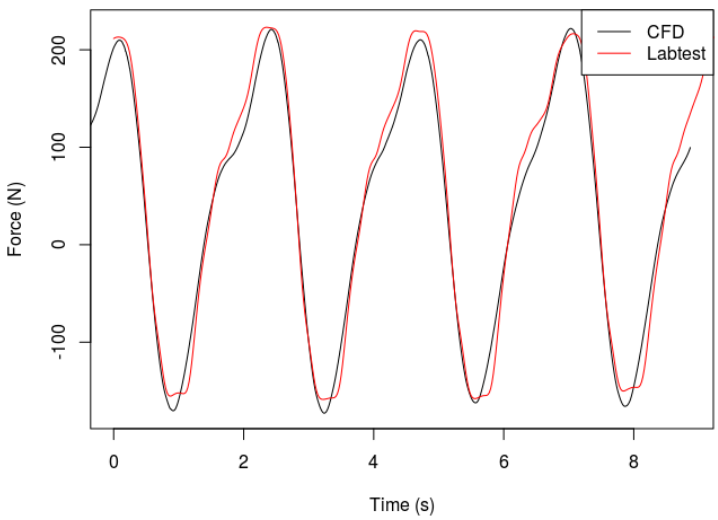

Figure 4.10: Comparison of physical and numerical modelling of a static case (Floating CCell concept modelled at 1:15 scale. Equivalent full scale regular wave parameters: T=8s, H=1.5m)

4.2.3 Dynamic Test

A similar set up was used for the dynamic test in the wave tank but with the piston unlocked and the proportional valves set to a constant voltage for the seawards and shorewards motion. This was again replicated in the NWT with only the paddle modelled, and the PTO represented simply as a damper with angular damping coefficients separately prescribed for the direction of rotation. The amplitude of the force is well matched by the NWT, as shown in Figure 4.11, however the shape of the force signal from physical testing is more triangular than the sinusoid predicted by the NWT. Figure 4.12 shows in more detail the relationship between angular position and force found in the two tests. Although the numerical model captures the range in the magnitude of the force on the paddle it does not fully predict the pitch motion of the device. This is particularly true of the seawards portion of the cycle (-ve pitch angle), where the NWT under-predicts the maximum seawards displacement. If the displacement is lower then the velocity of the prime mover is also reduced, overall this amounts to a smaller power prediction from the NWT.

This discrepancy is a result of the lack of equivalence between the PTO modelling in the two approaches. The physical PTO model exhibits non-linearities and compliance within the system. It does not provide a constant damping coefficient and this allows more movement at lower piston loads. Additionally, the construction of the physical model, with composites and a closed cell polyethylene foam positioned to achieve the desired neutral angle, may have also impacted the results. The pitch response of a device is linked to the centre of buoyancy, centre of gravity and moment of inertia. The values used in the simulation originate from a CAD model of the ideal construction of the device. However, as the paddle is made of composite glass fibres and then infused with resin, it is unclear how closely these values represent those of the physical model. A further difficulty in the tank testing was installing the device such that the pitch axis was at the same depth as depicted in the NWT (-0.56m) and then maintaining this throughout the tests due to the movement of the heave plate. If the device is more submerged then there is a larger profile on which the dynamic pressure from the waves can act and the buoyancy restoring moment is also larger.

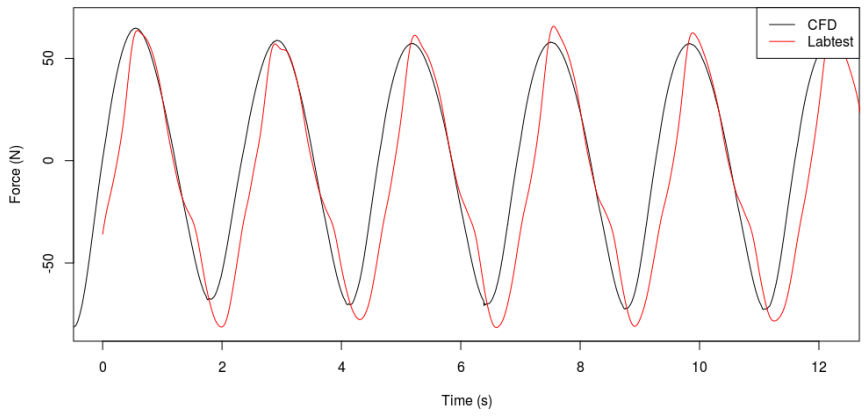

Figure 4.11: Comparison of PTO force from physical and numerical modelling of a dynamic case (Floating CCell concept modelled at 1:15 scale. Equivalent full scale regular wave parameters: T=8s, H=1.5m)

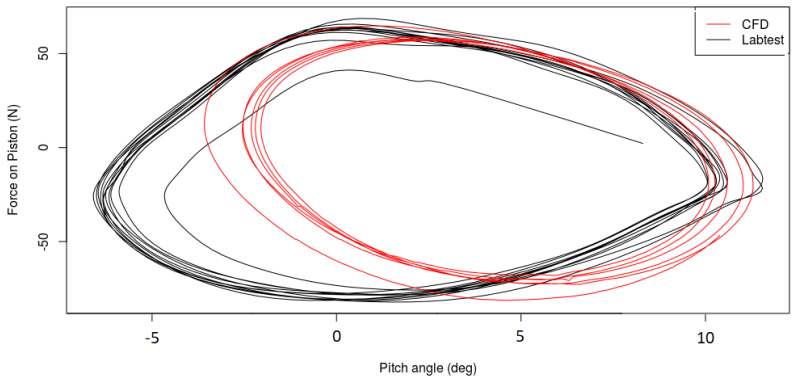

Figure 4.12: Comparison of motion and PTO force from physical and numerical modelling of a dynamic case (Floating CCell concept modelled at 1:15 scale. Equivalent full scale regular wave parameters: T=8s, H=1.5m)

4.2.4 Free Decay Tests

Free decay tests provide key information about the harmonic response of a device, offering the developer a better understanding of how the motion of the device decays after an initial disturbance. Analysis of the subsequent response, using techniques like the logarithmic decrement method, calculates the natural period and damping coefficients of the model.

The logarithmic decrement method (Holmes 2009), (Pecher 2017) assumes a single degree of freedom in the system and that the system is linear with oscillations about a constant centre. It considers the change in amplitude between the first peak and the n^{th} peak:

$$\delta = \frac{1}{n} ln \frac{x(t)}{x(t+nT)} \tag{4.18}$$

where $x(t)$ is the amplitude at time t and $x(t+nT)$ is the amplitude at the peak n periods away. In the analysis below a value of $n = 3$ was used.

From this estimate of δ, the damping ratio ζ is the calculated by:

$$\zeta = \frac{\delta}{\sqrt{4\pi^2 + \delta^2}} \tag{4.19}$$

and the natural frequency ω_n is:

$$\omega_n = \frac{\sqrt{4\pi^2 + \delta^2}}{T} \tag{4.20}$$

Free decay tests are beneficial in the analysis of an NWT as the model's ability to calculate the motion of the device is isolated with the simulation conducted in the absence of additional complexities such as the PTO system or the incoming wave field.

Pitch free decay tests were conducted in the physical and numerical wave tanks by initially displacing the otherwise un-damped device about the pitch axis by $\sim 10^o$ shorewards. The initial angular displacement should be kept small as with this assumption the frequency and period of the pendulum are independent of the amplitude of displacement.

Plotting the decay envelopes for the two decay tests, the response calculated in the NWT is similar to that recorded in the wave tank, Figure 4.13. However the paddle in the numerical simulation does not respond as quickly as was observed in the tank. This is confirmed by the calculated values, in Table 4.3, with the oscillation period for the numerical model 0.5seconds longer than that for the physical model. Though, the response in the numerical model is more damped.

An asymmetry in the device response is also demonstrated as the envelope calculated for the shoreward displacement ($+ve$), does not accurately predict the seaward motion. This trend is replicated in the numerical modelling.

The following factors are contributors to the discrepancy between the two tests and have been ranked by their likely significance:

(a) In the physical testing a single degree of freedom was not fully isolated as the heave plate was not clamped. This allowed a further rotation about the hinge at the seabed and the response of the paddle was influenced by the wider system. In particular when the device pitched shorewards, the heave-plate also lowers and the submerged volume of paddle increases, which in turn increases the resultant buoyancy force. This effect was not captured in the numerical modelling as only the paddle was modelled.

(b) The construction of the physical model may have impacted the decay results, as described in the dynamic tests. A similar sensitivity to centre of gravity and moment of inertia was reported by Palm et al. in free decay tests of a buoy (Palm et al. 2016), though interestingly they found that the CFD results were generally more damped than the experimental values, which is the converse of the results shown here.

(c) The logarithmic decrement method is based on a number of assumptions, including linearity and there is a degree of uncertainty in the calculations, which is influenced by the number of periods between the first and last peaks. Intuitively, increasing the number of periods improves the estimations but the measurement error then becomes more significant. It has been suggested that the ideal number of periods is 3 or 4, with higher damping systems requiring fewer periods to minimise uncertainty (Tweten, Ballard, and Mann 2014). Ideally, the average values from a number of these tests would be used to compare the validity of the NWT against the physical wave tank.

(d) The paddle geometry was rotated by the initial displacement of 10^o prior to being imported into the model. Therefore, the best-case mesh was created for the initial displacement and mesh distortion was present throughout the simulation, particularly in the seawards motions.

It is also worth noting that the natural frequencies are all well below the wave frequencies used in the experiments ($2.3 \leq \omega \leq 6.08$ rad/s), Table 4.3, so it is unlikely that any of the results were influenced by resonant effects. The natural frequency scales similarly to wave frequency, thus at full scale these natural periods would be in the range of $21 < T < 47$s, which is beyond that expected in any realistic sea state.

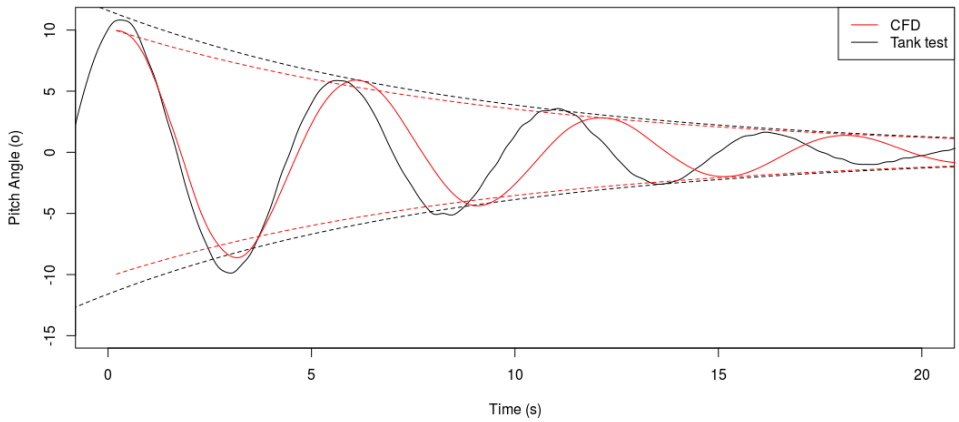

Figure 4.13: Pitch response from free decay test in numerical (CFD) and physical tank tests. Floating CCell concept modelled at 1:15 scale.

Table 4.3: Comparison of numerical and physical free decay tests key output parameter

	Physical Model	**Numerical Model**
Oscillation Period (s)	3.97	4.48
ω_n (rad/s)	0.252	0.224
Damping Ratio	0.0693	0.0784

4.3 Applicability of Linear Theory

To analyse the applicability of linear theory for modelling an OWSC such as CCell, an alternative linear modelling methodology has been used as a comparison against the fully non-linear CFD solver. The intention is to provide an evidence based assessment of the usefulness of linear theory in the development of CCell and an understanding of when and how the linear assumptions employed by linear BEM codes are violated. To evaluate this, the radiation coefficients (damping and added mass) for pitch mode oscillations derived from NEMOH and the CNWT will be compared. This also isolates the calculation of basic hydrodynamics from the effect of waves generation or PTO representation as the motion of the paddle is prescribed and in quiescent water. For this analysis the fixed-base CCell concept will be used and the output will also be compared against the results derived for a similarly sized flat paddle. This additional comparison is included to disambiguate the effect of OWSCs in general, and that of a device with an asymmetric fluid-structure interaction. This analysis was conducted with models at full scale, as noted in Section 3.1, the scaling of coefficients for low K_C number is less successful and leads to the overestimation of the drag in particular.

4.3.1 Determination of K_C Number

The K_C number, as described in Section 2.3.4, is used as an indicator of the importance of inertial and drag forces, as well as when potential theory is applicable. It is relevant for both

stationary bodies in oscillating flow and oscillating bodies in quiescent fluid. By inputting the formulations for the velocity into the equation for K_C number, Equation (2.36), it is clear that in both surge and pitch mode oscillations the K_C number is invariant to time period.

- For surge mode oscillations $U_o = \omega X_o$ where X_o is the amplitude of the displacement. Leading to $K_C = \frac{2\pi X_o}{D}$ where D is the diameter of the cylinder (or extent in x of the paddle)
- For the Pitch Tests the velocity is more convoluted: $U_o = \sqrt{D^2 + L_V^2}\frac{\Theta_o \omega}{4}$, where Θ_o is the amplitude of the angular displacement and L_V is the vertical extent of the paddle. This leads to $K_C = \sqrt{D^2 + L_V^2}\frac{\Theta_o \pi}{2D}$.

In normal operation it is expected that the paddle will oscillate with displacement amplitudes between 5^o and 20^o, which for pitch mode leads to a K_C number between 0.207 and 0.83. Considering an equivalent displacement at the SWL in surge mode tests (which would be between 0.247m and 0.995m when the hinge is located 2.85m beneath the SWL) the K_C number is evaluated to be between 0.62 and 2.5. Therefore, in the flow range that is considered in this study the dominant hydrodynamic force is inertial as the K_C number is small. In addition as $K_C < 3$ potential theory is normally considered acceptable, suggesting that the use of BEM codes to calculate the hydrodynamic coefficients is justified.

However, the large amplitudes of motion, particularly those over 0.3rad (Crooks et al. 2016) in the pitch mode tests, suggest a violation of the small amplitude assumption, even though the K_C numbers are below unity. Large motions such as these increase the influence of nonlinear processes which the BEM fundamentally cannot calculate. Furthermore, alterations to the free surface particularly in pitch mode, lead to stronger nonlinear interactions, which will also erode the accuracy of the BEM output.

4.3.2 BEM Modelling

An open source BEM software package NEMOH has been used to solve the linear wave-structure interaction problem and calculate the hydrodynamic coefficients that specify the influence of the surrounding fluid on the WEC. NEMOH is based on the usual linear assumptions that the flow is inviscid, incompressible and irrotational, the wave amplitude and body motions are small and the sea bed is horizontal (Babarit and Delhommeau 2015).

By solving the boundary value problem it is able to then calculate the hydrodynamic coefficients (Added mass and radiation damping), the pressure field and Froude-Krylov forces on the body, the far field velocity potentials and the near field surface elevation. Apart from the mesh of the submerged part of the body, it requires the water depth, degrees of freedom and wave frequencies and directions to be specified in the Nemoh.cal file, Figure 4.14

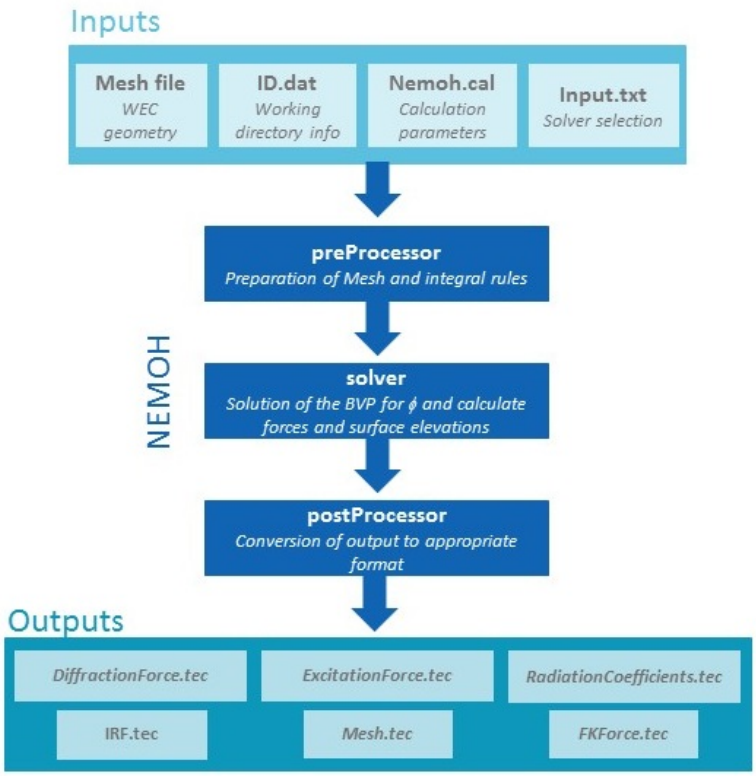

Figure 4.14: Work flow of the open-source BEM solver NEMOH, adapted from (Babarit and Delhommeau 2015)

A Matlab wrapper has been written for NEMOH to accelerate the set up and help the user correctly implement the tools. However, this is not able to handle more complex geometries such as the CCell device. Alternatively, NEMOH can be run from the command line along with another programme, Meshmagick, to provide meshing functionality. Though when run from the command line the user must specify the Hydrostatics.dat, KH.dat and Inertia_hull.dat files in the mesh folder themselves. The process for simulation is given below:

- Convert the STL file into a NEMOH appropriate file. The NEMOH solvers are expecting quadrangular panels, though triangles can be used if one of their vertices is repeated, which is done with the meshmagick command:

```
1 meshmagick <name>.stl -o <name>.mar
2
```

- Calculate the inertia, stiffness matrix and centres of gravity and buoyancy. Again meshmagick can be used, though it expects that the material has a homogeneous density. For the correct stiffness in a hinged device, the z coordinate can be specified.

```
1 meshmagick <name>.mar -hs --zcog <zcog>
2
```

  This step must be done with the full paddle meshed as the calculation does not work if the mesh is not closed.

- Clip the mesh to provide only the submerged part of the device.

```
meshmagick <name>.mar -c Oxy -o <name>.mar

```

- If the device is symmetric, then only half of the paddle must be described.

```
meshmagick <name>.mar -c /Oxz -o <name>.mar #this clips the Oxz plane leaving
  normals in the +ve y direction

```

  However, meshmagick does not update the header of the mesh file (.mar) and this must be done manually: if only half of the mesh is shown this top line should read $2\ 1$., but if the whole mesh is described then it should be $2\ 0$.

- Retrieve the information about the mesh itself such as the number of panels and nodes, which is required in Nemoh.cal, by using:

```
meshmagick <name>.mar -i

```

The initial comparison of the hydrodynamic excitation torque amplitude, Figure 4.15, as predicted by NEMOH, shows that the CCell has a much larger peak amplitude, with the difference between the flat paddle and CCell diminishing as the period of the oscillation increases. Both devices have a similar response with regard to frequency, with the peak hydrodynamic torque located between 2-3 seconds. Though in the expected operation frequency range, NEMOH predicts that the curvature of CCell has little effect.

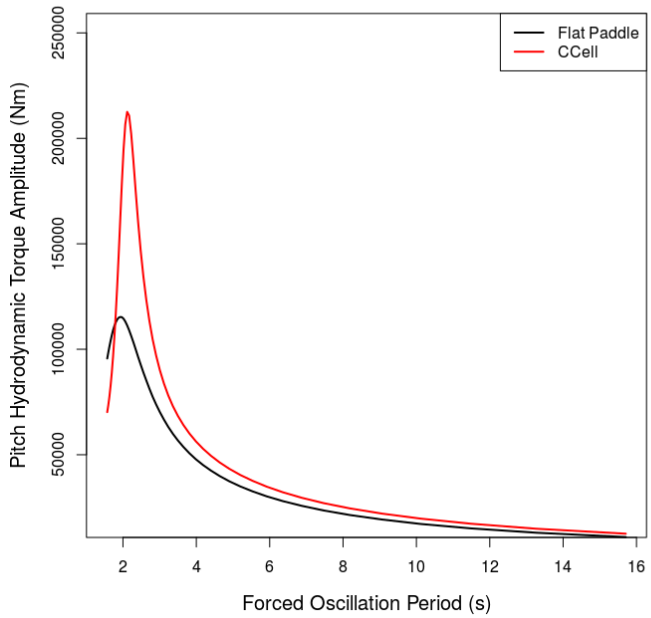

Figure 4.15: Excitation torque amplitude for pitch mode oscillations, as calculated by NEMOH for a flat paddle and CCell.

```
boundaryField
{
    ...
    ccell
    {
        type        angularOscillatingDisplacement;
        origin        (0 0 -2.85);
        axis        (0 1 0);
        angle0        0;
        omega       0.8976;
        amplitude     0.2618;
        value         uniform (0 0 0);
    }
    ...
}
```

Code Listing 4.1: FOT specification in pointDisplacement boundary condition in OpenFOAM

4.3.3 Forced Oscillation Tests

An experimental way to determine hydrodynamic coefficients is to conduct Forced Oscillation Tests ("FOT") which involve forcing a body in fluid to oscillate and measuring the required force to move the body as well as the subsequent motion of the body. They can therefore be used to validate numerical estimates of hydrodynamic torque coefficients.

In physical laboratory tests the determination of the added mass coefficient is complicated by another element of the force also in phase with acceleration: the inertia of the device itself. To decouple the effect of this, the FOT would often first be carried out in air with the assumption that aerodynamic resistance from this oscillatory motion is negligible. FOTs can be replicated in NWTs by prescribing the motion of the body and then analysing the resultant pressure forces. The benefit of conducting FOTs in an NWT is that the forces are already decoupled, in fact no information about the mass or construction of the body need even be supplied for these tests. In OpenFOAM this is done by altering the boundary field for the WEC body in the pointDisplacement file as shown in Code Listing 4.1.

For these tests, the relaxation zones at either end of the domain have remained in place to prevent reflections of the radiated waves. The width of the tank has been increased to provide at least three oscillations before transverse reflections affect the fluid pressure field and impact the result. If similar tests were conducted in a towing tank, which typically is not very wide, the effect of these reflections should also be considered. The paddle's considered in this analysis are the fixed-base CCell paddle and an equivalently dimensioned flat paddle.

Looking at the surface profile and radiation pattern from the flat paddle and the CCell device indicates the differences in their hydrodynamic performance, Figure 4.16. The radiation pattern of the flat paddle, more clearly visible in Figure 4.16a, is itself flatter than that of the curved paddle. It is common to assume that small devices behave as point absorbers, which in pitch mode creates a dipole pattern. However, even at this size there are clear differences between the two radiation patterns.

Eddies are clearly formed as both paddles move seaward, with the vortex created at the wing of the CCell paddle remaining attached for longer than the one created by the flat paddle. The surface elevation on the seaward side of the CCell is also much higher than that for the flat paddle, which is due to the bottom profile of the CCell device directing the fluid. Interestingly

in the shoreward motion the CCell paddle does not appear to generate vortical structures, or if they are present their strength is much reduced compared to those created by the seaward motion.

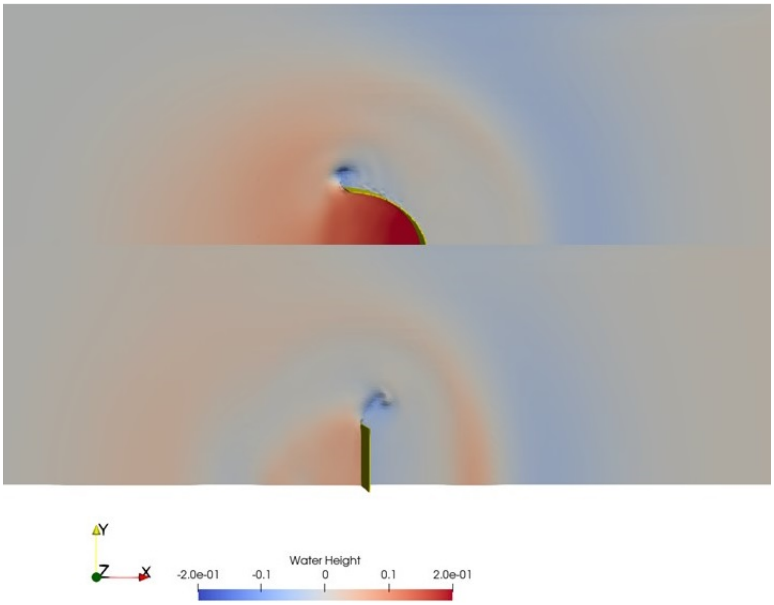

(a) Surface profile from Seaward pitching motion

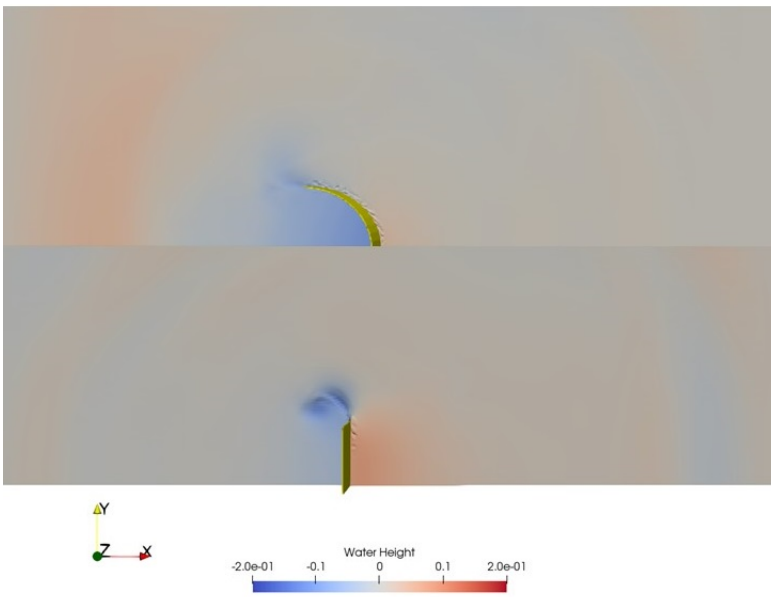

(b) Surface profile from Shoreward pitching motion

Figure 4.16: Comparison of Flat Paddle and CCell forced oscillation tests in CFD [FOT test: T=7s, $\Theta_o = 15^o$]. Colouration depicts the height of the water surface (m) where 0m indicates SWL

A comparison was also made between the CCell device and a cylinder of the same diameter. However, as the effect of buoyancy for the cylinder is much larger than the thin profile of the CCell device, the comparison was instead made in surge mode. It is clear from Figure 4.17 that the cylinder's response is much more likely to be well represented by linear theory due

to the absence of vortices. Downstream of the devices however, the radiation pattern is very similar.

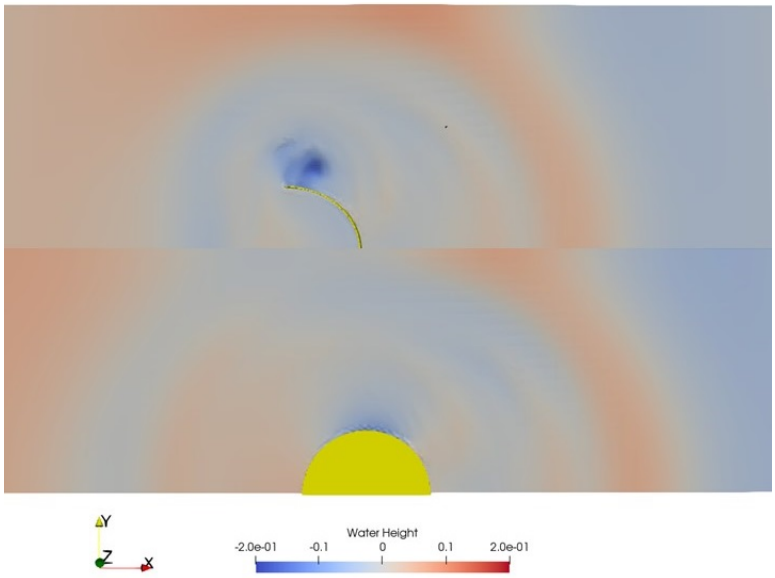

Figure 4.17: Surface profile for the CCell device and equivalently wide cylinder from seaward surging motion. Colouration depicts the height of the water surface (m) where 0m indicates SWL

Determination of Hydrodynamic Coefficients

If the flow is stationary and the body is moving then the calculation of the inline force parallel to the motion is not equivalent to that depicted by Morison's equation as discussed in Section 2.3.3. When the water is still there is no ambient dynamic pressure fields, thus the Froude Krylov force term is zero and the resultant hydrodynamic force on the body due to inertia, F_I, is instead calculated by Equation (4.21). The negative sign indicates that the hydrodynamic force is resisting the acceleration of the object and therefore is acting in the opposite direction. Therefore, the force on the WEC in FOTs is equivalent to the radiation force Equation (2.29).

$$F_I(t) = -\rho C_a V \dot{u} \tag{4.21}$$

Having collected the time series for the velocity, acceleration and force, there are a number of options to post process the data and obtain the coefficients. The most simple method comes from the realisation that the two force components are 90^o out of phase, therefore:

- when the velocity is maximum, at t_1, the acceleration is zero: $F_R(t_1) = -B_{55}\omega\theta_0 cos(\omega t)$
- when the acceleration is maximum, at t_2, the velocity is zero: $F_R(t_2) = M_{55}\omega^2\theta_0 sin(\omega t)$

The accuracy of the results determined in this fashion can be compromised by the time resolution of the data and any small error in the velocity measurement can lead to deviation of the coefficients due to the steepness of the curves (Journee and Massie 2001). Another approach that is commonly employed is the use of the Fourier series. The premise of a Fourier transform is to decompose a time dependent signal into the sum of a mean value and a series of cosine and sine functions with different amplitude coefficients. As this is analogous to the

equation for the hydrodynamic force, by solving for the Fourier coefficients, the added mass and hydrodynamic damping can also be found. In the case of this study and the asymmetry of the CCell WEC with respect to its shoreward and seaward profiles, it is expected that the hydrodynamic coefficients may be different according to the direction of motion, i.e. shoreward or seaward. If the Fourier method is used, a full time period is required to determine the values and this difference is lost. Therefore, the more simplistic method is used to identify the coefficients at multiple points throughout the wave cycle. The concern for the numerical accuracy is also reduced in a NWT due to the small timesteps used in the progression of the simulation.

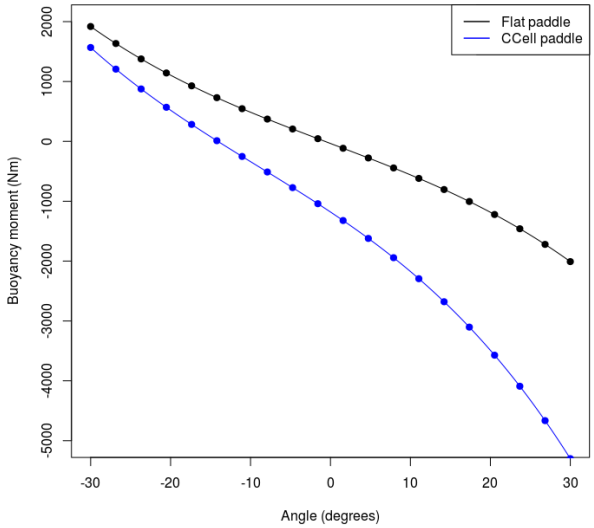

Figure 4.18: Comparison of buoyancy moment for a Flat paddle and CCell

For the pitch mode tests the restoring moment due to buoyancy must also be considered. The buoyancy moment for the flat paddle and CCell are compared in Figure 4.18, where the effect of the asymmetrical device is clear. The flat paddle, has the same buoyancy profile irrespective of whether it is oriented towards the shore (positive angle) or the sea (negative angle). However, the restoring moment for the CCell paddle is much larger when it pitches shoreward as the back face has a larger volume than the “wings” of the paddle.

Flat Paddle CFD Analysis

The torque profile for the flat paddle throughout a single oscillation cycle of 7s period is shown in Figure 4.19. Like the buoyancy moment, the torque profile appears to be the same for both seaward and shoreward motions. Furthermore, using the hydrodynamic coefficients determined for either motion has negligible effect on the predicted torque, shown here by the red and blue dashed lines. The use of the coefficients does however, underestimate the amplitude of the torque. This may be due to the manner in which the buoyancy moment was calculated, as it used the SWL, though as shown in Figure 4.16 there is some alteration in the surface elevation throughout the tests.

The results of the FOT tests are plotted such that the cycle begins and ends at the most shoreward position and the paddle is in the most seaward position at wave period fraction

$t/T = 0.5$. With this timeline the seawards and shorewards radiation damping coefficients are evaluated at $t/T = 0.25$ and $t/T = 0.75$ respectively. For the derivation of added mass coefficients the seaward value is the one evaluated at the most shoreward position $t/T = 0.5$, just as the device reverses its motion and begins to move seaward, similarly the seawards added mass is evaluated at $t/t = 0$ or 1.

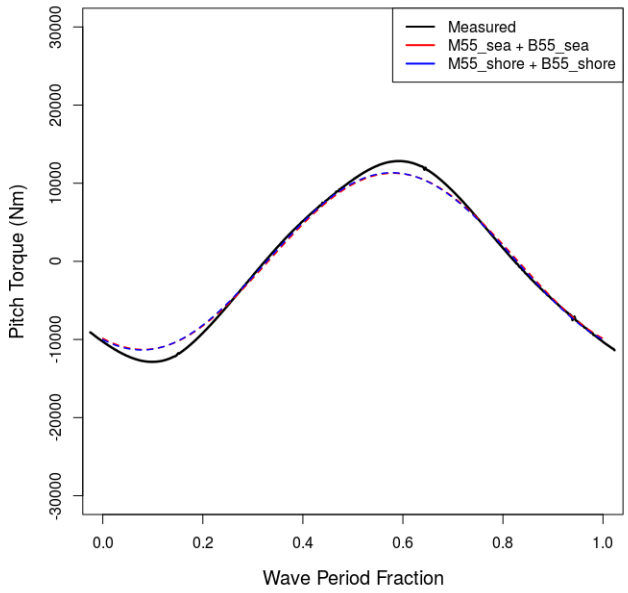

Figure 4.19: Comparison of hydrodynamic pitch torque from CFD and that calculated using hydrodynamic coefficients determined by Morisons method for a Flat Paddle. [FOT test: T = 7s, $\Theta_o = 15^o$]

The phase of the overall torque, suggests that both inertial and drag components play an important role, though the amplitude of the inertial component is larger, Figure 4.20.

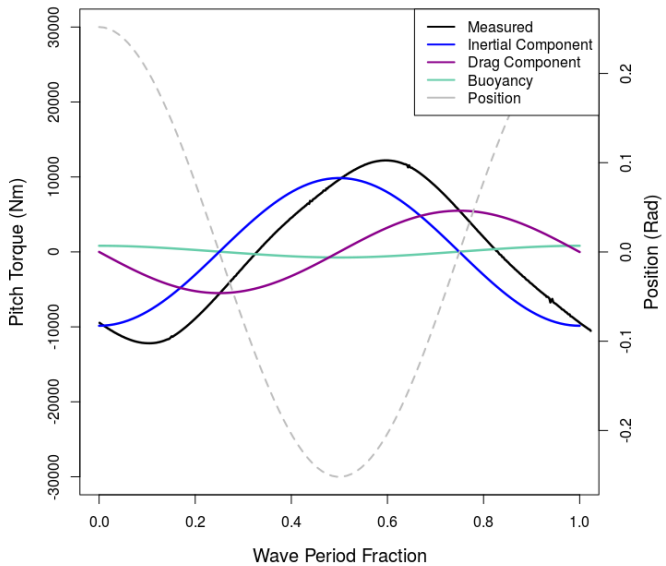

Figure 4.20: Variation of contribution from different torque components over one oscillation cycle for a Flat paddle in pitch. [FOT test: T=7s, $\Theta_o = 15^o$]

CCell Paddle CFD Analysis

Figure 4.21, demonstrates the asymmetry of the hydrodynamic coefficients for the CCell paddle. If only the coefficients calculated from the seaward motion are used, then the amplitude of the hydrodynamic torque is over predicted when the device is at the most seaward point, shown by the red dashed line. Conversely, if the shoreward coefficients are used then the amplitude of torque is under-predicted when the device is at its most shoreward position, denoted by the blue dashed line. For the closest comparison between the torque measured in the CFD calculation and that calculated by the hydrodynamic coefficients, a piecemeal approach must be adopted. For every quarter wave cycle the most appropriate inertial and drag coefficients are used, leading to the segmented solid coloured line. However, this still fails to predict the first bump in the CFD data, suggesting that other complexities have not been fully captured by the hydrodynamic coefficients, most likely due to the change in the surface elevation and its effect on the buoyancy moment.

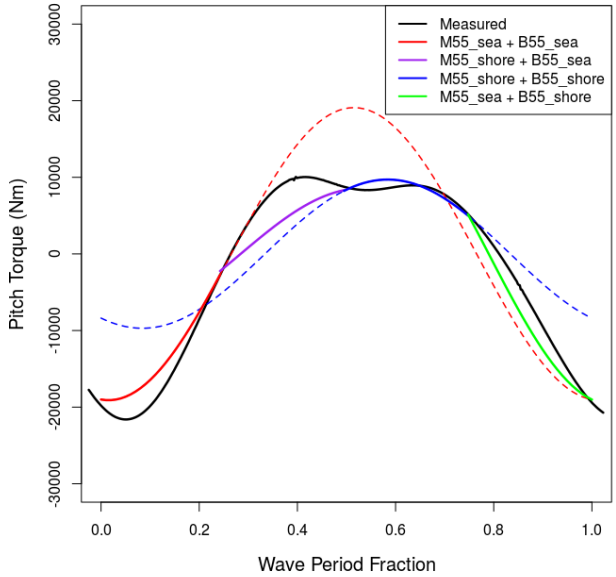

Figure 4.21: Comparison of hydrodynamic pitch torque from CFD and that calculated using hydrodynamic coefficients determined by Morisons method for CCell. [FOT test: T=7s, $\Theta_o = 15^o$]

The torque profile for CCell differs from that of the flat paddle, comparing oscillations of 7s in Figures 4.21 and 4.19, as it has a double peak with increased torque either side of its most seaward position. The profile at the shorewards position is also narrower with nearly double the magnitude of the torque acting at the seaward position, again demonstrating the device asymmetry. Considering the magnitude of the respective components in Figure 4.22, their contributions to overall torque during the shorewards motion ($0.5 > t/T > 1$) are similar to the flat paddle with the inertial torque dominating. However, the drag component for the seaward motion is much reduced for the curved paddle, resulting in the overall torque aligning more closely to the inertial torque profile.

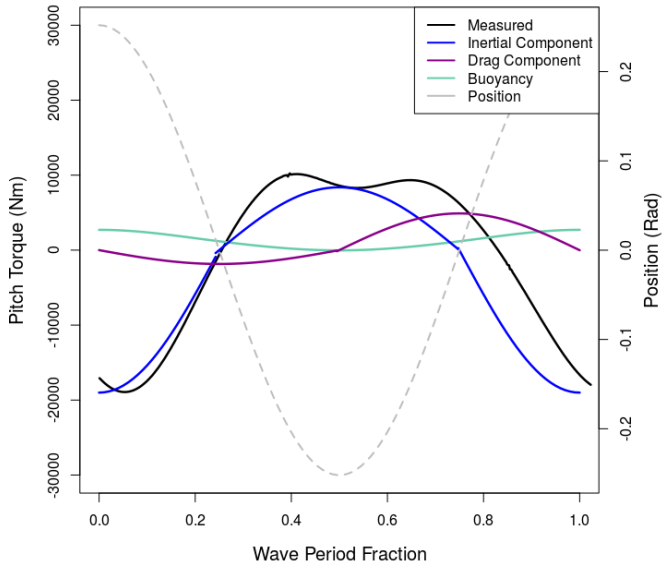

Figure 4.22: Variation of contribution from different torque components over one oscillation cycle for CCell in pitch mode. [FOT test: T=7s, $\Theta_o = 15^o$]

4.3.4 Comparison of Modelling Strategies

It was conjectured that NEMOH would be able to more accurately predict the hydrodynamic coefficients of the flat paddle, due to the simplicity and symmetry of its geometry. As for the CCell paddle, which has distinct seawards and shorewards coefficients, the accuracy is expected to be limited as the NEMOH analysis does not differentiate the direction of motion, providing a single coefficient. In the comparison between NEMOH and CFD derived coefficients, it is clear that there is a large discrepancy between the two methods. Firstly, considering the flat paddle, both the added mass, Figure 4.23, and the damping coefficient, Figure 4.24, are underestimated by NEMOH. However, the profiles for the flat paddle are similar for both types of coefficients, though the defining peaks of the NEMOH curves occur at larger periods of oscillation in the CFD analysis.

Perhaps because the shoreward profile of the CCell device is more similar to that of a simple cylinder, the added mass values calculated by NEMOH are more representative of the shoreward coefficients from the numerical FOT tests. A similar narrow peak is observed, though like for the flat paddle, the maxima occurs at an increased period of oscillation. The effect of the asymmetry erodes closer to this maximum, as the difference in the seaward and shoreward added mass reduces. The relationship between CCell's seaward added mass and oscillation period appears to follow a similar pattern as the flat paddle, as there is a less defined peak and the values plateau towards an apparent upper bound. The magnitude of CCell's seaward added mass is, however, much larger than that of the flat paddle as calculated by the FOT tests.

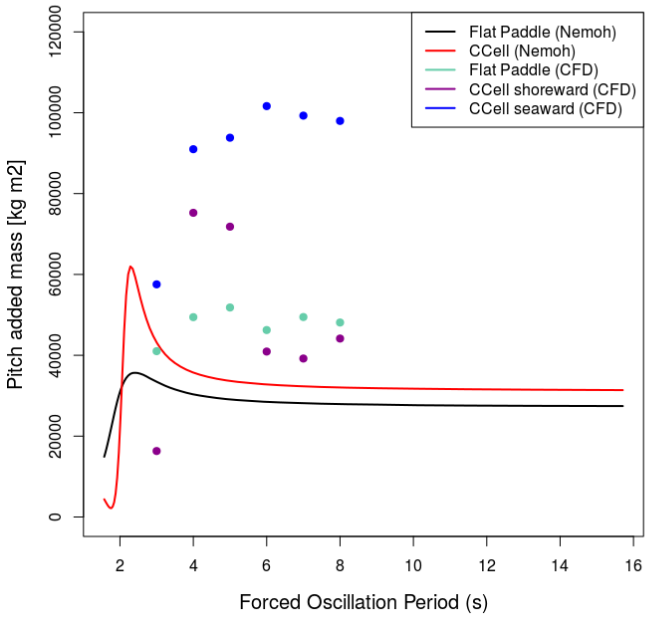

Figure 4.23: Comparison of Pitch added mass for a flat paddle and CCell calculated by NEMOH and CFD [FOT test: $\Theta_o = 15^o$]

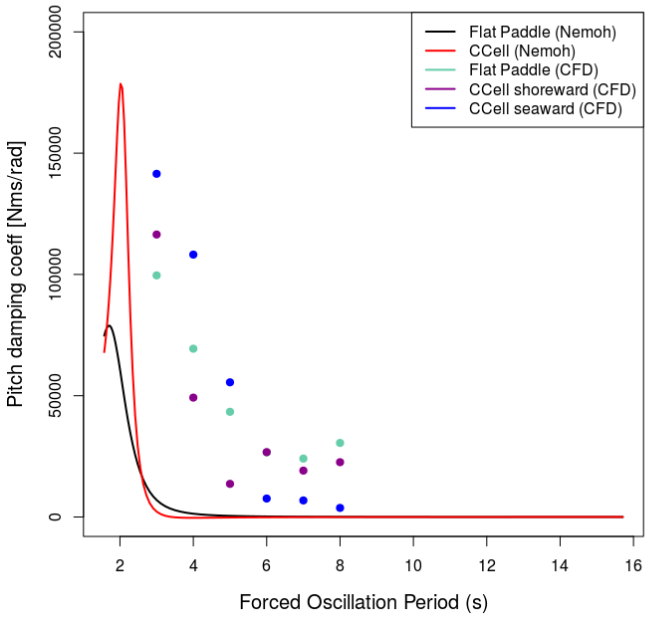

Figure 4.24: Comparison of Pitch damping coefficients for a flat paddle and CCell calculated by NEMOH and CFD [FOT test: $\Theta_o = 15^o$]

For both directions of motion the radiation damping in larger periods of oscillation is lower for the CCell paddle than a flat paddle of comparable width, Figure 4.24. This is also captured in the NEMOH analysis, between periods of 3-4s, before the damping of both devices reduces to

zero in increasingly slow oscillations. As expected, the damping coefficients, defined by both methods, become significantly larger as the associated velocities increase in faster oscillations. Interestingly, the radiation damping in the seaward motion of the CCell paddle is the most affected, going from the lowest of the three CFD calculated values at periods above 7s to the highest in oscillation cycles below 5s in length.

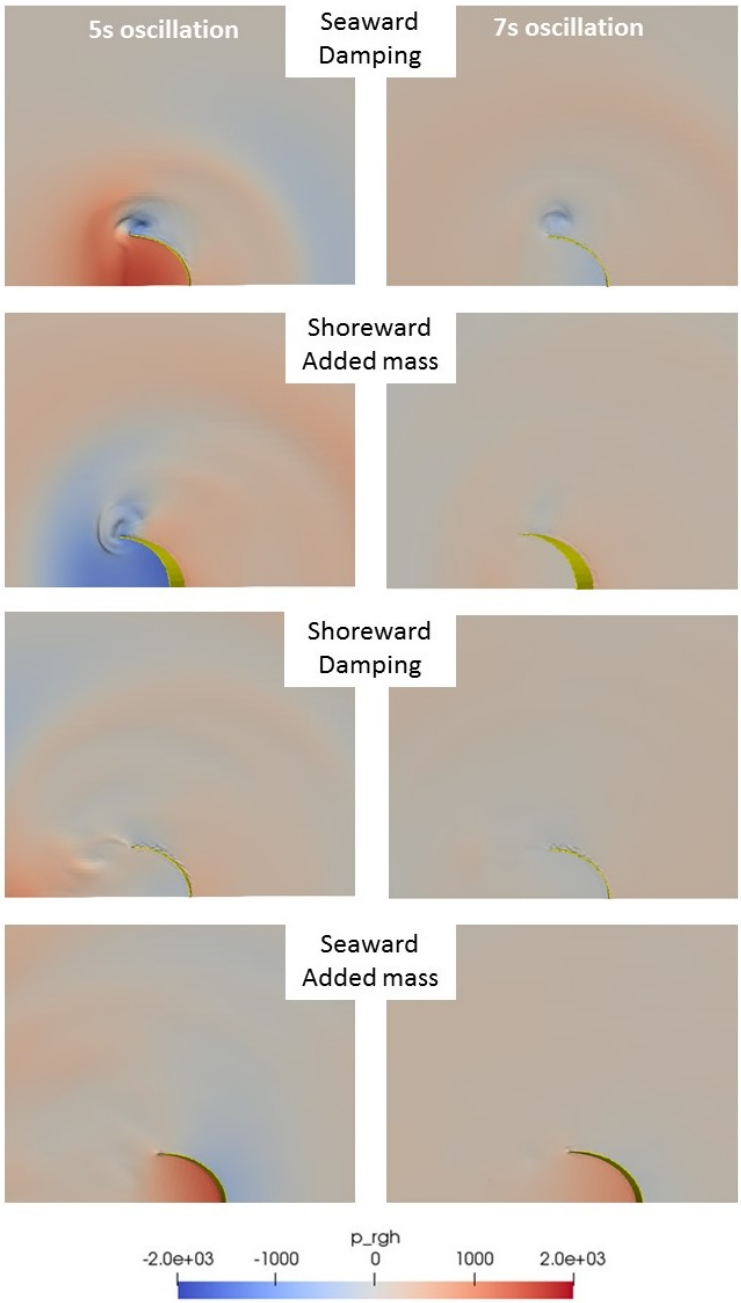

Figure 4.25: Dynamic pressure field (Pa) at times when the pitch added mass and damping coefficients are calculated. Comparison between 5s and 7s oscillation

The coefficients are calculated by considering the hydrodynamic torque on the paddle at the relevant point in the cycle, thus the dynamic pressure around the paddle is shown in

Figure 4.25 to better understand why there is a significant change in the coefficients as the oscillation period reduces from 7s to 5s.

There is little observable difference in the dynamic pressure plots for the shoreward damping or seaward added mass, save for a marginally larger pressure differential and slightly more defined vortex for the 5s period of oscillation. However, in the first half of the cycle there are marked differences. When the paddle is travelling seawards at its fastest (Seaward damping frame) there is a positive pressure on the seawards side of the paddle for the 5s oscillation, whereas for the 7s oscillation this dynamic pressure is negative. The reason for this is thought to be gravitational: in the 7s oscillation the water on the seawards side of the face has sufficient time to wash down and away from the face, creating a trough infront of the paddle. This does not happen in the 5s oscillation, thus a larger volume of water moves with the paddle and when the paddle then begins to slow down, the water continues moving. As the departing water is moving faster than the paddle, a void is created on the seaward side of the paddle, which creates the larger pressure differential across the paddle observed in the 5s shoreward added mass frame.

Physically radiation damping encapsulates the ability of a moving body to create waves in a fluid. Therefore, looking again at the 5s seawards damping frame, it appears that the vortex at the paddle wing increases the effective width of the paddle, creating a longer wave front.

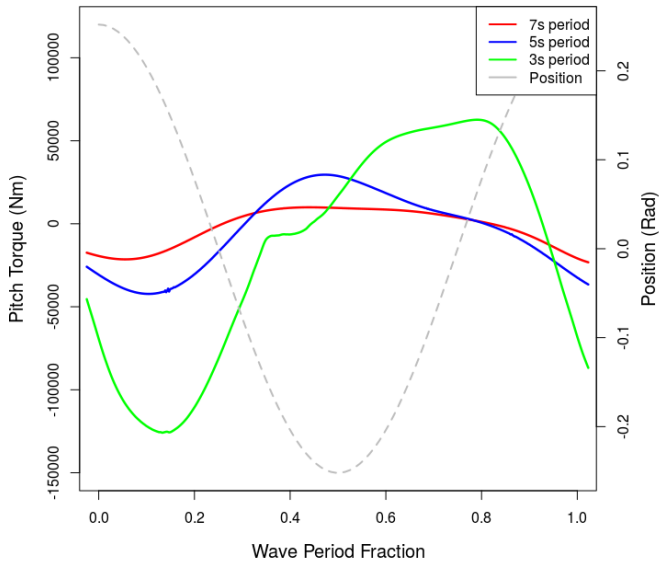

Figure 4.26: Comparison of torque profile measured by CFD for 3 s, 5s and 7s period of oscillation of the CCell paddle in pitch mode, where $\Theta_o = 15^o$.

The associated velocity and acceleration of the paddle must increase to achieve the same amplitude of displacement when the paddle oscillates over a shorter time period. This influences the torque profile, with the peak amplitude of the inertial component more pronounced for longer oscillations. However, when the period of oscillation is reduced to 3s, the peak amplitude moves later in the oscillation cycle becoming more in phase with the drag component, Figure 4.26.

Interestingly for the fastest oscillation, depicted by the green trace, there is a flattened section equivalent to zero torque. Figure 4.27 highlights the interaction between the device and the free surface, where particularly at high frequencies, the forced oscillation test can lead to overtopping of the device. The chaotic mixing and turbulent dissipation of the spilling water rejoining the fluid region on the shoreward side of the paddle, reduces the torque required to move the water. The surface piercing nature of the device, leads to stronger non-linear interactions, and reduces the ability of the BEM code to accurately represent the fluid dynamics.

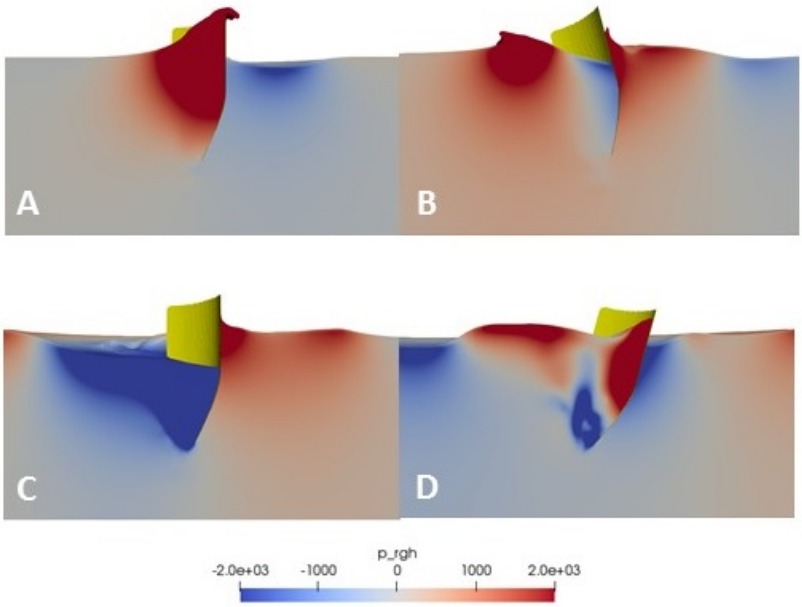

Figure 4.27: Dynamic pressure field (Pa) at times when coefficients are calculated for 3 second oscillation. A: Seaward Damping. B: Shoreward Added Mass. C: Shoreward Damping. D: Seaward Added Mass.

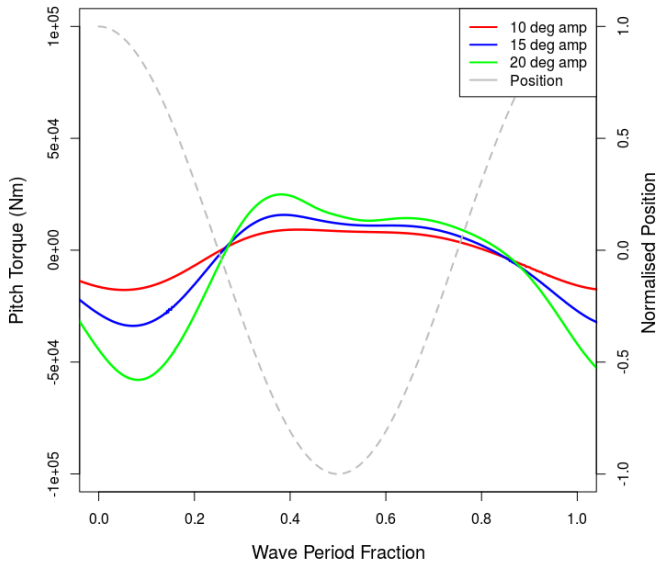

Figure 4.28: Effect of amplitude for 6s oscillation of CCell paddle.

The amplitude of oscillation used for the analysis so far was $15^o(0.262rad)$, which was expected from evaluation of K_C number to be in the permissible range for linear assumptions. However, it is clear that there is a marked difference between the linear and non-linear evaluation of the hydrodynamic coefficients. The effect of amplitude is now evaluated to explore its impact on the coefficients derived from the CNWT. The results for a 6s oscillation of the CCell paddle are shown in Figure 4.28, where it is evident that increased amplitude of the forced oscillation results in a larger torque magnitude. The shape of the torque profile is not greatly affected, however, the asymmetry of torque is amplified as the peak torque at the shorewards position increases more than that at the seawards position.

Of the four coefficients calculated for CCell, it is the seaward added mass that is most impacted by amplitude of oscillation particularly at longer periods of oscillation, as shown in Figure 4.29, where the seaward added mass values diverge. For an 8s oscillation the 20^o amplitude calculates a seawards added mass $\sim$ 20% greater than that for the 15^o amplitude. This divergence is explained by gravitational effects, as the lower amplitude oscillations move slower for the same period, allowing the water on the seawards side of the face to wash down and away from the face, creating a trough in front of the paddle. By contrast, the shorewards added mass, along with the damping coefficients, Figure 4.30, are almost invariant to amplitude of oscillation (up to 20^o) for periods of oscillation of 6s and above. Below a period of 6s, the relationship is complex and no conclusive statements can be made due to the differing mechanisms at play e.g. increased velocity and impact of over-topping and down-rushing water.

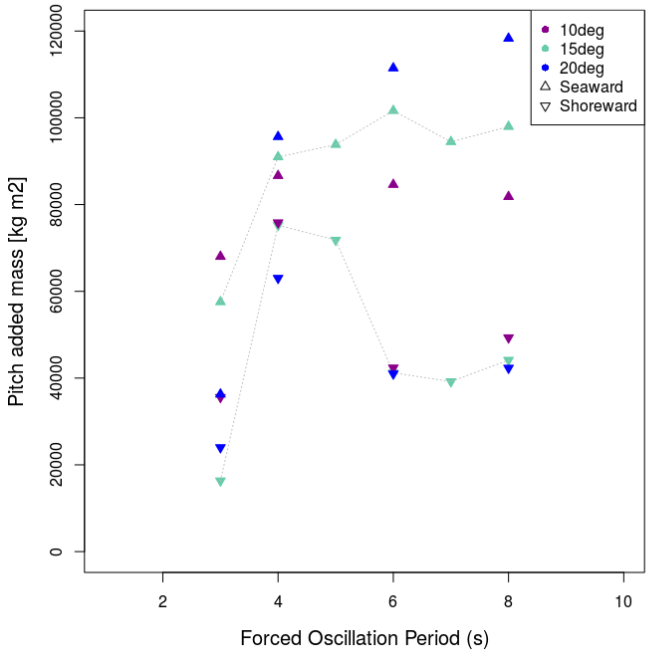

Figure 4.29: Added mass calculated from forced oscillation tests of CCell with different amplitude

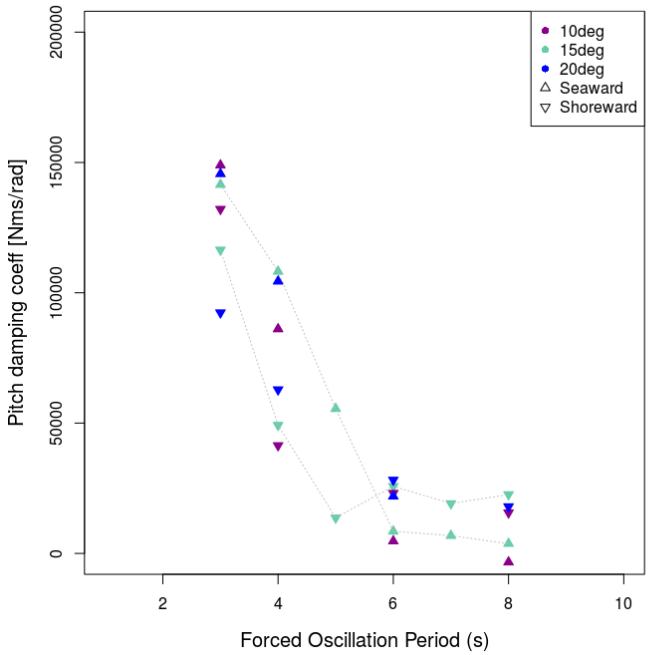

Figure 4.30: Damping coefficients calculated from forced oscillation tests with different amplitude

4.4 Discussion and Chapter Conclusions

Prior to this research placement the sponsor company was limited to simulations of stationary paddles, with limited understanding of the accuracy of the resulting solution. Numerical error and uncertainty in CFD modelling emerge from a number of sources, including machine rounding, iterative convergence, truncation and spatial or temporal discretisation. The intention of this chapter has been to identify the most appropriate solver choices and domain meshing to reduce these errors and create a stable and robust CNWT that can be used in a wide range of wave conditions.

Meshing of the computational domain must achieve a balance between the solution accuracy and the minimum total number of cells, as this is indicative of the execution time required. Therefore, in modelling water waves where the domain must extend to multiple wave lengths, a graduation of cell size is adopted to provide higher concentration of cells in areas of increased velocity. As the energy distribution of a wave reduces further down the water column, a method was developed to determine cell size based on the underlying kinematics. This approach was used alongside a measure of cells per wave height at the SWL to conduct a grid independence study (for surface elevation and force on a stationary paddle) that could be extrapolated to other wave conditions.

For the successful implementation of dynamic simulations, the acceleration relaxation parameter was identified as being influential in the stability of the solution. A sensitivity analysis found that the relation for the acceleration factor suggested in (Devolder, Pál Schmitt, et al. 2015) removed non-physical acceleration spikes and paddle motions and prevented simulation failure.

Laboratory testing of the floating CCell paddle provided an opportunity to validate the CNWT. However, there are a number of limitations in the numerical modelling of the floating concept, as only the paddle was simulated, pitching about a fixed hinge axis. The physical modelling tested the full assembly, including the heave plate and seabed anchoring, which allowed an additional degree of freedom in pitch. The outputs from the laboratory testing were also directly impacted by the efficacy of the piston and wider PTO subsystem, which was not represented in the numerical model. This includes any compliance in hydraulic hoses or frictional effects within the piston. Additionally, the damper used in the numerical modelling is idealised as a binary device that switches the damping level dependent on the direction of motion of the paddle. In reality, the damper is nonlinear, with the damping a function of the incident flow speed through the valve orifice.

These differences complicate the comparison of laboratory data with numerical data, and lead to the design of specific tests with additional measures in place to isolate, or decouple, different aspects of the CNWT. For example, the paddle was held rigidly to be compared against static simulations, where the effect of the heave plate or mesh motion are removed. Furthermore, free decay tests were used in which the PTO was detached to gain an understanding of the body motion solver and mesh morphing. From these tests and other normal operational tests, it was deduced that the elements hindering complete validation were the heave plate and the simplicity of the PTO representation.

In Chapter 3, the theoretical motivations and reasoning from previous numerical studies as

to why CFD would be the most appropriate method for asymmetric WEC design and optimisation were established. In the final section of this chapter an evidence-based justification was sought. The main distinguishing feature between CFD and other commonly used BEM software is the assumption of linearity and use of potential theory. In order to evaluate the suitability of these assumptions, the radiation coefficients calculated by each method were compared for the shallow water CCell paddle and a flat paddle of the same maximum height and width. The CNWT was adapted to simulate forced oscillation tests, with the added benefit that this type of test eliminates the effect of the PTO, wave generation and any sensitivity to buoyancy or mass distribution, that would otherwise complicate comparison. NEMOH was found to underestimate the coefficients across the board, though a similar relationship with regards to oscillation frequency was identified by both methods. Accuracy was particularly compromised for the asymmetric CCell paddle, as the BEM code provides a single coefficient whereas the CNWT demonstrated that coefficients for the shorewards and seawards motions are distinct. The surface piercing nature of an OWSC leads to nonlinearities that cannot be computed by potential theory and leads to solution inaccuracy even for oscillations with a K_C number well within the normally accepted range. Indeed, the analysis demonstrated that the device is inertia dominated within the working frequency range, as indicated by the small K_C number.

Part III

Numerical Investigations

Chapter 5

Design of Prime Mover and Estimating Power Output

The design and optimisation of a WEC is an involved process due to the sheer number of variables at play and the occasionally conflicting metrics with which they are judged. It is important that the developer has a clear understanding of the wave structure interaction and the rationale for different design choices. The output of this chapter is the development of a strategy for the interrogation of the design's geometric parameter space and streamlined method of evaluating the power performance. This will include a discussion of:

- Methods to determine the operational envelope for a particular deployment location.
- Most influential geometric parameters on device performance including variation due to wave conditions.
- How performance is evaluated and how to ensure a fair comparison particularly when using CFD as an optimisation tool.
- Effect of using different software on the predicted absorbed power.

The methodology presented in Chapter 4 is adopted in all CNWT simulations throughout this Chapter with the computational domain assuming symmetry about the x-z plane and extending to two wave lengths in the x-axis. The cells are concentrated around the paddle and the free surface, with increasing cell size in areas of lower mass-flux in order to reduce the overall number of cells to $\approx$600,000. It is assumed that by emulating the set up used for the laboratory floating paddle, the fidelity of the solution for the pilot deployment fixed-base concept is also comparable to that demonstrated by the physical model testing. The following simulations have been conducted at full scale with respect to the deployment site for the fixed-base pilot device. One issue introduced by modelling the fixed base system at full-scale is the choice of minimum cell size. At full scale, a finer grid size is required to fully resolve the boundary layer phenomena, however, the proximity of the device to the seabed leads to greater distortion of boundary cells. Overall, the fidelity of the solution should improve as the complications and inaccuracies introduced due to different scaling laws governing viscous effects and wave forces, have been removed. Additionally the fixed base system is better represented by the NWT as there is no longer a heave plate or second degree of freedom.

5.1 Wave Resource

Wave conditions are not uniform around the world's oceans and coastlines. The wave resource in each location is dependent on prevailing wind conditions, such as the trade winds, the fetch length and more local conditions, including bathymetry and currents. This creates a wide variety in predominant wave conditions, for example, the Cape peninsula in South Africa or the Atlantic Coast of Portugal experience much larger waves in comparison to the relative calm of the Mediterranean or Carribean sea. Consequently, a wave energy device designed for one location may be quite distinct from that optimised for other predominant sea states. There is not a blue print for WECs and designs will change dependent on both resource available and the markets that the harnessed power aims to serve. Clearly the design and optimisation process must begin with an understanding of what the expected wave conditions are. This first section will demonstrate how the operational envelope is determined for a given deployment location and how this translates to design conditions for evaluation of device performance.

A seastate can be defined by four main parameters: significant wave height, peak frequency, spectral shape and directional spread. The wave spectrum characterises the energy (or wave elevation variance) distribution with regards to frequency and direction, as discussed in Section 2.2.4. The British Standards recommendations for site characterisation for power performance assessment state that a minimum of three months measurement is required, however to account for seasonal variation, a full year is necessary (International Electrotechnical Commission 2012). As well as the spectral data, the directionality; water depth; tidal variation; current magnitude and direction; wind speed and direction; and density of water are all required to fully characterise the site. Although these are the requirements for WEC test facilities such as EMEC or Wave Hub, a similar undertaking would be expected of the WEC developer for a deployment site.

There are a number of options available to the developer to obtain the relevant spectral data, which are often used in combination to improve accuracy or tune wave models.

- Direct Field Measurement
  - Surface piercing wave gauges generally need supporting structure (e.g. oil/gas platform or dock) but these themselves impact the wave field. However, they are better at measuring steep waves than alternative measurement techniques as they are fixed into position with waves moving past (Eulerian).
  - Bottom mounted devices are limited to shallower water depths whilst these pressure-based measurements offer reduced accuracy as a linear wave assumption must be adopted to recover the free surface. Acoustic Doppler Current Profilers ("ADCPs") more traditionally measure currents, thus are capable of providing the underlying wave orbital velocities as well as directional and mean water level data.
  - Wave buoys follow the wave surface (Lagrangian measurement) and are complicated by their moorings, which can result in them being dragged or held at maximum extension. Lagrangian buoy motion is also problematic in steep waves with the buoy recording wider peaks and sharper troughs.
- Satellite measurements from radar altimeters have been used by the Joint Altimetry

Satellite Oceanography Network since the programs inception in 1992 to provide global sea surface heights, with an accuracy of a few centimetres. The current satellite (Jason-3) orbits the globe on a 9.9 day repeat cycle (EUMETSAT 2016) and will be replaced in 2020 by the Sentinel 6A (European Space Agency 2019).

- Numerical models using wind measurements or forecasts can be used to predict wave spectra. Their accuracy depends on the quality of wind data, and in deep water can achieve high accuracy predictions except in abnormal storm conditions such as hurricanes or cyclones (Adcock and P. H. Taylor 2014).

At the beginning of the design process it is unlikely that site specific data is available and the developer cannot afford to wait until a sufficient record is accrued. As an initial indication of representative conditions, the US National Oceanic and Atmospheric Administration ("NOAA") routinely runs and validates the WaveWATCH III model to forecast wave conditions and has a large store of historical data. The model provides statistical data for every 3 hour period at a 0.5^o resolution using the Global Forecast System's wind fields at 10m altitude as input (NOAA-Environmental Modelling Centre 2016). The bathymetry data used is made up of contour lines with 500m steps, therefore the model output is most accurate for deep water. This method has been adopted to provide a wave scatter diagram, Figure 5.1, for the grid node closest to the pilot deployment location and which is representative of the Mayan Riviera on Mexico's east coast.

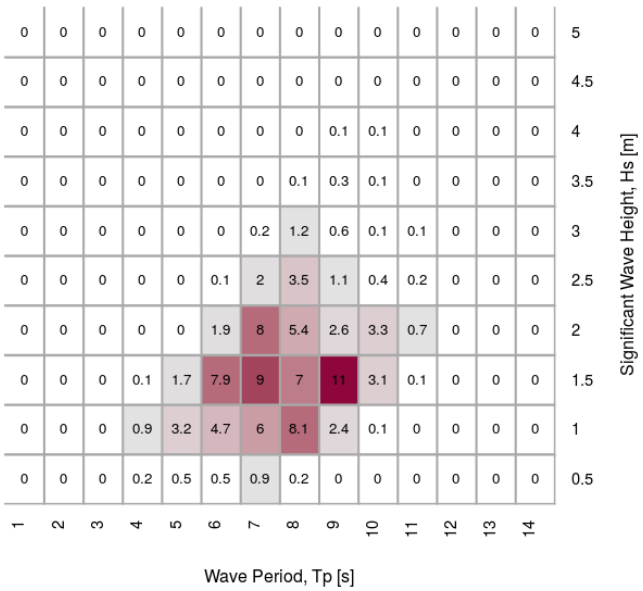

Figure 5.1: Wave scatter diagram for Cozumel from 10 years of data recorded between 2005 and 2015

In a sea state there are a number of processes that affect the energy distribution and spectral shape. Energy is input by the wind acting on the water surface, there is non-linear redistribution of energy within the spectrum, and energy is dissipated through waves breaking. Therefore, the assumption of a stationary spectrum is incorrect as the spectral shape may differ quite significantly from the point of measurement and the point of interest, particularly in shallow water.

The relevant British Standards (International Electrotechnical Commission 2012) considers the wave field statistically equivalent if the energy flux between two points (the measurement location and the WEC location) differs by less the 10% for 90% of the time. Alternatively, a spatial transfer model is required such as SWAN (Delft University of Technology 2019).

The JONSWAP spectrum provided by the NOAA modelling reflects deep water conditions. As waves propagate through shallower water they are affected by the bathymetry, with the greatest impact occurring in longer wavelengths as their kinematics penetrate further down the water column. It is therefore likely that a transfer model is needed. However, this requires bathymetry of a sufficient resolution to progress the data from the NOAA node to the deployment location and it must then also be validated. Furthermore, bathymetry data has historically been difficult and expensive to gather. As an example, a quote was received for €16,000 for an 800km^2 area resolved at 10m, increasing to $\sim$ €74,000 for a 2m resolution.

Previous studies have demonstrated the applicability of the TMA transformation of JONSWAP for coastal wave spectra (C. Whittaker et al. 2016) as it accounts for the limit imposed on the height of the longer-period waves due to the shallower water (Hughes 1984). Figure 5.2, demonstrates the impact of the TMA transformation on the normalised spectrum, with the peak of the JONSWAP spectrum much narrower than the spectrum for reduced depth.

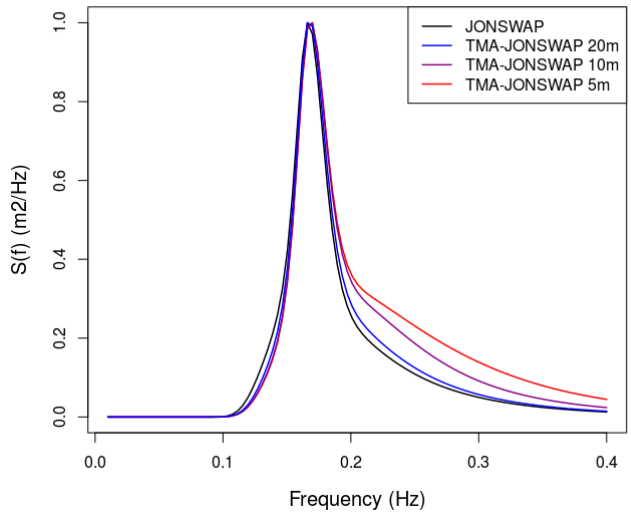

Figure 5.2: Normalised spectral density for JONSWAP and the TMA spectrum for different water depths.

For initial design work at a new site, the TMA spectrum is selected on the basis of literature for sites which are somewhat comparable and will be used to transform the deep water scatter diagram to accommodate the chosen water depth of 5m, Figure 5.3. The limits on the dimensions of the CCell device discussed in Section 5.2, have in part dictated the maximum water depth in which the device can be deployed. However, there are a number of other cost factors that motivate the decision to deploy in shallow water. Being in close proximity to the shore, smaller or less specialised boats can be used for maintenance and installation, and routine repairs can be conducted in shorter weather windows as the transportation time to site

is reduced. Additionally, power export is also increased as there are less transmission losses due to shorter cables.

For the first real-sea deployments, a more sheltered location is also beneficial to reduce the risk of extreme loads. By the time waves have reached the near shore area, they have been effectively filtered both in terms of maximum size and direction. However, there are other underlying changes to the wave, particularly the surge force which is targeted by an OWSC, thus the average energy capture will not necessarily be reduced. When the wave length is large compared to the dimensions of the WEC, it can be shown that the surge force is proportional to the horizontal wave particle acceleration and the combination of the body's displaced mass and added mass. Therefore, as the water depth reduces and the orbital of the water particle motion lengthens with trajectories becoming progressively elliptical, the surge force increases proportionally to the horizontal wave particle amplitude. This effect is apparent once the non-dimensional water depth (kh) reduces below 1.5, and at $kh = 0.5$ the surge force is almost 2.5 times larger than it would otherwise be in deep water (Folley, T. Whittaker, and Henry 2007). The relationship with wave number suggests that the increase in surge force will be greater in longer wave periods, thus siting the device in shallow water may generate the greatest improvements in capture width in the longer period, higher energy waves.

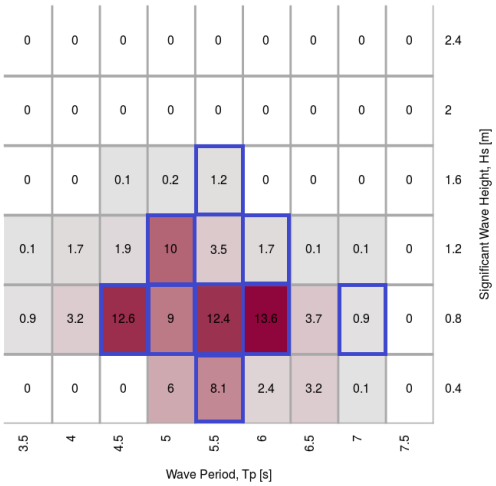

Figure 5.3: Wave resource at deployment location after transformation with TMA spectrum to provide regular sea states. Blue edged squares represent design waves: C1 (H = 0.4m, T = 5.5s), C2 (H = 0.8m, T = 4.5s), C3 (H = 0.8m, T = 5.0s), C4 (H = 0.8m, T = 5.5s), C5 (H = 0.8m, T = 6.0s), C6 (H = 0.8m, T = 7.0s), C7 (H = 1.2m, T = 5.0s), C8 (H = 1.2m, T = 6.0s), C9 (H = 1.6m, T = 5.5s)

It is infeasible to consider all possible operational sea states for the design and testing of a WEC. Instead it is recommended that a limited series of design sea states are chosen to cover the states that both contribute the most energy and occur most prevalently. The recommended strategy is to identify no more than 10 such conditions that contribute at least 2-5% of the total wave energy and occur for more than 44 hours annually (Pecher 2017). Nine sea states have been chosen accordingly and are outlined in blue in Figure 5.3. Sea states outside of the

operational window in which the WEC operates in a survival mode rather than attempting to optimise power generation are considered separately in Chapter 7.

Of all the wave parameters, the most influential to efficiency of power absorption is usually the wave period. It is often assumed that the effect of wave height is linear, and this results in the capture width ratio of the device being solely dependent on the wave period. Therefore, the peak wave period which corresponds to the highest product of wave energy and occurrence should be used for initial device design. In this case this corresponds to a wave period of 6 seconds. The key sea state to be considered in CNWT optimisation efforts will therefore be Co5 (H = 0.8m, T = 6.0s).

5.2 Evaluation of Parameter space

For the optimisation process to be beneficial the designer needs to ensure that the outcome will be economically feasible, taking into consideration the whole life cycle. Therefore, well defined limits for each variable need to be identified at the outset. For example, the CCell paddle will be manufactured from composites as one single part and eventually needs to be moved from the point of manufacture to the point of installation, by either road or sea. This would require that the device fit within a shipping container. Shipping containers come in standard sizes with a short (5.898m) or long (12.032m) configuration. The standard shipping container cross-section is 2.34m x 2.28m, whereas the “high cube” is 2.34m x 2.585m based on the dimensions of the door. For the pilot deployment this is critical, as the infrastructure is not in-place to manufacture on-site and the risk of using composites joints is currently too high. Therefore, these dimensional limits are strict. Once more testing has been conducted, it may be possible to develop a “modular” paddle that is transported in multiple sections and then joined dockside before final transportation and installation, thus allowing more flexibility with regards to dimensions.

A successful prime mover design must also adhere to a number of other design principles. Survivability, in particular, is of primary importance and if a passive survival strategy can be built into the response of the device, then the level of active measures that must also be employed is reduced. An OWSC is well placed in this regard: as the wave height increases there is a progressive decoupling of incident wave force and the transmitted loading on the device. This occurs due to both over-topping in large waves, and the reduction of the vertical projected area as the paddle pitches further shoreward.

The prime mover also impacts the design of the supporting structure. As the device reacts against the seabed, any increase in loads on the paddle will induce a larger reaction moment at the foundation. To increase the structural efficiency, and overall cost, the shortest load paths possible should be used, which may influence device sizing or placement. With these design conditions in mind, the parameter space of the fixed base CCell concept will be considered using the CNWT. Analysis will primarily be conducted with static simulations, evaluating impact on excitation torque, as dynamic simulations are more complex and computationally expensive, while fair comparison is only achieved with careful choice of damping.

At the beginning of the industrial research period, an earlier version of the CNWT was used to optimise the floating CCell paddle. The result of this optimisation was an increase of 62%

in power output from the initial device to the final iteration of the floating CCell device and a four-fold increase in output for a similarly sized flat paddle, as summarised in Table 5.1 from (Worden Hodge et al. 2017). This systematic interrogation of the design space was effective but it was time consuming as a lot of simulations failed. The root cause of these failures was found to be the poor selection of damping, which was based on trial and error and previous experience.

The fixed concept used in the pilot deployment does not occupy the same design space as the floating concept, which also relies on the dynamics of the support structure and is situated in deeper water, where the distribution of energy flux is quite different. However, knowledge gained from the earlier optimisation process can provide guidance and direction for a more formalised strategy and greater understanding of the fixed CCell parameter space.

Table 5.1: Results from Optimisation at 1:15 scale Tz=1.94s, H=0.167m wave

Paddle Design	**Width (m)**	**Height (m)**	**CWR**	**Power per surface area (W/m^2)**
Pre-Optimisation	0.633	0.792	0.249	7.81
Post-Optimisation	0.589	0.965	0.504	9.03
Large Flat paddle	0.589	0.965	0.126	3.79

5.2.1 Paddle Curvature

Using the often cited phrase that a “good wave absorber must be a good wave-maker” leads to a concerted effort to enhance the radiating properties of the WEC, resulting in favourable representation of small resonant WECs. As demonstrated in (Renzi, Doherty, et al. 2014), this interpretation neglects the diffracted wave field, which is an assumption that cannot be made in the case of the Oyster device, as the presence of the WEC clearly impacts the incident wave field. If the diffractive effects are ignored, then the wave excitation force on a surging or pitching body comes from the pressure difference along the wave, which can be very weak if the device is small compared to the wave length. It was shown that the Oyster device reflects and bends the incident waves and forms a shadow in the lee of the device, which together produces a definite change in the free-surface elevation between the two sides of the paddle. This pressure difference due to the diffractive dynamics is what drives the pitching motion of OWSCs such as Oyster and CCell.

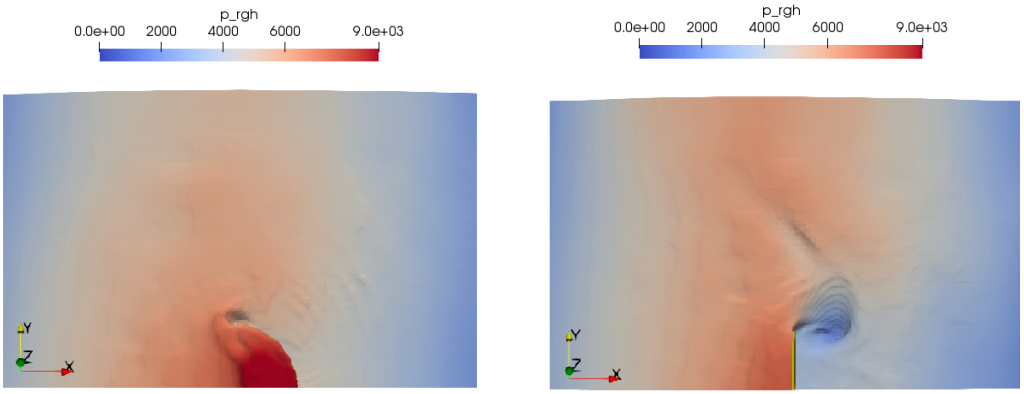

(a) CCell Paddle **(b)** Flat Paddle

Figure 5.4: Dynamic Pressure (Pa) at the water surface for a wave crest in a static simulation (Wave C8: T = 6s, H = 1.2m with waves travelling along the x-axis).

These diffractive effects can be seen in Figures 5.4 and 5.5 which show the dynamic pressure differentials across the Flat and Curved paddle shapes both at the water surface and through the water column in static simulations in one of the regular wave conditions identified for the deployment site. These demonstrate the effect of the paddle wings at focusing the flow towards the centre of the paddle, and preventing it from deflecting around the edges of the paddle in the crest, while holding back the reversing flow and accentuating the trough. This was found to be true for most of the working frequency range of the paddle, with the CCell paddle achieving a higher peak moment than the flat paddle in the crest and trough of most static simulations, as shown in Figure 5.6. However, in longer period waves the effect of the curvature reduced, particularly in the crest.

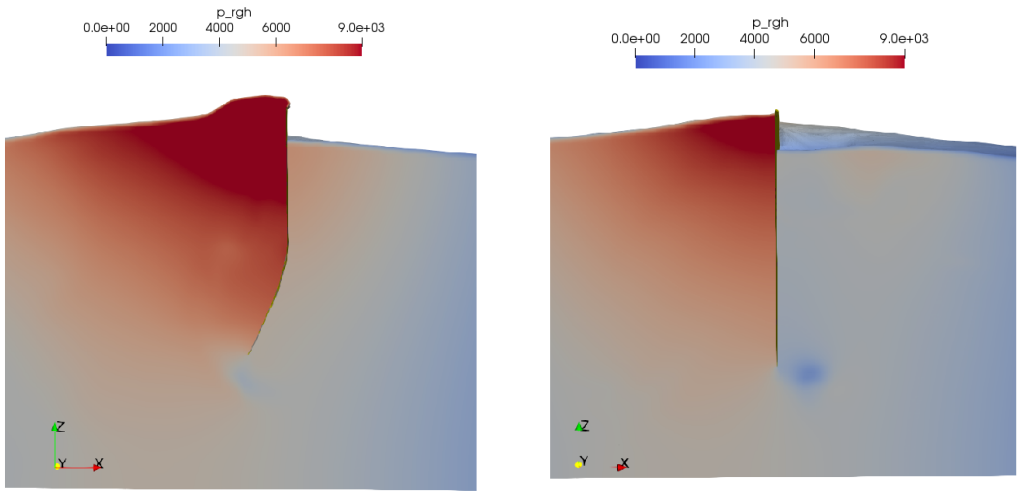

(a) CCell Paddle **(b)** Flat Paddle

Figure 5.5: Dynamic Pressure (Pa) through the water column at the centreline for a wave crest in a static simulation (Wave C8: T = 6s, H = 1.2m with waves travelling along the x-axis).

Also shown in Figure 5.6 is the ratio between trough and crest peak moments, where 1 indicates equivalence and 0.5 suggests the crest induces twice the moment as the trough. This ratio is fairly consistent for the flat paddle at lower period waves, reporting a ratio of

$\sim$0.65, though as the period increases so does the imbalance of the moments. This is due to the fluid field having more time to act on the hydraulic head at the edge of the paddle, infilling the void from the trough. Surprisingly, the peak moments in the crest and trough are more balanced for the asymmetric CCell device, save for very low period waves.

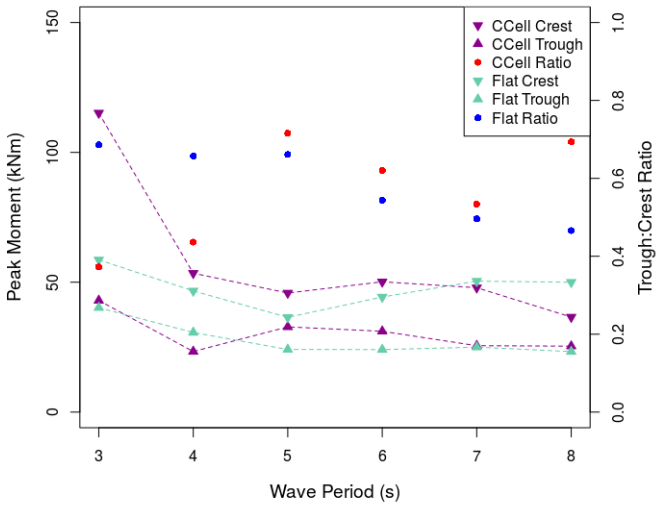

Figure 5.6: Amplitude of excitation moment on stationary paddles in waves of 1m height over a range of periods. The ratio of trough to crest peak moment is also shown on the right hand axis.

The flat paddle and semi-circular curved paddle offer two ends of the spectrum with regards to curvature. It was thought that a more triangular paddle could perform better as it is more streamlined in the shoreward direction, much like the bow of a boat. However, the converse was found to be true in regular waves, which is attributed to two mechanisms. The first is due to the fact that surging and pitching bodies rely on the pressure difference along the wave, thus if the paddle is more semi-circular there is a broader region that maximises the lengthwise pressure difference. The second mechanism is a result of the flow of the down rushing water on the seaward face when the paddle pitches upright from its most shorewards position. If the paddle shape is more triangular then the water converges on the central line, creating an extended trough over only a small area. A more circular paddle creates a less severe extended trough but over a larger area, improving the average pressure differential across the paddle. However, a more circular paddle does increase the surface area of the paddle and the associated cost of materials.

5.2.2 Paddle Height

The optimal height of the paddle is affected by both its extent above the water surface and the depth it reaches into the water column. Increasing the height of the paddle above the surface directly affects the amount of over-topping experienced by the device. Therefore, a taller paddle would mean a larger power capture in larger waves. However, the device only has a finite generating capacity determined by the PTO and any additional power capture would be wasted. Furthermore, in accordance with the survivability design criteria it is beneficial to have passive mechanisms like over-topping to reduce wave load, thus the paddle height above

the SWL should be determined to accommodate wave heights within the expected operational window.

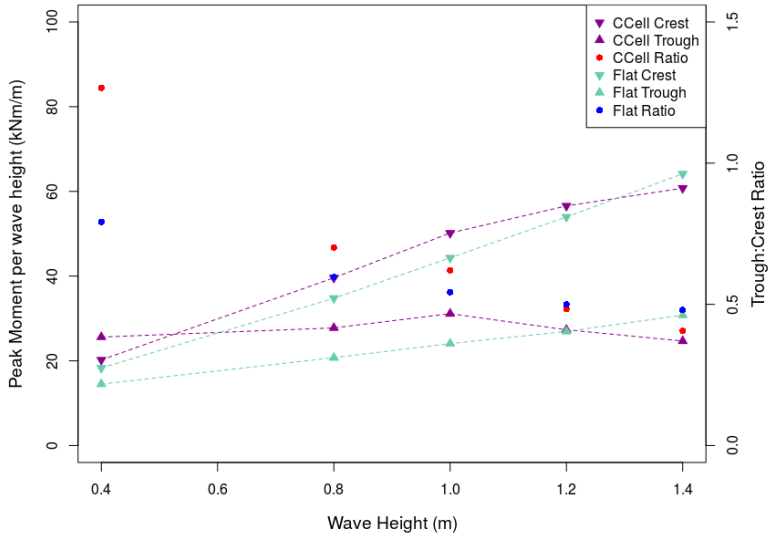

Figure 5.7: Peak wave induced torque with stationary paddles in waves with wave period T= 6s and varying wave heights.

To understand the relationship between wave height and induced loading on an OWSC, static simulations of the flat paddle and CCell were conducted in waves of varying wave height but with a fixed wave period of $T = 6s$[1]. For pitching devices with hinge points far below the water surface, the excitation moment is increased in a larger crest due to both the additional force of the wave and the fact that this force has a longer moment arm. This explains the gradient of the lines for crest moment in Figure 5.7 with the CCell and flat paddle following a similar gradient. The relationship between trough moment and wave height is also expected to have a positive gradient for an OWSC due to the diffractive effect and the increased portion of the paddle exposed to atmospheric pressure in a deeper trough. This is true of the flat paddle, though for the CCell paddle it appears that the diffractive dynamics of CCell are more effective in a trough when wave height is lower. As this change follows the inception of over-topping, it is believed that these effects are linked.

The imbalance of the moments in the crest and trough also increases with wave height, with the largest waves producing a moment over twice as large in the crest than in the trough. However, in the smallest waves this trend reverses for CCell and the excitation moment is actually larger in the trough than in the crest.

In the largest wave the peak crest moment per wave height is lower than expected for CCell. This is due to wave over-topping, which occurs for CCell at a lower wave height because of the funnelling effect of the shape of the CCell paddle. As 1.4m is at the limit of the operational window, it suggests that the CCell paddle is correctly sized for its deployment.

[1] These static simulations were conducted alongside the FOT simulations prior to the creation of the design waves, hence the choice of $T = 6s$ rather than $5.5s$

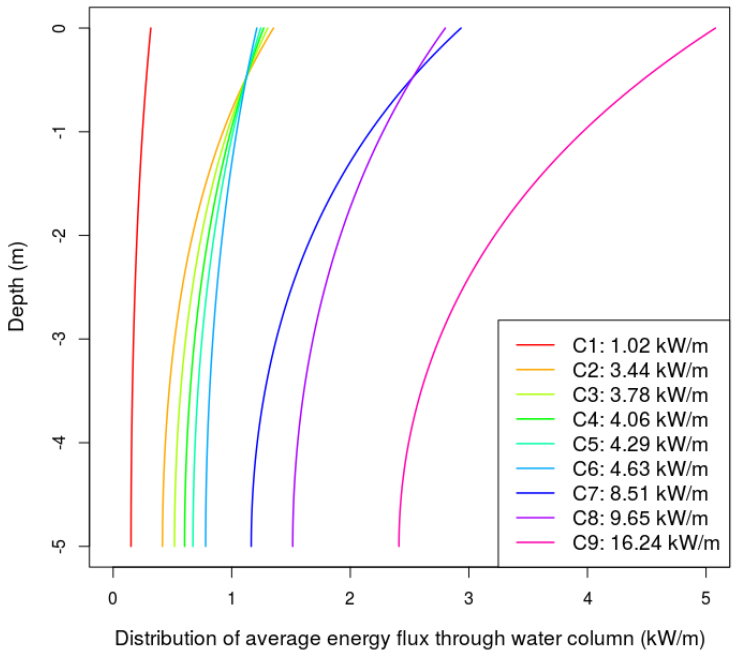

Figure 5.8: Distribution of energy flux per unit width throughout water column averaged over one wave period. The total average energy flux for each design wave condition is provided in the legend.

When the paddle is moving slower than the surrounding water, energy is transferred to the paddle. Conversely when the paddle is faster than the water particles, energy is dissipated. This is complicated by a pitching device as the horizontal velocity of the paddle varies with depth. As the device protrudes further into the water column there is a balance between the additional wave energy and the increased resistance to the motion of a larger paddle. If the device extends too far down the water column where there is little energy then the additional section only adds to the inertia of the paddle. This makes it less responsive to wave action and provides negligible additional power for extraction. However, if the paddle is smaller it immediately reduces the wave energy available to it.

Total energy flux in a wave is heavily dependent on the wave height with wave period having a comparatively smaller influence, however the distribution of energy in the water column is dictated by the wave period. Wave conditions C2-C6 have the same wave height (H=0.8m) but the wave period ranges from T=4.5s for C2 to T=7s for C6. As shown in Figure 5.8, the energy is more evenly distributed through the water column in longer period waves. Conversely in higher frequency waves, the energy is concentrated towards the surface. Therefore, in deployment locations with longer wave periods it may be increasingly beneficial to extend the paddle further in the water column.

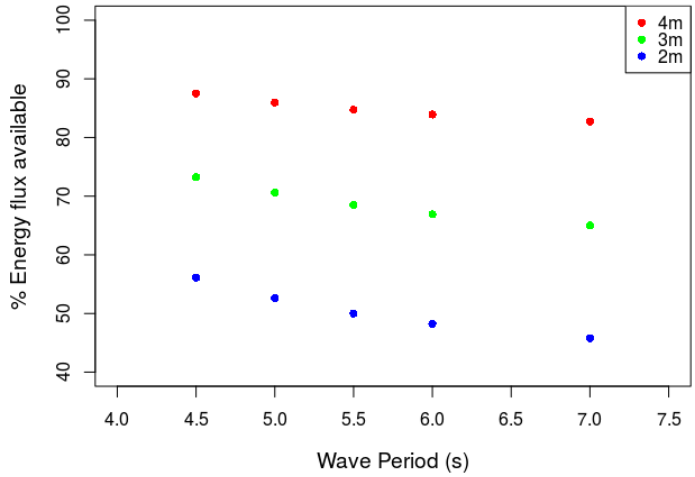

Figure 5.9: Percentage of wave energy available to different paddle heights in various period waves

Considering the percentage of energy available within the vertical limit of the paddle, as shown in Figure 5.9, suggests that the hinge placement at $z = -3m$ may be compromising the power capture. In addition, the support structure of the WEC reacts against the seabed and this higher hinge position creates a greater moment arm. However, this does not necessarily mean that the torque at the foundation is larger, as a lower hinge position increases the excitation force. The possible variation in the torque for this deployment is small due to the chosen water depth, thus this consideration has less influence on the final design decision. In future deployments this should be reconsidered and a configuration sought to minimise the foundation torque.

5.2.3 Paddle Width

Bodies much smaller than the wavelength of the incoming wave field have been shown to behave as point absorbers, or axisymmetric bodies, even if they are not symmetric (Todalshaug 2017). As the width of the body increases, a 2D representation is often adopted which is equivalent to a device of infinite width. This is the case in the terminator absorber model and assumes that all incident waves are refracted parallel to the incident wave direction, creating a standing wave pattern. At this 2D limit it suggests that the wave force increases linearly with width, allowing the developer to “design” the desired output, merely by adjusting the width. However, 3D effects are still important for the sizes considered by most wave developers, and for devices of finite width the force has been observed to initially increase with the square of width before it reaches the 2D limit (T. Whittaker and Folley 2012).

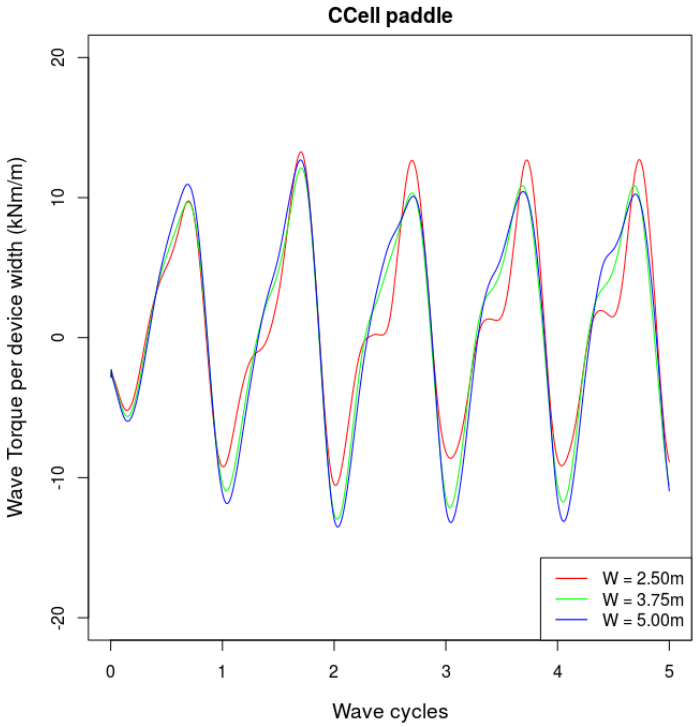

Figure 5.10: CCell paddle of various widths in a Co5 wave. Static simulations.

The CCell device considered for this application is much smaller than the devices investigated by Whittaker and Folley but it is still interesting to investigate the effect of CCell's width. In future iterations of the design the current limit on the width (2.5m) may be removed due to either the possibility of dock-side manufacture or innovation regarding the joining of composite sections. Figure 5.10 compares the peak torque per width of a CCell variant 1.5 and 2 times larger than the original, where there appears to be penalty for wider devices in the crest of the wave. However, the peak torque per width does increase in the trough of the wave because the wider paddle is better at holding back the reversing water. The profile of the torque also changes with the width as the flattened section about zero torque disappears for wider paddles. This is due to the vortices created at the paddle wings: their size does not change with the width of the paddle, but their effect is observed on a reduced portion of the device. The torque profiles do alter as the simulation progresses due to the turbulent effects of the vortical structures as they are washed backwards and forwards past the paddle.

5.3 Evaluation of Performance

To properly evaluate the performance of the device, the power output rather than the excitation torque must be considered. Values for excitation torque calculated by static simulations can be used to provide an indication of the theoretical power limit for a particular design. However, to provide a more accurate estimate of the power output of a device, numerical modelling is required. One of the main drawbacks for using a CNWT is the amount of time each simulation takes, therefore if multiple runs are required to determine appropriate damping levels, performance evaluation becomes increasingly cumbersome. This section details a

proposed method to identify the optimal damping for the device and compares the power outputs obtained from the CNWT and from WEC-Sim, a faster linear code. As WEC-Sim relies on the hydrodynamic coefficients being supplied externally, how much the different estimates for these values affect the power output calculation is also investigated.

5.3.1 Theoretical Power Limit

In the first steps of the design process it may be helpful to have an indicative estimate of the maximum achievable power absorption for the device in characteristic wave conditions. There are two approaches to this, either from the difference between the incident and resultant wave fields, or from the perspective of the device by considering the maximum force and velocity it could experience. Plotted together these form the limiting power absorption lines on Budal diagrams.

The first limit is concerned with the radiation pattern generated by oscillating systems. If the body is axisymmetric or very small in comparison to the wave length, then the size of the object has no bearing on the radiation pattern. As shown in Equation (5.1) (Todalshaug 2017), it is calculated only from the wave energy flux J in (W/m) and wave number k. For motions in heave the radiation pattern is a single source point with $\alpha = 1$, but for pitch or surge motions there is a dipole pattern, thus $\alpha = 2$. For a terminator body, it is assumed that any incident wave power is reflected or absorbed, thus the maximum is if all the power available along the length, L, of the body is absorbed $P \leq JL$.

$$P \leq \alpha \frac{J}{k} \tag{5.1}$$

The second limit is calculated from the maximum stroke s_{max} of the WEC's motion and the amplitude of the excitation force F_e on the body. The stroke limit defines the maximum velocity of the WEC as $|u| = \omega s_{max}$. An upper bound is identified by assuming that the radiation and that the wave force and velocity of the body are in phase, Equation (5.2).

$$P \leq \frac{1}{2} |F_e| \omega s_{max} \tag{5.2}$$

The corresponding limit lines have been calculated for both the flat paddle and CCell, which are plotted in the Budal diagram in Figure 5.11. The excitation force estimates were determined from the static CFD simulations shown in Figure 5.6 and a maximum stroke of 40^o was used. This analysis assumed waves of H=1m and if other wave amplitudes are considered the stroke power limit will increase proportionally, whereas the radiation limit will increase with the square of the wave height.

Use of the radiation pattern limits for a pitching point absorber provides a much larger maximum power limit than that calculated by the terminator theory, particularly for waves of $T \approx 3-4s$. The terminator device limit is the power estimate used in determination of the CWR and though it has been claimed that CWR in excess of unity is possible, it is unlikely that the values predicted by the point absorber radiation limit are possible. Although the devices considered are small in comparison to the wave lengths assessed, it appears that the terminator power limit is a better approximation in lower period waves. As a first estimate, the NEMOH derived

curves do provide an upper bound that falls within the range of those calculated by the CFD simulations. This analysis suggests that for initial device sizing, the linear code could provide an upper limit to the power output in longer period waves. However, NEMOH is unable to differentiate between the flat and curved paddle, therefore should not be used for further design refinement.

The assumptions used within this analysis are significant, particularly as the excitation force is evaluated for a stationary body. Any motion of the device reduces the relative velocity between the device and the wave, therefore the wave force reduces, as demonstrated by the Morison Equation (2.35). It also requires a well controlled system to remove any phase angle to align peak excitation force with peak velocity.

As a metric for expected energy capture these upper bounds are perhaps not very helpful, though they could be used for initial appraisal of other subsystems or the loads against which the device will need to withstand. However, the use of these linear codes in determining survivability is limited as will be discussed in Chapter 7.

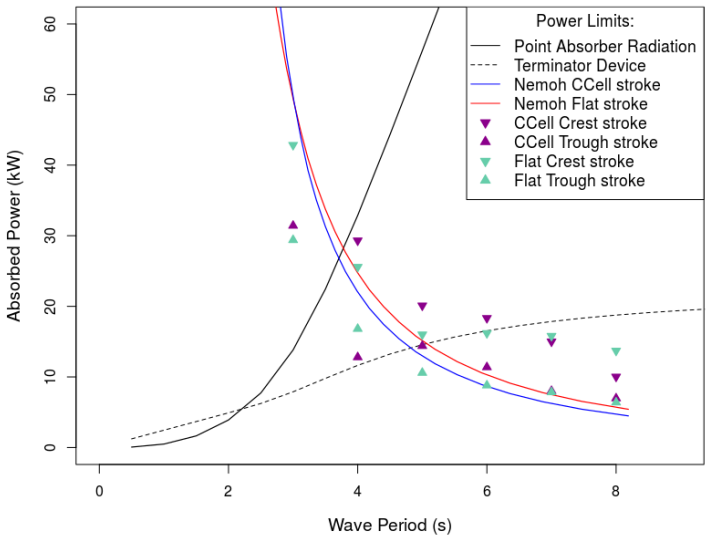

Figure 5.11: Power absorption limits for a OSWC in waves with 1m wave height

5.3.2 Optimal Damping Prediction

The power output of a WEC from a particular regular wave condition is affected by both the geometry of the prime mover and the damping. Damping restrains the oscillatory motion of the paddle by dissipating the energy and thus, for larger magnitudes of damping, the motion of the paddle is expected to be more restricted whilst lower damping values allow the paddle to move more freely. The relationship between power and motion is explained by a trade off between two energy loss mechanisms: when the motion of the paddle is overly restrained there is a significant loss of energy due to wave reflections from the seawards face of the paddle, and conversely when it is allowed to move more freely there is a dissipative energy loss due to radiating waves. Therefore, an optimal level of damping exists for a particular seastate as both a heavily damped system and a more freely moving paddle offer a reduced performance.

The effect of damping was considered in the tank testing of the floating device, detailed in Section 4.2.1, and the results from different levels of damping in various wave periods is shown in Figure 5.12, where 100% indicates the maximum control voltage to the valves and, therefore, the minimum resistance to the paddles motion. It is clear that the optimal level of damping is dependent on the frequency of the waves, with higher levels of damping achieving a higher power absorption in lower period waves. Conversely, in longer wave periods, a more freely moving paddle, namely that with a valve control voltage of 70-80%, is optimal.

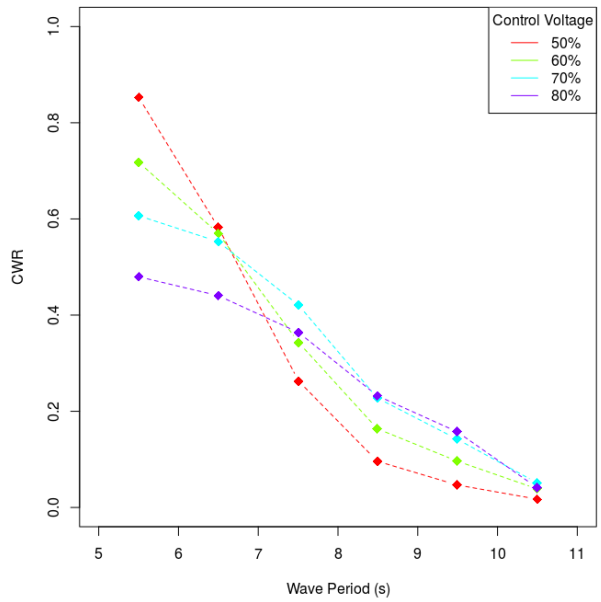

Figure 5.12: Capture Width Ratio calculated for the Floating CCell paddle from laboratory testing of various wave periods (reported at full scale) with the same wave height equivalent to H = 1.5m at full scale.

Software reliant on panel methods can run through a larger number of parameter iterations in a relatively short time frame, allowing the developer to trial many different damping values to analyse device performance. However, when CFD is used, a large volume of simulations is onerous. Therefore a robust method to predict the optimal damping conditions is required.

Potential flow models in the frequency domain represent the hydrodynamics as a balance between the wave force, added inertia and damping as shown in the complex form in Equation (5.3) (T. Whittaker and Folley 2012), with the PTO approximated as a rotational damper.

$$\left[-\omega^2(I + M_A) + C - i\omega(B + B_{PTO})\right]\theta = M_{exc} \tag{5.3}$$

Considering the power transfer in the system, the useful power harnessed by the PTO time-averaged over a regular wave cycle is determined by Equation (5.4).

$$\bar{P} = \frac{1}{2}\Re\left\{M_{PTO}\dot{\theta}^*\right\} = \frac{1}{2}B_{PTO}\omega^2\left|\theta\right|^2 \tag{5.4}$$

There exists an optimum condition that maximises the power absorbed by the PTO, which is

governed by the PTO damping value. The condition for the optimum PTO damping rate, B_{PTO}, can be obtained by differentiating the expression for time averaged power with respect to PTO damping and finding the maximum by equating this to zero. The outcome of this mathematical manipulation is Equation (5.5), which predicts that the optimal PTO damping is dependent on the wave frequency but not on the wave amplitude.

$$B_{PTO} = \sqrt{\frac{[C - \omega^2(I + M_A)]^2}{\omega^2} + B^2} \tag{5.5}$$

The FOT tests, described in the previous chapter, have provided estimates for the hydrodynamic coefficients and these have been used in Equation (5.5) to calculate optimal damping coefficients, as shown in Figure 5.13. Fortunately, there is only a single value per wave period predicted for the flat paddle, as direction of motion did not affect the hydrodynamic coefficients. However, the shoreward and seaward values for CCell present a range of possible optimal damping coefficients. Considering the values from FOT tests of different oscillation amplitude suggests that wave height may have an effect on the optimal damping. Larger waves are likely to induce a larger amplitude of WEC motion and in most wave periods this increases the range of possible damping coefficients. However, the baseline values from 15^o amplitude FOT tests will be used in the following power output analysis, as this was the largest data set and represents the expected device motion in the prevalent wave heights. For smaller amplitude wave conditions these predicted optimal damping values may overly restrict the device motion, where as in larger waves a higher level of damping may provide the highest CWR.

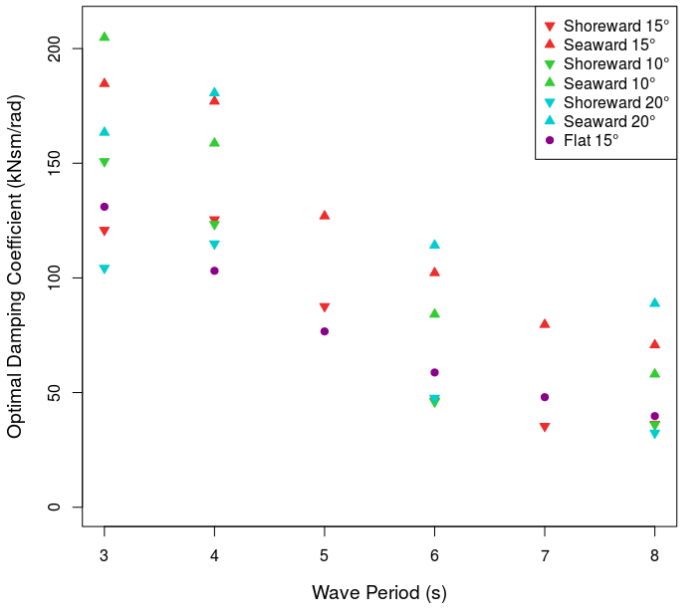

Figure 5.13: Optimal damping coefficients for waves of different period, as predicted by the added mass and radiation damping values calculated from FOT tests.

To make a fair comparison between different device geometries an effort should be made to ensure that they are being evaluated at their optimal damping condition. It is also important

that the device is evaluated when it is in a stable condition, which in regular waves demands oscillation about a mean position without drifting towards an end stop.

Velocities and pressures within waves are asymmetric with generally larger magnitudes in the crests than in the troughs. In addition, for a fixed hinge position, less of the paddle is submerged in a trough than in a crest. As shown in the previous chapter, the device may behave quite differently in shorewards and seawards motions and a damping pairing must be chosen to reflect this and stabilise the average motion. This could mean a large number of simulation runs in CFD if a trial and error method is adopted.

Although there is a difference in the shoreward and seaward damping coefficients predicted by potential theory in Figure 5.13, the imbalance is not in the right direction, i.e. it is the shoreward stroke that requires a higher level of damping to prevent drift. To approximate the necessary imbalance in damping values, the trough to crest ratio of peak excitation moment, as shown in Figure 5.6, will be used as a first guess for dynamic simulations in the CNWT.

5.3.3 Power Estimations

WEC-Sim is an alternative method to the CNWT that is commonly used to evaluate the power performance of a WEC design. It is based on a radiation and diffraction method, which solves the system dynamics in the time domain as prescribed by the Cummins Equation (3.2) by using linear hydrodynamic coefficients usually calculated by a frequency domain BEM code. In this study it has been used as a comparator for the power estimates calculated in the CNWT. As only regular waves are considered, it is easy to substitute the NEMOH radiation coefficients with the added mass and radiation damping calculated from FOT tests for the relevant wave frequency. However, the wave excitation and diffraction force as calculated by NEMOH, Figure 4.15 has been used in both WEC-Sim tests in order to evaluate the origin of any discrepancy in estimated power output.

The analysis will first consider the primary design wave condition, Co5, before considering the effect of wave period and wave height.

Primary Design Wave Condition

The results for the flat paddle in a single wave condition are presented in Figure 5.14, where the powers have been time-averaged over a wave cycle and the average of seven cycles has been used. There is a wide variation in the results from WEC-Sim, depending on the source of the hydrodynamic coefficients. The larger radiation damping and added mass values calculated in the FOT tests cause a 26% reduction in estimated maximum power output in comparison to the NEMOH coefficients. However, the maximum power output predicted by the OpenFOAM CNWT differs by only 8.6% to that calculated by WEC-Sim with CFD coefficients. For the flat paddle, the source of discrepancy appears to be the use of radiation coefficients derived from linear theory and when these are replaced by those evaluated from a non-linear technique, a good agreement is possible between WEC-Sim and a fully non-linear NWT.

A range of different levels of damping were analysed to identify these maximum power outputs. For the WEC-Sim simulations this was simple, as the same damping is used in both directions. However, in the CFD simulation this required some trial and error to first achieve a stable pairing, and the damping values referenced in Figure 5.14 are those used for the shoreward

motion. The trough to crest moment ratio predicted that the seawards damping should be 0.54 times the shoreward damping but this caused a seawards drift. The stable ratio was eventually found to be 0.62, a value 15% larger than that predicted by the static simulation. The method to predict the optimal damping was, however, successful for the CFD simulation. Of the seven various levels of damping trialled it reported the highest power output. Though, this was a much lower level of damping than the optimal value found for the WEC-Sim simulations.

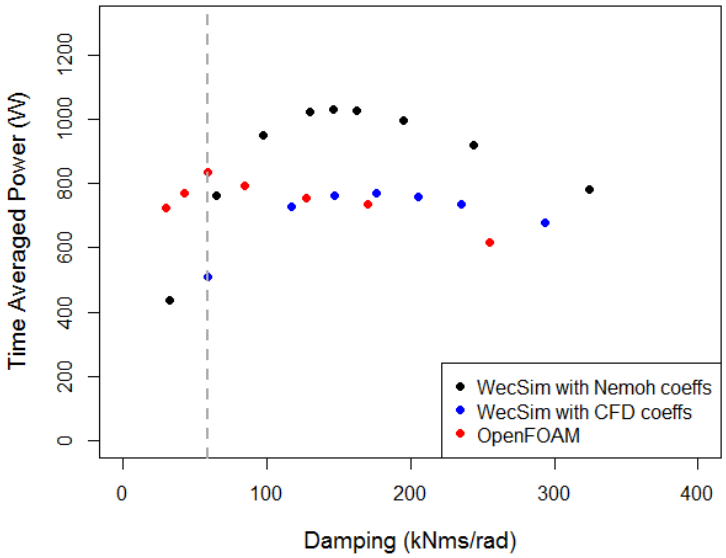

Figure 5.14: Time averaged power predictions for the flat paddle in a Co5 wave (H = 0.8m, T=6s) with different levels of damping. The optimal damping as predicted by potential theory is indicated by the grey dotted line.

The same study was conducted with the CCell paddle to investigate the effect of asymmetry in shorewards and seawards profiles. This involved an additional set of tests with WEC-Sim, as the seaward and shoreward CFD coefficients were considered separately, Figure 5.15. As observed for the flat paddle, the WEC-Sim simulations using the NEMOH coefficients report higher powers than those that used the FOT values. Additionally, the shorewards CFD coefficients predicted a higher power output than the seawards ones and this difference is driven by the substantially larger added mass in the seawards direction (see Figure 4.23).

The power capture predicted by the CNWT is significantly larger than the WEC-Sim estimations for the CCell paddle, with OpenFOAM reporting an additional 51.7% of the highest WEC-Sim prediction. This difference is due to the increased diffractive dynamics of the CCell paddle that is not be captured in the NEMOH excitation forces. The excitation force calculated by NEMOH is $\sim$24kNm, whereas the shorewards and seawards values from static simulations in the CNWT are 50.2kNm and 31.1kNm respectively. Inputting the average of these two excitation forces along with the shoreward CFD coefficients the WEC-Sim expected power output increases to 1208W, which is only 9.8% lower than the CNWT value of 1340W.

The optimal damping coefficient for CCell is again well predicted by potential theory. The true maximum power appears to lie between the damping values predicted for the shore and sea motions, though the seawards radiation coefficients provide a better estimate, as indicated by

the rightmost grey dotted line in Figure 5.15. The stable damping pairing was found to be 0.74, and like for the flat paddle this value is $\sim$ 15% larger than that predicted by the static simulation.

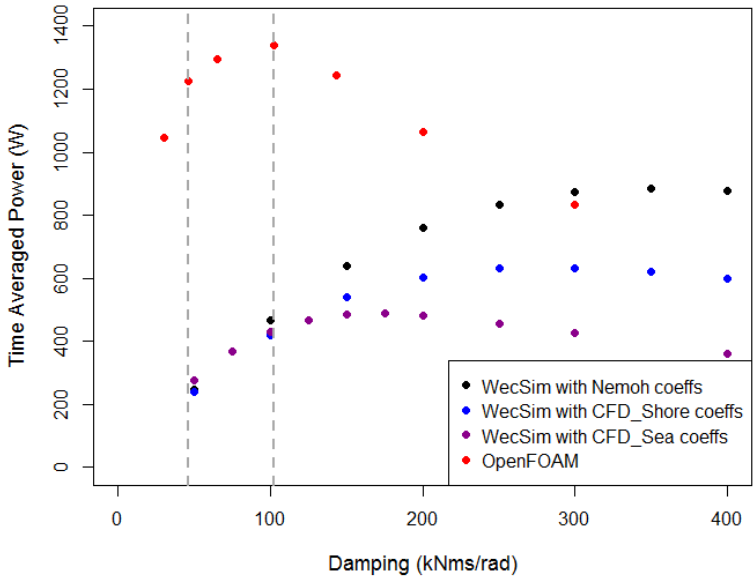

Figure 5.15: Time averaged power predictions for the CCell paddle in a Co5 wave (H = 0.8m, T=6s) with different levels of damping. The optimal damping as predicted by potential theory is indicated by grey dotted lines.

Effect of Wave Period

The study was extended to analyse the power output across the expected range of operational frequencies with the same wave height of 0.8m (wave cases Co2 - Co6). For the WEC-Sim simulations a variety of dampings were considered, thus the values presented in Figure 5.16, reflect the optimal output. However, as the number of simulations required to replicate this in the CNWT was excessive, only the predicted optimal values were used (for CCell this corresponded to the seawards prediction), though iterations were conducted to provide a stable pairing as required. Therefore, the outputs cannot be guaranteed to be optimal.

In a study comparing WEC-Sim predictions against experimental data collected from a 1:7 scale two sectioned attenuator, SeaRay, the error in total predicted power was found to be 24%, with WEC-Sim routinely over-predicting power absorption (So, Michelen, et al. 2017). A similar average difference between the WEC-Sim plus NEMOH and the CNWT simulation of the flat paddle was found for the range of seastates shown in Figure 5.16. Although the difference in CWR was only 0.021 on average, this equated to an over-prediction of 22.3%, though when the FOT test coefficients were used WEC-Sim predicted the power output to be 9.9% lower than the CNWT value. Conversely for the CCell paddle, WEC-Sim with NEMOH radiation coefficients under-predicted the CNWT power output by an average of 37.9% across the operational range of wave frequencies. This average difference increased to 58.0% and 67.7% when the shorewards and seawards FOT coefficients were used.

Clearly the benefits of the non-linearities that are afforded by the curved paddle are not captured in the WEC-Sim analysis, which suggests that the performance of CCell is worse than

the equivalently sized flat paddle. However, this is not what has been observed in previous rounds of laboratory testing of the floating concept nor is it the conclusion drawn from the CNWT data. The average increase in CWR for the CCell paddle over the flat paddle is 0.068, though in lower period waves this difference is as large as 0.104. This equates to a percentage increase of 69.8% across the sea states and for a wave period of 5s, CCell captures more than twice the peak wave power harnessed by the flat paddle.

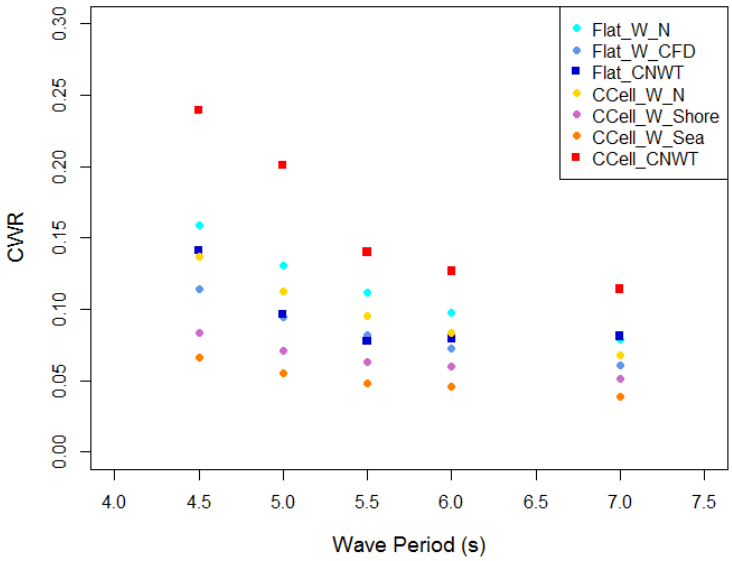

Figure 5.16: Capture width ratio for various regular waves with H=0.8m as calculated by different methods. W refers to output from WECSim simulations, where N refers to coefficients derived by Nemoh and CFD, Shore and Sea are coefficients derived from forced oscillation tests in the OpenFOAM. CNWT refers to output from full CNWT simulations.

Both types of paddle and all methods of evaluation report the same trend in an OWSC's performance, with a higher CWR in higher frequency waves. This trend also agrees with the output from previous tank testing of the floating OWSC shown in Figure 5.12 and can be explained by the underlying wave dynamics. The device targets the surge wave force and has been shown to be primarily driven by inertia within the operational frequency range. This is concerned with the horizontal acceleration of the water particles, which is proportional to the square of the wave frequency, thus is larger in lower period waves. As the device is most efficient in the least energetic waves, this helps to reduce the difference in power capture across different period waves, which is beneficial for the PTO system as the load factor is improved. For CCell the power difference across the periods tested is 724W, whereas for the flat paddle it is only 414W.

It was initially supposed that the asymmetry of the CCell paddle would amplify the imbalance in excitation force for different directions of motion. Interestingly, however, it is the flat paddle that requires a larger difference between the seawards and shorewards damping coefficients to prevent drift.

The trough to crest ratio evaluated from static simulations are consistently lower than the stable damping pairing found from trial and error, with a larger discrepancy in longer period waves, Figure 5.17. This under-prediction is expected when the trend demonstrated in Figure 5.7

is considered, as the waves used in the static simulations were 1m in height whereas the Co2-Co6 wave cases are only 0.8m. However, in some cases the prediction aligned perfectly, particularly for the flat paddle in shorter wave periods. As the maximum deviation between predicted and actual damping pairings was only 15%, it is recommended that this approach is used in future dynamic studies as a first guess.

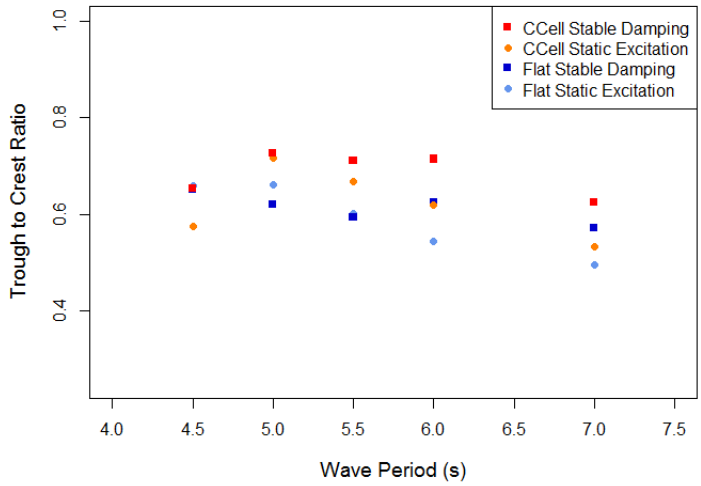

Figure 5.17: Trough to Crest excitation force ratio and Stable damping ratio in various waves with H=0.8m

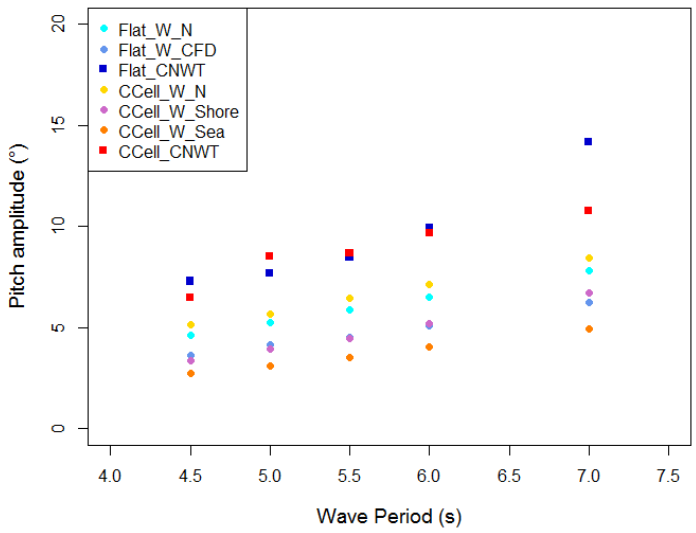

Figure 5.18: Amplitude of pitch motion for various regular waves with H=0.8m as calculated by different methods.

In longer wave periods, a lower level of damping was optimal, allowing the paddle to move more freely with the increased motion of the water particles. This leads to an associated increase in the amplitude of pitch motion. The CNWT predicted larger angular motions than WEC-Sim, though notably, all CNWT amplitudes are within the range considered as small amplitude motions and therefore linear assumptions should be permissible according to the K_C number.

As the amplitude for the majority of the wave periods did not exceed 10^o, coefficients derived from smaller amplitude FOT tests may have been more suitable.

Effect of Wave Height

The linear assumptions of WEC-Sim mean that the hydrodynamic efficiency of the WEC is dependent only on wave frequency. The CWR calculated for one wave height, will be the same for any height wave of the same frequency according to WEC-Sim. Clearly non-linearities such as over-topping would prevent this being true in large waves and outside the operational range of wave heights the CWR and wave height would progressively decouple.

However, the CWRs for the flat paddle evaluated in the CNWT do not support this assumption of linearity even within the operational range, where over-topping does not occur. As shown in Figure 5.19, larger wave heights report larger CWRs. For OWSC's pitching about the seabed this is not unexpected due to the effect of the increased moment arm in larger crests. The smallest wave height also reports a higher CWR, however the power absorbed is only 335W, thus has little influence in overall power performance estimates.

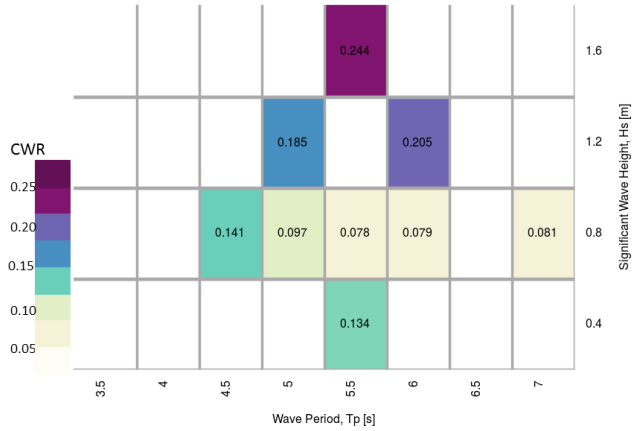

Figure 5.19: Capture width ratio for flat paddle in design sea states as calculated by the CNWT

These are not guaranteed to be the maximum capture values, as the shoreward damping was assumed to be the same as the 0.8m waves of the relevant frequency, with adjustment to the seawards value to provide stability. This supposition was found to be untrue in previous lab testing, where more power was captured from larger waves of the same frequency when the paddle was allowed to move more freely. However, considering the change in optimal damping for larger amplitude motions in Figure 5.13 it suggests that a higher level of damping may improve power absorption and further investigation is required.

The amplitude of motion predicted by the CNWT for the two largest waves (Co8 and Co9) is 24.96^o and 27.25^o, which is above the 17.2^o limit for applicability of potential theory. Therefore, the prediction from WEC-Sim for these wave conditions should be expected to be of limited accuracy.

5.4 Discussion and Chapter Conclusions

Optimisation of a device must take into account more than just the maximisation of the hydrodynamic efficiency. The prime mover is only one part of the wider system, and decisions about its shape and size impact the design and cost of both the underlying structure and PTO system. Other significant cost elements are also impacted, with the increased size complicating the transportation and installation, whilst some designs may become infeasible when the manufacturability is considered. Therefore cost efficiency as well as hydrodynamic efficiency must be maximised. For design optimisation to be an efficient process, the developer must have a firm grasp of any size, or other, limitations from the outset. Then the performance, within the identified parameter space, can be evaluated in relevant wave conditions.

For the initial stages of design, the exact deployment location may not be known, or if it is then relevant site data may not yet have been collected that encapsulates the variability of the resource. Alternative sources of wave data, such as NOAA's numerical model can be used for the closest grid node. Spatial transformation models could then be used, however, if sufficient bathymetry data is also unavailable, then the TMA transformation can be used to provide an indicative depth-limited wave climate.

The optimisation process for the OWSC may initially prioritise simulation speed to condense a wide range of design options. Particularly for sizing of the device for the wave resource, the theoretical limits of power output can be considered, including the limit induced by the maximum stroke. For this analysis, it was found that the BEM linear code provided a good estimate for the theoretical bounds of maximum power absorption.

For more refined design optimisation, static simulations in the CNWT can be used to evaluate the effect of certain parameter alterations to the wave excitation moment on the paddle. Any complex hydrodynamic effects such as significant alteration to the surface elevation due to diffraction would not be resolved by codes dependent on potential theory. NEMOH was found to significantly underestimate the wave excitation force of CCell, particularly in the wave crest.

In order to consider the actual power absorption of the device a time domain code is required to take into account external mechanical forces such as the PTO or mooring force. Dynamic simulations in the CNWT could be used, or alternatively, a faster code such as WEC-Sim, which relies on the hydrodynamic coefficients supplied by other means. There is a vast time penalty for using the CNWT: for a single 200s WEC-Sim simulation on one core it takes just 7-8s, whereas a 45s CFD simulation conducted in parallel on 20 cores takes closer to 23hrs and this increases in larger wave conditions.

However, WEC-Sim has previously been shown to over-predict power output. A third strategy was suggested in which radiation coefficients derived from FOT tests in the CNWT were input into WEC-Sim instead of those predicted by potential theory. The power output was then compared to that calculated in the CNWT. This provided a close estimate for the flat paddle as the radiation coefficients were unaffected by direction of motion and the excitation force was reasonably predicted by NEMOH. However, for CCell the performance is governed by non-linear diffractive effects and WEC-Sim significantly underestimates its potential. Only when all coefficients predicted by NEMOH were replaced by CNWT equivalents did the power

predictions come within 10% of each other. However, even if all the coefficients predicted by the CNWT are implemented in WEC-Sim, the problem of asymmetry persists and at best WEC-Sim could provide an upper and lower bound.

When the operational frequency range was considered, WEC-Sim with FOT coefficients predicted an average 9.9% lower CWR for the flat paddle than that computed by the CNWT. The best estimate by WEC-Sim under-predicted the output from the CNWT for CCell by 37.9%. If only WEC-Sim had been used, the developer would have concluded that a curved paddle worsens the achievable power absorption, however, the CNWT predicted that CCell increases the CWR by an average 69.8% for the five wave periods analysed. All three methods did however, agree on the trend in OWSC performance, with a larger CWR in shorter wave periods for both paddles. The variation in power performance estimates increases significantly when larger wave heights are investigated as WEC-Sim assumes linearity with regard to wave height, whereas in the CNWT the CWR was shown to increase as long as over-topping did not occur.

Furthermore, in the initial stages of design the developer may be concerned with the average motion of the device in prevalent wave conditions, as it can inform analysis of expected wear rates and operational life of particular components. The values predicted by WEC-Sim and the CNWT differ sufficiently enough for this to have a considerable impact on such an analysis.

Chapter 6

PTO Design, Modelling and Bench Test Validation

This chapter considers the design of a hydraulic PTO for the pilot deployment of CCell in Mexico. To understand the impacts of a PTO the use of a linear damper was insufficient and required the development of a suitable model to be coupled to the CFD solver. This chapter considers the following:

- Types PTO systems available to WEC developers and their applicability to CCell.
- Impact of different damping profiles.
- The development of an alternative model that incorporates the effect of each part of the hydraulic system.
- Building and benchmarking of physical test system.

The high-fidelity PTO model was the subject of a paper presented at the 28th International Ocean and Polar Engineering Conference in Sapporo, Japan in 2018 under the title *"Coupled Modelling of a Non-Linear Wave Energy Converter and Hydraulic PTO"* (Worden Hodge et al. 2018).

6.1 Choice of PTO

WECs are designed to convert the energy from waves into a mechanical motion, which is then transformed into electrical power through the PTO system. The design of such a system must overcome a number of challenges, including: variable torque and velocity profile; marinisation and device robustness; and high conversion efficiencies for an attractive price tag. Wave energy developers have sought to customise drive train systems from a number of other industries to tackle this vital problem and reduce the risk associated with layering prototypes within prototypes.

From the inception of the wind energy industry wind turbines have utilised planetary or helical gearboxes to achieve a Revolutions per Minute ("RPM") consistent with electricity generation (the overall gear ratio can be around 1:120). However, component defects and variability of the

wind resource leads to significant stresses and fatigue loading on gears and bearings. This vulnerability results in gearboxes requiring an intensive maintenance regime contributing a significant cost to the overall turbine operation. The problems with gearboxes are compounded in wave energy applications where there is an even greater variation in speed and torque profile thus reliability issues are likely to be exacerbated and maintenance will be hindered in sub-sea deployments.

The opportunity to remove this complex component is therefore attractive, and much effort has been focused on the development of direct drive machines to improve turbine reliability. Direct drive solutions reduce the energy conversion process to a single stage, with additional benefits such as reduction in components, increased efficiency and reduced noise. However, in order to deliver this high torque at low RPM, the dimensions of the device must increase and the associated weight would require design of a suitable support structure. In a wave energy application the size of the generator would likely impact device hydrodynamics and it would also need to be operated in a fully flooded condition leading to biofouling and corrosion management issues (The University of Edinburgh 2017).

Rotational devices have an advantage that their use is widely distributed, from conventional energy conversion systems to ship propulsion, and they are well suited to over-topping devices or OWCs. However, an OWSC device such as CCell only undergoes partial rotation leading to uneven wearing of gears or bearings in a rotational PTO system. For this application a linear device may be more suitable, though any linear solution only allows a finite displacement and in extremes there is a risk of collision with mechanical end stops. An alternative mechanical solution for linear motion is the ball screw, which translates linear motion to rotational motion and vice versa. One such concept, (Umbra Cuscinetti S.p.A. 2017), is based on the reversal of a highly-efficient electro-mechanical actuator often used in the aerospace industry, which directly converts to electricity and allows active control. Although the original technology may be mature, it has not fully been transferred to application within WECs as it has yet to be fully marinized and there are issues with limiting the torque in large seas.

Linear generators are an innovation driven almost exclusively by the wave energy industry. It has in particular been developed by AWS for use with their submerged pressure differential device. This solution requires a completely bespoke design for the device, which increases both development time and associated risks. The technology is also complex and its size is dependent on the rated force resulting in very large machines: the 2MW device described in (Polinder, Damen, and Gardner 2004) and (Polinder, Damen, and Gardner 2005) had a weight of 400 tonnes. The use of permanent magnets and the attractive forces between translator and stator also require careful design of the support structure.

Hydraulic systems are particularly well matched to wave energy applications as they are capable of high forces at low speeds and have a high power density. A force density comparison conducted in (Bard and Kracht 2013) for a 100kW (100kN) peak device, showed that an air-cored electrical generator had a specific force of 66N/kg whereas a hydraulic system constructed from off the shelf components had a force density of 1430N/kg. Thus for smaller units, hydraulic solutions are the most practical and many hydraulic components are already certified for offshore environments due to their track record in various drive train applications. However, the efficiency of hydraulic PTOs is low due to multiple energy conversion steps

and the inherent losses associated with hydraulic components. In particular proportional valves, which are the conventional approach for load control, throttle the flow and dissipate a large amount of energy, which significantly reduces efficiency. In applications where energy conservation is a priority control is most readily achieved with a variable displacement motor. Pelamis engineers pioneered a new variable load hydraulic primary power transmission using a number of chambers in a hydraulic ram that offered a binary pressure level: high or low. These switched states could then be combined to provide a quantised approximation of a continuously varying load profile, while removing losses otherwise introduced from throttling. Artemis Fluid Power's Digital Displacement Pump-motor ("DDPM") technology uses a similar technique and is currently being used in tangent with the Pelamis PTO concept to reduce the quantisation errors (Artemis Intelligent Power 2017). Though the complexity and cost of the resulting device will likely mean it caters only to high-power applications.

In order to assess the relevance of different PTO strategies a number of different factors must be considered:

- Cost: The PTO system represents a large portion of the overall cost of a WEC, therefore directly impacts the overall economics.
- Controllability: A WEC must operate efficiently in a wide range of sea conditions to produce an attractive Levelised Cost of Energy ("LCOE"). Suitable control algorithms can extend the operational bandwidth of the device, but often require active control which is prevented by rectification. Energy smoothing or storage methods can also reduce the responsiveness and bandwidth of the control system.
- Reliability: Continuous operation offshore in a harsh environment requires a robustly designed and built device. Ease of maintenance and availability of replacement parts also impact the reliability of the device, as they reduce any down time due to failure.
- Maturity: The use of tried and tested technology, which is well understood and widely distributed has a direct impact on cost and reliability. Although some systems may be mature in their original application, there are a number of hurdles to overcome before they are considered mature in the marine industry, primarily marinization.
- Power density: Transportation and installation of large and heavy PTO systems is undesirable. Collocation of the PTO system with the prime mover may also be difficult if the PTO is so large that it affects the device hydrodynamics.
- Applicability: Not all PTO concepts are suitable for every WEC type. This is influenced by size, degree of freedom of motion and placement of PTO system.

Each of the PTO types have been assessed for the CCell application according to these factors and have been allocated a score between 0 and 5 in each category, where a higher score reflects better performance. The results of this assessment are displayed in Figure 6.1. The interaction of the CCell WEC with wave motion produces a large torque but low angular rotational speed. Considering the available PTO system types, only the linear hydraulic actuator and the ball screw solutions are viable options for a lower power OWSC. Although the hydraulic solution allows limited control and reduced efficiency, it out-performs in cost and maturity. Hence due to their high power density, compact size and robustness, a linear actuator coupled with an hydraulic motor is considered the most applicable option.

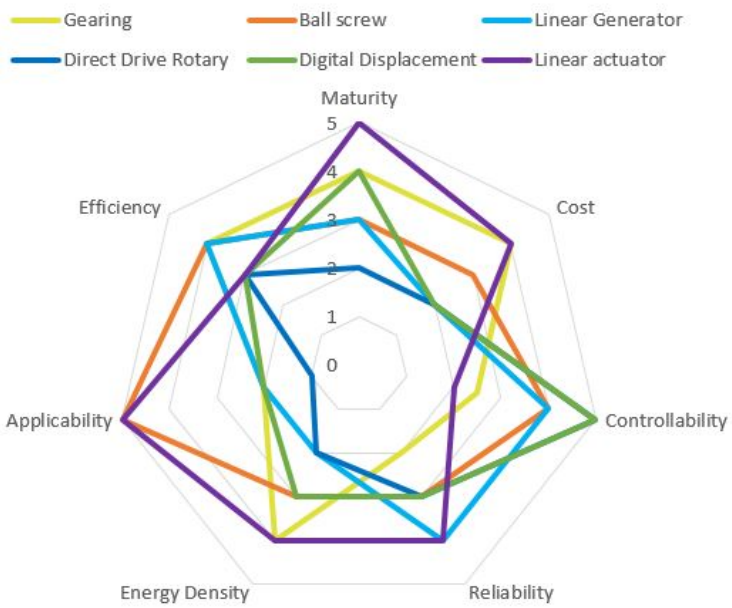

Figure 6.1: Analysis of suitability of different PTO types for use with CCell

A simplified hydraulic PTO is shown in Figure 6.2, which is of the same architecture as hydraulic circuits often proposed for WEC applications, most commonly heaving buoys (Sandia National Laboratories 2015), (Cargo 2012). The general purpose of the PTO is to produce a smooth power output by decoupling the CCell motion from the power generation. The motion of the CCell prime mover directly drives an equal area piston and this forces the fluid through a set of four check valves to rectify the flow and transform the bidirectional flow into a uni-directional flow for the motor. The electrical generator is coupled directly to the motor shaft, hence both rotating machines experience the same rotational speed. Accumulators are used at the inlet and outlet of the hydraulic motor to maintain a constant pressure differential across the motor. This prevents large and frequent deviations in motor rotational speed and means that the motor can be sized for average rather than maximum power capture. This energy storage smooths out power peaks allowing the electrical generator to operate more efficiently. A pressure relief valve is also connected across the motor terminals to limit the torque produced by the motor.

Power losses in an hydraulic circuit are predominantly from the motor due to internal flow leakage, viscous effects and Coulombic friction torque losses[1] in the motor. The efficiency of hydraulic motors depends on rotational speed and pressure difference though is most substantially reduced when run at part displacement.

There are also pressure losses due to fluid friction through pipework and across check valves, both of which will increase with increased piston velocity and fluid flow. The frictional force in the cylinder is dominated by the Coulombic component, thus although the actual force is independent of velocity it will contribute more significantly at lower velocities.

[1] Coulomb damping is a constant mechanical damping that dissipates energy due to friction from the relative motion of two surfaces in contact.

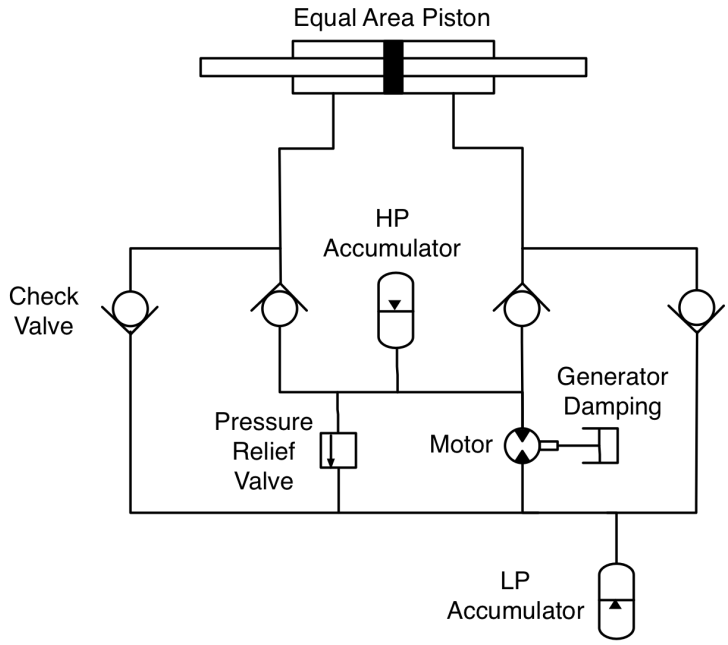

Figure 6.2: Schematic of hydraulic PTO circuit, with pressure relief valve set to 250bar

6.2 Numerical Representation of PTO

One conclusion drawn from the literature review in Chapter 3 is that it appears WEC modelling has so far either utilised low fidelity hydrodynamics models with a fully modelled PTO, or at the other end, used high-fidelity CFD simulations to increase the accuracy of the hydrodynamics but relied on a simplified linear damper to account for PTO forces.

Increasing the fidelity of other components of the WEC system can be achieved without a significant additional increase in the computational cost, thus makes the use of CFD more efficient in terms of time required and output. This was highlighted in the successful coupling of CFD with a secondary solver to compute the mooring cable dynamics (Palm et al. 2016). A similar coupling with a non-linear hydraulic power take-off model is presented in this section. This holistic approach provides high fidelity in both the hydrodynamics and the power output, which would considerably increase the confidence in the results obtained from numerical models and more importantly from a developers' perspective reduce the uncertainty in LCOE models and the risk in technology development.

6.2.1 Simplified damping profiles

The PTO system in a WEC extracts energy from relative motion between two bodies: the device and the water in an oscillating water column; two parts of the device in an articulated body, or in this case the prime mover and the sea bed. This energy extraction can be simulated as a linear damper or a linear spring-damper system. Most simply the CCell PTO can be modelled as a rotational damper Equation (4.5) in an idealised binary device that switches the damping rate (Nms/rad) dependent solely on the direction of motion of the paddle. Additional effects can easily be incorporated to this linear damper system in the CFD environment. For

example, the effects of stiction through increased frictional force at zero velocity or approximation of mechanical end stops through increased ramping of the damping coefficient beyond a particular angular displacement. Hydraulic PTOs can be better represented by a Coulombic damping model (Babarit, Hals, et al. 2012) as the motor and piston both have surfaces moving in contact with each other and are affected by friction. The accumulators, if large enough, also exhibit a near constant pressure differential across the high and low pressure sides of the hydraulic circuit. An alternative modelling method is shown in Equation (6.1) which takes into consideration these non-linearities providing a constant damping force.

$$F_{PTO} = -sign(\dot{x})A_{cy}\Delta P \tag{6.1}$$

where A_{cy} is the cross sectional area of the piston, $\dot{x}$ is the linear velocity of the piston and the maximum ΔP is the rating of the pressure relief valve.

6.2.2 Development of realistic model

In reality the damping force produced by the PTO is a function of the flow through the hydraulic components and their specification. Ultimately the solution of the hydraulic circuit must satisfy the continuity equation for a compressible fluid, Equation (6.2).

$$\rho(Q_i - Q_o) = \rho\frac{dV}{dt} + V\frac{d\rho}{dt} \tag{6.2}$$

The Bulk Modulus κ, is a measure of how incompressible or resistant to compressibility a substance is (where compressibility $= 1/\kappa$).

$$\kappa = -V\frac{dP}{dV} \tag{6.3}$$

However, as the mass is constant, the following is true $\rho V =$ constant, therefore

$$\frac{d\rho}{\rho} = \frac{-dV}{V} \tag{6.4}$$

Hence Equation (6.5) must be satisfied for any change of volume e.g. when the piston moves, and Q_i and Q_o are the flows in and out of the volume V respectively.

$$Q_i - Q_o = \frac{dV}{dt} + \frac{V}{\kappa}\frac{dP}{dt} \tag{6.5}$$

Considering the electrical equivalent circuit, where the flow is current and the pressure is voltage, Kirchoff's junction rule is applicable and must be satisfied within the model. Thus the other condition on Q that must be satisfied is that all the flows into or out of an intersection must equal zero.

The solution of the flows and pressures within the hydraulic PTO have been calculated following the flow diagram presented in Figure 6.3. The main solution of the PTO model rests on a root finding algorithm that equates the flow from the piston and accumulator to that following either the path through the motor or the pressure relief valve, (Part D). The flow from the

piston is dictated by the velocity of the rod, the area of the cylinder and compressibility of the hydraulic fluid (Part A), whereas the motor and pressure relief flows (Part C) are driven by the pressure difference between the “blocks” upstream and downstream of the motor (Part B). Thus an iterative method is used to evaluate the system until the block pressures that provide adherence to Kirchoff’s junction rule are identified. The Brent-Dekker method has been chosen due to its fast but robust performance by making use of the fast-convergence of the secant or inverse quadratic method where possible, with the bisection method providing a reliable back up. To prevent any unnecessary increase in CPU time due to mixed-language programming and communication between modules, the PTO model has been coded in C++ and compiled alongside OpenFOAM. A description of the methodology and handling of different hydraulic components is given below, and the code is listed in Appendix B.

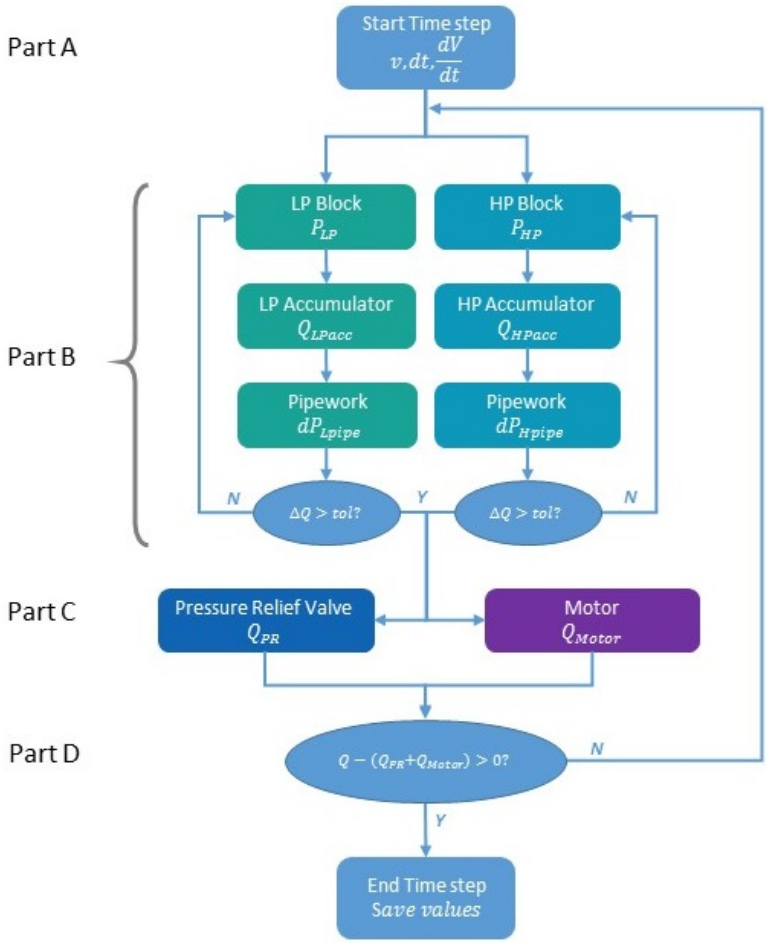

Figure 6.3: Flow chart for in-house PTO model

Motor Assuming an ideal motor, the flow through the motor Q_m and rotational speed ω are related by the motor displacement D, Equation (6.6). The motor and generator torque are equivalent, thus producing a relation, Equation (6.7), between the pressure drop and rotational speed, where C_G is the generator damping. The generator is modelled as a simple rotational damper with varying damping coefficient meaning that the resistive torque imposed by the

generator can be altered by varying this damping coefficient.

$$Q_m = D * \omega \tag{6.6}$$

$$T_m = dP * D = C_G * \omega = T_G \tag{6.7}$$

Substituting Equation (6.6) into Equation (6.7), provides the pressure drop as a function of the flow through the motor, Equation (6.8). Or to incorporate losses through the system, the volumetric and mechanical efficiency of the motor are included in Equation (6.9).

$$dP = C_G * \frac{Q}{D^2} \tag{6.8}$$

$$dP = C_G * \frac{\eta_v Q}{\eta_{mech} D^2} \tag{6.9}$$

Valves The pressure relief valve is included in parallel with the motor to ensure that the motor does not experience a pressure drop in excess of its operational values. The valves permits flow in only one direction, with the valve opening once the pressure differential, ΔP exceeds the cracking pressure. Above this the orifice area increases with the pressure differential until a maximum area is reached, any further increase in the pressure differential then only increases the flow. The flow rate through the valve is calculated with Equation (6.10), where ΔP_t is the minimum pressure for turbulent flow.

$$Q = C_D * A\sqrt{\frac{2}{\rho}} * \frac{\Delta P}{(\Delta P^2 + \Delta P_t^2)^{1/4}} \tag{6.10}$$

Accumulators The inclusion of accumulators typically allows a smaller motor to be used as the accumulator smooths out any perturbations in the flow supplied to the motor as well as increasing the efficiency and storing energy for interruptions. Accumulators are composed of two sections: one gas filled, and one liquid filled, which are separated either by a metal sheet like in the piston type or diaphragm as in the bladder type. They exploit the compressibility of gas, Equation (6.11), allowing the volume and pressure of the hydraulic liquid to vary. The change of volume within the accumulator within a time step is equivalent to the flow into it. For stability it is assumed at each time step that the pressure of the gas is equivalent to that of the liquid at the inlet.

$$P_1 V_1^k = P_2 V_2^k \tag{6.11}$$

The pressure and volume are associated through Equation (6.12), where the precharge pressure P_{pr} of the accumulator is the pressure of the gas when the accumulator is empty of liquid.

$$(P_g + P_A)(V_T - V_F)^k = (P_{pr} + P_A)V_T^k \tag{6.12}$$

Code-to-Code comparison

The solution of a hydraulic circuit in a way such as the one described above is not novel, and a number of commercial software (e.g. Simscape Fluids, Amesim) offer component libraries to model and analyse custom fluid power systems. These port-based approaches facilitate quick

model construction of new systems, and when the required parameters for each component can be obtained, experimentally or otherwise, a good correlation is achieved between the simulation and the test bench (Antolin-Urbaneja et al. 2015). As a comparison for the code developed in house, the same circuit was built in Simscape Fluids, the pressure drop across the motor calculated by both methods is shown in Figure 6.4. The small discrepancy (6.7%) in the range is due to the simplification included in the in-house code of numerically rectifying the flow, rather than solving for the flows within the manifold. The Simscape model uses adaptive time stepping to optimize the performance of the simulation. However, this causes the time step to reduce below $\sim\ 1e^{-11}s$ at the turning points, whereas the in-house code achieved convergence with a constant time step of $0.1s$. The computational time required for the two methods also greatly differs, with Simscape taking $66.11s$ and the in-house code taking $0.257s$ to compute $300s$ of simulation using a single core 2.7GHz intel Xeon processor. In the coupled model, the time step is set by the OpenFOAM solver which also uses adaptive time stepping, though in the simulations conducted for this study the time step did not fall below $1.62e^{-5}s$.

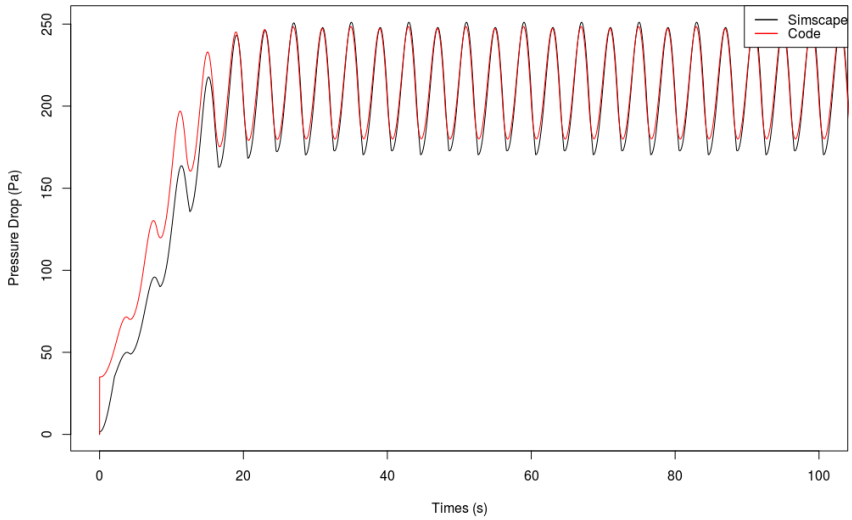

Figure 6.4: Comparison of the pressure drop across the motor calculated by each method.

Coupling Model with CFD

The in-house code has been coupled with OpenFOAM as part of a user defined rigidBody-Dynamics restraint. The inputs required for the coupling are the current time step and the initial estimate of the angular velocity of the paddle from the calculated pressure force on the body. The PTO model uses these to compute the pressure difference across the piston, and the resulting damping moment for such an angular velocity. The solver then iterates until the solution for the time step converges and the simulation proceeds to the next time step where the wave conditions at the boundary are updated. The process diagram for the coupled model is shown in Figure 6.5.

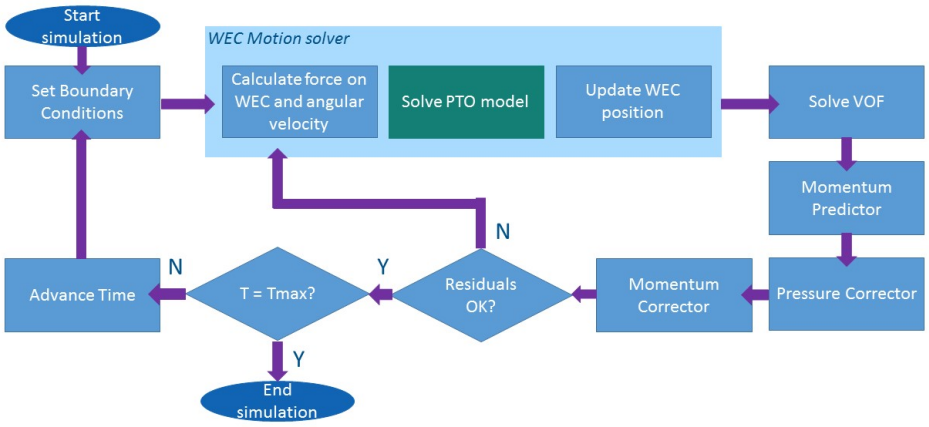

Figure 6.5: Process Diagram of OpenFoam coupled with PTO Model

6.2.3 Comparison of simple and realistic PTO models in CFD NWT

As a comparison of the effectiveness of the higher-fidelity approach to modelling a WEC, three simulations were conducted with the fixed bottom CCell device: one used the simple linear damper, the second a Coulombic damper, and the third used the coupled CFD-PTO model. To calculate the damping force used in the Coulomb case it was assumed that the maximum pressure difference across the piston is 250 bar and that this maximum force would be generated in phase with the maximum angular velocity. Therefore the RMS value of this force, 66kN, was used as the equivalent steady force throughout the cycle. This force was then also used to calculate the equivalent damping coefficient for the linear damper, with the angular velocity specified as the mean velocity for the paddle to move 30 degrees within half a wave cycle. From the description of this procedure it is clear that choosing a single value to represent the PTO circuit is in itself challenging, and would require a number of iterations to achieve the same pitch motion of the device. Each model was run with three different wave conditions that are representative of deployment conditions for the pilot device. One of the wave conditions was purposefully chosen to be lower power (H=0.5m, T=6s) to evaluate the effect of using a constant damping force.

The mean power over the final three wave periods has been calculated by multiplication of the angular velocity of the paddle and the PTO torque at each time step. This mean power is presented in Table 6.1 for each simulation. The increased motion of the paddle calculated by the hydraulic PTO simulation results in an increase in the predicted mean power compared to linear damper, whereas the Coulombic damper simulations consistently predict a lower power output. The least-energetic wave condition produces the largest percentage discrepancy between the different models.

However, there is a computational time penalty for the hydraulic PTO model. It requires 7.9% more time than the linear damper to compute the same number of wave periods in the first wave condition, but 54% more in the low power wave where in general less CPU time is required. The increase in execution times is a result of the larger angular velocity of the paddle

in the hydraulic simulations. OpenFOAM uses adaptive time stepping, which automatically reduces the time step when velocities are larger to preserve the CFL condition and maintain solution stability.

Table 6.1: Comparison of simulation outputs for different models

Wave	Model	Execution Time (s)	% Diff Time	Mean Power (W)	% Diff Power
H=1m T=6s	Linear	56,119	-	2,875	-
	Coulomb	53,928	-3.9	2,724	-5.3
	Hydraulic	60,579	7.9	3,541	23.2
H=0.5m T=6s	Linear	21,526	-	411	-
	Coulomb	20,902	-2.9	48	-88.3
	Hydraulic	33,195	54.2	637	55.0
H=1m T=8s	Linear	69,384	-	2,147	-
	Coulomb	65,180	-6.1	1,306	-39.2
	Hydraulic	75,500	8.8	2,467	14.9

The effect of the different PTO modelling methods is obvious in Figure 6.6, with a marked increase in range of motion for the hydraulic PTO modelling. As previously mentioned, characterising the full system with a single value (either the damping coefficient or the Coulombic force), introduces considerable uncertainty in their choice, and it appears that they are overdamped as the pressure does not reach the maximum value of 250 bar. In particular the Coulomb damper significantly restricts the motion at the initiation of the simulation, when the velocities are low and in the low power wave prevents the device moving at all, Figure 6.7. The constant damping force does not take into account the reduced flows through the system. This also overestimates the stiction in the hydraulic circuit, as the zero crossing points are extended in Figure 6.8. If a variable sea state were modelled with lulls in the wave train, the Coulomb damper method may lead to an underestimation of performance of the device. The simple damper, in comparison does not emulate these static moments at the turning points of the motion, resulting in a more sinusoidal device motion.

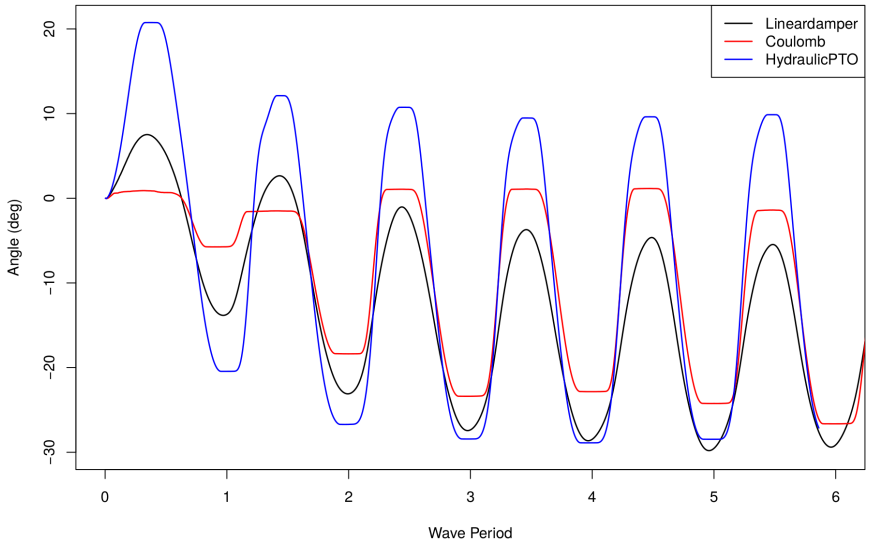

Figure 6.6: Pitching motion of the paddle in a regular wave (H=1m, T=6s)

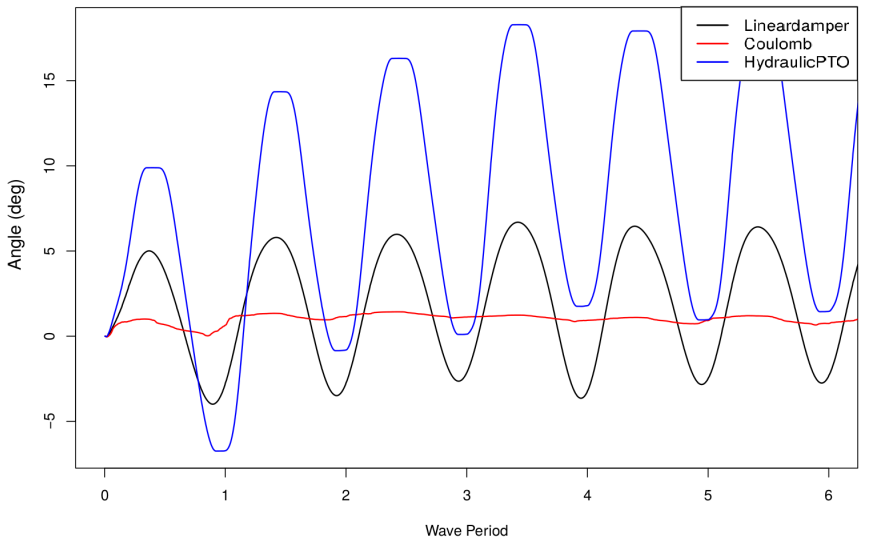

Figure 6.7: Pitching motion of the paddle in a regular wave (H=0.5m, T=6s)

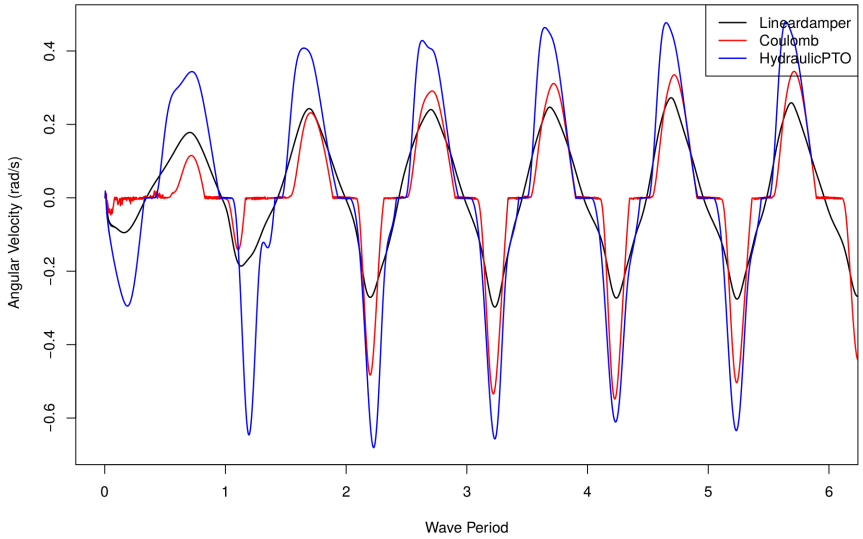

Figure 6.8: Angular velocity of the paddle in a regular wave (H=1m, T=6s)

The importance of a fully two-way coupled simulation is also evident, as the paddle motion calculated by the hydrodynamic model impacts the damping force and likewise the damping force impacts the motion of the device. Both simplistic models underestimate the peak angular velocities, meaning that analysis of the PTO performance as part of a post processing exercise would not provide an accurate representation. This would be particularly problematic if the intended use is to assess the behaviour of the device in more extreme conditions.

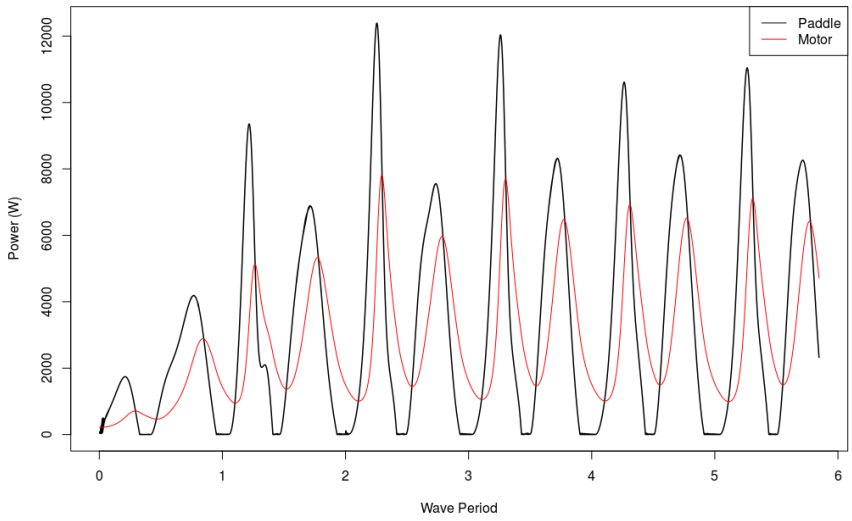

Figure 6.9: Comparison of absorbed power calculated simply ($M_{PTO} * \dot{\theta}$ and as evaluated from the hydraulic motor torque and rotational speed in a regular wave (H=1m, T=6s)

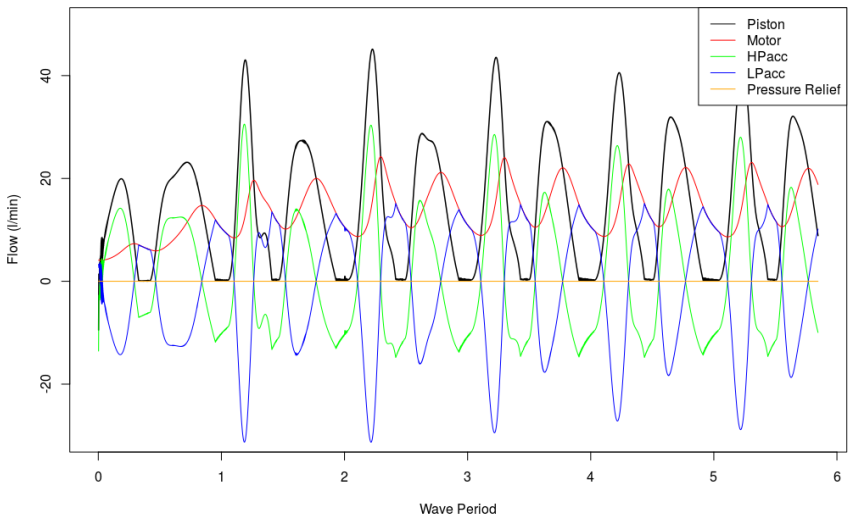

Figure 6.10: Tracking flows through the PTO system in a regular wave (H=1m, T=6s)

The effect of the accumulators is clear in Figure 6.9 where the simple power calculation (as the product of damping torque and paddle angular velocity) is compared to the power output of the hydraulic motor. The power output does not drop to zero when the angular velocity is zero, as the accumulators smooth out these fluctuations by compensating the flow through the motor when there is little to no flow from the piston itself. The accumulator volume and pressure fall when the check valves are closed, thus the speed of the motor reduces as well. The flows in and out of the accumulators is further demonstrated in Figure 6.10, where the sign convention for the accumulators is +ve when fluid is entering the accumulator. There is also a phase shift such that the peak power from the hydraulic motor is delayed in comparison to the peak power calculated from force and angular velocity. The mean power calculated at the hydraulic motor is 3,267W, reflecting a loss of 7.7% compared to the simple power calculation, as the power computed takes into consideration the mechanical and volumetric efficiency of the hydraulic motor and provides a more accurate power to be used within MAEP calculations.

6.3 Bench Test Validation of PTO Model

This section discusses the motivation behind the PTO architecture for the pilot deployment of CCell, as well as the individual specification for key hydraulic and electrical components, and the telemetry system. Assembly of the PTO system for bench testing provided the opportunity to attempt validation of the PTO model. The motor speed profile calculated by a regular wave CFD simulation was used as an input to drive the PTO system, while the hydraulic pressures and output power were recorded through the telemetry system for comparison against the CFD values.

6.3.1 PTO Architecture

In 2018 Zyba shifted focus to a low power commercial application supplying electricity to an artificial reef structure, which uses an electrolytic process to encourage the growth of limestone

and coral to target coastal protection and coral restoration. Cost is a primary motivator for the design of the first deployment in real conditions. To reduce complexity in this initial deployment, the artificial reef is the sole receiver of electricity produced by CCell therefore there is more flexibility with regards to power output, with the reef behaving as a variable energy sink. Real estate within the PTO capsule is also tight, with overall weight significantly impacting ease of installation, as the rest of the device is designed to be installed using only small boats. To address these concerns the bulky and costly high pressure accumulator, which is a key component in the conventional hydraulic PTO circuitry described previously, was removed. Although the use of paired high and low pressure accumulators smooths the power generation, it also reduces the control bandwidth of the system. Therefore, removal of the high pressure accumulator allows increased experimentation and analysis of control algorithms. With integration of a suitable telemetry system, relevant operational data can be collected to provide key learnings for future devices that may prioritise electricity provision to mini-grids.

The inclusion of the low pressure accumulator effectively provides an oil tank to replace any oil lost through leakage from the motor or the piston rod, whilst it also protects against cavitation at the motor. In a variation of the in-house model which excludes the HP accumulator, the low pressure accumulator is modelled as a minimum acceptable pressure in the system. The main effect of removing the high pressure accumulator, Figure 6.11, is that the flow through the motor, and hence motor power, drops to zero in each half wave cycle. These increased accelerations and decelerations will likely erode the lifetime of the system. The maximum motor power output now also coincides with the peak power calculated from force and angular velocity of the paddle.

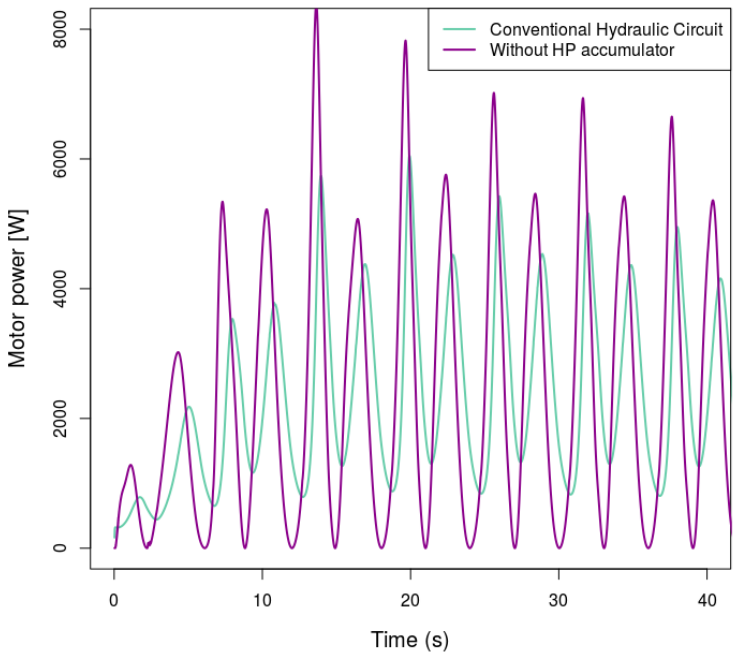

Figure 6.11: Comparison of modelled power output of an hydraulic motor in a circuit with and without a high pressure accumulator.

Figure 6.12 demonstrates the effect of removing the high pressure accumulator with regard to the damping profile that the prime mover experiences. The simple damping profiles, linear and Coulomb damping, are presented alongside that calculated by the PTO model for the conventional hydraulic circuit and that without the accumulator. It is clear that the conventional circuit behaves much like a Coulombic damper, while the system suggested for this deployment is more aligned to the linear profile. Furthermore, it points to the fact that the linear and Coulombic simulations were overdamped in comparison to the fully simulated hydraulic system. It is possible that the hydraulic system could be run in a characteristic condition to provide an understanding of the damping it provides and then, to reduce the time penalty of the PTO coupled simulations, other similar seastates could be investigated using the simplified profiles.

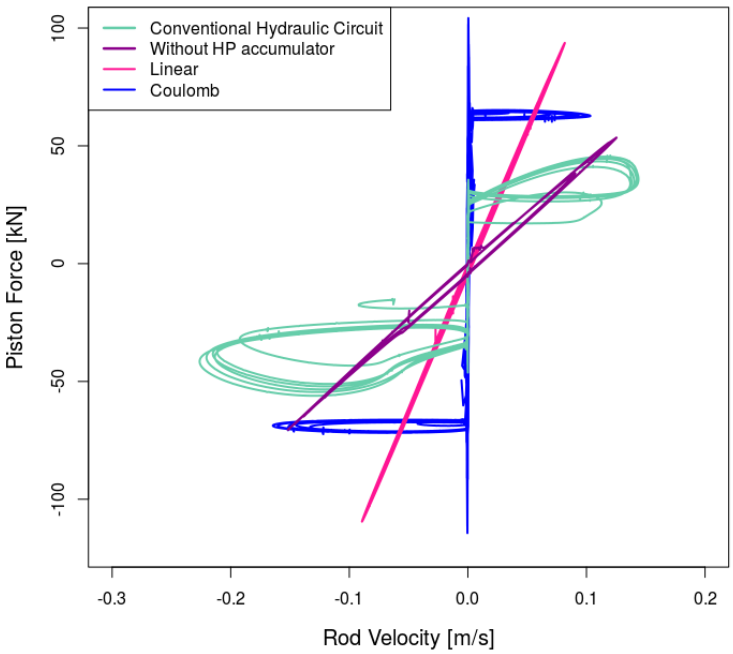

Figure 6.12: Comparison of damping profiles from different numerical representation

6.3.2 PTO Component Specifications

Hydraulic Hardware

Off-the-shelf components were prioritised for the pilot deployment to reduce costs. However, some components had to be designed for the particular application. For example the piston, due to its attachment points and exposure in sub sea conditions, required customisation to ensure longevity and low friction. The piston is a double acting equal-area (or non-differential) piston such that for the same magnitude of rod velocity, it will produce the same fluid flow irrespective of direction. It has a stroke of $510mm$, a bore diameter of $80mm$ and a rod diameter of $40mm$.

Geared hydraulic motors offer a high power density from a simple construction which limits the

cost and servicing requirements of the device. The design principle of a gear motor is that the high pressure fluid drives two gears (one is attached to a shaft, and the other is the "idle" gear) which interface in the middle preventing the recirculation of fluid from the low pressure outlet to the inlet. Physical sizing of the motor is an important consideration. To accommodate the flow, a smaller motor could be used with a higher pressure difference across it, however, a larger motor with lower pressure would achieve a longer life. Initial sizing can be found through Equation (6.7), however, the maximum specifications from the manufacturer must also be considered. The pressure relief valve used in this circuit cracks at $250bar$ and is fully open at $300bar$, thus for it to protect the motor, the motor must be rated to a higher maximum inlet pressure than $250bar$. Furthermore, to allow larger variation in pressures within a wave cycle and, in particular, prevent over pressure at the outlet port, a bidirectional motor was chosen as mono directional motors can often only accept counter pressures of $6bar$.[2] Motors are also designated a maximum rotational speed to prevent accelerated wear. For the series of motors considered for this application the maximum speed is $4000RPM$ (JBJ Techniques Ltd 2016), thus an $11.5cc/rev$ motor is chosen based on Equation (6.6) and the operational maximum piston speed of $0.2ms^{-1}$. The pressure drop across the motor for the required power output is anticipated to be $25bar$, far below the maximum pressure rating of the rest of the components.

The viscosity of the hydraulic oil influences both the mechanical and volumetric efficiency of a hydraulic motor, creating an optimum operating range where overall efficiency is maximised. Frictional losses in hydraulic systems vary linearly with viscosity, thus if the fluid is too viscous the mechanical efficiency will be low. Conversely, if the viscosity of the fluid is too low then internal leakage in the motor becomes an issue and the volumetric efficiency is eroded. Viscosity of the working fluid reduces as the temperature increases and also with age as longer molecules break down. For the chosen motor a viscosity between $10-100cSt$ is recommended. Other considerations for the oil are its environmental qualities and its anti-wear characteristics. Contamination of the hydraulic fluid is the root cause for most early failures of hydraulic motors. The clearances within a gear motor are minimal, thus any particles in the fluid act as abrasive elements eroding exposed surfaces and increasing the number of contaminants. Synthetic oils are more expensive but offer better lifetime and, of primary importance for this application, can be made to be readily biodegradable with low toxicity. The chosen oil has a density of $918kg/m^3$, a Bulk Modulus of $1.529e^9Pa$ and a viscosity of $46.7cSt$ at 40^oC which drops to $8.2cSt$ at 100^oC (Panolin 2016).

Electrical Hardware

Coupled to the hydraulic motor shaft is a generator. Conventionally, a generator is an electromagnetic machine that produces direct current (DC) and an alternator creates alternating current (AC). Though it is common (e.g. in cars) to use an alternator coupled with a rectifier to provide DC as they are more efficient due to the construction. A DC generator has the windings on the rotor and magnetic field on the stator, however the windings are the heaviest part, thus an alternator, which uses the opposite construction, can work at higher speeds and produce more power at lower speeds. For these machines to operate and generate current a magnetic field must first be created. This can be achieved using permanent magnets, which is

[2]For use in an hydraulic circuit with HP and LP accumulators, a mono directional motor would be suitable.

beneficial as no electrical connection is required to the rotor and the magnetic field is always present. However, as well as being costly, they suffer from demagnetisation over time; allow no control over the rotor flux; and produce maximum efficiency only at a pre-defined condition. Alternatively, a magnetic field can be produced from the flow of current as dictated by Ampere's law, which is exploited in electro magnetic generators. This requires an electrical connection to the rotor, and provision of electrical current from an external source e.g. a battery or a smaller permanent magnet alternator on the same shaft.

Two generators were provided for the testing to evaluate their relative performance and applicability to the system requirements:

- the WindBlue DC-520 generator (WindBlue Power 2016), a modified car alternator using a Neodymium rare earth magnet for the rotor with a built in rectifier that provides unregulated DC output. The design is brush-less to reduce friction and increase reliability, and the shaft is stainless steel to provide corrosion protection.
- A custom built electro-magnet generator comprising of four individual alternators connected to the main shaft through a 1:2.5 gear ratio. Additional smoothing is provided from the angular placement of the coils, such that there is effectively twelve phase rectification, with the output from the individual alternators connected in series.

Initial bench testing of the two generators at a variety of rotational speeds and resistive loads provided the expected damping profiles, Figures 6.13 & 6.14 from evaluation of Equation (6.13). It is clear that the custom generator provides more damping and requires a larger torque at lower rotational speeds. This is due to the additional inertia on the shaft and the friction between the gear teeth. However, as the electro-magnetic generator requires a voltage input to excite the coils and generate electricity, at low speeds the excitation voltage could be reduced to regulate the damping experienced by the motor.

$$P = VI = T_m\omega = C_G\omega^2 \tag{6.13}$$

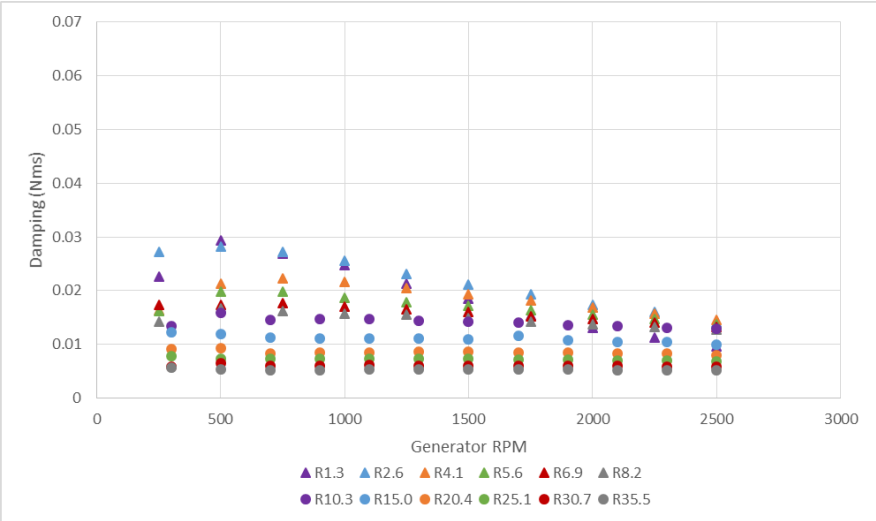

Figure 6.13: Damping profile of the WindBlue DC-520 generator. The series names reflect the resistance of the load bank for each set of tests (R1.3 = 1.3Ω).

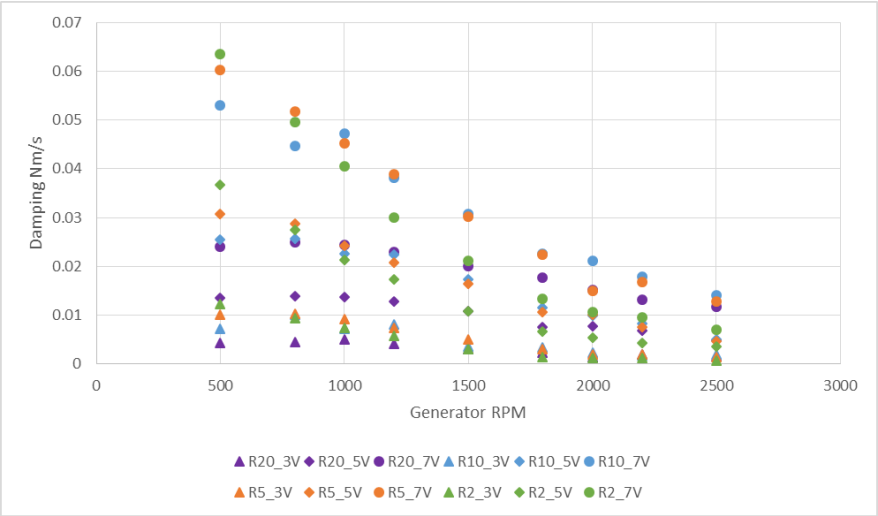

Figure 6.14: Damping profile of the custom EM generator. The series names reflect the resistance of the load bank for each set of tests and the excitation voltage used for the coils (R20_3V = 20Ω with 3V coil excitation).

In the pilot deployment, the CCell device will supply electricity for an electrolytic process to accelerate the growth of a common naturally occurring form of calcium carbonate, Aragonite, on an artificial reef. To drive the electrolysis of sea water a threshold theoretical voltage of 1.23V must be met. Due to activation barriers a slight over-potential is beneficial with the rate of reaction proportional to the electrical charge supplied to the seawater. However, competing side reactions occur and will dominate depending on the over-potential. For example, if the current densities are too high then the concentration of the hydroxyl ions increase and Brucite (a magnesium hydroxide mineral that is soft and structurally weaker) rather than Aragonite precipitates (Goreau 2012).

The output voltage can be controlled through a power converter, to ensure that the voltage remains within suitable limits throughout the wave cycle. In order to achieve this a digital device capable of fast communication and change of state is required. The chosen Power Regulation Module ("PRM") is a high efficiency DC to DC converter, operating from a 36.0 to 75.0 Vdc input to generate a regulated 20.0 to 55.0 Vdc output. This is then followed by a current multiplier to step the voltage down by a further fixed factor of eight. The output voltage of the PRM is set by the TRIM pin such that the output is twenty times the TRIM pin voltage. In order to alter the voltage of the TRIM pin, a digital rheostat is used. The required resistance is calculated with Equation (6.14) before being converted to a digital value and sent to the rheostat chip over the SPI interface.

$$R = R_1 * \frac{V_{trim}}{(V_{ccint} - V_{trim})} - R_6 \tag{6.14}$$

where $R_1 = 10k\Omega, R_6 = 0.68k\Omega$ and $V_{ccint} = 3.28V$

The PRM operation has some hysteresis with regards to acceptable voltages: it requires at least 33V to operate from an off state, but if it is already on then it will continue to operate down to 26V. Similarly, for over-voltage, the device will operate up to 88V if already operating but the input voltage then needs to reduce to 79V to turn back on if the 88V threshold is

exceeded. These thresholds have been included in the graphical presentation of the voltage characteristics for the two generators, Figures 6.15 & 6.16. Considering these limitations on providing useful power to the end load, the custom EM generator has been chosen as it provides more flexibility in the control of its output through manipulation of the excitation voltage. In future iterations, once more data is available from the initial deployment, a PM generator may be reconsidered as altering the voltage output of the PRM is equivalent to alteration of load resistance and may provide adequate control.

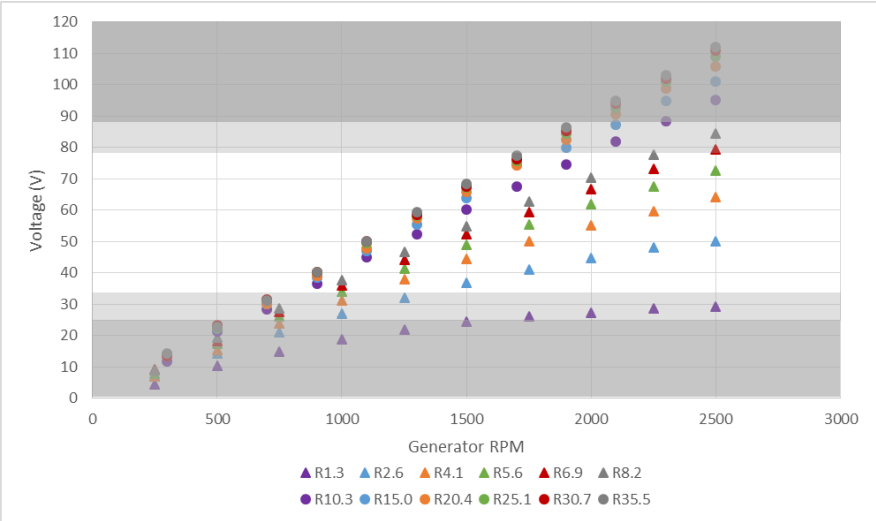

Figure 6.15: Voltage output from characterisation tests of the Permanent Magnet Generator

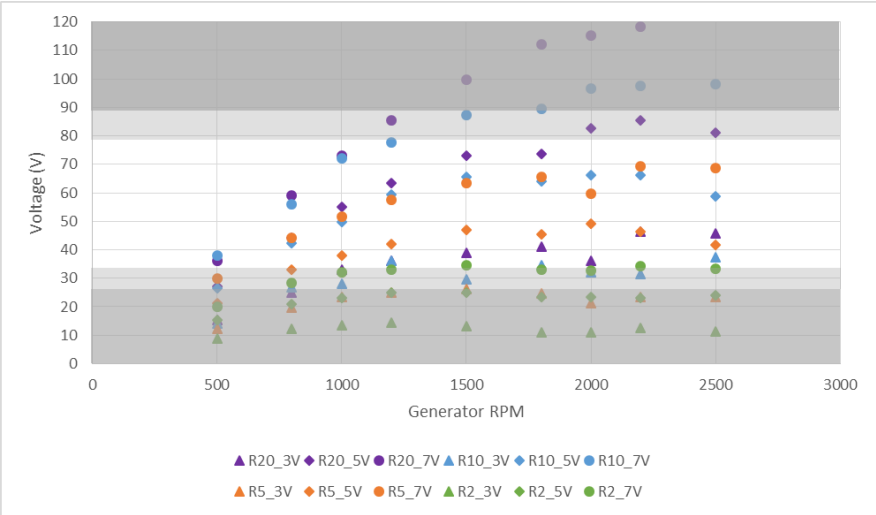

Figure 6.16: Voltage output from characterisation tests of the custom EM Generator

Telemetry

Instrumentation serves a purpose at all stages of development. In prototype testing it is a critical feedback mechanism and data source for future optimisation of operation strategies and for validation of numerical models. In more mature deployments, such as in offshore wind turbines and conventional power plants it provides real time information to liaise with the grid

operator, or can monitor the health of the system to optimise the maintenance schedule. For WECs, the size and accuracy of such a system will be more of a priority than in other more easily accessible power plants as maintenance is altogether more costly in an unforgiving marine environment.

Smaller scale projects that automate sensing and measurement of data have been revolutionised by the advent of small single-board computers and micro controllers such as those developed by Raspberry Pi Foundation and Arduino. These boards provide innovative and easily customisable control solutions at a low cost and low power requirement. The Raspberry Pi is a general-purpose computer that has the ability to run multiple programs, whereas the Arduino is more simplistic and can only run one program on repeat. Together these boards form the basis of the telemetry system for the CCell WEC device in a Master-Slave (MS) configuration, with the Pi operating as the overall control and the Arduino providing data acquisition and implementation of control strategies.

The sensors provide a mapping of the health and output of the system, with current and voltage sensors located at the input and output of the PRM regulator and at the input to the artificial reef. These provide an indication of the efficiency of the power conditioning system and track the power supplied to the reefs. Long-term averages of the pressure measurement on either side of the motor, along with an indication of the hydraulic oil temperature to indicate expected oil viscosity, provide information about the degradation of hydraulic system, including potential oil leaks. Additionally, the difference in pressure can be combined with information from the accelerometer (located separately) to give the damping force and velocity of the prime mover. The specification of each sensor type is detailed in Table 6.2 and they have been selected to minimize power requirement. Generally the sensor and ADC chips interface with the Arduino using Serial Peripheral Interface (SPI), a serial communication interface used for short-distances and is composed of a four-wire bus (serial clock, master output/slave input, master input/slave output, and a device select pin). In order to minimise data handling errors digital values from the sensors are decoded and analysed at the Pi level rather than converting to real values on the Arduino.

Table 6.2: Specification of sensors used within pilot telemetry system

Sensor	Type	Range & Output	Power	Interface	Resolution
High Pressure	Parker PTSB4001B1C2	0-400 bar 0-5V	12V 6mA	12bit ADC with SPI [ADS820]	$\pm$0.2 bar
Low Pressure	Parker PTDVB0601B1C2	0-60 bar 0-5V	12V 6mA	12bit ADC with SPI [ADS820]	$\pm$ 0.03 bar
Hydraulic Oil Temperature	LMT86 precision CMOS temperature sensor with $\pm 0.4^oC$ typical accuracy	150 - 0^oC 0.42 -2.1V	3.3V 5.4uA	12bit ADC with SPI [ADS7044] NB using 1/2 range	$\pm$ 0.1^oC
Current	1mΩ current shunt and Current sense amplifier with 60V/V gain	0-40 A 0-2.4V	3.3V 4.1mA	12bit ADC with SPI [ADS7044] NB using 1/2 range	$\pm$ 20 mA
Voltage	Voltage divider and Current sense amplifier with 20V/V gain	0-90V 0-2.4V	3.3V 2.6mA	12bit ADC with SPI [ADS7044] NB using 1/2 range	$\pm$ 46 mV

6.3.3 Validation Test Set-up

The PTO system used for bench testing is the same design that is intended for deployment. However, a number of alterations have been made to accommodate physical limitations of the laboratory environment. Once deployed, the PTO system will be driven by the CCell paddle, but for this testing an exterior pump has been used to provide the flow of hydraulic oil. The displacement of the external pump is $4.2cc/rev$[3] and it is driven by a 2.2kW three phase AC motor. The piston's hydraulic ports are attached to the flange ports, however, to accommodate the external pump in this installation an additional 3m of 1/2" hydraulic hose have been attached to both. As rubber is thermally insulating it is expected that the hydraulic oil will be hotter in these tests than in operational conditions as the submerged steel piston would provide an additional surface for heat dissipation. This may reduce the volumetric efficiency of the pump and motor as the viscosity of the hydraulic fluid reduces. Finally, the electric load from the artificial reef has been replaced with a passive load bank for the testing.

A block diagram of the test system is shown in Figure 6.17 along with an annotated photo of the physical test system in Figure 6.18.

[3] chosen purely because of its availability

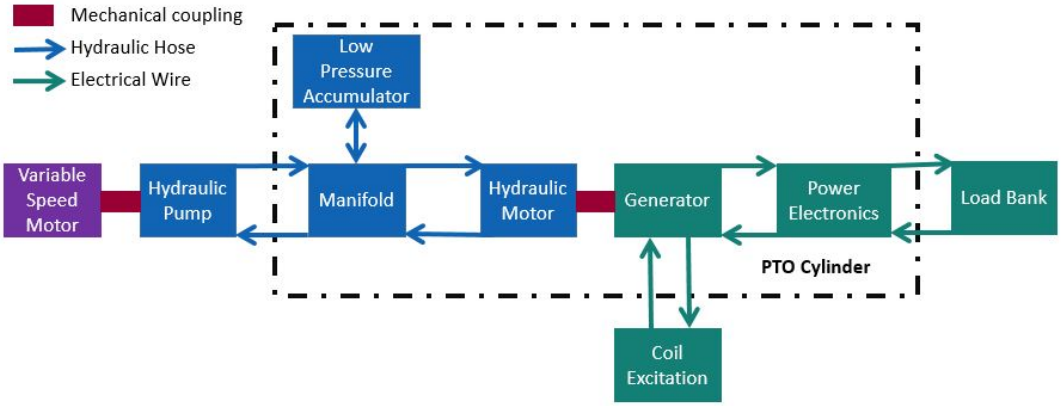

Figure 6.17: Block diagram of test set up for hydraulic and electrical components.

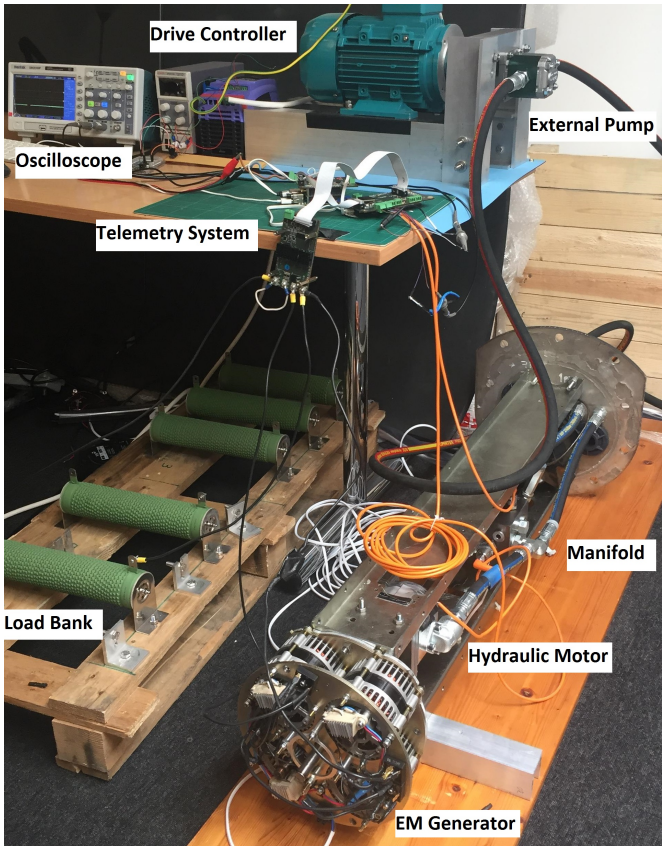

Figure 6.18: PTO test system set-up

Initial commissioning tests of the system involved running the system with a constant flow to evaluate the associated pressure drop across the motor, Figure 6.19. This was achieved by driving the external pump at a series of different rotational speeds. It was assumed that the rotational speed of the generator scales exactly with the ratio of displacements between the external pump and the hydraulic motor (i.e Generator: External motor = 11:4.2). In reality this is not true as there is some leakage flow. However, without a sensor to accurately measure the rotational speed of the generator shaft this relation has been adopted. For ease

of comparison in later analysis, rotational speeds are always given as that of the motor and generator coupling, not that of the external pump.

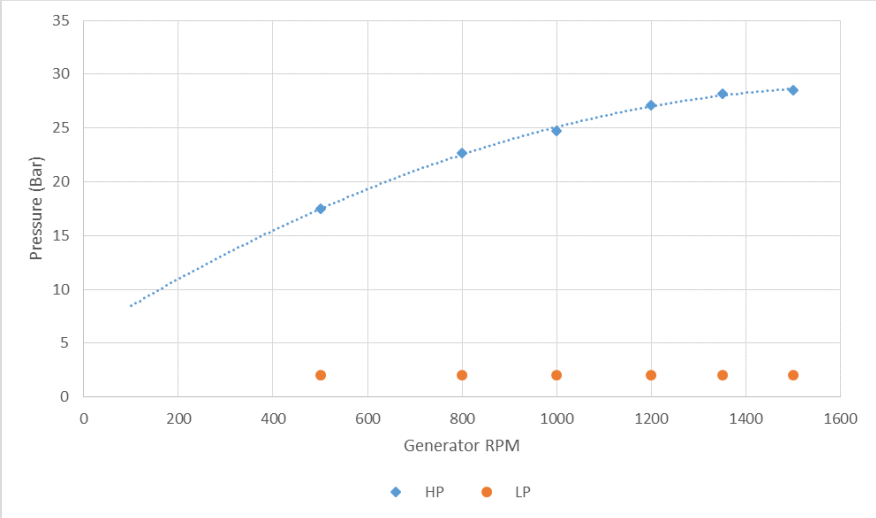

Figure 6.19: Hydraulic Pressures developed in PTO system due to constant flow tests (10 Ohm load and 5V excitation of EM coils)

A regular wave condition, which was representative of the pilot deployment location (T=6s, H =0.7m) was chosen for CFD simulation to calculate the expected generator rotational speed. Variable speed tests were conducted on the PTO system by controlling the external motor to drive the generator at the rotational speed predicted by CFD. This signal was reproduced using Fourier analysis of the stabilised section of the CFD simulation. The ten largest amplitude components were then chosen to approximate the signal, Figure 6.20. A second Arduino due was programmed to control an 8bit digital potentiometer with SPI interface (Microchip 2008), updating its resistance between $0 - 10k\Omega$ in accordance with the fitted RPM signal on every loop through its program. A 10V potential was connected across the end terminals of the potentiometer and the wiper was used as the analogue input voltage signal to a variable frequency drive (Invertek Drives 2016) to operate the exterior motor.

The damping value used for the tests was chosen to ensure that the rotational speed of the external motor did not exceed the maximum value of 6000RPM. This equated to a constant generator damping value of 0.03Nm/s for the CFD tests and in the physical tests a load of 10Ω was used with an excitation voltage of 5V, as according to Figure 6.14 this is the closest approximation from the values previously tested. The telemetry system was set up to record the generator voltage and high and low pressures within the manifold at a rate of 10Hz.

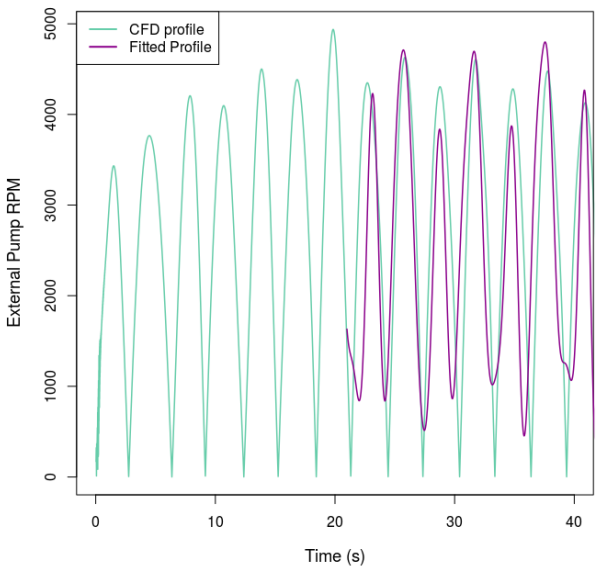

Figure 6.20: RPM signal provided to controller from Fourier Analysis of CFD predicted speed profile.

6.3.4 Validation Results & Discussion

The system and power output are characterised by two values: the flow, which translates to generator RPM, and the pressure difference, which stipulates the damping force that the prime mover experiences. These validation tests used a specified flow as the input allowing analysis of the resulting system pressures to evaluate the accuracy of the PTO model. The pressure recorded by the high pressure sensor (red line) in the physical test is compared to that predicted by the CFD simulation (purple line) in Figure 6.21. Although the general trend in the data is comparable, the CFD data fails to predict the high frequency components and spikes in pressure. This may be because of the dynamic nature of the system, which has been modelled as quasi-static and ignores, for example, the dynamics of check valves or right angled bends for simplicity. However, it is the gradient of the rising pressure line which differs most significantly to that predicted by CFD, whereas the deceleration profiles are much closer aligned. This suggests that the starting or acceleration torque is the parameter which is poorly defined.

To test this hypothesis the variation of the hydraulic pressure on the high pressure side of the manifold has been calculated for the RPM profile using the pressure curve fitted from the constant RPM tests in Figure 6.19. These results are much closer to that predicted by CFD, though the flattened peaks of the calculated data (black line) may be unfounded, as the constant pressure tests only considered rotational speeds up to 1500RPM, whereas the variable RPM test incurred a maximum 1878RPM.

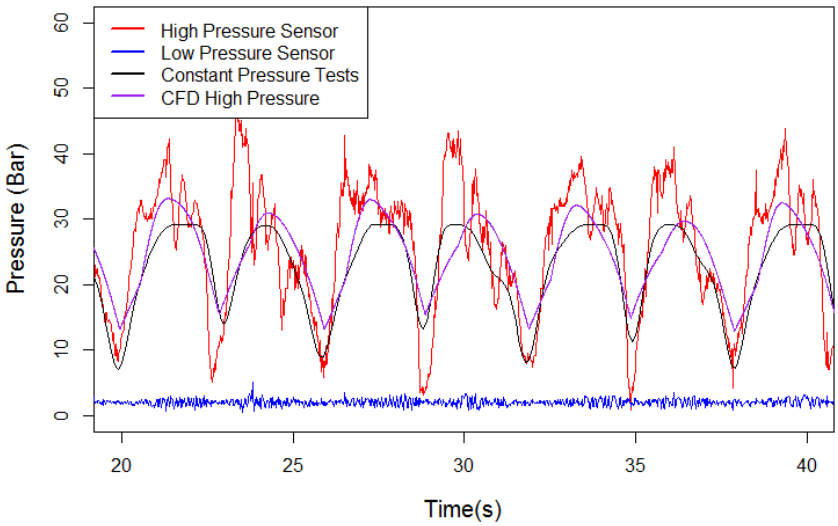

Figure 6.21: Comparison of predicted and recorded Hydraulic pressures (M5 wave with "high" damping)

To further test the hypothesis that the system dynamics during rapid accelerations are the source of the discrepancy, the control signal for the RPM was scaled with respect to time, so as to reduce the accelerations experienced. The frequencies of the Fourier components were reduced to a quarter of the initial values and the results were then plotted alongside the previous "fast" results but with a t/4 scale, Figure 6.22. This provided a much closer comparison to the CFD values. It should be noted that the speed signals differ slightly between the CFD and physical tests due to approximations made in the Fourier analysis, however, the gradient of the pressure change as the generator accelerates is still steeper in the "slow" physical tests.

The hydraulic motor and generator coupling are represented by an analytical model that calculates the leakage flow and frictional torque at each condition rather than relying on an efficiency parameter. It is the frictional torque τ_{fric} that impacts the pressure drop across the motor:

$$\tau_{fric} = (\tau_{noload} + K_{TP}\triangle P)\overbrace{tanh\left(\frac{4\omega}{\omega_{nom}}\right)}^{B} \tag{6.15}$$

where K_{TP} is the proportionality constant between friction torque and pressure drop, τ_{noload} is the minimum torque required to turn the motor shaft and ω_{nom} is the standard operating condition at which the motor performance is characterised. The output torque ($\tau_{out} = C_G\omega$) is thus the difference between the ideal torque ($\tau_{ideal} = D\triangle P$) and the frictional torque, which can be rearranged to provide a relation between pressure drop and rotational speed:

$$\triangle P = \frac{C_G\omega + \tau_{noload}B}{D - K_{TP}B} \tag{6.16}$$

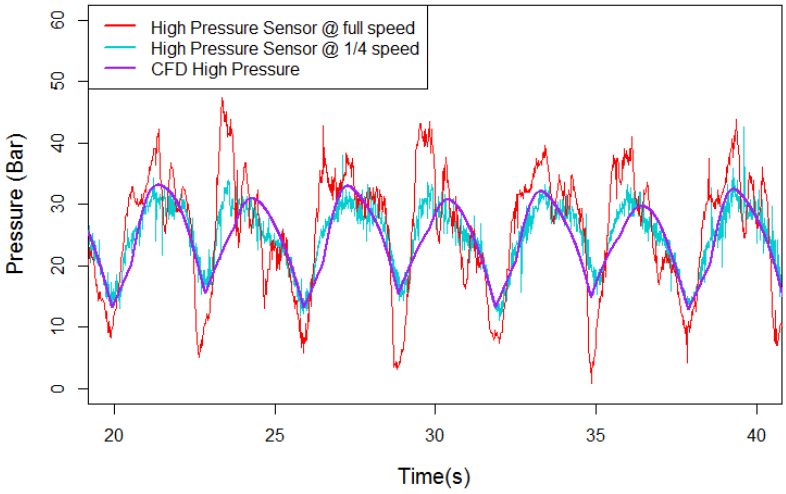

Figure 6.22: Impact of motor acceleration on recorded high pressures

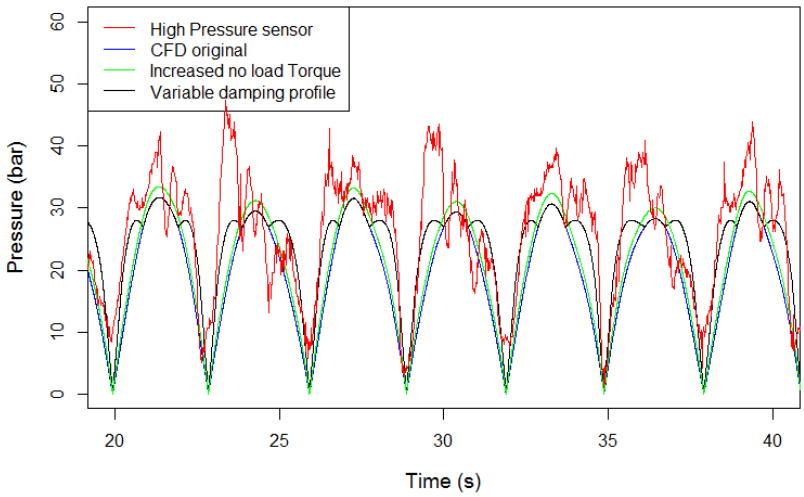

Figure 6.23: Sensitivity analysis around parameters affecting pressure drop across the hydraulic motor

Considering Equation (6.16), the two main influencers on the pressure drop are the generator damping value and the hydraulic motor parameters K_{TP} and τ_{noload}. Figure 6.23 compares the impact of these parameters for the given speed profile, as there is a degree of uncertainty surrounding their appropriate values. The “Increased no load torque” test case represents a fivefold increase in both the K_{TP} and τ_{noload} values, however, this alteration only affects the peak value. The “Variable damping profile” adopts a staged generator damping profile, with generator damping values doubled for rotational speeds below 500RPM and then slowly ramped down to the $0.03Nm/s$ baseline, Figure 6.24. Clearly the assumption that the generator damping is constant is a weakness of the PTO model, the generator damping is greatly

affected by its rotational speed. Although choosing a constant damping value for rotational speeds below 500RPM may appear bold when compared to the real generator damping profile, it seems that a better estimate is unnecessary. The heightened generator damping value at low rotational speeds creates a pressure profile that aligns very closely to the rate of pressure increase recorded in the physical tests. Furthermore, implementation of an accurate generator damping profile within the PTO model is likely to hamper stability of the simulation due to vast changes in damping for only a small change in the rotational speed.

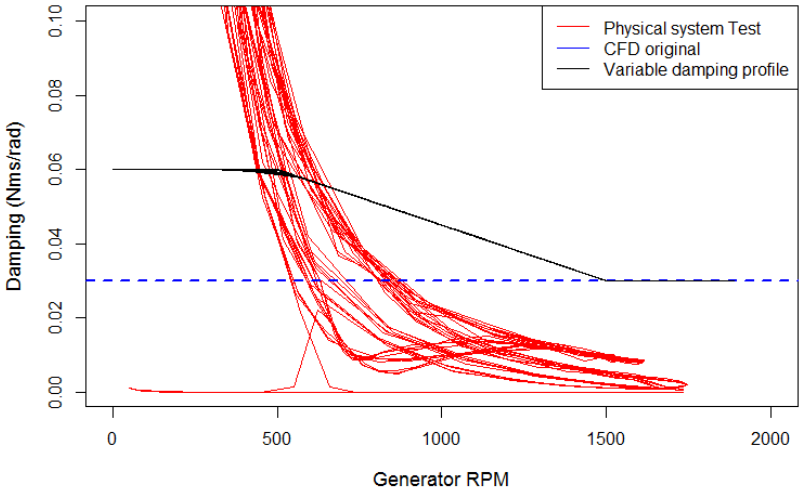

Figure 6.24: Damping profile from physical testing (M5 wave with “high” damping)

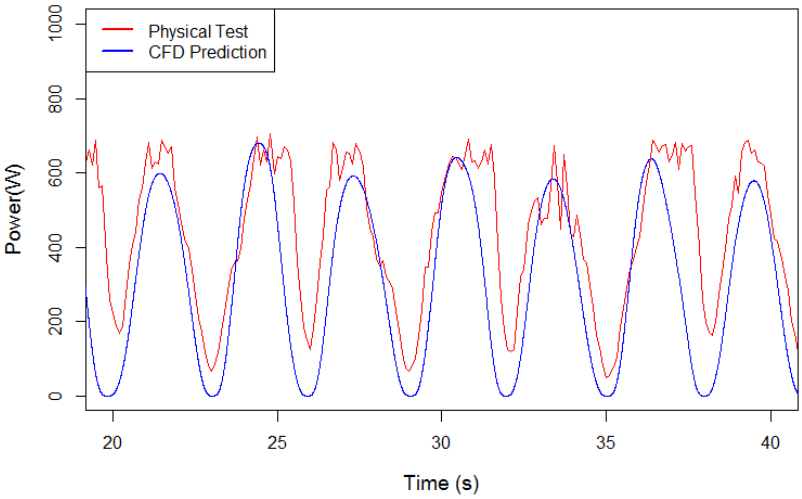

Figure 6.25: Comparison of predicted and recorded output power (M5 wave with “high” damping)

Although the power output is a secondary variable that, in the physical test, is predicated by the

rotational speed of the generator, it is still interesting to compare its value against the predicted values, Figure 6.25. The power output calculated by the model does not take the conversion from mechanical to electrical energy into consideration. A generator efficiency profile with respect to RPM was obtained from the initial bench testing of the EM generator and has been used to scale the CFD data appropriately.

The power curves predicted by CFD are not as broad as those measured in the physical tests, suggesting that the inertia of the system is not fully captured. Calculating the average energy in a wave cycle from both the physical and CFD data, it was found that the CFD under-predicts the power capture by 28.7%. If the “slow” version of the physical test is used, this reduces to 19.4%.

6.4 Chapter Conclusions

This chapter has focused on how the energy harnessed by the prime mover of the WEC is converted into useful electrical energy. For most devices this is a two stage process, transforming either a linear motion into a rotational motion, or increasing the velocity of an already rotational motion, so that a conventional generator can be used to generate electricity. The most robust and mature offering, with considerable power density is a hydraulic PTO. For an OWSC like CCell, this would be connected to the prime mover by an hydraulic cylinder driving the fluid through a motor. A conventional hydraulic system employs an accumulator on either side of the motor to smooth the flow and ultimately the electrical output. The effect of the accumulators is to provide a near constant pressure difference across the hydraulic cylinder. An alternative hydraulic circuit, without the high pressure accumulator, was proposed for the initial deployment of the CCell device, to provide both cost and space savings. In order to analyse the effect of this alteration a PTO model was developed and successfully coupled to OpenFOAM. It was found that the conventional hydraulic circuit could be represented by a Coulombic damper, whereas the new circuit behaved more like a linear damper. However, in lieu of a high fidelity PTO model it is difficult to choose an appropriate value for either the damping coefficient or force, to characterise the whole PTO system. Improper selection of these parameters may drastically alter predicted power output or motion of the device, though they are useful in initial specification and sizing of the hydraulic system.

The pilot PTO was built and the initial commissioning tests provided the opportunity to validate the PTO model. The PTO model was set up with the parameters specified for the individual components and output the predicted generator RPM signal for a regular wave (T = 6s, H= 0.7m). The PTO system was then driven so as to replicate the generator RPM and the power and hydraulic pressures were recorded and compared to those output by the CFD simulation. In the absence of rapid accelerations the PTO model predicted the pressures accurately, however, further work is required to incorporate the system dynamics and variable damping profile of the generator.

Chapter 7

Extreme Loading of a WEC

Survivability is a key metric for marine renewable energy devices as extreme forces are a key cost driver in their design. Therefore, a greater understanding of the hydrodynamics and the transmitted structural loading is required throughout the design process to prevent premature device failure. This chapter considers observations and learnings from early lab testing (for more details see Section 4.2.1) conducted in 2016 by Zyba engineers, including the author, with the floating CCell concept. This guides the development of three key studies in the CNWT which are expected to generate peak loadings and stresses on the system. These include:

- Occurrence of slamming and the pressure distribution within such an event.
- Effect of directional waves and impact of design measures to mitigate transverse loading.
- Identification of the maximum wave envelope for the deployment location and specification of design cases.

7.1 Device Failure and Design Criteria

To promote survivability in the design of a structure in the marine environment an understanding must first be established as to how the device may fail. Appropriate safeguards and design criteria can then be developed to safeguard against these failure modes. A Failure Mode and Effects Analysis ("FMEA") systematically identifies possible failure modes and root causes throughout a system and estimates their relative risk with regards to probability of occurrence, consequence and method of detection. The outcome of the FMEA can then be fed back into the design process to limit or avoid risk.

An initial high level assessment of the likely failure modes of CCell's four main subsystems are given in Table 7.1 together with a list of possible root causes in Table 7.2. One area of concern is the bonding of composites to non-composite materials as there is limited experience or understanding of long-term behavior of the material when submerged and exposed to consistent cyclic loading, ultimately this may lead to the fracture or detachment of the prime mover. Mitigation measures are primarily through design however, selection of manufacturers and addition of suitable test programs such as destructive testing can also reduce uncertainty and

risk during the development process. Once installed, regular maintenance and inspections, as well as remote monitoring to detect material failures can reduce the possibility or severity of failures. This analysis is in no way comprehensive, it merely exemplifies the scale of variety of eventualities that must be considered in the detailed design of a WEC. Furthermore, this is only the first stage of the FMEA, the second part is more arduous as lack of operational data raises uncertainty surrounding the risk analysis. For many components, reliability data must be borrowed from other industries, attributing a conservative safety factor to acknowledge the mismatch of applications or environments. Although not all failures can be de-risked through numerical modelling, there are a number that can be better informed through appropriate techniques. Comprehensive de-risking methodologies are critical for the wave industry to progress.

Table 7.1: Failure Modes associated with the CCell WEC

Prime Mover	Hydraulics	Electronics and Instrumentation	Support structure
Seized Bearings	Oil Leak	Uncontrolled Power Supply	Uprooting
Misalignment	Loss of Pressure	Electrical Short	Structural Failure
Fracture	Loss of Torque	Generator Overload	Incorrect Orientation
Detachment	Breach of watertight enclosure	Battery Failure	Deformation
Lack of Buoyancy	Seal failure	Communications Failure	

Table 7.2: Root causes of failure associated with the CCell WEC

Mechanical	Electrical	Structural	Environmental	Hydraulic
Mechanical Overload	Conducting debris	Material Defect	Biofouling	Contamination
Vibrational Fatigue	Insulation degradation	Manufacturing Defect	Collisions	Overpressure
Poor thermal management	Calibration error	Design fault	Entanglement	Insufficient Lubrication
Connection Failure	Software Design Fault	Installation Error	Corrosion	Hose Puncture
Maintenance Error	Soldering defect	Exceeded limit state	Scour	Maintenance Error
	Loss of connection	Fatigue	Sediment Deposits	

A recent study of a particular WEC's failures over three years (Kenny et al. 2017) found that a number of major structural and hydraulic failures occurred soon after deployment and were

under-predicted by the FMEA. These were attributed to a range of human error, design faults and assembly errors. It also noted that failures due to corrosion, wear or fatigue, which are more likely to occur at the end of the service life of a device, were over-predicted (perhaps unsurprisingly given the length of the deployment). The lack of accuracy in the failure predictions from the FMEA and prevalence of design faults suggests that the modelling methods used did not sufficiently capture the device interactions to assess the relevant failures.

The life of a WEC can be severely shortened without a full understanding of the impact of operational and extreme loads on the device. Limit states are often used in structural and offshore engineering as a method of specifying design criteria and ensuring the functionality and safety of a structure. They are conditions beyond which a structure is no longer fit for purpose as it does not fulfil the criteria of design. These are classified into four categories, (International Electrotechnical Commission 2016):

- Serviceable Limit States ("SLS") encapsulates normal operation within observed limits such as deformation, corrosion or excessive motion beyond what is permitted by e.g. PTO or moorings.
- Ultimate Limit States ("ULS") are associated with the maximum load-bearing capacity of the structure. The limits may be component deformation or buckling, loss of static equilibrium or sinking.
- Fatigue Limit States ("FLS") corresponds to cyclic loading and cumulative damage due to repeated loads.
- Accidental Limit States ("ALS") represents accidental or abnormal loading that for example offshore structures manned by personnel would need to maintain sufficient structural integrity to allow evacuation.

To ensure that the structural members of the device meet the criteria for the SLS or ULS, a prediction of the maximum expected loading must be calculated. Large uncertainty and associated financial risk surrounding these loads may lead to an overly conservative design, therefore accuracy is key. However, prediction of extreme loads is one of the most difficult components of the design process for WECs. Firstly, relevant conditions must be determined that will produce a characteristic extreme load. Secondly, the device response must be evaluated, but these extreme conditions are at the limit of what is possible in modelling techniques. As mentioned in Chapter 3, physical modelling is not sufficient to evaluate extreme conditions due to the scales at which the tests must be performed. Laboratory tests are limited by the ability of the wave makers to generate the steepest waves, resulting in scales of $\sim 1:45$ being used (Paulsen et al. 2019). Similarly, linear codes are ineffective as such analysis falls far outside the realms of where the linear assumptions are valid. In extreme conditions with steep waves, complex wave-structure interactions and non-linearities become increasingly important. Therefore, CFD is well placed to improve confidence in design responses and loads, reducing previously over-inflated safety factors and unnecessary structural costs employed to ensure device survival.

For devices that are constructed from composites, CFD is additionally valuable. With a much wider scope in the material design process composites provide versatility in the structural composition: additional layers can be added at critical points to provide strength; discontinuities

in section thickness can be eliminated with a gradual change in layering between the varying sections; and alignment of fibres can dissipate stresses from regions of high-load. To ensure an efficient design, a higher level of modelling and understanding of local stress concentrations is required to analyse the fatigue life due to the high cyclic stress profile experienced by coastal structures. This can be provided by coupling the output of CFD simulations for key design cases to composite modelling software such as that included with ANSYS. The pressures on each cell face of the paddle as calculated by OpenFOAM are mapped with a ray tracing function to the STL mesh of the structure in ANSYS to obtain the corresponding stresses. The output of this coupling is used to inform the structural design team in the selection of an appropriate composite lay up to ensure the design meets the limit states. This could be used with an individual extreme event to inform the SLS or ULS, alternatively it could be used to evaluate the FLS if output from a range of operational conditions is coupled with the distribution of sea state occurrence.

7.2 Wave Slam

Slam loads are encountered in many marine engineering problems: wave impact on a stationary wall; the underside of ships and boats impacting on the water surface due to their bow pitching over waves; or water entry of a life-raft. All of these can be characterised by increased magnitude of loading over a limited temporal duration, usually preceded by a significant relative motion.

In Peregrine's review of wave impact on walls (Peregrine 2003), it was demonstrated that during a slam event the peak pressures greatly exceed those that are explained through wave theory. Due to the short time-scales, in the range of 10-100ms at full scale, these peaks must be dominated by inertial effects rather than gravity. It was also found that the most violent impacts occurred when the incoming wave was on the brink of overturning, with a near vertical front face. However, the impact with the wall is not "flat". The preceding trough is rapidly filled by the incoming wave, thus reducing the vertical face of the wave, and eventually the free surface converges accelerating the water close to the wall into a vertical jet. Peregrine termed this "flip-through", noting that the water jet originates from a small region of high pressure without an actual impact occurring. Also as the effect is not due to gravity, "flip-through" may appear at any rigid boundary, vertical or otherwise.

Wave impact on a stationary wall is strongly influenced by the shape of the wave. However, unless the PTO seizes and the WEC is stationary, slamming on a WEC is also dependent on the device motion which in turn is affected by the incident wave. The full-scale prototype Oyster device experienced slamming events in rough seas states, leading to multiple studies being conducted to characterise and understand the implication of these events. Using a high speed camera to capture the event in a lab setting at 40^{th} scale, Wei et al. both validated a CFD model (in Ansys FLUENT) and investigated the physics of the slamming process (Yanji Wei, Abadie, et al. 2016) .

They surmised that the process initiates with the paddle furthest shoreward and any residual water running back down the seaward face. The restoring moment from buoyancy then induces the paddle to begin pitching seawards, further accelerating the down rush of water on the seaward face. The downward momentum of this water causes a drop in surface elevation on

the seaward side of the paddle, which is exaggerated by the paddle blocking the reversing flow in the wave trough. As the water level is reduced so is the resistance to the paddle's motion, resulting in a large angular velocity. Wei et al. estimated that this portion of the event lasted a quarter of a wave cycle, conversely the second stage in which the impact occurs lasts just one tenth of a wave period. The paddle then interacts the water surface inducing an impulsive torque loading and generating a water jet. As the torque reaches a peak, the paddle quickly decelerates ending with the paddle in the most shoreward position. Unlike wave impact on a stationary wall, this slamming event occurs ahead of the wave crest.

For a flat paddle the small contact angle between the water surface and the flap, was found to strongly influence the pressure impulse, much like how shallow angled wedges undergo smooth water entry while broad angled wedges experience slam, (Renzi, Y. Wei, and Dias 2018). The following section is dedicated to investigating whether the same slam phenomena is observed for a curved paddle and how it might be characterised. Initially this involves scrutiny of laboratory data, and then the CNWT is used to provide further insight into the wave-structure interaction during such an event.

7.2.1 Lab Testing of Floating CCell Device

It is conjectured that a water entry event for a curved paddle would be quite different to that of a flat paddle. The entire width of the flat paddle has to break the water in order to enter, where as the "wings" of the curved paddle break the surface of the water creating an entry point for the rest of the body. The resultant resisting force of the water increases with the surface area of the object hitting the water, therefore the curved paddle impulsive loading should be much smaller. However, when considering the above description of slamming for a flat paddle, this may have little consequence. As discussed previously, the curved paddle creates a larger difference in water height between the seaward and shoreward face in a trough. Furthermore, when the paddle pitches shoreward, the curvature of the paddle encourages the water on front surface of the paddle to collect at the core. This may further contribute to the localised enhanced trough when down-rush occurs.

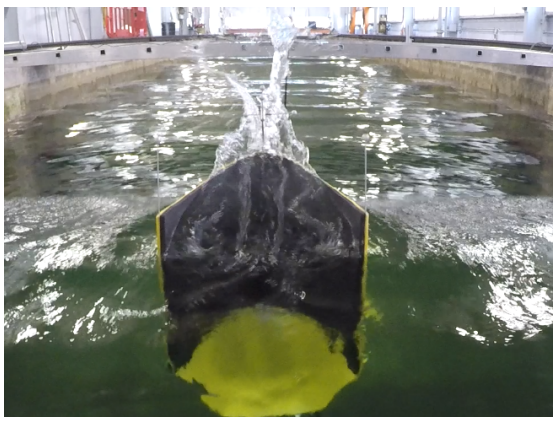

Figure 7.1: Still image of a slam event from lab testing (Irregular wave Tp = 1.98s, Hs = 0.167m, 1/15th scale)

Analysis of laboratory tests conducted with the floating concept, indicates a few special conditions that induced potential slamming events. These slamming events have been identified by

selecting runs with steep waves (either in regular or irregular seas) and analysing the relevant video footage for the characteristic water jet, Figure 7.1, at times when the paddle moved with large angular velocity.

The aim of the lab testing was to provide a baseline output of the device, when no control system was employed, to understand the hydrodynamic efficiency of the prime mover. Prior to the final performance tests, the "optimal" damping for each wave case was selected by slowly stepping through the levels of damping and analysing the results to identify the case that provided highest power output. In the tank testing damping was provided by poppet needle valves controlled by solenoids to resist the flow of hydraulic oil from the piston, offering maximum damping when fully closed and minimum damping when fully opened[1].

It was only during these preliminary damping tests that slamming was observed in regular waves with a steepness of $ak = 0.164$. This occurred in two distinct situations:

- When damping levels were altered causing sudden changes in the paddle's angular velocity.
- Low levels of damping, which caused the paddle to oscillate around a more shoreward mean position.

The former will not be considered in the subsequent analysis as the variations in damping levels convolute the problem by adding another variable with which to contend. The fact that slamming otherwise only occurred in regular waves when it was lightly damped aligns with the idea that an undamped device would be the worst case scenario for slam (Henry et al. 2014). With no restraint against the device's motion, larger angular velocities would develop prior to impact.

Slam was also identified in irregular long-crested waves where wave steepness of the individual wave exceeded $ak \approx 0.155$, however, it only occurred in the second or third wave in a consecutive train of large waves. The preceding large wave pushes the device shorewards inducing a restoring torque due to buoyancy, then in the large trough the paddle accelerates seawards, increasing the relative velocity between the paddle and next wave crest. Depending on the incoming wave face, there is a slamming event. Interestingly, although the waves were steeper and angular velocities higher in the regular wave slamming events, they produced much smaller and less violent water jets than those created in the irregular wave case (compare Figure 7.2:F with Figure 7.1). This suggests that, like for wave impact on a wall, the wave shape and turbulent effects from the previous wave are also important parameters as non-linear response is caused by the influence of memory to preceding time series.

[1] A further description of the tank testing is given in Section 4.2.1.

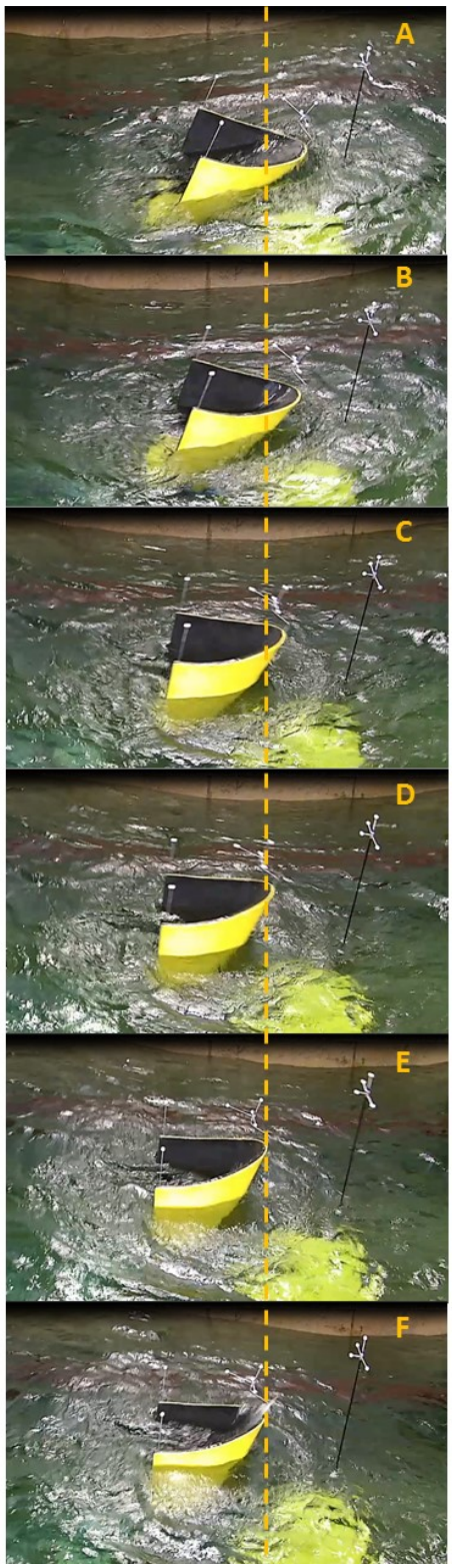

Figure 7.2: Photographic series from tank testing depicting a slam event in regular waves (T = 1.936s, H = 0.3m). A: Paddle in most shorewards position, B: Water rushing down seaward face, C: Minimum water elevation inside paddle, D: Water is entrained from the sides, E: Inception of water jet, F: Paddle in most seawards position and water jet full formed.

7.2.1.1 Slam in Regular Waves

Figure 7.2 shows the main stages leading up to and during a slam event in a regular wave. It starts in the same manner as that described by Wei et al, in the most shorewards position [A]. As the previous wave crest passes and the restoring moment is able to overcome the torque due to dynamic pressure, the paddle begins to right itself with water rushing down the seaward face [B]. A relatively wide flat paddle is less likely to be greatly impacted by 3D effects, however, because of the curvature and narrow width, these are important for the curved device. This is observed as the direction of flow reverses and the down rushing water creates an exaggerated trough on the seaward side [C], the difference in water elevation forces water around the edges of the wings which is entrained into the centre of the paddle. These opposing vortices meet in the centre, causing a ridge of water at the centre line [D], which is enhanced by the incoming wave crest. A “flip-through” like event, as coined by Peregrine (Peregrine 2003), then occurs to initiate the water jet [E]. The incoming wave crest continues to build and the water jet fully develops as the paddle begins to reverse its direction of motion from the most seawards position [F]. One of the obvious differences to the slam event described for a flat paddle is that the curved paddle and water surface do not appear to have a small contact angle. The surface of the curved paddle is sloped away from the water surface.

Figure 7.3 is a combined plot showing the position, velocity, force and surface elevation during multiple slam events in a regular sea. A shorewards direction is indicated by a positive angular position or velocity, similarly a positive force is by convention towards the shore. The surface elevation was captured by a sonic wave probe positioned “inline” with the device, as indicated in Figure 4.6. However, as the device dynamically pitches about its PTO hinge as well as the mount on the sea bed, it is not truly inline. Therefore, its use is purely indicative and no absolute conclusions regarding effect of surface elevation can be drawn from it.

From the PTO force plot it is not immediately obvious that a slam event has occurred. Unlike in the analysis conducted with a flat paddle (Henry et al. 2014), where a slam event increased the recorded pressure by over 300% and (Yanji Wei, Abadie, et al. 2016) found a similar percentage increase in torque, there is only a small increase in the force on the piston. There are four main hypotheses for the lack of distinguishing peak force:

- According to other literature regarding wave slam (Renzi, Y. Wei, and Dias 2018), a sampling rate of at least 1-10kHz is required to capture the pressure impulse as the peak pressures act for approximately only 1 ms. However, the sampling theorem requires that a signal be sampled at at least twice the highest frequency that is present in the signal (Blahut 2002), therefore the minimum sampling rate to capture a 1 ms is 2kHz. Henry et al (Henry et al. 2014) reported using a sampling rate of 3.96kHz for their data acquisition system. Unfortunately this was not possible during the tank testing and measurements were recorded at 100Hz, therefore it is likely that the true peaks are not completely resolved, as this limited the capture to events of 20ms.
- Whether or not the event is captured is also dependent on the natural frequency of the instrumentation. A pressure transducer typically has a high natural frequency which results in a response time of < 1ms, however, a strain gauge type force transducer, as used in this tank testing, is much less stiff and has a slower response time. The proximity

of the forcing oscillation and the natural frequency of the instrumentation can also impact the accuracy of the measurement.

- The geometry of the paddle is such that in moderate slam events, the effect is so localised that it has minimal impact on the overall force. However, it would be detected by a pressure probe placed on the surface of the paddle and remains of importance to the composite design of the paddle.
- To ensure sufficient buoyancy in the scale model, a layer of foam lined the seaward face of the paddle. It is likely that this dampened any impulse effect, reducing any additional force that would otherwise be recorded by the in-line force transducer.

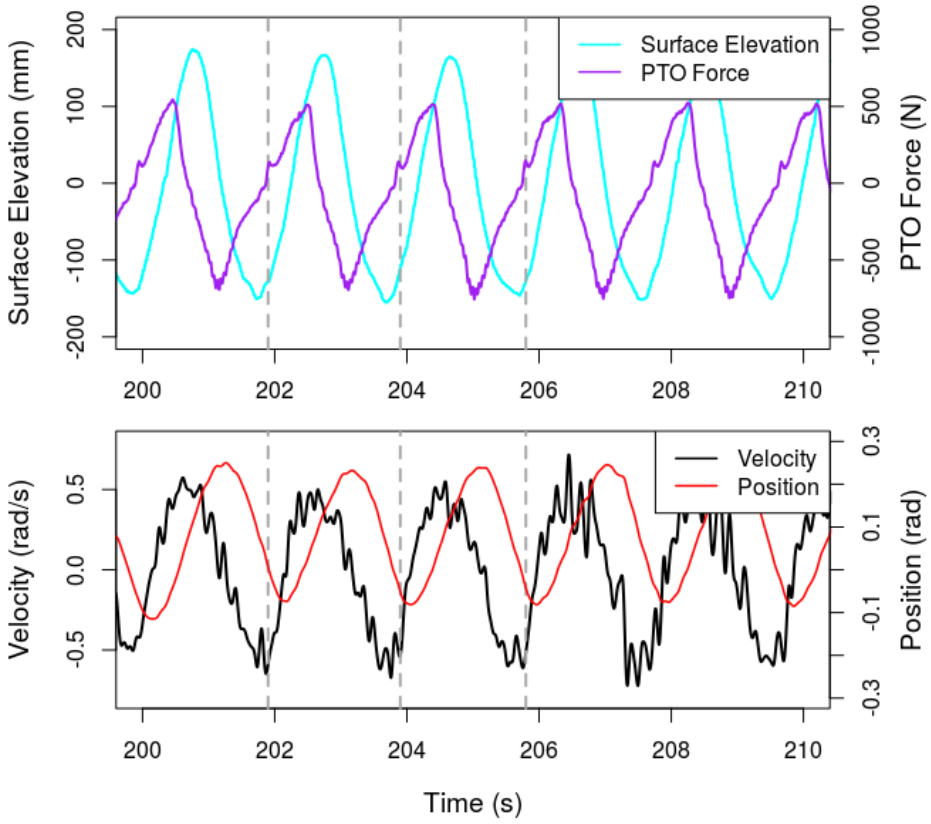

Figure 7.3: Surface elevation recorded by sonic wave probe (turquoise), Force on piston (purple), prime mover velocity (black) and prime mover position (red) during a series of slam events. The location of the slam is indicated by the vertical dotted lines.(Regular wave T = 1.936s, H = 0.3m, 1/15th scale)

However, some features have been captured in Figure 7.3. Slam events in three wave cycles have been highlighted with vertical dotted lines. These coincide with a rapid deceleration as the paddle reaches its most seawards position, as well as the inception of the water jet. The peak force and the timing of its occurrence also uncovers another difference between the slam event experienced by the curved paddle and the flat paddle. The flat paddle is essentially in free fall before impact and then must overcome substantial added inertia to reverse its direction of travel, this is demonstrated in the asymmetry of its motion (Figure 10 of (Yanji Wei, Abadie, et al. 2016)). Conversely, the curved paddle has already begun to decelerate before

the slam event occurs and the more streamlined nature of the paddle in shorewards motion allows the device to change direction more rapidly. The velocity profile is therefore much more symmetrical between shoreward and seaward motion. This is aided by the protruding bottom "shelf" included in the floating lab paddle design, which means that even as the paddle pitches seaward, there is some added inertia due to the shelf, preventing "free fall".

The repeated slamming event analysed above was observed in the preliminary testing where different levels of damping were trialled to identify optimal performance. Although the damping used during the slamming event was sub-optimal, it was very close to the values chosen for the performance testing in which slamming did not occur. These values are displayed in Table 7.3 where 0% represents a fully closed valve and the device is effectively stationary except for compressibility effects.

Table 7.3: Control voltage of poppet valve during Regular wave tests.

Wave conditions	Slamming?	Shorewards Control Voltage (%)	Seawards Control Voltage (%)
Regular T = 1.936s, H = 0.3m	Y	76	62.5
Regular T = 1.936s, H = 0.3m	N	79.5	62.5
Irregular Tp = 1.98s, Hs = 0.167m	Y	75	65

Both regular tests had the same level of damping for the seawards motion, but the shorewards motion was more restricted when slamming occurred. This counters the theory that an undamped device would experience the worst impulsive loading. However, considering the angular positions in Figure 7.4, there is another contributing factor. Although the slam event was more damped, it nevertheless had a larger range of motion and associated angular velocity. This is due to the fact that the device was oscillating about a more shorewards mean position, and thus had a larger buoyancy restoring moment to accelerate it seawards. It may also have altered the dynamics of the incoming wave field, exacerbating the down rush or vortical structures on the seaward side.

Interestingly, the shape of the force maxima is also altered in the case in which slam occurs. From analysis of the video, this appears to be a coincidence, which is connected more to the angular position of the device rather than the fact that slam occurred. The incoming wave crest is channelled by the geometry of the device gaining enough elevation to over-top. However, as the device pitches further shorewards, the body of water does not have sufficient forward momentum to pass over the edge of the paddle. Instead, gravity brings it back downwards, with the weight of the water impacting on the seaward face leading to the delayed peak force, Figure 7.4.

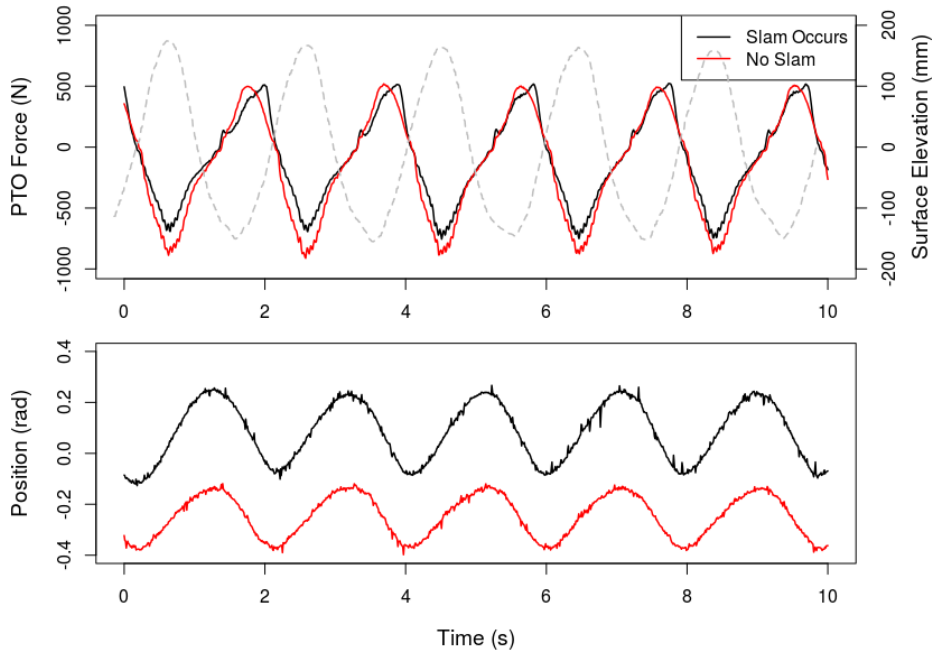

Figure 7.4: Comparison of angular position and PTO force for two similar regular wave tests in which only one experiences slam. (Regular wave T = 1.936s, H = 0.3m, 1/15th scale)

7.2.1.2 Slam in Irregular Waves

Identification of a slam event from the PTO load trace alone is more difficult in irregular long-crested waves. Perhaps more characteristic is the high velocity of the paddle preceding the slam and the manner in which it decelerates afterwards. Two such events are presented in Figure 7.5, however they are quite different. The first event, occurring at $T \approx 109.8s$, enhances the peak force from the underlying dynamic wave pressure. The device also undergoes a significant acceleration ahead of the impact, introducing considerable asymmetry to the velocity profile. This is likely due to the flatter trough of the incident wave train, as the trough itself is not particularly deep in comparison to the other slam events[2]. The incoming wave crest is also larger and steeper. The second event, occurring at $T \approx 210.8s$, more closely aligns with the slam events experienced in regular waves: with the creation of a force discontinuity just prior to the paddle reaching its most seawards position and ahead of the peak force from the wave crest.

[2]It should be noted that the discontinuities present in the wave surface profile do not represent reality, they are due to the sonic probes inability to accurately process breaking or white water.

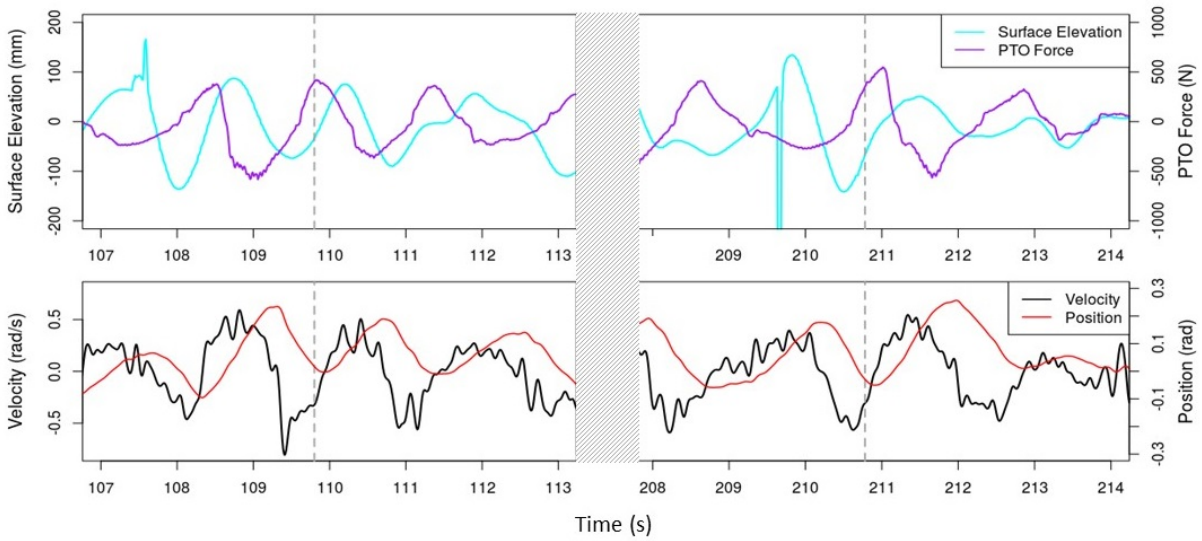

Figure 7.5: Surface elevation recorded by sonic wave probe (turquoise), Force on piston (purple), prime mover velocity (black) and prime mover position (red) during two slam events. The location of the slam is indicated by the vertical dotted lines.(Irregular wave Tp = 1.98s, Hs = 0.167m, 1/15th scale)

As the true extent of the increased pressure or torque has not been captured, the maximum force cannot be compared between the two cases. However, considering the size and velocity of the water jets created by the impact, the relative size of the peak pressure can be suggested. Images of the two slam events are shown in Figure 7.6, capturing the initial [A] and fully developed [B] water jet. The first slam event is clearly more violent than the second, and the vortices entraining water into the centre of the paddle also appear more defined.

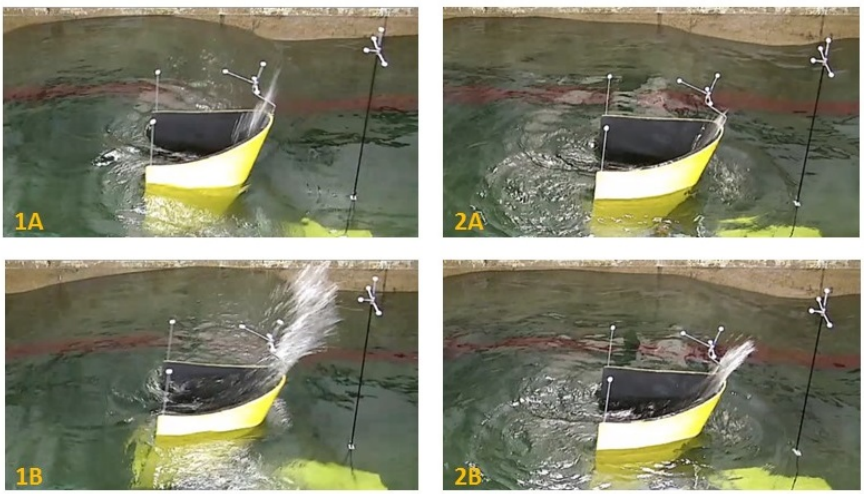

Figure 7.6: Photo series of two slam events (Occurring at 109.6s (1) and 210.9s (2)) showing the inception (A) and fully developed (B) water jet.

7.2.2 Numerical Implementation in CNWT

The number of variables that influence whether or not slamming occurs complicates the effort to replicate the above phenomena in the CNWT. The level of damping, water elevation profile, device position and structural properties all influence the phenomena and must be accurately defined, which is not possible retrospectively. Additionally, the device in the laboratory had two degrees of freedom: the paddle pitching about its hinge and the full device pitching about the seabed. However, by isolating some of these variables, the CNWT can be used to provide some insight particularly with regards to the wave shape as it is entrained into the seaward face and the local pressure profile of the subsequent impact. In the regular wave cases both the wave and device motion are periodic and well defined. A similar approach to that employed for the forced oscillation tests can been used to drive the paddle, replacing the calm water with the incoming wave field. Trial and error was used to ascertain the correct phasing between an approximated sinusoidal profile of the device position and the relevant wave conditions, using the video recording for visual validation. With this process, it was possible to simulate the water and pressure profile during a moderate slam event.

The outcome of this simulation is shown in Figure 7.7, with snapshots from three perspectives at key time points during the phenomena. The first perspective highlights the pressure profile on the paddle; the view from above shows the direction of flow of the surrounding water; and the view from the side focuses on the local steepness of the entrained water. In the first time frame, the down-rush of water is nearly complete and it is clear that the curvature of the paddle has channelled this to the core. This results in the enhanced trough effect being very localised, as shown in the next time frame where the water elevation is at a minimum. The steepness of the waterfront as it is entrained by the paddle is over four times steeper than the underlying wave conditions and in closer proximity to the front surface of the paddle this increases to $\sim$ 9.3 times before becoming near vertical. The water particles are also at the point of reversal in their orbits, and the lower water elevation and associated pressure inside the curve of the paddle induces water to flow around the paddle wings. It is this fluid motion that creates the “ridge” of water on the centreline that is visible in the laboratory videos, Figure 7.6.

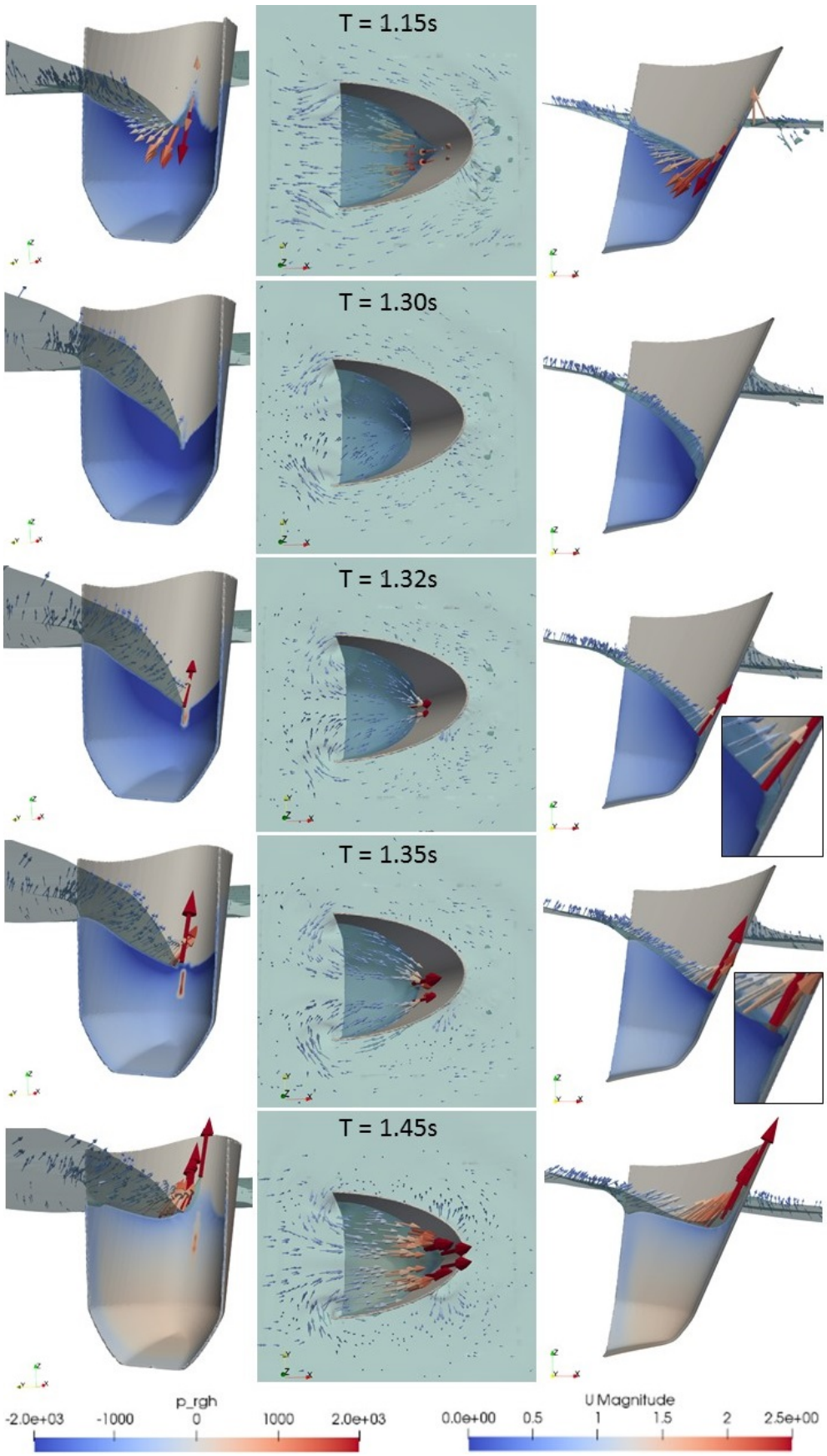

Figure 7.7: Slam Event as predicted by CFD NWT. The arrows are both coloured and scaled in size according to the magnitude of the velocity (m/s), and are aligned with the direction of the velocity. The paddle is coloured to represent the dynamic pressure (Pa), i.e. the pressure minus the hydrostatic contribution. (Regular wave T = 1.936s, H = 0.3m, 1/15th scale)

This inflowing fluid advances and elevates the water surface, with the water profile at the centre of the paddle nearing vertical, at T=1.32s. This creates a high pressure pocket of air that drives the high velocity water jet, as seen in the two subsequent time frames. It should be noted that the simulation has been conducted with an incompressible solver which cannot take into account the compressibility effects of an air bubble and its collapse. Although compressibility does impact energy dissipation in the final stages of bubble collapse (Rowlatt and Lind 2017), modelling the fully compressible Navier Stokes equations would increase the computational time required, and for the time being is deemed unnecessary. Additionally, evaluation of bubble collapse at this reduced scale leads to a more conservative, or safer, estimate of maximum pressure as the trapped air at small-scale is relatively stiffer than the air in larger air pockets at full scale.

The time trace for dynamic pressure of an undisturbed wave field would be near sinusoidal, hence the effect of the paddle's presence and the slam event are clear. In areas away from the slam event, the pressure profile is smooth. Any prolonged periods for which zero pressure is recorded (e.g. probes D, E and F) are explained by their exposure above the water surface. Location A is continually submerged, and does not experience a pressure peak due to the slam but preceding the event it records a much lower pressure. Probes B and C are positioned around the location of the air bubble when it first forms. There is a clear local impact event, with the peak dynamic pressure recorded at B reaching just over twice what the maximum would otherwise be due to the dynamic pressure of the incoming wave field. As mentioned, this event is considered a fairly moderate example of slam compared to the irregular events witnessed in the wave flume. However, for the design of the composite paddle, it is critical that the structural and material design teams are aware of the location and magnitude of these pressure "hotspots".

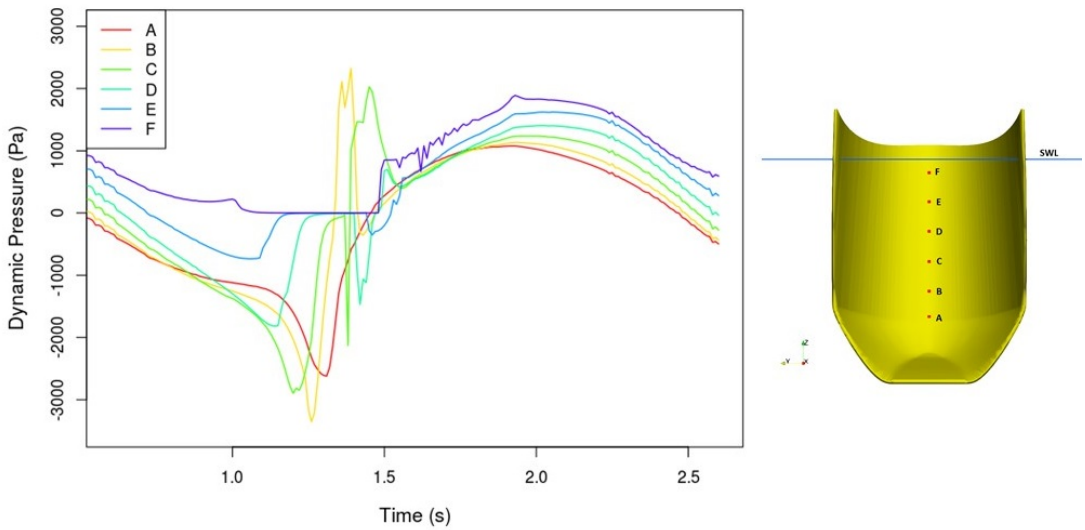

Figure 7.8: Dynamic pressure throughout wave cycle at different probe locations below SWL along the centreline of the paddle, as indicated by the diagram on the right. At the mean angular position these are: z_A = -0.511m, z_B = -0.429m, z_C = -0.328m, z_D = -0.220m, z_E = -0.106m and z_F = 0.012m.

7.3 Directional Waves

Unlike the point absorber or other symmetric types of WEC, the OWSC is designed to operate in a particular direction of waves. The device's heading relative to the incoming wave field has a significant impact on the overall loading of the structure and the subsequent power output. During the design and installation of the device, careful consideration must be given to the prevalent wave direction. This is affected both by the wind resource from which the waves originate and, in shallow water, the bathymetry of the surrounding area.

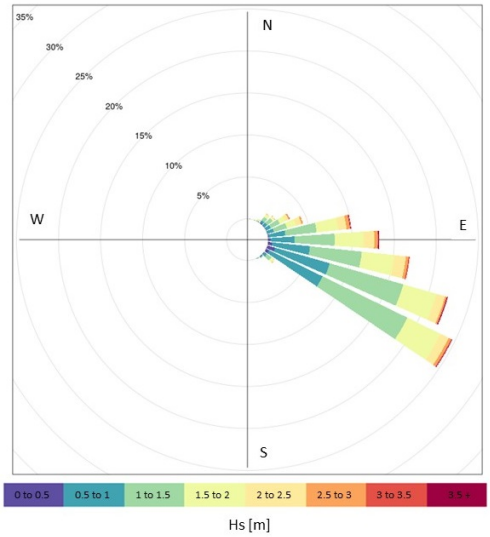

Figure 7.9: Wave rose for observed data at pilot deployment location 2005-2015

A wave rose for the closest grid point of the NOAA data is shown in Figure 7.9, characterising the direction of the wave resource in the area surrounding the pilot deployment location. Due to the presence of mainland Mexico to the west of the deployment location, the waves only originate from the east, through the Carribean Sea, with south easterly the most frequent direction.

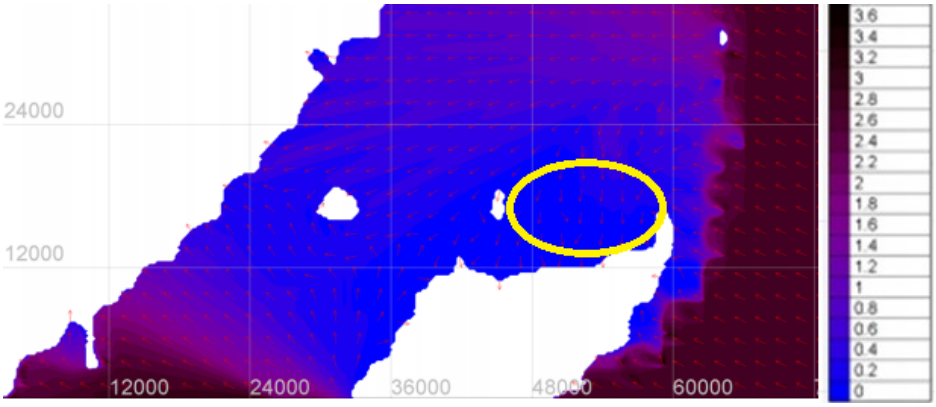

Figure 7.10: Progression of wave resource due to bathymetry at pilot deployment location. Arrows depict wave rays. Colour contours represent significant wave height (m). Deployment location indicated by yellow ring.

Inputting this wave direction along with the bathymetry of the area into the SWAN wave model, the progression of these short-crested wind-generated waves is calculated in the coastal region. The output from this simulation is shown in Figure 7.10, where there is a clear energy shadowing behind the island (white region) and the direction of the wave rays refract to become perpendicular to the shore. This refraction establishes a clearly defined prevalent wave direction for the installation site. However, if placement is incorrect, if there is coastal sediment transport and morphological changes, or if there are strong local wind effects, then the loading from sub-optimally oriented waves must also be considered.

This section analyses findings from the laboratory testing of the floating CCell device to understand the impact of directional loading and the effect of design measures to reduce undesirable lateral loading. The methodology for replication in the CNWT is also detailed and output from directional simulations is studied to provide understanding of the wave-structure interactions.

7.3.1 Lab Testing of Floating CCell Device

During the tank testing conducted in November 2016, the orientation of the paddle with respect to the incident wave direction was varied to 10° and 30° and the effect on the performance investigated (see Figure 4.6 for respective orientation). If the paddle is oriented at an angle to the incident wave angle, the force from the waves is no longer in line with the piston motion. Therefore, a portion of the wave force does not create useful work and instead presents as a lateral loading on the paddle.

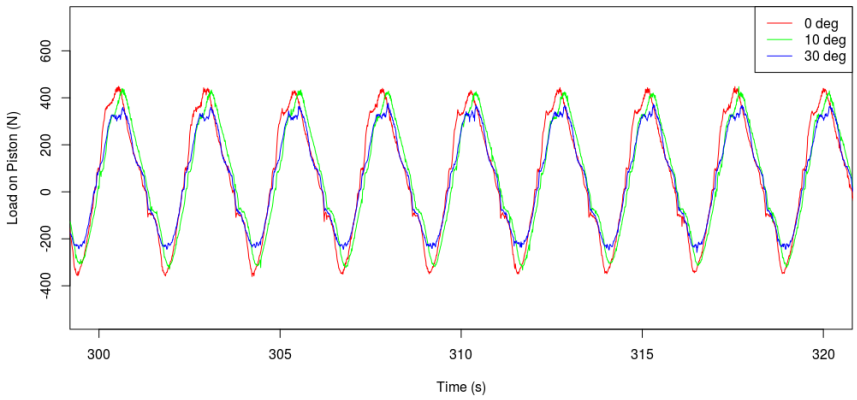

(a) Load on piston at different orientations to incident wave.

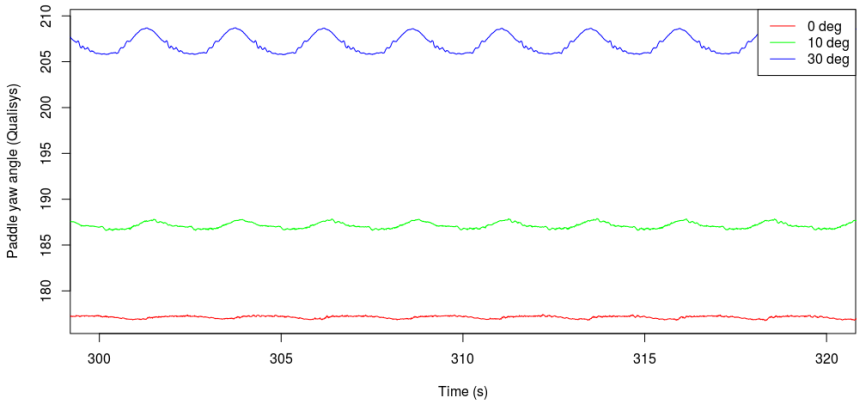

(b) Paddle's yaw motion at different orientations to incident wave.

Figure 7.11: Performance of Paddle at different orientations to the incoming wave (H=0.233m, T=2.453s).

Figure 7.11a presents the forces on the PTO which shows a clear, but small,reduction in loading as the orientation of the paddle increases from 0° to 30° in a regular wave. The data shown in Figure 7.11a is selected at the same damping level for each orientation. Although the system was designed to be rigid there was some flexure due to the lateral loads, which is apparent in the yawing motion shown in Figure 7.11b. At 30° this is quite significant and the cyclic loading at this angle could increase the wear and stresses on the supporting structure of the device.

Four regular and two irregular long-crested wave conditions spanning the operational frequency band were tested and the powers were obtained from the optimal damping level in each case. It was found that the preferred level of damping reduced as the device was oriented further from the incident wave direction. The change in efficiency of power capture in relation to the output for the optimally oriented device is shown in Table 7.4. By way of comparison, the reduction of inline force if the device is oriented at 10^o or 30^o degrees, would result in a drop in percentage points of 1.52 and 13.4 respectively, if simple geometry is considered.

For wave cases directed at 10° to the paddle there is only a small drop in efficiency of power capture. More interestingly, for most of the cases at the 30^o heading, the reduction in efficiency

is much less than that predicted by geometry, giving credence to the theory that the paddles' curvature and wings aid energy capture in directional seas. The only anomaly to this finding is the highest frequency regular wave condition, suggesting that the ability of the device to capture energy from a directional sea is also dependent on the frequency of the incoming wave field. Furthermore, the waves tested at different orientations all had relatively large amplitudes. It is expected that in lower amplitude waves the reduction in efficiency would not be as profound, as the shape of the top of the paddle is designed to promote overtopping and reduce lateral loading when the incoming wave direction differs significantly to the design orientation of the paddle.

Table 7.4: Change in capture width ratio when paddle oriented at 10° and 30° to incident regular waves when compared to the optimal orientation. (NB CWR is reported here out of 100)

	Change in CWR	
Wave Conditions	**10^o**	**30^o**
Regular (H = 2.5m, T = 5.5s)	-7.47	-29.7
Regular (H = 2.5m, T = 7.5s)	-0.95	-7.82
Regular (H = 3.5m, T = 9.5s)	-0.05	-3.01
Regular (H = 4.5m, T = 6.5s)	-2.54	-10.45
Irregular (Hs = 2.5m, Tp = 7.7s)	-0.4	-2.1
Irregular (Hs = 3.5m, Tp = 9.1s)	-2.3	-5.2

Roll Mechanism To increase survivability of the device, a roll capability was introduced into the design, such that if the device is hit by waves that differ significantly from the design condition, the lateral forces on the paddle and support structure are minimised. The roll mechanism was locked for the majority of the tests, however a few cases oriented at 30° were repeated to investigate the functionality of the roll mechanism. As shown in Figure 7.12a, the unlocked roll mechanism allows the paddle to roll freely. The roll mechanism is mounted onto the A-frame at an angle to the horizontal, therefore when the paddle is allowed to roll there is also some yawing motion. This is shown in Figure 7.12b, where the yawing motion is closely in phase with the rolling motion, when the roll mechanism is unlocked. This results in the paddle being at minimal yaw when the wave peak meets the paddle, and is thus more aligned with the incident wave direction than when the roll mechanism was locked.

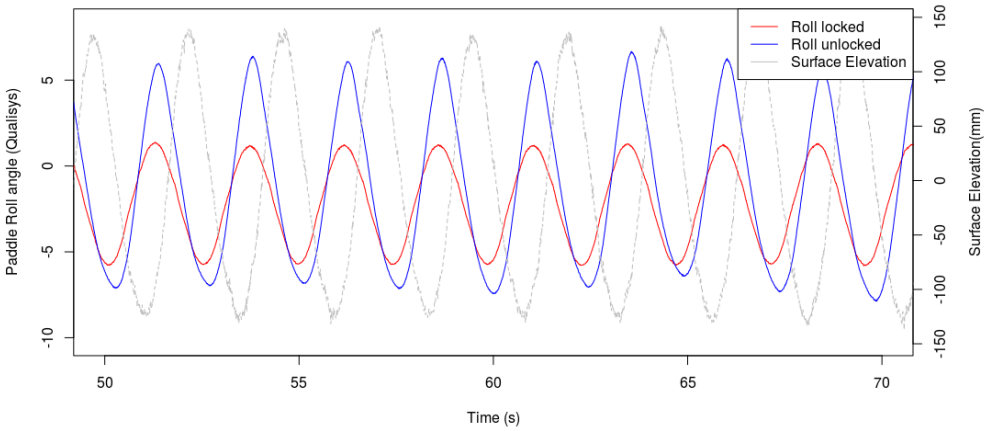

(a) Paddle roll motion.

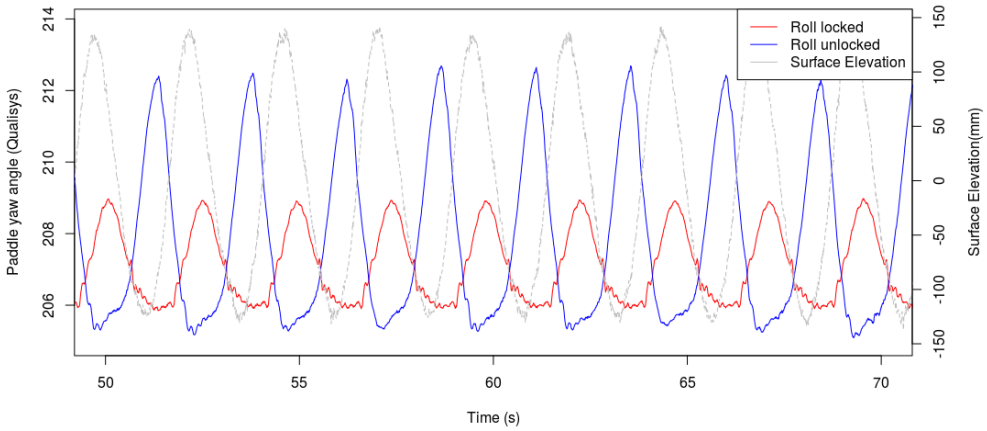

(b) Paddle yaw motion.

Figure 7.12: Motions of paddle with and without roll mechanism enabled for a regular wave (H=0.233m, T=2.453s).

The effect of the coupled yaw-roll motion is an increased load on the piston at the wave peak, as shown in Figure 7.13.

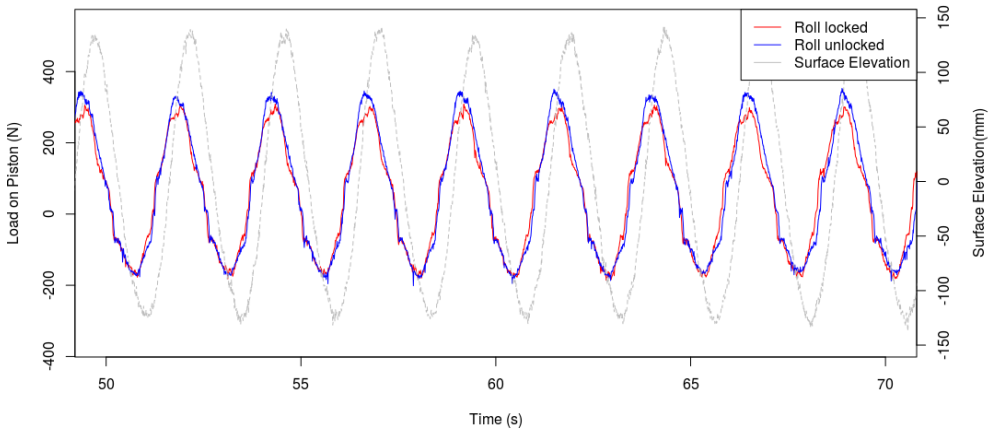

Figure 7.13: Piston Loading from paddle with and without roll mechanism enabled for a regular wave (H=0.233m, T=2.453s).

Allowing the system to move more freely in the direction of the waves alleviates the loading experienced in the rest of the support structure and foundations. This is shown in Figure 7.14, where the yawing of the base structure is significantly reduced with the roll mechanism unlocked.

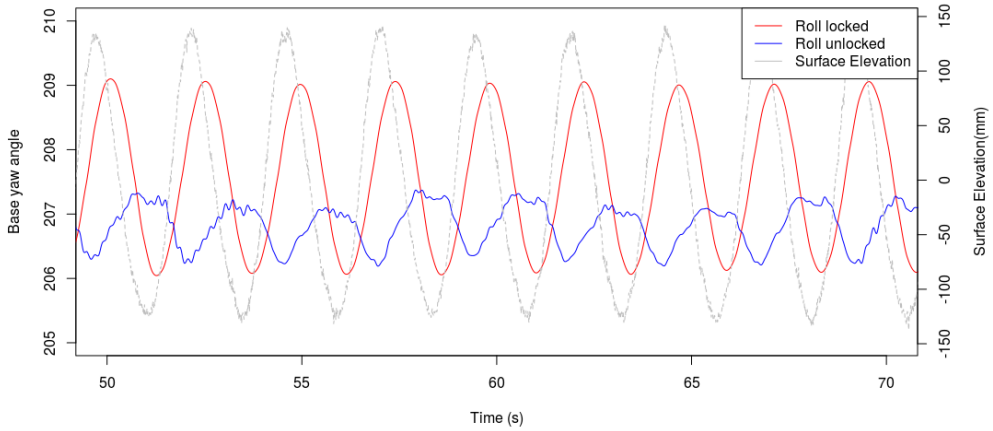

Figure 7.14: Effect on base structure of paddle with and without roll mechanism enabled for a regular wave (H=0.233m, T=2.453s).

7.3.2 Numerical Implementation in CNWT

To simulate directional waves, the same methodology is used as in the physical laboratory tests: the paddle is oriented at an angle about the z-axis. The rest of the CNWT remains as previously described, the only difference being that the symmetry plane is no longer used and the whole domain must now be included in the calculation.

The CCell geometry is easy to manipulate prior to the meshing, however correct formulation of the dynamics is more difficult. The transformation involves Eulerian angles with the standard ZYX (i.e. rotate first about Z then Y then X). All specification of joints and bodies is carried out

in the dynamicMeshDict and there are two ways of specifying a rotation about a transformed axis:

(a) Specify the inertia in global coordinates pre-transformed for the desired rotation, then specify the joint and restraint axis as the desired axis.

(b) Specify the inertia in local coordinate system and then put required rotation matrix in the transform variable, then specify the joint and restraint axis as y-axis.

The output from the motion solver is presented in the coordinates local to the body. This includes, the orientation, angular velocity, restraint forces and moments, all of which are more useful if the axes are aligned with the motion of interest, e.g. pitch is about y-axis. Therefore the second option is used for directional simulations. The forces function object however, has no knowledge of the transformation dictated by the dynamicMeshDict, hence it writes quantities in global coordinates unless a coordinate system is explicitly supplied.

To simulate the Roll mechanism as well as the PTO system, multiple degrees of freedom must be implemented in the dynamicMeshDict, an example of this specification in the OpenFOAM dictionary files is given in Appendix C.

Three simulations were conducted in the same regular wave conditions: one with the paddle aligned with the direction of the wave, the second at a 30^o heading and the third at a 30^o heading but with the roll mechanism enabled. Figure 7.15 demonstrates the impact of the non-optimal direction on the paddle's motion and the pitch moment, when the system is subjected to the same (non-optimal) damping levels. The paddle oriented at 30^o has both a smaller angular motion and a smaller pitch moment, when compared to the optimally oriented paddle. Due to the shape of the paddle directing the inflowing water, the pitch moment for the rotated paddle is near equivalent to the normal pitch moment as predicted by the 0^o heading simulation (i.e. $My_{0^o}cos(30^o)$), indicated by the black dotted line. The roll moment is roughly half the pitch moment in the wave crest, however in the wave trough they are comparable presumably due to the bluff nature of the body in roll. When the roll mechanism is included, the pitch moment reduces further, particularly in the wave crest, though interestingly, this induces a larger pitch motion.

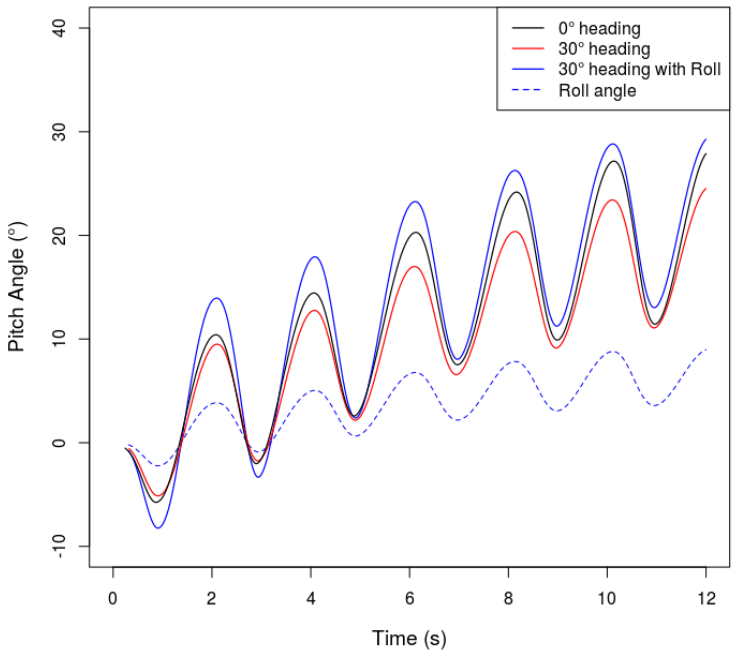

(a) Angular motion

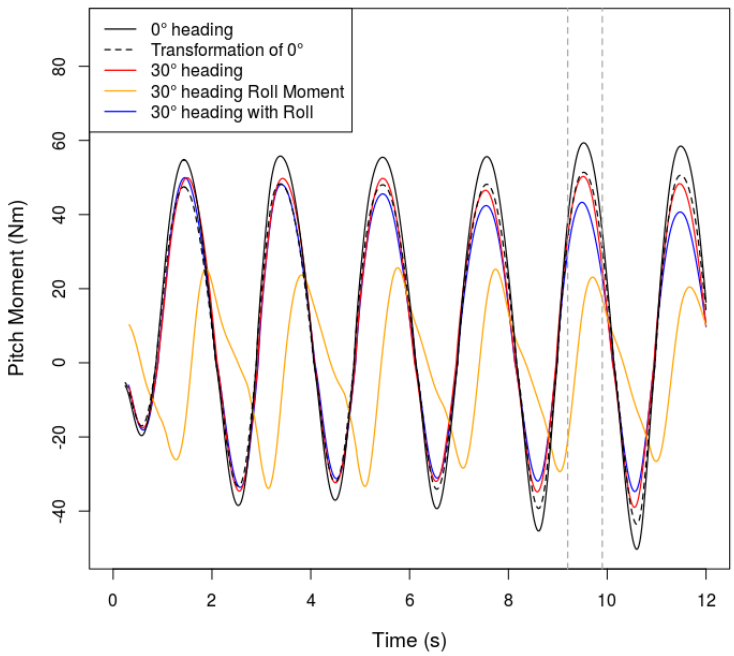

(b) Calculated pitch moment

Figure 7.15: Directional Comparison of the floating CCell device in a regular wave (H = 0.167m, T = 1.937s, Scale = 1:15) as computed by the CNWT.

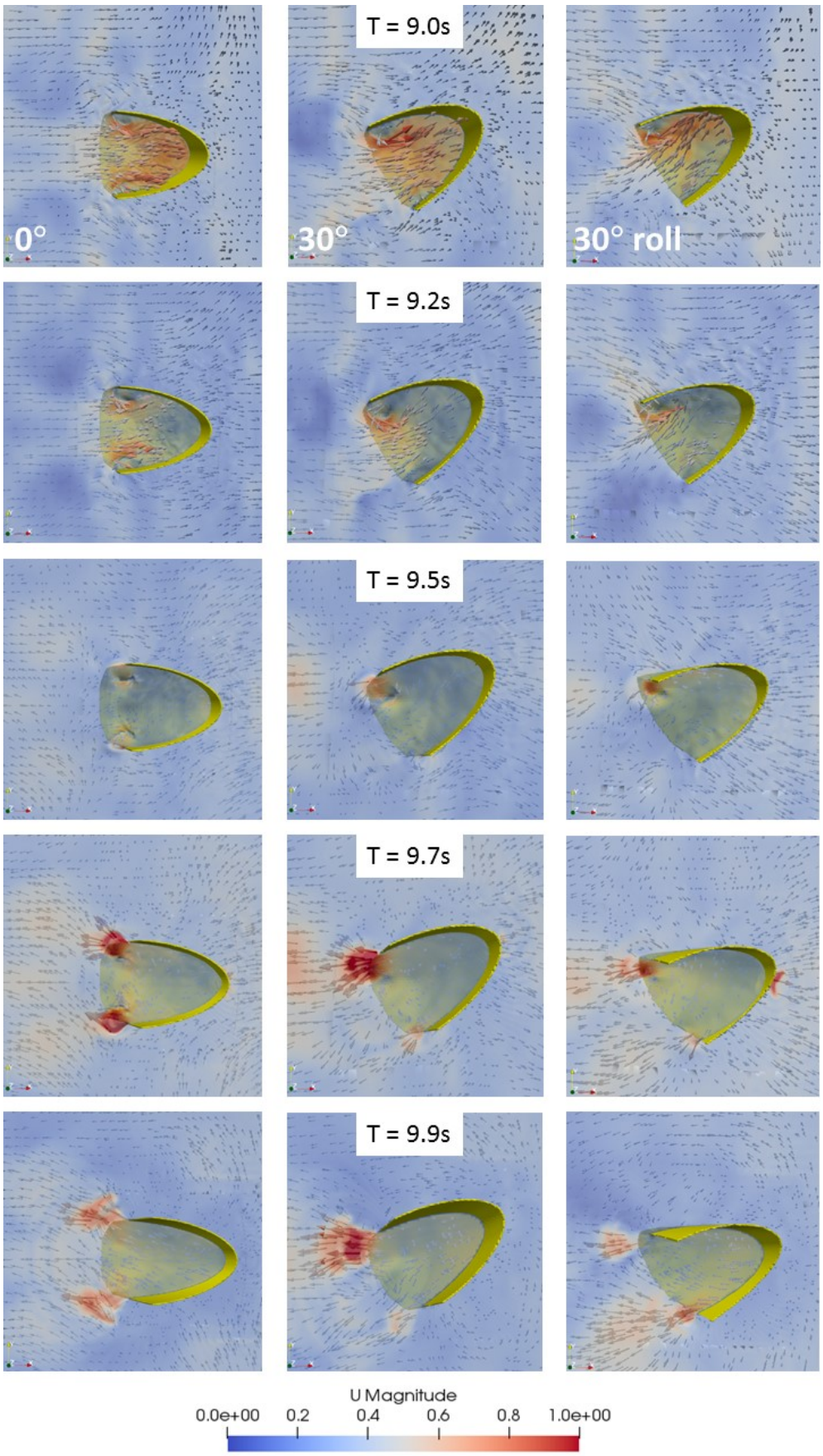

Figure 7.16: Snapshots of the floating CCell paddle oriented to the direction of a regular wave (T = 1.936s, H = 0.167m, 1/15th scale) with the headings 0^o, 30^o and 30^o with the roll capability allowed. The domain is coloured according to the velocity magnitude (m/s)

Snapshots of the three simulations have been taken between the times indicated by the vertical dotted lines in Figure 7.15b to capture the underlying fluid dynamics over a maximum. These snapshots are presented in Figure 7.16 and arranged with a timestep per row and a simulation per column. In the first frame, water is entrained from a crest width larger than the width of the paddle entry area, which is just as true for the 0^o scenario as the rotated cases. An area of low momentum fluid is created at the wing tip, inside the paddle with the low pressure of this area inducing a curvature and associated increased velocity of the flow. This is more apparent in the directional cases and the overall impact is that the incoming flow becomes re-oriented with the paddle's centreline. At T = 9.2s, the symmetry of the flow for the 0^o condition, means that there is nowhere for the water to move to except upwards, increasing the local surface elevation. However in the directional cases, as the curvature is stronger on the side closest to the incoming wave, the water is guided around the concave face of the paddle. For the paddle that allows roll, this promotes motion in the secondary degree of freedom, visible at T = 9.5s. As the water then begins to flow out of the paddle, T = 9.7s, the asymmetry is again clear, with one tip experiencing the wave trough ahead of the other. The paddle with the roll mechanism enabled, traces almost a circular path, with water entrained for longer and eventually rushing out by the aft wing, T = 9.9s.

Asymmetric loading can have a deleterious effect on the overall structure, particularly with the cyclic nature of wave loading. Measures such as the roll mechanism can remove the unwanted lateral loading, however this is at the expense of power capture, and the additional degree of freedom may further complicate the control system. Analysis of the impact on both unwanted loading and power output for the operational and extreme envelope of wave conditions can aid the developer's decision of which to prioritise.

7.4 Shallow Water Extremes

Marine structures are usually designed such that the probability of failure is less than a particular value per year. This probability is encompassed by return periods, for example there is a probability of 0.01% that a 100 year wave will occur in any given year. However, if the design life is much less than the return period then this decision becomes uneconomic. The standard within the industry appears to be a design life of no more than thirty years, therefore a return period of 50 years is more appropriate to a WEC developer. According to the manual for coastal and shoreline engineering constructed from rock, if the design life of a structure is 30 years there is a 45% chance that it will encounter a 1 in 50 year event, whereas for a 1 in 100 year event this reduces to 26% (CIRIA, CUR, CETMEF 2007). The more economical design criteria comes at the cost of the developer accepting more risk and there is an increased likelihood that the structure will require major repairs during its operational lifetime.

One issue that is inextricably linked to the use of return periods is what the 50 year or 100 year event may look like as deduced from the length of observed data available. A return period is usually used to identify a rare event, thus in the observed data it may only occur once, but as the length of the data series increases the supposed return period may change, i.e. what was a once in ten year event was actually a once in 20 year event. If considering still rarer events, it may be that such an event has not yet been recorded. Therefore statistical models are employed to predict the relevant magnitudes. However, the underlying assumption that the

sampled events follow a static distribution is also incorrect when confronted with global climate change. For example, warmer waters yield stronger hurricanes with heavier rainfall (National Climate Assessment 2019) suggesting that the frequency of higher category hurricanes will increase. Other interannual geographical phenomena such as El Niño and the North Atlantic Oscillation also require longer data sets to properly account for their variation in statistical models.

The problem is convoluted by the different recording time scales of the distributions. The observed data is often bulk statistics of the sea state parameters such as significant wave height and peak period, recorded at a regular interval e.g 3 hours. This provides a long term distribution characterising the resource at a particular location. However, it is the short term distribution surrounding these sea state parameters which identifies the maximum wave heights. The Rayleigh Probability distribution has been identified as the most suitable model for occurrence of random wave heights. It is from this that the definition of significant wave height is derived as the centroid of the top third area beneath the Rayleigh distribution curve. A similar analysis can be conducted for the top 10% or top 1% of waves in a particular sea state. The probability Q of a particular wave height h occurring is defined in Equation (7.1).

$$Q(h) = e^{-2\frac{h^2}{H_s^2}} \tag{7.1}$$

However it is more instructive to calculate the inverse of this: how many events would need to be observed for this wave height to occur. From this inversion, the maximum wave height for a particular number of waves can be calculated by Equation (7.2). A three hour storm event is generally accepted to include approximately 1000 waves, therefore the maximum wave height in a particular storm could be calculated using $N_R = 1000$.

$$H_{max} = H_s\sqrt{\frac{ln(N_R)}{2}} \tag{7.2}$$

For a WEC developer it is not the extreme wave height that is of ultimate relevance but the extreme loading on the WEC. This is influenced by the incoming wave field as well as system dynamics and interdependencies. Although extreme loads are more likely to occur in bigger waves, the peak loads may not coincide with the highest wave. As seen in Section 7.2, the shape of the wave and preceding motion had a larger impact on the occurrence of slam than the height of the individual wave crest.

Computation of these extreme loads is expensive, as due to their extreme nature, the probability of them occurring is low. Thus if undertaking a Monte Carlo approach, a large number of simulations (numerical or physical) is required to confidently encompass such rare events. Alternative techniques to propagate uncertainty from the stochastic nature of the surface elevation to the ultimate WEC loading have been proposed e.g. Polynomial Chaos Expansion (Nguyen, Manuel, and Coe 2019), which drastically reduces the number of simulations for a similar output ($10^6 \rightarrow 500$). However, the required number of simulations is still prohibitive to CFD techniques and such studies have relied on WAMIT to provide estimates of the PTO extension and force in extremes. As previously discussed, the validity of these codes reduces when non-linearities are present, which is exacerbated in extremes. Therefore an alternative approach is sought to provide understanding of extreme loads on a WEC. The remaining part

of this section details the theory behind this approach and how it has been implemented in the CNWT.

7.4.1 Deterministic Approach to Extremes

In the Oil & Gas sector, a method has been developed to replace lengthy probabilistic experiments with a deterministic extreme design wave. This “NewWave” methodology is used extensively to model and assess interactions between extreme waves and offshore structures. The theory calculates the surface elevation around a crest based on probabilistic analysis, providing the average shape of an extreme wave profile for a given spectrum (Tromans, Anaturk, and Hagemeijer 1991). Since its conception it has been successfully used for extreme loading studies in both the Gulf of Mexico (Santo et al. 2013) and the North sea (Walker, P. Taylor, and R. E. Taylor 2004), and outperforms alternative strategies that use Stokes Fifth order.

The main principle of NewWave theory is energy focusing. The spectral components of the sea state are superposed by adjustment of their phases to focus the wave energy at a particular time and location. This is beneficial not only in numerical modelling, but in physical modelling too as it both reduces run times and avoids long wave re-reflections. The shape is dictated by the autocorrelation function which is proportional to the Fourier transform of the energy spectrum for the given sea state. The maximum amplitude is then defined by a scaling parameter to give the required crest amplitude based on the return period.

Using a finite number of sinusoidal components, N, a focused wave group has the surface elevation calculated by Equation (7.3).

$$\eta(x,t) = \sum_{n=0}^{N} a_n cos(k_n(x - x_f) - \omega_n(t - t_f)) \tag{7.3}$$

where the subscript f represents the focal time and position for the extreme wave. The amplitude of the individual components, a_n, is defined in Equation (7.4)and is a function of the energy spectrum, $S_n(\omega)$, the frequency discretisation, $\Delta\omega_n$ and the crest amplitude A_{cr} which is based on the desired return period N_R and is equivalent to $H_{max}/2$.

$$a_n = \frac{A_{cr} S_n(\omega)\Delta\omega_n}{\sum_n S_n(\omega)\Delta\omega_n} \tag{7.4}$$

Traditionally the NewWave formulation has been used and validated in cases where the non-dimensional water depth, kh, exceeds 1.6. The underlying assumptions of NewWave are that the dominant factor affecting wave evolution is linear frequency dispersion. In shallow water the effect of frequency dispersion lessens and other non-linearities become more significant. However, more recent studies, for example comparison to wave buoy data recorded in the southwest of the UK (C. Whittaker et al. 2016) have demonstrated good agreement down to $kh \approx 0.4$. This confirms the suitability of the NewWave profile to determine loading of coastal structures in pre-breaking waves.

Whittaker et al. also concluded that idealised spectra can be used to predict these average extremes though it is important that the appropriately shaped spectrum is chosen as they have been shown to play an important role in determining extreme responses in studies of offshore

platforms. In their analysis, the JONSWAP spectrum computed a NewWave profile with a slower amplitude decay that fell outside the 95% confidence intervals on the mean profile. However, the NewWave profiles created from the linearised field data and the TMA spectrum, showed excellent agreement. This is an important finding as for many sites the only data available is bulk statistics averaged over a particular time window. There is often no analysis of individual waves and what the extreme may look like.

Considering the available wave buoy data for the pilot deployment location shown in Figure 5.1, the largest and steepest seastate recorded is Hs = 4m and Tp = 9s. Within the 10 years of data recorded, this has been observed in only 22 of the 29,200 3-hour windows. The non-dimensional water depth for this case is $kh = 0.52$, thus is in the range evaluated as acceptable by Whittaker et al. The NewWave profile for this seastate has been computed with a number of different spectral shapes to show the effect of increasingly shallow water on the surface profile, Figure 7.17. As the waves enter shallower water, there is more interaction with the sea bed, causing waves to shoal and ultimately break, dissipating some of the spectral energy. The TMA spectrum takes into account the limited height of low frequency components in shallow water, providing a NewWave profile which is more compact in the time domain than the equivalent JONSWAP spectrum.

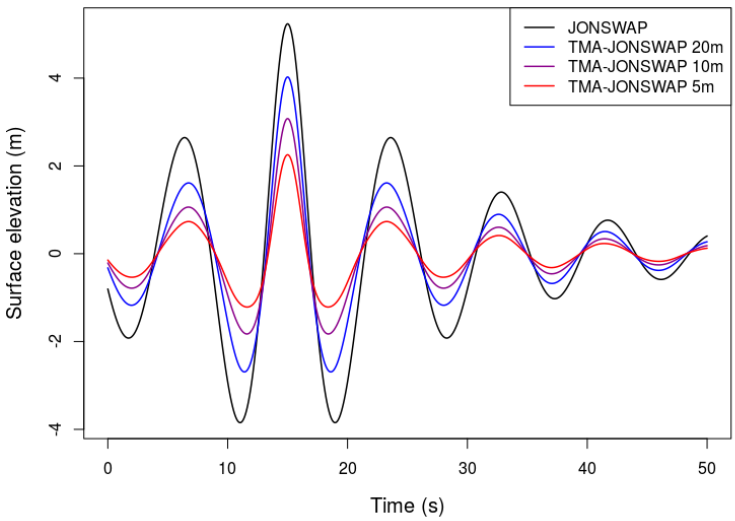

Figure 7.17: NewWave profile for different spectra defined with a seastate of Hs = 4m, Tp = 9s with 100 frequency components and the largest of 1000 waves. The focusing time is 15s.

7.4.2 Numerical Implementation in CNWT

The waves2Foam toolbox can be extended to include the NewWave formulation with relative ease, as the functionality for irregular waves already exists which calculates and stores the required amplitude, wave number, phase and frequency of each of the wave components. The TMA spectrum has been phased and scaled to provide the desired NewWave profile according to Equation (7.4), with the code and example parameter inputs included in Appendix C. The validity of a similar extension was demonstrated in (Ransley 2015), though the specific code

implementation was not supplied. Ransley's numerical solution for wave run-up and pressure on a vertical cylinder in a deep water NewWave extreme was found to successfully predict physical modelling measurements. Conclusions drawn from this previous work regarding appropriate set up have been incorporated into the present study.

Two wave-only cases have been trialled in the CNWT and the surface elevation recorded by numerical probes situated at the end of the inlet relaxation zone and at the specified NewWave focal point. The output from these probes has been compared to the theoretical values expected, Figure 7.18. The mesh used for these simulations was effectively 2D, as it was only one cell wide. The same approach as described in Section 4.1.3 was used to reduce the mesh resolution in regions of the domain with low velocity gradients, leading to a 2D domain of 75,625 cells with a resolution of 30 cells per metre of wave height for the wave zone.

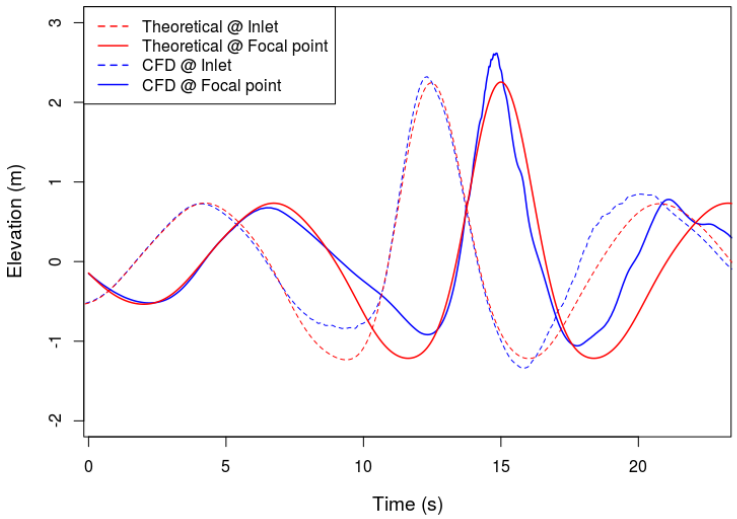

(a) NewWave profile based on a TMA-JONSWAP Spectrum Hs = 4m, Tp = 9s, depth = 5m

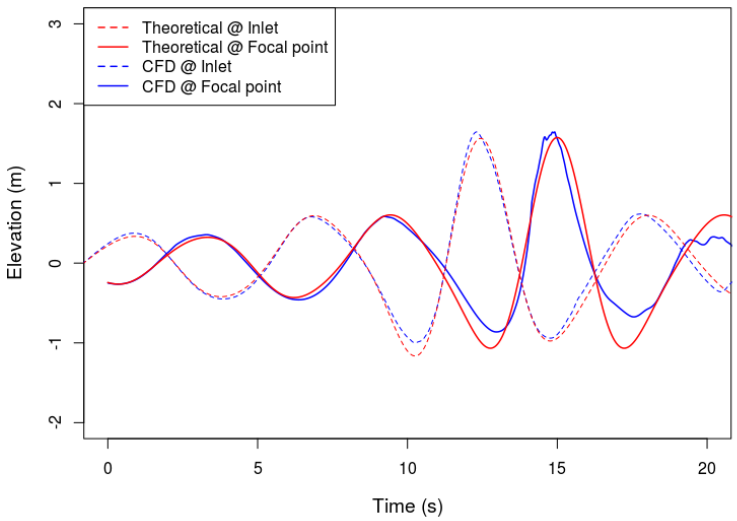

(b) NewWave profile based on a TMA-JONSWAP Spectrum Hs = 2.8m, Tp = 6s, depth = 5m

Figure 7.18: Comparison of theoretical NewWave wave train and that produced by the CNWT

In the first NewWave profile it appears that the main wave crest is initially well defined, however, the CNWT is less able to accurately represent the trough ahead of the extreme. At the focal point there is a clear divergence between the surface profile calculated by the CNWT and the theoretical value for the larger wave. Attempts were made to alter the relaxation zone and further refine the mesh however, no improvement was acheived on these results. The discrepancy is therefore thought to be the result of the wave interacting with the seabed, leading to shoaling and subsequent breaking of the wave 5m downstream of the focal point. In order to analyse the effect of only the NewWave profile, a smaller wave (Hs = 2.8m, Tp=6s) of similar steepness is chosen that is less affected by shoaling prior to reaching the focal point.

It is this NewWave profile, shown in Figure 7.18b, that will be used in the subsequent analysis of the impact on the CCell structure.

The CCell device was positioned such that the hinge point was 7.5m from the inlet. This was also chosen as the NewWave focal point to occur at 15s. The computational domain was expanded to allow a 3D simulation, with a width of 6.3m. As the device was oriented in-line with the incoming wave field, symmetry was assumed and only the y-positive half of the domain was simulated. This equated to a total of 2,551,700 cells to allow for the same resolution in the wave zone as used in the wave-only simulations. It is clear that 3D simulations quickly become restricted by the available computational hardware. Both static and dynamic simulations were conducted with parallel processing on 20 Intel Xeon E5-2680 cores at 2.8GHz. The 25 second static simulation took 124.6 hours to complete, whereas the dynamic simulation failed at t = 15 seconds having taken 218 hours. This increase in execution time is not surprising as the time required to update the mesh at each iteration can take as long as 2.4 seconds when the velocity of the paddle is high. The increased magnitude of velocity of the water particles also requires a reduction in time step to adhere to the Courant number. The peak angular velocity of the paddle was $0.8rads^{-1}$ and the maximum fluid velocity calculated within the domain was $10.37ms^{-1}$ in the dynamic simulation.

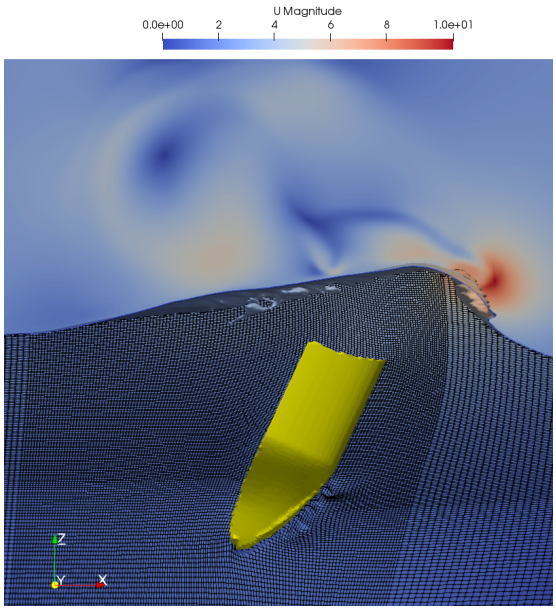

Figure 7.19: Snapshot of the dynamic simulation of CCell subject to a NewWave profile (TMA-JONSWAP Spectrum Hs = 2.8m, Tp = 6s, depth = 5m) just prior to simulation failure [T =15s]. The domain is coloured according to the velocity magnitude (m/s)

Figure 7.19 depicts the last time step saved prior to the dynamic simulation failing. The highest velocity is calculated in the air. Although it is not entirely clear how abnormal these velocities may be, as they are in the same order of magnitude as the water, this has often been cited as an issue in simulation stability (Ransley 2015). The VOF method is known to calculate unphysical momentum transfer and spurious air flows, causing the adjustable time step to plummet to values as low as $1e^{-11}s$ prior to the simulation failing. This issue is usually testament to excessive mesh deformation or mediocre mesh design. As seen in the figure,

it is more likely to be the latter as there is a clear discontinuity in the mesh just upstream of the high velocity region. Although the mesh is the same as that used in the static simulation, the additional mesh deformation has exacerbated the problem.

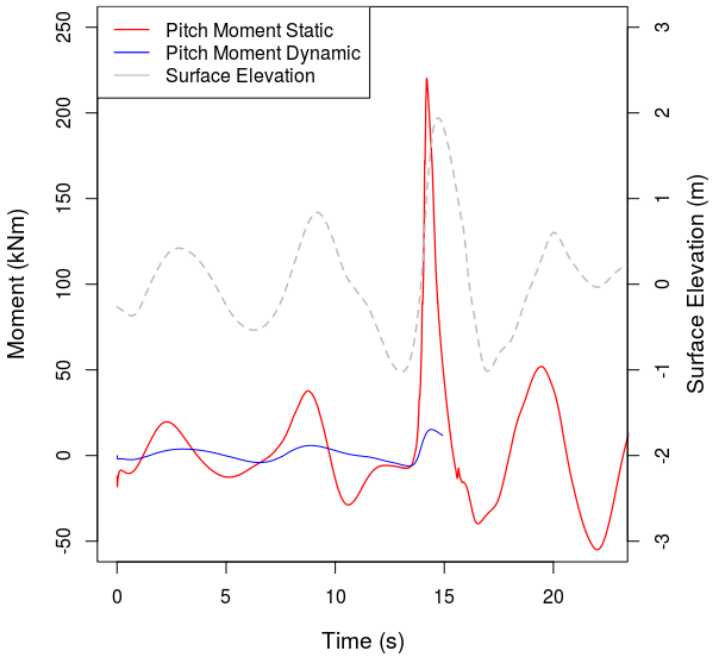

Figure 7.20: Comparison of pitch moment on a CCell paddle in a dynamic and static simulation due to loading from NewWave profile (TMA-JONSWAP Spectrum Hs = 2.8m, Tp = 6s, depth = 5m)

Considering the pitch moment on the static CCell device, as shown in Figure 7.20, the peak loading appears highly dynamic, with considerable magnitude and a short duration, particularly in escalation, similar to that described in wave slam events. The peak load coincides with the formation of a water jet, Figure 7.21 as the momentum of the water is diverted upwards when it becomes constricted by the presence of the paddle. This enhances the surface elevation and leads to instability of the crest downstream of the paddle at $t = 15.4s$. The peak moment occurs at $t \approx 14.4s$, ahead of the wave crest focal time of $t = 15s$, as beyond $t = 14.4s$ the height of the crest greatly exceeds the top edge of the paddle allowing much of the highest energy water particles to over-top the device.

A similar sequence of images is shown in Figure 7.22 for the dynamic simulation prior to its failing. In addition to the fact that the paddle moves with the wave rather than resisting it, the angled position of the paddle when it encounters the wave crest promotes further over-topping. This progressive decoupling in larger waves is a key design feature in the survivability of the device. There is no water jet like in the static simulation, however, the presence of the paddle does augment the wave profile and it appears that it induces wave breaking downstream of the paddle.

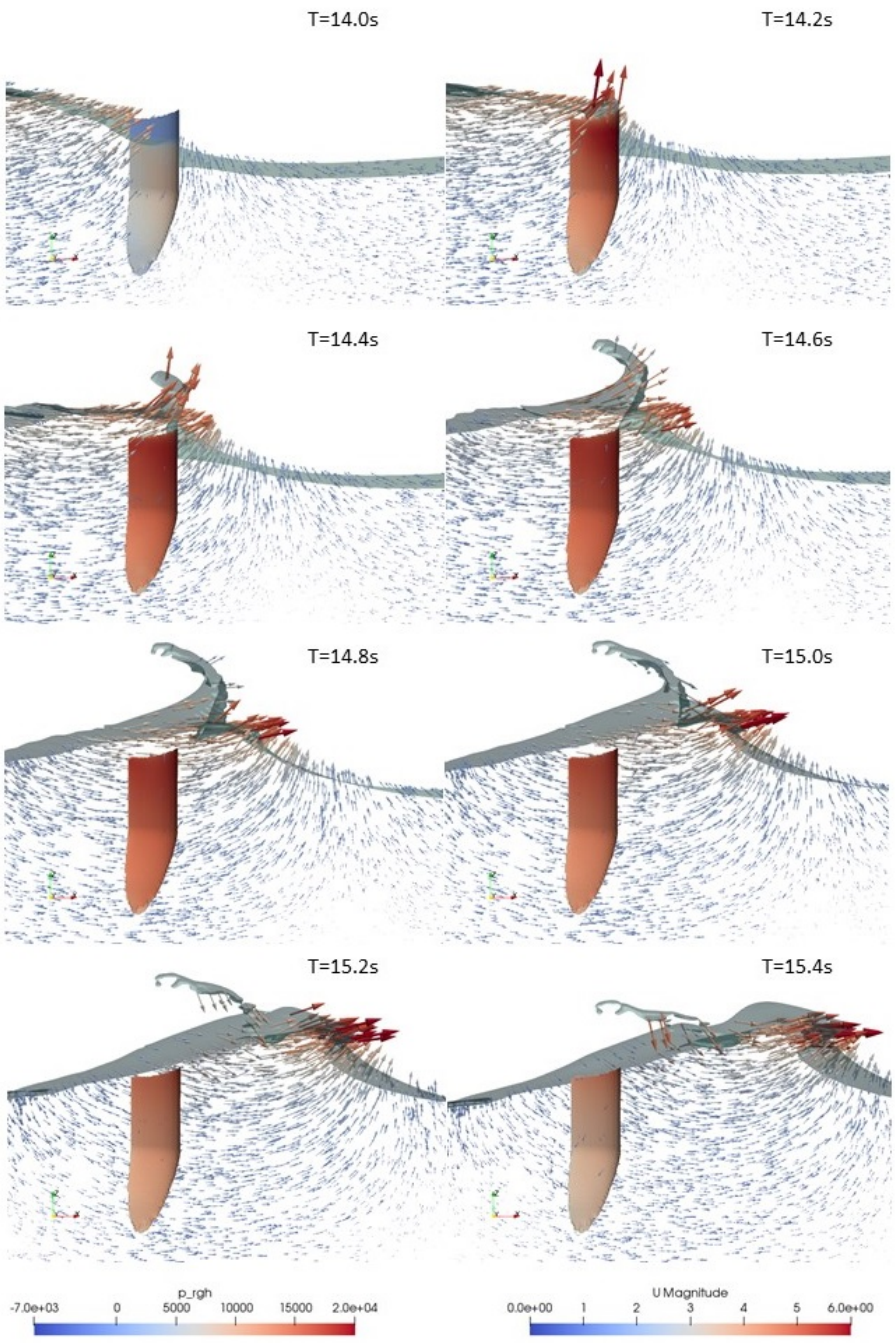

Figure 7.21: Snapshots from a static simulation of the CCell pilot device subjected to a NewWave profile (TMA-JONSWAP Spectrum Hs = 2.8m, Tp = 6s, depth = 5m). The paddle is coloured to represent the dynamic pressure (Pa). The arrows are both coloured and scaled in size according to the magnitude of velocity (m/s) and are aligned in the direction of the velocity.

The static simulation does not represent a normal operational state. The loading on the device when it is stationary in an upright position is much higher than the expected serviceable loads when the device is able to move with the waves. Comparing the peak pitch moments as

the structure is hit by the incoming NewWave crest, the static simulation calculates a value ~ 14.5 times that calculated in the dynamic simulation. This analysis is important though, as stipulated in technical specifications (International Electrotechnical Commission 2016) fault design situations when the device is operating with a single major system failure should also be included in design load cases. For it to be in this locked state, another component must have failed (e.g. bearing seized, PTO locked, piston deformed) and therefore it is unlikely that such a force could be resisted without something else giving way further. However, this can be used within the design process to reduce the magnitude of consequences: if the device is in this situation what can be sacrificed over other subsystems? The piston may be much less expensive to replace than the prime mover, for example, so a bolt could be selected to shear at a particular load in an attempt to preserve the paddle by letting it pitch freely and shed the load.

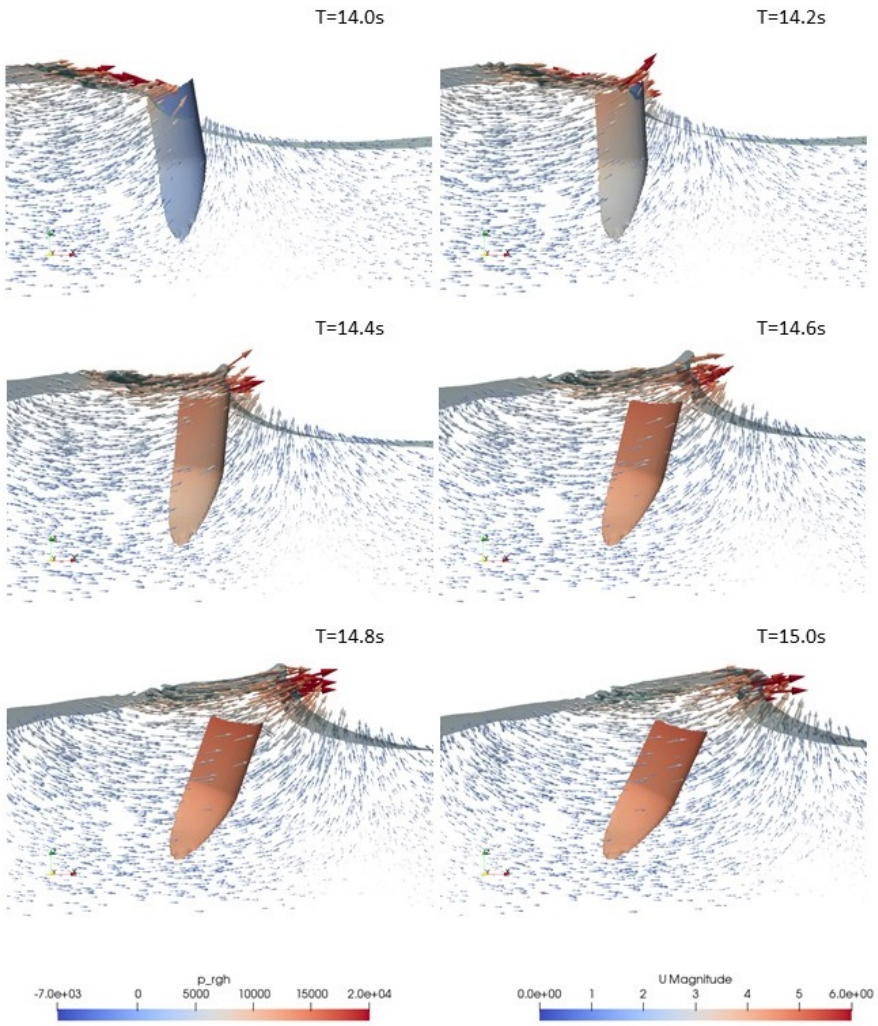

Figure 7.22: Snapshots from a dynamic simulation of the CCell pilot device subjected to a NewWave profile (TMA-JONSWAP Spectrum Hs = 2.8m, Tp = 6s, depth = 5m). The paddle is coloured to represent the dynamic pressure (Pa). The arrows are both coloured and scaled in size according to the magnitude of velocity (m/s) and are aligned in the direction of the velocity.

7.5 Discussion and Chapter Conclusions

Consideration of failure modes and survivability in extremes is all about risk analysis. The value that is afforded to the developer through a well devised modelling programme is the reduction in uncertainty surrounding this risk. During the design process, the developer must be aware of the magnitude and impact of structural loading that reflects the various conditions the device will be exposed to throughout its lifetime. These design load cases must consider both operational and extreme conditions as well as abnormal or accidental loads during transportation or installation. Combinations of extreme conditions and fault scenarios should also be explored. Informed by prior physical model testing and design practices in the oil and gas industry, three particular scenarios were identified as possible cases for heavy or abnormal loading, these are wave slam, directional waves and extreme waves. This chapter then discussed the development and output of suitable strategies and functionality to aid the understanding of the wave-structure interaction in these cases.

Although the sampling rate of the data acquisition system in tank testing was not high enough to properly capture peak loading, some conclusions could be drawn from a more qualitative analysis of the slam events, which were identified by their water jets. The constituents for a large slam event have been identified as: a train of large, relatively steep waves with flattened troughs; and a device with low damping to promote a large maximum shorewards angle and associated restoring moment prior to the impact. The 3D wake effects also influence the local steepness of the wave as it encounters the paddle wall and channels the water to the core of the paddle. It is clear that the loads are highly sensitive to the precise conditions the device is exposed to when it begins pitching seaward and when the slam occurs. This includes the exact position of the device and local wave shape.

The slam analysis has also raised some questions. It appears that the bottom shelf of the lab paddle provides resistance to the seaward motion and may reduce the overall slam load. For the fixed bottom device both the size of the shelf and location of the hinge point have been altered, which is expected to diminish this resistive effect and may result in increased angular velocity and subsequent slam loading. Furthermore, the floating device would be deployed in much deeper water, where waves are better approximated by linear wave theory as used in the tank testing. In the shallower waters of the pilot deployment site, the waves will be Cnoidal, which are characterised by flatter troughs that may exacerbate the slam problem.

Through trial and error, a pseudo-representative solution of a moderate slam event was achieved the CNWT, finding peak localised pressures twice as large as the peak pressures induced at the wave crest. However, this numerical investigation highlighted the difficulty in using numerical models alone. The probability of choosing the right states of the variables that effect occurrence of slam is slim and would require a large number of time intensive iterations. Further understanding of what incites slam, or concurrent physical investigation is recommended.

In shallow water the directionality of waves is effectively filtered due to bathymetry. However, this does not guarantee that the device will only encounter wave loading from the predominant direction. The impact on the power capture due to directional waves was found to be dependent on wave frequency, as observed in tank testing, though in most cases the reduction in

power is less than that anticipated from simple geometrical analysis. The design of the curved paddle alters the flow pattern to better align with the pitch axis, however this induces significant transverse loading on the support structure. The roll mechanism can alleviate this by allowing the paddle to follow a more circular path of motion.

An attempt was also made to identify a single maximum loading scenario of the paddle using a method adopted from the Oil & Gas industry called NewWave. Although stability issues persisted in the dynamic simulation of the NewWave design case, an estimate of the relative magnitude of loading in dyanmic and static extremes was found to be approximately fifteen-fold, with a slam like event occurring in the static simulation.

Furthermore, the qualitative observations of the surface elevation and wave dynamics in these extreme cases demonstrate the complex effects encountered in large waves that the CNWT is capable of simulating. It is not possible to evaluate this type of non-linear behaviour with other models as they would be operating far outside the region in which their assumptions are valid.

However, there are limits to the ability, or applicability, of CFD especially when computational time or cost are considered in the balance. For numerical modelling to be advantageous to the understanding of extremes, the developer must focus on quality rather than quantity of simulations, with carefully selected design cases. For example conducting a NewWave simulation at a non-optimal direction would be very time intensive as domain symmetry can no longer be used. However, by gathering an understanding of directionality in smaller waves, a suitable coefficient could be devised for the design process.

Part IV

Closing

Chapter 8

Conclusions

8.1 Conclusions drawn from Literature Review

Efforts to harness energy from the waves have been in development for the past 40 years. The initial progress that was spurred on by the Oil crisis was a false start for the industry, however, since the millennium there has been a concerted effort to develop a commercially viable WEC device. The opportunity to address the energy trilemma with a renewable resource that is available in abundance around the UK has not been overlooked by the government and a number of schemes to incentivise this innovation have been conceived. However, the initial promise of the sector has yet to materialise.

The marine environment is one of the harshest on the planet and the engineering challenge of designing a device to endure conditions at sites that have been chosen for their increased energy, should not be underestimated. The legitimacy of the industry has been repeatedly undermined by such overly-optimistic evaluations and development trajectories.

The cost of full-scale prototypes has been historically destabilising and higher fidelity numerical modelling is essential in progressing the performance of the technology as well as comprehensively de-risking the device before these costs are incurred. Improved performance-to-cost ratios of computers and the advent of cloud computing have removed many of the barriers to entry for WEC developers to use sophisticated fully non-linear numerical models. However, it is difficult for a developer to justify the additional computational expense and expertise required to accurately implement CFD unless its power and value are fully exploited.

Open-source CFD tool boxes like OpenFOAM, are unique in that they allow access to the source code and it can be directly customised and freely parallelised. Together this allows a higher technological performance level to be achieved at lower costs and technology readiness levels. Assessment of existing numerical strategies available to WEC developers, as well as the likely non-linearities that affect the operation of OWSCs, concluded that the CFD approach is necessary. OpenFOAM's VOF interface method has been used to solve the governing Navier-Stokes equations for a two phase domain, establishing the basis of a CNWT.

8.2 Modelling WECs in Operational Conditions

Two of the most important metrics on which the viability of a wave energy project is judged is the estimate of the project's power production and the measure of uncertainty associated with that prediction. There are four main sources of uncertainty that affect the MAEP calculation: wave measurement instruments; limited duration of wave resource data set; accuracy of wave propagation models; and limitations of methodology used to determine device performance. Although, variability in wave climate is often cited as being responsible for a large portion of reported uncertainty, the outcomes of this work suggests that the last source of uncertainty is also sizeable. Clearly, at later stages in the development process, the CWR matrix would be more accurately populated from physical test data in irregular seas. However, at the early stages of design, when many key decisions are made, inaccuracies in power estimates in regular waves (which have been observed in excess of 30%) can influence the design decisions with some concepts wrongly discarded.

8.2.1 Non-linear Hydrodynamics

At TRL 4 it is recommended that medium scale physical tests and time domain modelling be used for design optimisation and power performance matrix characterisation. Time domain models based on the Cummins equation can model transients but they still fundamentally rely on hydrodynamic coefficients derived from other sources (numerical or physical). Therefore, the appropriate definition of these hydrodynamic coefficients is intrinsic to the accuracy of the power estimates.

Previous research has suggested that potential theory is accurate for pitching devices up to a 0.3rad oscillation amplitude, or for $K_C < 3$, but for OWSCs this demarcation appears incorrect. Linear codes may be sufficient for certain modes of motion or for more simple geometries such as spheres or cylinders but an OWSC (either flat or curved) has important contributions from radiation, diffraction and viscous effects, as shown in the CNWT. The increased motions of the free surface and large vortical structures that get washed back and forth past the device compromise the reliability of potential theory as the core assumptions are rendered invalid. This is particularly true of the expected linear relationship between excitation force and wave height, which was revealed to be unfounded for OWSCs from static simulation in the CNWT.

In a comparative exercise evaluating radiation coefficients predicted by FOT tests in the CNWT and the BEM code NEMOH, it was found that the methods predict a similar relationship with regards to frequency of oscillation though NEMOH consistently calculates coefficients of smaller magnitude. When input into a WECSim simulation of a flat OWSC, the use of the FOT coefficients translated to an average 26% reduction compared to the power estimated by NEMOH values across the operational frequency range for a 0.8m wave.

Furthermore, unlike the flat paddle, the CCell device behaves very differently depending on direction of motion and has distinct seawards and shorewards radiation coefficients. This directionality is overlooked in the BEM analysis and it cannot be incorporated in the current formulation of WECSim. However, the bigger source of error in the analysis of CCell was the estimation of excitation force from NEMOH.

8.2.2 Non-linear PTO

One of the most important sub systems regarding the ultimate power output is the PTO system. The mutual dependency of the hydrodynamics of the WEC and the resulting PTO damping force require that the two systems are solved together in a coupled manner. Non-linearitites of the flow in hydraulic systems, particularly those that incorporate accumulators, are not sufficiently represented by a linear damper and to achieve TRL 5, full non-linear simulation of the integrated sub system is required.

A close comparison between the high-fidelity PTO model and commercial codes was achieved for the pressure drop across the motor due to sinusoidal piston motion, with the maximums equivalently predicted but the amplitude of fluctuation underpredicted by $\approx$6.7%. The high-fidelity PTO model also offered a significant reduction in computational time, taking only 0.257s to compute 300s of simulation time instead of the 66.11s required for Simscape. The new PTO model was then fully coupled to the CNWT, with bidirectional flow of information, to provide more realistic damping restraint on the WEC. One issue encountered with the PTO model is the need to correctly parameterise real hydraulic components, which are not often supplied in such detail by the part manufacturer. However, it is beneficial in the design process to both size required components and inform initial control parameters.

Through comparison with the existing simplified PTO models, it was found that a hydraulic PTO without accumulators can be reasonably simulated as a linear damper, whereas the inclusion of accumulators is better approximated with a constant force. However, determination of a single parameter to represent the full system is difficult to predict and can have a significant impact on the accuracy of power or motion estimation. This was particularly evident for the Coulombic representation of the PTO system as an overly large constant force prevented any motion in smaller waves and in average wave conditions the angular velocity was half the value predicted by the high-fidelity PTO model.

8.2.3 Physical Modelling and Validation

A continuing frustration of the work conducted in this thesis has been lack of data to properly validate the CNWT extensions and strategies that have been developed. However, a concerted effort has been made to fully exploit the data and resources available, with tests designed to isolate different functionality of the CNWT and match capabilities as closely as possible. Decoupling of different model attributes can inform the developer of the origin of any errors or uncertainties as well as improve the confidence in less complex scenarios. Therefore, in addition to characterisation of the power performance matrix the developer should also conduct:

- Free decay tests with the PTO unattached
- Wave loading of the stationary structure
- Undamped testing in operational conditions
- FOT tests both in the water and in the air
- Centre of gravity and inertia analysis for composite paddles

In order to capture relevant information, the instrumentation must also be carefully considered and should include:

- Full motion capture of the device through a system such as Qualisys
- Measurement of the wave field up stream, inline and downstream of the device
- Surface mounted pressure probes and wave gauges near the centre line of the paddle on both faces
- Force transducers on the piston and on the support structure.

The sampling rate of data capture is also vitally important to success of validation studies, for example, the impulsive nature of slam loading requires a sampling rate of at least 2kHz to sufficiently capture the event.

8.3 Evaluating and Enhancing WEC Survivability

Evaluation of a device's survivability is a complex task. There are a number of failure mechanisms to consider over a variety of timescales as well as considerable uncertainty in the conditions that induce the largest loads on a WEC and how often they occur. In addition, analysis of WEC dynamics in extreme waves is limited by scale in physical wave tanks, whilst in numerical modelling the steepness of the waves and amplitude of WEC motion can compromise accuracy.

Long term simulations, or a large quantity of shorter ones, are not feasible in the CNWT to sufficiently populate a statistical analysis. An alternative deterministic method was sought to investigate the maximum loading on a WEC. This involved the use of the NewWave profile, the average shape of an extreme for a given spectrum. However, determination of an appropriate scaling parameter for the crest is more difficult. In deep water, rogue waves have been observed that are too large and appear too often to be consistent with Rayleigh type statistical models. Other effects such as crossing seas and current interactions may lead to impractically large wave heights that should have theoretically broken, yet have been encountered. In shallow water, interactions between the waves and the bathymetry also impacts extremes and it is unclear what the subsequent height may be as shoaling may induce breaking long before the extreme reaches the deployment site. To overcome this, the TMA transformation was used to accommodate the spectral changes due to finite depth and a 1 in 1000 wave of the steepest sea state was chosen.

The excessive size and steepness of the wave induced some instability in the numerical formulation in the CNWT as it transitioned from the relaxation zone to the rest of the domain. In the absence of experimental data it was unclear whether this was a result of shoaling or inadequate definition of fluid properties. A sea state of similar steepness and occurrence was instead selected and a mesh with 30 cells per metre of wave height was found to represent the crest well, though the simulated troughs were not as deep as the NewWave profile dictated.

Successful static simulations of the CCell paddle were conducted showing the complexities of the surface profile at wave impact, though the mesh design needs further work for dynamic simulations in very steep or breaking waves. However, the simulation progressed sufficiently

to demonstrate the reduction in reaction forces possible from determination of appropriate survival strategies. Progressive decoupling of induced forces from large waves is inherent to the design of an OWSC due to both overtopping and the reduction of the vertical projected area as the paddle pitches further shoreward. By allowing the paddle to move more freely with the waves, the forces are also reduced. In comparison to a stationary paddle, the lightly damped paddle reduce the reaction torque by more than fourteen-fold. The only issue with a completely undamped paddle, is the limit imposed on the motion due to the finite stroke of the piston.

As with the use of frequency modelling in WEC dynamics, adopting other practices used for offshore structures in the Oil and Gas industry should be carefully considered. The NewWave extreme event was devised to analyse extreme loading of large static structures and evaluate design considerations such as the location of the deck of a platform. Use of this type of design wave assumes that the maximum loading is directly correlated to the maximum crest height. However in the case of dynamic WECs, the maximum loading is affected by other interdependencies and dynamics within the system such as the previous position or motion of the device, the direction of the incoming wave and the control of the PTO system. Exceptionally high loads can occur when the device is stationary in large waves, but equally shock loads or impulse loads are possible if the device suddenly stops e.g. due to physical end-stops in the PTO system.

Wave slam has been noted as a particular challenge for OWSCs. However, the occurrence of slam loading is highly sensitive to wave shape, turbulent wakes and WEC dynamics (including restoring moment due to buoyancy, inertia and level of PTO damping). From analysis of the wave structure interaction it was concluded that slam may be worse for the pilot deployment paddle than it was for the floating concept evaluated in tank testing. This is because the waves in shallow water have flatter troughs and the bottom shelf of the paddle, which previously prevented free fall, has been removed. The number of influencing parameters restrict the ability of numerical modelling to evaluate slam unless the required conditions have been predetermined in tank testing of, crucially, regular waves as these are easier to replicate numerically.

The cyclic nature of wave loading and dynamics of a WEC, even in small waves, can greatly impact the life of individual components used within the WEC. Although, the CNWT cannot be used to directly investigate the processes such as fatigue, which occur over long time scales, it can inform probabilistic methods with estimates of loads and motions for different operational and extreme wave conditions.

8.4 Recommended CNWT strategy

Accuracy of CFD simulations are hampered by both modelling assumptions and numerical errors. In the development of the CNWT a number of solver parameters and domain configurations have been considered to reduce the effect of these errors. The main conclusions drawn from the initial specification of the basic CNWT are:

- Truncated computational domains induce wave reflections from the boundaries unless suitable absorption or dissipation techniques are used. From previous studies, it was

found that the relaxation zone method was most appropriate when short or steep waves are modelled. However, proper implementation increases the domain size by at least an additional wave length, incurring significant additional computational expense. These relaxation zones are currently only employed at the inlet and outlet boundaries, however, the 3D nature of the wave-structure interactions create radiating waves from the WEC in all directions.

- VOF methods are known to suffer from diffusion of the free surface, thus a high concentration of cells with equal height and width are required for good representation. In highly nonlinear waves and areas of turbulence, a finer mesh should be used and adaptive time stepping should always be enabled to preserve the CFL stability criterion in transient conditions. However, an excessive amount of cells requires more memory and takes longer to solve. Therefore, careful mesh design is used to concentrate cells in areas of high mass flux. Using the inherent numerical dissipation that comes with spatial discretisation, graduation of cell size away from areas of interest can be used to prevent wave reflections.
- To expedite the simulation in the CNWT, mesh distortion rather than re-meshing at each time step has been used. However, this imposes a limit on the maximum motions that can modelled in the CNWT prior to the simulation failing. OpenFOAM's mesh deformation functionality has been successfully used in displacements up to $\pm 45^o$, provided that the initial mesh has appropriate non-orthogonality and skewness. This is sufficient for most modelling applications, except, for example, an undamped paddle in large waves.
- An influential parameter for stability in dynamic simulations was found to be the acceleration relaxation factor, which needed to be sufficiently small to prevent unrealistic spikes in acceleration. In order to determine this factor, the relative magnitude of the device's mass and added mass are used.

Initiatives like the CCPWSI can help developers verify the specification of their CNWT and may delay the need for physical modelling. However, for full validation of the numerical model and to understand feasibility of manufacture or installation physical models are still required. A combined program of both higher-fidelity numerical modelling and physical modelling can also overcome some of the scaling issues of relying solely on tank testing, or the uncertainty issues of simulations. Increased confidence in these model outputs, with a clearer indication of realistic performance and a better understanding of maximum device loading can accelerate the WEC design process and attract investors.

From the perspective of the sponsor company, the desired output of this work was a robust modelling methodology to be used throughout the design process: from initial specification when first approached about a new deployment site to more detailed design work. Through the work conducted in this thesis a recommended strategy for using the CNWT to evaluate WEC designs has been developed:

- Characterise the operational wave climate of the deployment location with no more than 10 regular wave conditions that incorporate both the highest energy and highest occurring seas. These should also cover a range of frequencies and wave heights in order to provide an understanding of the effect of both parameters. From these 10 sea states one or two key wave conditions should be prioritised for a more thorough analysis.

- Conduct FOT tests with oscillation periods that reflect the range of wave frequencies and an average oscillation amplitude to calculate radiation coefficients. Input these values into the damping equation derived from potential theory to determine the expected optimal level of damping.
- Conduct static simulations to provide an estimate of excitation moment and the ratio of the peak values experienced in the trough and crest of the wave. A value $\sim$10-15% larger than this provides a good approximation to the seaward to shoreward damping ratio for a stable dynamic simulation.
- Evaluate the cycle-averaged power output over at least 7 cycles of a dynamic simulation in each of the characteristic wave conditions.
- Investigate the effect of waves from a non-optimal direction by orienting the paddle in the CNWT and implement multiple degrees of freedom to allow roll and pitch motions.
- Identify design cases that reflect appropriate limit states of the device and individual sub systems. The induced torques or pressure distributions in these cases can be input into other FEM software to ensure efficient structural design.

8.5 Impact

The work detailed in this thesis not only provides analysis on a particular design but has developed a best practice for WEC optimisation in a CNWT for the sponsor company. This was delivered as a series of templates for simulation set-up, which are automated from a single parameter specification file. OpenFOAM does not have a user interface and the user must input parameters in a number of different files and folders, thus without this specification there is a considerable chance of incorrectly setting up the simulation and wasting computing time.

Prior to this doctoral research only stable simulations of static paddles were reliably achieved. Achieving the enhanced modelling capabilities has involved analysis of key parameters such as meshing, rigid body dynamics, wave generation and absorption and solver stability to refine the CNWT. Through the increased understanding of the wave-structure interactions provided by the CNWT, the pilot deployment design was chosen and simulations predict that its CWR in predominant wave conditions is 69.8% larger in comparison to an equivalent flat paddle. The structural design team have also gained confidence in the sizing of supporting elements as previously they had relied on moments induced on a stationary paddle.

Limitations of the CNWT were identified as firstly, the linear representation of the PTO system and secondly, the ability to evaluate the device in non-optimal conditions. This led to the development of suitable extensions to the CNWT including: a high-fidelity hydraulic PTO model; specification for FOT tests; implementation of multiple degrees of freedom in directional waves; and formulation of a deterministic extreme wave profile. Together these tools allow a rigorous assessment of the viability of a candidate paddle design in operational and non-optimal conditions, which can be conducted within three weeks. Previously, much of this information could not have been gathered without tank testing at multiple scales to allow for limitations when considering survivability. Although these physical tests are still required during the development of a WEC and are invaluable in assessing the ease of deployment

and maintenance, they can be delayed so that the developer only incurs expensive prototype demonstration when sufficient confidence is gained in the concept.

8.6 Further Work and Future Considerations

Lab testing

Validation, or further understanding of the limits of the CNWT through experimental data, in both operational and extreme loading cases, would increase confidence in the model outputs and allow the device to be more thoroughly tested and de-risked prior to expensive prototype demonstrations. However, as physical model testing also involves some approximations an understanding of the uncertainty from experimental estimates is also required, which can only come from real sea tests. Without increased transparency between developers or from bodies such as WES this will remain a barrier.

Irregular waves

Except for the NewWave profiles, all wave conditions considered in the CNWT have thus far been regular, monochromatic waves. However, this is not representative of real wave conditions. Irregular waves defined by sea spectra will always be problematic in modelling as the simulations must be of finite time length, which introduces limits to their accuracy. Furthermore, both physical and numerical wave tanks suffer from increased reflections as the length of the simulation increases. Attempting to investigate irregular waves in the CNWT is likely to be an inefficient use of resources, however assuming performance estimates from regular waves defined by the peak period and significant wave height is clearly flawed. The alternative is to use RAOs or power transfer functions though as this work has shown the assumption of linearity with regards to wave height is of limited accuracy for an OWSC. To truly progress in this area a large quantity of real deployment data is required.

Improvements to CFD

A number of improvements could still be made to the proposed CNWT to optimise specification of parameters for stability and accuracy of solution. These relate mainly to choice of solvers and their effect on the representation of the surface profile. Further optimisation of the mesh, boundary conditions and size of the domain should also be conducted to reduce execution times.

The only validation possible for the CNWT in this work was data from the laboratory testing of the floating system, in which Stokes was appropriate, thus Stokes wave theory has been adopted throughout. However, consideration of the Ursell number for the deployment conditions suggests that Cnoidal theory is more representative and that linear theory becomes unstable. Wave generation and absorption of these more non-linear waves, including wave breaking, and their underlying kinematics should also be further evaluated.

Control

A significant contributor to the ultimate success of a WEC will be the implementation of a suitable control strategy to both optimise power output in operational conditions and reduce loading in extreme conditions. This will be achieved through a control system, which provides a time-varying damping profile. For PTO systems incapable of bi-directional power flows, as is the case for the hydraulic PTO used in CCell, this is limited to resistive loading control, which alters only the amplitude of the prime mover's velocity. Passive strategies such as latching could be used to hold back the paddle when the velocity reduces and then release it at an appropriate point in the cycle to optimise the power capture. Currently the effect of such a strategy cannot be evaluated in the CNWT. It is possible to extend the formulation of the motion restraint, as was done to incorporate directionality of motion. However, this could dramatically alter the stability or execution time due to the iterative nature of the solution.

References

Adcock, Thomas A A and Paul H Taylor (Oct. 2014). “The physics of anomalous (‘rogue’) ocean waves”. In: *Reports on Progress in Physics* 77.10, p. 105901. DOI: 10.1088/0034-4885/77/10/105901. URL: https://doi.org/10.1088%5C%2F0034-4885%5C%2F77%5C%2F10%5C%2F105901.

Anonymous (May 3, 2019). Personal communication with former employee of Aquamarine.

Antolin-Urbaneja, Juan et al. (Mar. 2015). “Modeling Innovative Power Take-Off Based on Double-Acting Hydraulic Cylinders Array for Wave Energy Conversion”. In: *Energies* 8, pp. 2230–2267. DOI: 10.3390/en8032230.

Arnold, Alex (2010). *Port Kembla wave generator on sea floor*. URL: https://www.illawarramercury.com.au/story/628562/port-kembla-wave-generator-on-sea-floor/. Accessed on 2019-05-03.

Artemis Intelligent Power (2017). *Hybrid Digital Displacement hydraulic PTO for wave energy: WES Power Take Off Stage 2 Project Public Report*. Tech. rep. URL: https://library.waveenergyscotland.co.uk/development-programmes/power-take-off/stage-2/pt21_art/.

AW Energy (2018). *WaveRoller - Plug into wave energy*. URL: http://aw-energy.com/wp-content/uploads/2018/03/a5_web_pdf_spreads.pdf. Accessed on 2019-05-05.

AWS Ocean Energy Ltd (2016). *Submerged wave power buoy - reliable and affordable wave power solution.* URL: http://www.awsocean.com/technology.html. Accessed on 2019-05-07.

Babarit, Aurélien (2015). “A database of capture width ratio of wave energy converters”. In: *Renewable Energy* 80, pp. 610–628. ISSN: 0960-1481. DOI: https://doi.org/10.1016/j.renene.2015.02.049. URL: http://www.sciencedirect.com/science/article/pii/S0960148115001652.

Babarit, Aurélien and Gérard Delhommeau (Sept. 2015). “Theoretical and numerical aspects of the open source BEM solver NEMOH”. In: Proceedings of the 11th European Wave and Tidal Energy Conference. URL: https://hal.archives-ouvertes.fr/hal-01198800.

Babarit, Aurélien, Matt Folley, et al. (2013). “On the modelling of WECs in wave models using far field coefficients”. In: Proceedings of the 10th European Wave and Tidal Energy Conference.

Babarit, Aurélien, J. Hals, et al. (2012). “Numerical benchmarking study of a selection of wave energy converters”. In: *Renewable Energy* 41, pp. 44–63. DOI: 10.1016/j.renene.2011.10.002. URL: https://www.scopus.com/inward/record.uri?eid=2-s2.0-84155172206%5C&doi=10.1016%5C%2fj.renene.2011.10.002%5C&partnerID=40%5C&md5=31bbbf034626083d3d9d917f27ff53c1.

Babarit, Aurélien, Hakim Mouslim, et al. (2009). “On the Numerical Modelling of the Non Linear Behaviour of a Wave Energy Converter”. In: Proceedings of the International Conference on Offshore Mechanics and Arctic Engineering. URL: http://dx.doi.org/10.1115/OMAE2009-79909.

Bakker, André (2006). *Applied Computational Fluid Dynamics*. URL: http://www.bakker.org/dartmouth06/engs150/03-cnsrv.pdf. Dartmouth College Online Lecture Notes Accessed on 2019-05-16.

Bard, Jochen and Peter Kracht (2013). *Linear Generator Systems for Wave Energy Converters*. Tech. rep. URL: https://www.sdwed.civil.aau.dk/digitalAssets/97/97525_d3.2.pdf.

Bateman, Will (2018). *CCell*. URL: https://www.ccell.co.uk/technology-ccell.php. Accessed on 2019-05-07.

Blahut, Richard E. (2002). "25 - Information Theory and Coding". In: *Reference Data for Engineers (Ninth Edition)*. Ed. by Wendy M. Middleton and Mac E. Van Valkenburg. Ninth Edition. Woburn: Newnes, pp. 25-1 - 25–31. ISBN: 978-0-7506-7291-7. DOI: https://doi.org/10.1016/B978-075067291-7/50027-3. URL: http://www.sciencedirect.com/science/article/pii/B9780750672917500273.

Carcas, M., G. Davies, and G. Edge (2017). *Wave & Tidal Energy: State of the Industry*. Tech. rep. ClimateXChange. URL: https://www.climatexchange.org.uk/media/3100/state-of-the-wave-and-tidal-industry-report.pdf.

Cargo, Christopher (2012). "Design and Control of Hydraulic Power Take-Offs for Wave Energy Converters". PhD thesis. University of Bath.

Carnegie Clean Energy (2017). *What is Ceto?* URL: https://www.carnegiece.com/wave/what-is-ceto/. Accessed on 2019-05-07.

CCP-WSI (2017). *Collaborative Computational Project in Wave Structure Interaction: Working Group*. URL: https://www.ccp-wsi.ac.uk/. Accessed on 2019-04-16.

CFD Direct (2017). *About OpenFoam*. URL: https://cfd.direct/openfoam/about/. Accessed on 2019-05-09.

CIRIA, CUR, CETMEF (Jan. 2007). *The Rock Manual. The use of rock in hydraulic engineering (2nd edition)*. C683, CIRIA, London, ISBN 978-0-86017-683-1.

Craft, T. J. (2018). *Unsteady Problems*. URL: http://cfd.mace.manchester.ac.uk/twiki/pub/Main/TimCraftNotes_All_Access/cfd1-pt7.pdf. Accessed on 2019-05-06.

Crooks, David et al. (2016). "Oscillating Wave Surge Converter Forced Oscillation Tests". In: *Volume 6: Ocean Space Utilization; Ocean Renewable Energy*. International Conference on Offshore Mechanics and Arctic Engineering. DOI: 10.1115/OMAE2016-54660.

Cummins, W. E. (1962). "The impulse response function and ship motions". In: *Symposium on Ship Theory* 9, pp. 101–109. URL: www.scopus.com.

Davidson, Lars (2005). *Numerical Methods for Turbulent Flow*. URL: http://www.tfd.chalmers.se/~lada/comp_fluid_dynamics/postscript_files/chapter_6.pdf. Chalmers University of Technology Online Lecture Series Accessed on 2019-05-15.

DBEIS (2017). *Contracts for Difference Second Allocation Round Results*. URL: https://assets.publishing.service.gov.uk/government/uploads/system/uploads/attachment_data/file/643560/CFD_allocation_round_2_outcome_FINAL.pdf. Accessed on 2019-05-07.

Dean, R. G. (1965). "Stream function representation of nonlinear ocean waves". In: *Journal of Geophysical Research (1896-1977)* 70.18, pp. 4561–4572. DOI: 10.1029/JZ070i018p04561. eprint: https://agupubs.onlinelibrary.wiley.com/doi/pdf/10.1029/JZ070i018p04561. URL: https://agupubs.onlinelibrary.wiley.com/doi/abs/10.1029/JZ070i018p04561.

Dean, Robert and Robert Dalrymple (1993). *Water Wave Mechanics for Engineers and Scientists*. Advanced Series on Ocean Engineering - World Scientific.

Delft University of Technology (2019). *SWAN*. URL: https://www.tudelft.nl/en/ceg/about-faculty/departments/hydraulic-engineering/sections/environmental-fluid-mechanics/research/swan/. Accessed on 2019-08-16.

Devolder, Brecht, Pieter Rauwoens, and Peter Troch (2017). "Application of a buoyancy-modified k-w SST turbulence model to simulate wave run-up around a monopile subjected to regular waves using OpenFOAM". In: *Coastal Engineering* 125, pp. 81–94. ISSN: 0378-3839. DOI: https://doi.org/10.1016/j.coastaleng.2017.04.004. URL: http://www.sciencedirect.com/science/article/pii/S0378383917302107.

Devolder, Brecht, Pál Schmitt, et al. (Sept. 2015). "A Review of the Implicit Motion Solver Algorithm in OpenFOAM to Simulate a Heaving Buoy". In: Proceedings of the 18th Numerical Towing Tank Symposium (NuTTS'15). URL: https://pureadmin.qub.ac.uk/ws/files/17075637/NuTTS_18_2015_Devolder_et_al.pdf.

Devolder, Brecht, Peter Troch, and Pieter Rauwoens (2018). "Performance of a buoyancy-modified k-w and k-w SST turbulence model for simulating wave breaking under regular waves using OpenFOAM". In: *Coastal Engineering* 138, pp. 49–65. ISSN: 0378-3839. DOI: https://doi.org/10.1016/j.coastaleng.2018.04.011. URL: http://www.sciencedirect.com/science/article/pii/S0378383917304696.

Douglas, J. et al. (2011). *Fluid Mechanics*. Pearson Education Limited.

Edinburgh Designs (2016). *Edinburgh Designs About Us*. URL: http://www4.edesign.co.uk/our-story/. Accessed on 2019-04-15.

Edwards, Emma (2018). *Introduction to the Linear Panel Method WAMIT*. URL: http://web.mit.edu/2.29/www/img/projects/spring_2018/emma.pdf. Accessed on 2019-05-03.

EUMETSAT (2016). *Jason-3*. URL: https://www.eumetsat.int/website/home/Satellites/CurrentSatellites/Jason3/index.html. Accessed on 2019-08-16.

European Space Agency (2019). *Sentinel 6 - Mission Summary*. URL: https://sentinel.esa.int/web/sentinel/missions/sentinel-6/mission-summary. Accessed on 2019-10-08.

Evans, D. V. (1976). "A theory for wave-power absorption by oscillating bodies". In: *Journal of Fluid Mechanics* 77.1, pp. 1–25. DOI: 10.1017/S0022112076001109.

Fenton, John D. (1990). *Nonlinear Wave Theories. Chapter in The Sea: Vol. 9. Ocean engineering science*. Wiley-Interscience. URL: https://books.google.co.uk/books?id=83e6ygAACAAJ.

Folley, Matt, Trevor Whittaker, and Alan Henry (June 2007). "The effect of water depth on the performance of a small surging wave energy converter". In: *Ocean Engineering* 34 (8-9).8-9, pp. 1265–1274. ISSN: 0029-8018. DOI: 10.1016/j.oceaneng.2006.05.015.

Folley, Matt, Trevor Whittaker, and J. van't Hoff (Sept. 2007). "The Design of Small Seabed Mounted Bottom Hinged Wave Energy Converters". English. In: Proceedings of the 7th European Wave and Tidal Energy Conference, pp. 1–10. URL: http://citeseerx.ist.psu.edu/viewdoc/download?doi=10.1.1.463.6232%5C&rep=rep1%5C&type=pdf.

Gingold, R. A. and J. J. Monaghan (Nov. 1977). "Smoothed particle hydrodynamics - Theory and application to non-spherical stars". In: *Monthly Notices of the Royal Astronomical Society*, pp. 375–389. URL: http://adsabs.harvard.edu/full/1977MNRAS.181..375G.

Giorgi, Giuseppe and John V. Ringwood (Aug. 2018). "Comparing nonlinear hydrodynamic forces in heaving point absorbers and oscillating wave surge converters". English. In: *Journal of Ocean Engineering and Marine Energy* 4.1, pp. 25–35. DOI: 10.1007/s40722-017-0098-2.

Goreau, Thomas J. (2012). “Marine Electrolysis for Building Materials and Environmental Restoration”. In: *Electrolysis*. Ed. by Vladimir Linkov and Janis Kleperis. Rijeka: IntechOpen. Chap. 13. DOI: 10.5772/48783. URL: https://doi.org/10.5772/48783.

Greenshields, Chris (2016). *OpenFOAM User Guide V4*. Tech. rep. CFD Direct. URL: https://cfd.direct/openfoam/user-guide-v4/.

Guy, Ryan L. (2015). *Smoothed Particle Hydrodynamics Fluid Simulation*. URL: http://rlguy.com/sphfluidsim/. Accessed on 2019-08-03.

Hannon, Matthew, Renée Van Diemen, and Jim Skea (Nov. 2017). *Examining the Effectiveness of Support for UK Wave Energy Innovation since 2000 : Lost at Sea or a New Wave of Innovation?* Published by the University of Strathclyde’s International Public Policy Institute (IPPI). Glasgow. URL: https://strathprints.strath.ac.uk/62210/.

Henry, Alan et al. (May 2014). “The Characteristics of Wave Impacts on an Oscillating Wave Surge Converter”. In: *Journal of Ocean and Wind Energy* 1.2, pp. 101–110. ISSN: 2310-3604. URL: https://www.researchgate.net/publication/283634078_The_Characteristics_of_Wave_Impacts_on_an_Oscillating_Wave_Surge_Converter.

Hinch, John (2017). *Boundary Integral Method*. URL: http://www.damtp.cam.ac.uk/user/hinch/teaching/CMIFM_Handouts/BIMHandout.pdf. Accessed on 2019-05-03.

Holmes, Brian (2009). *Tank Testing of Wave Energy Conversion Systems, Marine Renewable Energy Guides*. Tech. rep. European Marine Energy Centre Ltd.

Hughes, Steven A. (1984). *The TMA shallow-water spectrum -description and applications*. Tech. rep. Technical Report CERC84-7. US Army Engineer Research Station.

International Electrotechnical Commission (2012). *Marine energy – Wave, tidal and other water current converters – Part 100: Electricity producing wave energy converters – Power performance assessment*. Tech. rep. TS 62600-100:2012. BSI Standards Publication.

– (2016). *TC 114 - Marine energy - Wave, tidal and other water current converters- Part 2: Design requirements for marine energy systems*. Tech. rep. TS 62600-2:2016. BSI Standards Publication.

Invertek Drives (2016). *OptiDrive E3: AC Variable Speed Drive User Manual V2.0*. URL: https://www.invertekdrives.com/client-uploads/download-manager/user-guides/GB_Optidrive_E3_User_Guide.pdf.

Iturrioz, A. et al. (2015). “Validation of OpenFOAM® for Oscillating Water Column three-dimensional modeling”. In: *Ocean Engineering* 107, pp. 222–236. ISSN: 0029-8018. DOI: http://dx.doi.org/10.1016/j.oceaneng.2015.07.051. URL: http://www.sciencedirect.com/science/article/pii/S0029801815003649.

Jacobsen, Niels G., David R. Fuhrman, and Jørgen Fredsøe (2012). “A wave generation toolbox for the open-source CFD library: OpenFoam®”. In: *International Journal for Numerical Methods in Fluids* 70.9, pp. 1073–1088. ISSN: 1097-0363. DOI: 10.1002/fld.2726. URL: http://dx.doi.org/10.1002/fld.2726.

Jacobson, Paul T, George Hagerman, and George Scott (Dec. 2011). “Mapping and Assessment of the United States’ Ocean Wave Energy Resource”. In: DOI: 10.2172/1060943.

JBJ Techniques Ltd (2016). *Gear Motors*. URL: https://www.jbj.co.uk/e-publications/ALM-series-gear-motors-from-jbj-Techniques-Limited/43/. Accessed on 2019-06-04.

Journee, J.M.J. and W.W. Massie (2001). *Offshore Hydromechanics, Chapter 12 - Wave Forces on Slender Cylinders*. Accesesd on 2019-06-15. Delft University of Technology. URL: https://ocw.tudelft.nl/wp-content/uploads/OffshoreHydromechanics_Journee_Massie.pdf.

Kempener, Ruud and Frank Neumann (2014). *Wave Energy Technology Brief*. Tech. rep. URL: https://www.irena.org/documentdownloads/publications/wave-energy_v4_web.pdf.

Kenny, Calum et al. (Aug. 2017). "Lessons Learned from 3 Years of Failure: Validating an FMEA using Historical Failure Data". In: Proceedings of the 12th European Wave and Tidal Conference. URL: https://pdfs.semanticscholar.org/d372/bbbee4633106727f1255d4e8a68754e9f678.pdf?_ga=2.90280922.1557618103.1573318239-276092223.1573318239.

Kersale, Evy (2018). *Potential Flows*. URL: http://www1.maths.leeds.ac.uk/~kersale/2620/Notes/chapter_4.pdf. University of Leeds Online Lecture Series Accessed on 2019-05-03.

Kingston, William (2017). "Review Essay: Examining the Effectiveness of Support for UK Wave Energy Innovation since 2000. Lost at Sea or a New Wave of Innovation?" In: *Prometheus* 35.2, pp. 145–158. DOI: 10.1080/08109028.2018.1486534. URL: https://doi.org/10.1080/08109028.2018.1486534.

Ko, Haeng Sik et al. (2018). "Numerical and Experimental Study for a Cylindrical Wave Energy Converter With Different Rotational Axes". In: Proceedings of The 28th International Ocean and Polar Engineering Conference. URL: https://www.onepetro.org/conference-paper/ISOPE-I-18-477.

Launder, B.E. and D.B. Spalding (1974). "The numerical computation of turbulent flows". In: *Computer Methods in Applied Mechanics and Engineering* 3.2, pp. 269–289. ISSN: 0045-7825. DOI: http://dx.doi.org/10.1016/0045-7825(74)90029-2. URL: http://www.sciencedirect.com/science/article/pii/0045782574900292.

Lee, C.-H. (1995). *WAMIT Theory Manual*. Dept. of Ocean Eng. , MIT. URL: https://www.wamit.com/Publications/tmanual.pdf.

Loh, T. et al. (2016). "Numerical modelling of the WaveRoller device using OpenFOAM". In: Proceedings of the 3rd Asian Wave & Tidal Energy Conference. URL: https://www.researchgate.net/profile/Teng_Tan_Loh/publication/309618807_Numerical_Modelling_of_the_WaveRoller_Device_Using_OpenFOAM/links/59f27081a6fdcc1dc7bb194a/Numerical-Modelling-of-the-WaveRoller-Device-Using-OpenFOAM.pdf.

Longuet-Higgins, M. and E. Cokelet (1976). "The deformation of steep surface waves on water - I. A numerical method of computation". In: *Royal Society*. URL: https://royalsocietypublishing.org/doi/pdf/10.1098/rspa.1976.0092.

Luo, Y. et al. (2014). "Nonlinear 2D analysis of the efficiency of fixed Oscillating Water Column wave energy converters". English. In: *Renewable Energy* 64, pp. 255–265. URL: www.scopus.com.

Majid, Bhinder et al. (Jan. 2012). "Effect of viscous forces on the performance of a surging wave energy converter". In: Proceedings of the Twenty-second International Offshore and Polar Engineering Conference.

McCombes, T., C. Johnstone, and A. Grant (2011). *Tank Testing Protocols*. Tech. rep. Equitable Assessment of Marine Energy Converters. URL: http://www.homepages.ed.ac.uk/shs/Wave%5C%20Energy/Equimar%5C%20protocols.pdf.

McNatt, Cameron (2017). *Mocean Energy: Our technology*. URL: http://www.moceanenergy.com/technology.html. Accessed on 2019-05-07.

Menter, Florian R. (Jan. 1993). "Zonal Two Equation k-omega Turbulence Models for Aerodynamic Flows". In: AIAA Fluid Dynamics Conference, pp. 93–2906.

Michell, J. H. (1893). “XLIV. The highest waves in water”. In: *The London, Edinburgh, and Dublin Philosophical Magazine and Journal of Science* 36.222, pp. 430–437. URL: https://doi.org/10.1080/14786449308620499.

Microchip (2008). *MCP413X: 7/8-Bit Single/Dual SPI Digital POT with Volatile Memory*. URL: http://ww1.microchip.com/downloads/en/DeviceDoc/22060b.pdf. Accessed on 2019-06-28.

Mingham, Clive G et al. (2004). “Non-linear simulation of wave energy devices”. In: *The Fourteenth International Offshore and Polar Engineering Conference*. International Society of Offshore and Polar Engineers.

Mundon, T., B. Rosenberg, and J. Rij (2017). “Reaction Body Hydrodynamics for a Multi-DOF Point-Absorbing WEC”. In: *Proceedings of the Twelfth European Wave and Tidal Energy Conference*. Ed. by A. Lewis. ISSN: 2309-1983. EWTEC. University College Cork, Ireland.

National Climate Assessment (May 2019). *Could climate change make Atlantic hurricanes worse?* URL: https://www.climate.gov/news-features/climate-qa/could-climate-change-make-atlantic-hurricanes-worse. Accessed on 2019-10-30.

Newman, J. N. (2018). *Marine Hydrodynamics*. eng. Cambridge: The MIT Press. ISBN: 9780262344999. URL: http://www.oapen.org/download/?type=document%5C&docid=1004046.

Nguyen, Phong T. T., Lance Manuel, and Ryan G. Coe (Mar. 2019). “On the Development of an Efficient Surrogate Model for Predicting Long-Term Extreme Loads on a Wave Energy Converter”. In: *Journal of Offshore Mechanics and Arctic Engineering* 141.6. ISSN: 0892-7219. DOI: 10.1115/1.4042944. URL: https://doi.org/10.1115/1.4042944.

NOAA- Environmental Modelling Centre (2016). *NOAA WAVEWATCH III*. URL: https://polar.ncep.noaa.gov/waves/index.shtml?. Accessed on 2019-08-16.

Ocean Energy Forum (2016). *Ocean Energy Strategic Roadmap 2016, building ocean energy for Europe*. Tech. rep. URL: https://webgate.ec.europa.eu/maritimeforum/sites/maritimeforum/files/OceanEnergyForum_Roadmap_Online_Version_08Nov2016.pdf.

Omidvar, Pourya (2010). “Wave Loading on Bodies in the Free Surface Using Smoothed Particle Hydrodynamics”. PhD thesis. University of Manchester.

Page, Lewis (2007). *Wave power prototype sinks after seven weeks*. URL: https://www.theregister.co.uk/2007/11/09/aquabuoy_wave_power_renewable_sinks/. Accessed on 2019-05-03.

Palm, Johannes et al. (2016). “Coupled mooring analysis for floating wave energy converters using CFD: Formulation and validation”. In: *International Journal of Marine Energy* 16, pp. 83–99. ISSN: 2214-1669. DOI: http://dx.doi.org/10.1016/j.ijome.2016.05.003. URL: http://www.sciencedirect.com/science/article/pii/S2214166916300327.

Panolin (2016). *Panolin HLP Synthetic Oil datasheet*. URL: https://www.lubexcel.com/repo/docs/A17-4682-35020.en%20HLP%20SYNTH.pdf. Accessed on 2019-06-04.

Parkinson, Giles (2014). *CETO wave energy machine swept away in cyclone, report says*. URL: https://reneweconomy.com.au/ceto-wave-energy-machine-destroyed-cyclone-reports-say/. Accessed on 2019-05-03.

Paulsen, Bo Terp et al. (2019). “Probability of wave slamming and the magnitude of slamming loads on offshore wind turbine foundations”. In: *Coastal Engineering* 143, pp. 76–95. ISSN: 0378-3839. DOI: https://doi.org/10.1016/j.coastaleng.2018.10.002. URL: http://www.sciencedirect.com/science/article/pii/S0378383917301928.

Pecher, Arthur (2017). “Experimental Testing and Evaluation of WECs”. In: *Handbook of Ocean Wave Energy*. Ed. by Arthur Pecher and Jens Peter Kofoed. Cham: Springer International

Publishing, pp. 221–260. ISBN: 978-3-319-39889-1. DOI: 10.1007/978-3-319-39889-1_9. URL: https://doi.org/10.1007/978-3-319-39889-1_9.

Penalba, Markel, Giuseppe Giorgi, and John V. Ringwood (2017). "Mathematical modelling of wave energy converters: A review of nonlinear approaches". In: *Renewable and Sustainable Energy Reviews* 78, pp. 1188–1207. ISSN: 1364-0321. DOI: https://doi.org/10.1016/j.rser.2016.11.137. URL: http://www.sciencedirect.com/science/article/pii/S1364032116308784.

Penalba, Markel, Thomas Kelly, and John Ringwood (Aug. 2017). "Using NEMOH for Modelling Wave Energy Converters: A Comparative Study with WAMIT". In: Proceedings of the 12th European Wave and Tidal Energy Conference. URL: http://www.eeng.nuim.ie/coer/wp-content/uploads/2017/08/Penalba-et-al.2017_Using_NEMOH_for_Modelling_WEC_Comparative_Study_with_WAMIT.pdf.

Peregrine, D. H. (2003). "WATER-WAVE IMPACT ON WALLS". In: *Annual Review of Fluid Mechanics* 35.1, pp. 23–43. DOI: 10.1146/annurev.fluid.35.101101.161153. URL: https://doi.org/10.1146/annurev.fluid.35.101101.161153.

Polinder, H., M. E. C. Damen, and F. Gardner (2004). "Linear PM Generator system for wave energy conversion in the AWS". In: *IEEE Transactions on Energy Conversion* 19.3, pp. 583–589. URL: http://citeseerx.ist.psu.edu/viewdoc/download?doi=10.1.1.469.2146%5C&rep=rep1%5C&type=pdf.

– (2005). "Design, modelling and test results of the AWS PM linear generator". In: *European Transactions on Electrical Power* 15.3, pp. 245–256. DOI: 10.1002/etep.56. eprint: https://onlinelibrary.wiley.com/doi/pdf/10.1002/etep.56. URL: https://onlinelibrary.wiley.com/doi/abs/10.1002/etep.56.

Ransley, Edward (2015). "Survivability of Wave Energy Converter and Mooring Coupled System using CFD". PhD thesis. University of Plymouth.

Renzi, E., K. Doherty, et al. (2014). "How does Oyster work? The simple interpretation of Oyster mathematics". In: *European Journal of Mechanics - B/Fluids* 47. Enok Palm Memorial Volume, pp. 124–131. ISSN: 0997-7546. DOI: https://doi.org/10.1016/j.euromechflu.2014.03.007. URL: http://www.sciencedirect.com/science/article/pii/S0997754614000429.

Renzi, E., Y. Wei, and F. Dias (2018). "The pressure impulse of wave slamming on an oscillating wave energy converter". In: *Journal of Fluids and Structures* 82, pp. 258–271. ISSN: 0889-9746. DOI: https://doi.org/10.1016/j.jfluidstructs.2018.07.007. URL: http://www.sciencedirect.com/science/article/pii/S0889974618301373.

Rowlatt, Christopher F. and Steven J. Lind (2017). "Bubble collapse near a fluid-fluid interface using the spectral element marker particle method with applications in bioengineering". In: *International Journal of Multiphase Flow* 90, pp. 118–143. ISSN: 0301-9322. DOI: https://doi.org/10.1016/j.ijmultiphaseflow.2016.11.010. URL: http://www.sciencedirect.com/science/article/pii/S0301932216301975.

Sandia National Laboratories (2015). *Reference Model Project*. URL: http://energy.sandia.gov/energy/renewable-energy/water-power/technology-development/reference-model-project-rmp/.

Santo, H. et al. (2013). "Average Properties of the Largest Waves in Hurricane Camille". In: *Journal of Offshore Mechanics and Arctic Engineering*. URL: http://dx.doi.org/10.1115/1.4006930.

Saulnier, J.-B. et al. (2009). “Mean Power Output Estimation of WECs in Simulated Sea-States”. In: *Proccedings of the 8th European Wave and Tidal Energy Conference*. Uppsala, Sweden. URL: https://hal.archives-ouvertes.fr/hal-01156320.

Schmitt, Pál, Sylvain Bourdier, et al. (June 2012). “Hydrodynamic Loading on a Bottom Hinged Oscillating Wave Surge Converter”. In: Proceedings of the Twenty-second International Offshore and Polar Engineering Conference. URL: https://www.researchgate.net/publication/271835125_Hydrodynamic_Loading_on_a_Bottom_Hinged_Oscillating_Wave_Surge_Converter.

Schmitt, Pál and Björn Elsäßer (2015). “On the use of OpenFOAM to model oscillating wave surge converters”. In: *Ocean Engineering* 108, pp. 98–104. ISSN: 0029-8018. DOI: https://doi.org/10.1016/j.oceaneng.2015.07.055. URL: http://www.sciencedirect.com/science/article/pii/S0029801815003686.

– (2017). “The application of Froude scaling to model tests of Oscillating Wave Surge Converters”. In: *Ocean Engineering* 141, pp. 108–115. ISSN: 0029-8018. DOI: https://doi.org/10.1016/j.oceaneng.2017.06.003. URL: http://www.sciencedirect.com/science/article/pii/S0029801817302986.

Schmitt, Pál et al. (2016). “Development and validation of a procedure for numerical vibration analysis of an oscillating wave surge converter”. In: *European Journal of Mechanics - B/Fluids* 58, pp. 9–19. ISSN: 0997-7546. DOI: https://doi.org/10.1016/j.euromechflu.2016.02.005. URL: http://www.sciencedirect.com/science/article/pii/S0997754615300352.

So, R., C. Michelen, et al. (July 2017). “Statistical Analysis of a 1:7 Scale Field Test Wave Energy Converter Using WEC-Sim”. In: *IEEE Transactions on Sustainable Energy* 8.3, pp. 1118–1126. ISSN: 1949-3029. DOI: 10.1109/TSTE.2017.2656863.

So, R., A. Simmons, et al. (2015). “Development of PTO-SIM: A Power Performance Module for the Open-Source Wave Energy Converter Code WEC-SIM”. In: Proceedings of the 34th International Conference on Ocean, Offshore and Arctic Engineering. ASME. URL: https://energy.sandia.gov/wp-content/uploads/2014/06/SAND2015-2069C.pdf.

Southgate, H N (1988). “Wave Breaking, A review of techniques for calculating energy losses in breaking waves.” In: URL: eprints.hrwallingford.co.uk/1247/1/SR168.pdf.

Steen, Sverre (2014). *Experimental Methods in Marine Hydrodynamics*. URL: http://www.ivt.ntnu.no/imt/courses/tmr7/index.htm.

Sustainable Energy Research Group (2012). *Anaconda Wave Energy Converter Concept*. URL: http://www.energy.soton.ac.uk/anaconda-wave-energy-converter-concept/. Accessed on 2019-05-07.

Techet, A. (2005). *Lecture notes on Marine Hydrodynamics (13.021)*. URL: https://ocw.mit.edu/courses/mechanical-engineering/2-20-marine-hydrodynamics-13-021-spring-2005/.

Tethys (2018). *Mutriku Wave Power Plant*. URL: https://tethys.pnnl.gov/annex-iv-sites/mutriku-wave-power-plant. Accessed on 2019-05-05.

The Carbon Trust (2011). “Accelerating marine energy: The potential for cost reduction – insights from the Carbon Trust Marine Energy Accelerator”. In: URL: https://www.carbontrust.com/media/5675/ctc797.pdf.

The Crown Estate (2012). “UK Wave and Tidal Key Resource Areas Project: Summary Report”. In: URL: https://www.marineenergywales.co.uk/wp-content/uploads/2016/01/Summary-Report-FINAL.pdf.

The European Marine Energy Centre Ltd (2015). *Aquamarine Power*. URL: http://www.emec.org.uk/about-us/wave-clients/aquamarine-power/. Accessed on 2019-05-07.

– (2017). *Pelamis Wave Power*. URL: http://www.emec.org.uk/about-us/wave-clients/pelamis-wave-power/. Accessed on 2019-05-07.

The Orcadian (2019). *Penguin device goes under*. URL: https://www.orcadian.co.uk/penguin-device-goes-under/. Accessed on 2019-05-03.

The Queen's University Belfast (2002). *Islay Limpet Wave Power Plant*. Tech. rep. URL: https://tethys.pnnl.gov/sites/default/files/publications/Islay_LIMPET_Report.pdf.

The University of Edinburgh (2017). *C-GEN Direct Drive PTO: WES Power Take Off Stage 2 Project Public Report*. Tech. rep. URL: https://library.waveenergyscotland.co.uk/development-programmes/power-take-off/stage-2/pt21_uoe/pt21_uoe_wes-public-report/.

– (2018). *FloWave Ocean Energy Research Facility*. URL: https://www.flowavett.co.uk/facility. Accesesd on 2019-04-15.

Todalshaug, Jørgen Hals (2017). "Hydrodynamics of WECs". In: *Handbook of Ocean Wave Energy*. Ed. by Arthur Pecher and Jens Peter Kofoed. Cham: Springer International Publishing, pp. 139–158. ISBN: 978-3-319-39889-1. DOI: 10.1007/978-3-319-39889-1_6. URL: https://doi.org/10.1007/978-3-319-39889-1_6.

Tromans, Peter S., Ali R. Anaturk, and Paul Hagemeijer (1991). "A New Model For The Kinematics Of Large Ocean Waves-Application As a Design Wave". In: The First International Offshore and Polar Engineering Conference. URL: https://www.researchgate.net/profile/Peter_Tromans2/publication/244960121_A_new_model_for_the_kinematics_of_large_ocean_waves-application_as_a_design_wave/links/5a845445a6fdcc201b9ecc5c/A-new-model-for-the-kinematics-of-large-ocean-waves-application-as-a-design-wave.pdf?origin=publication_list.

Tweten, Dennis J., Zach Ballard, and Brian P. Mann (2014). "Minimizing error in the logarithmic decrement method through uncertainty propagation". In: *Journal of Sound and Vibration* 333.13, pp. 2804–2811. ISSN: 0022-460X. DOI: https://doi.org/10.1016/j.jsv.2014.02.024. URL: http://www.sciencedirect.com/science/article/pii/S0022460X14001515.

Umbra Cuscinetti S.p.A. (2017). *Reciprocating Ball Screw Generator (ReBaS): WES Power Take Off Stage 2 Project Public Report*. Tech. rep. URL: https://library.waveenergyscotland.co.uk/development-programmes/power-take-off/stage-2/pt21_umb/.

US Army Corps of Engineers (2002). *Coastal Engineering Manual - Part II*. Tech. rep. URL: https://pdhonline.com/courses/c772/Part-II-Chap_1entire.pdf.

van't Hoff, J. (2009). "Hydrodynamic Modelling of the Oscillating Wave Surge Converter". PhD thesis. Queen's University Belfast.

Versteeg, H. and W. Malalasekera (2007). *An Introduction to Computational Fluid Dynamics: The Finite Volume Method*. Pearson Education UK. URL: http://ebookcentral.proquest.com/lib/ed/detail.action?docID=5136615.

Vyzikas, Thomas (2014). *Best practice report: Application of numerical models and codes*. Tech. rep. MERiFIC Project. URL: https://archimer.ifremer.fr/doc/00324/43550/43111.pdf.

Walker, D.A.G., P.H. Taylor, and R. Eatock Taylor (2004). "The shape of large surface waves on the open sea and the Draupner New Year wave". In: *Applied Ocean Research* 26.3, pp. 73–83. ISSN: 0141-1187. DOI: https://doi.org/10.1016/j.apor.2005.02.001. URL: http://www.sciencedirect.com/science/article/pii/S0141118705000052.

WAMIT, Inc (2016). *WAMIT User Manual Version 7.2*. Tech. rep. URL: https://www.wamit.com/manual.htm.

Wave Dragon (2017). *Wave Dragon: Technology*. URL: http://www.wavedragon.co.uk/technology-2/. Accessed on 2019-05-07.

Wave Energy Scotland (2019). *Wave Energy Scotland: Programmes*. URL: https://www.waveenergyscotland.co.uk/programmes/. Accessed on 2019-05-05.

Wavestar Energy (2011). *The Wavestar Machine*. URL: http://wavestarenergy.com/. Accessed on 2019-05-07.

Weber, J. (2012). "WEC Technology Readiness and Performance Matrix – finding the best research technology development trajectory". In: 2012. URL: https://www.icoe-conference.com/publication/wec_technology_readiness_and_performance_matrix_finding_the_best_research_technology_development_trajectory/.

Wei, Ge and James T. Kirby (1995). "Time-Dependent Numerical Code for Extended Boussinesq Equations". In: *Journal of Waterway, Port, Coastal, and Ocean Engineering* 121.5, pp. 251–261. DOI: 10.1061/(ASCE)0733-950X(1995)121:5(251). URL: http://ascelibrary.org/doi/abs/10.1061/%5C%28ASCE%5C%290733-950X%5C%281995%5C%29121%5C%3A5%5C%28251%5C%29.

Wei, Yanji, Thomas Abadie, et al. (2016). "Wave interaction with an Oscillating Wave Surge Converter. Part II: Slamming". In: *Ocean Engineering* 113, pp. 319–334. ISSN: 0029-8018. DOI: https://doi.org/10.1016/j.oceaneng.2015.12.041. URL: http://www.sciencedirect.com/science/article/pii/S0029801815007106.

Wei, Yanji, Ashkan Rafiee, et al. (2015). "Wave interaction with an oscillating wave surge converter, Part I: Viscous effects". In: *Ocean Engineering* 104, pp. 185–203. ISSN: 0029-8018. DOI: https://doi.org/10.1016/j.oceaneng.2015.05.002. URL: http://www.sciencedirect.com/science/article/pii/S0029801815001705.

Wello Oy (2018). *Technology: Penguin's competitive advantage*. URL: https://wello.eu/technology/. Accessed on 2019-05-07.

Whittaker, C.N. et al. (2016). "The average shape of large waves in the coastal zone". In: *Coastal Engineering* 114, pp. 253–264. ISSN: 0378-3839. DOI: https://doi.org/10.1016/j.coastaleng.2016.04.009. URL: http://www.sciencedirect.com/science/article/pii/S0378383916300448.

Whittaker, Trevor and Matt Folley (2012). "Nearshore oscillating wave surge converters and the development of Oyster". In: *Philosophical Transactions of the Royal Society A: Mathematical, Physical and Engineering Sciences* 370.1959, pp. 345–364. DOI: 10.1098/rsta.2011.0152. URL: https://royalsocietypublishing.org/doi/abs/10.1098/rsta.2011.0152.

Wilcox, David C (1998). *Turbulence modeling for CFD*. Vol. 2. DCW industries La Canada, CA.

WindBlue Power (2016). *DC-520 High Wind Permanent Magnet Alternator*. URL: http://www.windbluepower.com/Permanent_Magnet_Alternator_Wind_Blue_High_Wind_p/dc-520.htm. Accessed on 2018-07-15.

Windt, Christian, Josh Davidson, and John V. Ringwood (2018). "High-fidelity numerical modelling of ocean wave energy systems: A review of computational fluid dynamics-based numerical wave tanks". In: *Renewable and Sustainable Energy Reviews* 93, pp. 610–630. ISSN: 1364-0321. DOI: https://doi.org/10.1016/j.rser.2018.05.020. URL: http://www.sciencedirect.com/science/article/pii/S1364032118303629.

Windt, Christian, Josh Davidson, Pál Schmitt, et al. (2019). “On the Assessment of Numerical Wave Makers in CFD Simulations”. In: *Journal of Marine Science and Engineering* 7.2. ISSN: 2077-1312. DOI: 10.3390/jmse7020047. URL: http://www.mdpi.com/2077-1312/7/2/47.

Wolgamot, Hugh A and Colm J Fitzgerald (2015). “Nonlinear hydrodynamic and real fluid effects on wave energy converters”. In: *Proceedings of the Institution of Mechanical Engineers, Part A: Journal of Power and Energy* 229.7, pp. 772–794. DOI: 10.1177/0957650915570351. URL: https://doi.org/10.1177/0957650915570351.

Worden Hodge, Caitlin et al. (2017). “Performance analysis of the CCell wave energy device”. In: Proceedings of the 12th European Wave and Tidal Energy Conference.

– (2018). “Coupled Modelling of a Non-Linear Wave Energy Converter and Hydraulic PTO”. In: Proceedings of the 28th International Ocean and Polar Engineering Conference. URL: https://www.onepetro.org/conference-paper/ISOPE-I-18-368.

Appendix A

OpenFOAM solver choices

fvSchemes

```
/*--------------------------------*- C++ -*----------------------------------*\
| =========                 |                                                 |
| \\      /  F ield         | OpenFOAM: The Open Source CFD Toolbox           |
|  \\    /   O peration     | Version:  dev                                   |
|   \\  /    A nd           | Web:      www.OpenFOAM.org                      |
|    \\/     M anipulation  |                                                 |
\*---------------------------------------------------------------------------*/
FoamFile
{
    version     2.0;
    format      ascii;
    class       dictionary;
    location    "system";
    object      fvSchemes;
}
// * * * * * * * * * * * * * * * * * * * * * * * * * * * * * * * * * * * * //
ddtSchemes
{
    default         CrankNicolson 0.9;
}

gradSchemes
{
    default         Gauss linear;
}

divSchemes
{
    div(rhoPhi,U)   Gauss limitedLinearV 1;
    div(phi,alpha)  Gauss vanLeer;
    div(phirb,alpha) Gauss interfaceCompression;
    div(phi,k)      Gauss linearUpwind limitedGrad;
    div(phi,omega)  Gauss linearUpwind limitedGrad;
    div(((rho*nuEff)*dev2(T(grad(U))))) Gauss linear;
}

laplacianSchemes
{
    default         Gauss linear corrected;
}

interpolationSchemes
{
    default         linear;
}

snGradSchemes
```

```
{
    default          corrected;
}

wallDist
{
    method meshWave;
}
// ************************************************************************* //
```

fvSolutions

```

/*--------------------------------*- C++ -*----------------------------------*\
| =========                 |                                                 |
| \\      /  F ield         | OpenFOAM: The Open Source CFD Toolbox           |
|  \\    /   O peration     | Version:  dev                                   |
|   \\  /    A nd           | Web:      www.OpenFOAM.org                      |
|    \\/     M anipulation  |                                                 |
\*---------------------------------------------------------------------------*/
FoamFile
{
    version     2.0;
    format      ascii;
    class       dictionary;
    location    "system";
    object      fvSolution;
}
// * * * * * * * * * * * * * * * * * * * * * * * * * * * * * * * * * * * * //

solvers
{
    "alpha.water.*"
    {
        nAlphaCorr      2;
        nAlphaSubCycles 1;
        cAlpha          1;

        MULESCorr       yes;
        nLimiterIter    5;
        alphaApplyPrevCorr  yes;

        solver          smoothSolver;
        smoother        symGaussSeidel;
        tolerance       1e-8;
        relTol          0;
    }

    "pcorr.*"
    {
        solver          PCG;
        preconditioner
        {
            preconditioner  GAMG;
            tolerance       1e-5;
            relTol          0;
            smoother        DICGaussSeidel;
            cacheAgglomeration no;
        }

        tolerance       1e-05;
        relTol          0;
        maxIter         100;
    }

    p_rgh
    {
        solver          GAMG;
        tolerance       1e-8;
        relTol          0.01;
```

```
59          smoother        DIC;
60      }
61
62      p_rghFinal
63      {
64          solver          PCG;
65          preconditioner
66          {
67              preconditioner  GAMG;
68              tolerance       1e-8;
69              relTol          0;
70              nVcycles        2;
71              smoother        DICGaussSeidel;
72              nPreSweeps      2;
73          }
74
75          tolerance       1e-8;
76          relTol          0;
77          maxIter         20;
78      }
79      cellDisplacement
80      {
81          solver          GAMG;
82          tolerance       1e-8;
83          relTol          0.01;
84          smoother        DIC;
85      }
86
87      cellDisplacementFinal
88      {
89          $cellDisplacement;
90          relTol          0;
91      }
92
93      "(U|k|omega)"
94      {
95          solver          smoothSolver;
96          smoother        GaussSeidel;
97          tolerance       1e-6;
98          relTol          0.1;
99          nSweeps         1;
100     }
101
102     "(U|k|omega)Final"
103     {
104         solver          smoothSolver;
105         smoother        GaussSeidel;
106         tolerance       1e-6;
107         relTol          0;
108         nSweeps         1;
109     }
110 }
111
112 PIMPLE
113 {
114     momentumPredictor   no;
115     nOuterCorrectors    3;
116     nCorrectors         1;
117     nNonOrthogonalCorrectors 0;
118     correctPhi          yes;
119     moveMeshOuterCorrectors yes;
120 }
121
122 relaxationFactors
123 {
124     equations
125     {
126         ".*"  1;
127     }
128 }
129
130
131 // ************************************************************************* //
```

Appendix B

PTO model

Brent Solver

In a number of the classes a root finding method is required. Brent's Method (Van Wijngaarden-Dekker-Brent Method) combines root bracketing, bisection and inverse quadratic interpolation to provide faster convergence when appropriate. The code used is listed below:

```
1     double brentNR(double (*f)(PTOModel*, double), double lower_bound=-0.001, double
      upper_bound=0.001, double tol=1E-15, double MAX_ITER=1000)
2     {
3         int iter;
4         double addon;
5         double a=lower_bound;
6         double b = upper_bound;
7         double c = upper_bound;
8         double d, e, min1, min2;
9         double fa = f(this,a);
10        double fb = f(this, b);
11        double fc , p, q, r, s, tol1, xm;
12        double EPS = 3.0e-8; // machine floating point precision.
13
14        //if((fa > 0.0 && fb > 0.0) || (fa < 0.0 && fb < 0.0))
15        //      std::cout << "Root must be bracketed in zbrent" <<std::endl;
16        fc = fb;
17        for (iter=1; iter<=MAX_ITER; iter++){
18            if((fb > 0.0 && fc > 0.0) || (fb < 0.0 && fc < 0.0)){
19                c = a;
20                fc = fa;
21                d = b-a;
22                e = d;
23            }
24            if(fabs(fc) <fabs(fb)){
25                a = b;
26                b = c;
27                c = a;
28                fa = fb;
29                fb = fc;
30                fc = fa;
31            }
32            tol1 = 2.0 * EPS*fabs(b)+0.5*tol; // convergence check
33            xm = 0.5*(c-b);
34            if(fabs(xm) <= tol1 || fb == 0.0) return b;
35            if (fabs(e) >= tol1 && fabs(fa) > fabs(fb)){
36                // attempt inverse quadratic interpolation
37                s = fb/fa;
38                if(a==c){
39                    p = 2.0 *xm *s;
```

```
                    q = 1.0 - s;
                } else {
                    q = fa/fc;
                    r = fb/fc;
                    p = s*(2.0 * xm *q*(q-r)-(b-a)*(r-1.0));
                    q = (q - 1.0)*(r - 1.0)*(s-1.0);
                }
                if (p > 0.0) q = -q; // Check whether in bounds
                p = fabs(p);
                min1 = 3.0*xm *q - fabs(tol1*q);
                min2 = fabs(e*q);
                if (2.0 *p < ( min1 < min2 ? min1 : min2)){
                    // Accept interpolation
                    e = d;
                    d = p/q;
                } else{
                    // Interpolation failed, use bisection
                    d = xm;
                    e = d;
                }
            } else{
                // Bounds decreasing too slowly, use bisection
                d = xm;
                e = d;
            }
            a =b; //move last best guess to a
            fa = fb;
            if(fabs(d)>tol1) // evaluate new trial root
                b += d;
            else{
                if (xm>=0.0)
                    addon = fabs(tol1);
                else
                    addon = -fabs(tol1);
                b += addon;
            }
            fb = f(this,b);
        }
        std::cout<< " Max no of iterations exceeded" <<std::endl;
        return 0.0; // should never get here
    }
```

PTOModel.h

```
#include "HydraulicFluid.h"
#include "Piston.h"
#include "PVBlock.h"
#include "PRelief.h"
#include "Accumulator.h"
#include "HydraulicMotor.h"
#include "Pipeline.h"
#include <cmath>
#define _USE_MATH_DEFINES

#define MIN(x, y)   ((x) < (y) ? (x) : (y))

class PTOModel
{
protected:
  double dt=0.005;
  double P_init = 15e5;

public:
  double Q_PARALLEL=0, Q_parallel =0;
  double Q_HPacc=0, Q_LPacc=0, Q_VALVE = 0, Q_MOTOR = 0;
  double Motor_HP = 0, Motor_LP = 0;

  HydraulicFluid _HydraulicFluid;
  Piston         _Piston;
  PRelief        _ReliefValve;
```

```
27    HydraulicMotor _HydraulicMotor;
28    Pipeline       _Pipeline;
29    PVBlock*       _HPBlock;
30    PVBlock*       _LPBlock;
31    Accumulator_HP* _HPAccumulator;
32    Accumulator_LP* _LPAccumulator;
33
34    int            _direction = 1;
35
36  //*** Constructor***//
37  PTOModel(double Dm = 5.37e-7, double Cg= 0.1)
38    : _HydraulicFluid( 813.2, 0.00000968866, 1.52979e9),
39    _Piston(80.0/1000, 40.0/1000, 510.0/1000),
40    _ReliefValve(_HydraulicFluid, 250e5, 300e5),
41    _HydraulicMotor(_HydraulicFluid, Dm, Cg),
42    _Pipeline(_HydraulicFluid, 0.0127, 3)
43    {
44      _HPBlock= new PVBlock(_HydraulicFluid, _Piston.getVol()/2 + _Piston.getDeadVol(),
        P_init),
45      _LPBlock = new PVBlock(_HydraulicFluid, _Piston.getVol()/2 + _Piston.getDeadVol()
        , P_init),
46      _HPAccumulator = new Accumulator_HP(50e5, P_init),
47      _LPAccumulator = new Accumulator_LP(7.5e5, P_init);
48    }
49
50  //*** Destructor***//
51  ~PTOModel()
52    {
53      delete _HPBlock;
54      delete _LPBlock;
55      delete _HPAccumulator;
56      delete _LPAccumulator;
57    }
58  //***Member Functions***//
59    void setdVdt_rectify(double v) // Calculate and set change in Volume due to linear
        velocity.
60    {
61      double dVdt = _Piston.dVoldt(v);
62
63      if((dVdt <0 &&_direction != 1) || (dVdt >0 &&_direction != -1))
64      {
65        _direction *= -1;
66        double tmp = _HPBlock->getVol();
67        _HPBlock->setVol(_LPBlock->getVol());
68        _LPBlock->setVol(tmp);
69
70      }
71      dVdt *= _direction;
72      _HPBlock->setdVdt(dVdt);
73      _LPBlock->setdVdt(-dVdt);
74    }
75
76    // solve flow into HP accumulator
77    static double Solve_Q_hp(PTOModel* A, double Q)
78    {
79      double pressure = A->_HPBlock->pressure(- A->Q_PARALLEL - Q);
80      double dPpipe =  A->_Pipeline.Pdrop(- A->Q_PARALLEL - Q);
81      double Q_acc = A->_HPAccumulator->flow(pressure- dPpipe); // Input = pressure,
        output = flow
82      return Q_acc - Q;
83    }
84
85    // solve flow into LP accumulator
86    static double Solve_Q_lp(PTOModel* A, double Q)
87    {
88      double pressure = A->_LPBlock->pressure(A->Q_PARALLEL - Q);// Input = dQ and dV/
        dt , output = pressure
89      double dPpipe = A->_Pipeline.Pdrop(A->Q_PARALLEL - Q);
90      double Q_acc = A->_LPAccumulator->flow(pressure + dPpipe); // Input = pressure,
        output = flow
91      return Q_acc - Q;
92    }
93
94    // Flow going across motor and pressure relief valve
```

```
95  static double Solve_Q_Parallel(PTOModel* A, double Q)
96  {
97    A->Q_PARALLEL = Q;
98    A-> Q_HPacc = A->brentNR(Solve_Q_hp);
99    A-> Q_LPacc = A->brentNR(Solve_Q_lp);
100
101   double HPQ = -Q - A->Q_HPacc;
102   double P_hp = A->_HPBlock->pressure(HPQ);
103   double dPpipe_h = A->_Pipeline.Pdrop(HPQ);
104   double LPQ =  Q - A->Q_LPacc;
105   double P_lp = A->_LPBlock->pressure(LPQ);
106   double dPpipe_l = A->_Pipeline.Pdrop(LPQ);
107
108   double dP = P_hp - P_lp -( dPpipe_l + dPpipe_h);
109   A->Q_MOTOR = A->_HydraulicMotor.flow(dP);
110   A->Q_VALVE= A->_ReliefValve.flow(dP);
111
112   return Q - (A->Q_MOTOR + A->Q_VALVE);
113 }
114
115
116  double brentNR(double (*f)(PTOModel*, double), double lower_bound=-0.001, double
      upper_bound=0.001, double tol=1E-15, double MAX_ITER=1000)
117  {
118   //......See Section: Brent Solver......//
119  }
120
121 void set(double velocity, double dt) //set the timestep in each of the blocks.
122 {
123   setdVdt_rectify(velocity);
124   _HPBlock->setDt(dt);
125   _LPBlock->setDt(dt);
126   _HPAccumulator->setDt(dt);
127   _LPAccumulator->setDt(dt);
128 }
129
130 double solveDampingForce()
131 {
132   Q_parallel = brentNR(PTOModel::Solve_Q_Parallel);
133   double HPQ = -Q_parallel- Q_HPacc;
134   double LPQ =  Q_parallel - Q_LPacc;
135   double P_hp = _HPBlock->pressure(HPQ);
136
137   double P_lp = _LPBlock->pressure(LPQ);
138   double dPpipe_h = _Pipeline.Pdrop(HPQ);
139   double dPpipe_l = _Pipeline.Pdrop(LPQ);
140
141   Motor_HP = P_hp - dPpipe_h;
142   Motor_LP = P_lp + dPpipe_l;
143
144   return fabs(P_hp -P_lp)* _Piston.getArea();
145 }
146
147 void step() // save current values and progress to next timestep
148 {
149   double HPQ = -Q_parallel - Q_HPacc;
150   double LPQ =  Q_parallel- Q_LPacc;
151
152   _HPBlock->nextTimestep(HPQ);
153   _HPAccumulator->nextTimestep(Q_HPacc);
154   _LPBlock->nextTimestep(LPQ);
155   _LPAccumulator->nextTimestep(Q_LPacc);
156 }
157
158 //**** Functions to give outputs to OpenFOAM ****//
159
160 double getPistonHP()
161 {
162     return _HPBlock->pressure(-Q_parallel - Q_HPacc);
163 }
164
165 double getPistonLP()
166 {
167     return _LPBlock->pressure(Q_parallel - Q_LPacc);
```

```
168   }
169
170     double getQ_HP()
171     {
172       return Q_HPacc;
173     }
174
175     double getQ_LP()
176     {
177       return Q_LPacc;
178     }
179
180     double getQMotor()
181     {
182       return Q_MOTOR;
183     }
184
185     double getQValve()
186     {
187       return Q_VALVE;
188     }
189
190     double getOmega()
191     {
192        return _HydraulicMotor.solve_omega(getDP());
193     }
194
195     double getRPM()
196     {
197       return getOmega()*60/(2*M_PI);
198     }
199
200     double getMPower()
201     {
202       return _HydraulicMotor.power(getDP(), getOmega());
203     }
204
205
206 };
```

Appendix C

Extreme Loading Code Listings

Directional Waves Multiple DoF

Example code specification for rotated paddle with multiple degrees of freedom

```
bodies
{
  ccell
  {
    type   rigidBody;
    parent     root;
    mass             280.09;
    centreOfMass     ( 0.277 0.0025 1.208); //centre of mass in relation to origin of
    body

    // inertia  (Ixx Ixy Ixz Iyy Iyz Izz) of body about centre of mass
    inertia    (414 0.21 -56.96 338.16 -0.64 175.84);

    // transform     (xaxis, yxis, zaxis) (origin of body )
    transform    (0.7071 0.7071 0 -0.7071 0.7071 0 0 0 1) ( 0 0 -2.5 );

    joint
    {
      type     composite;
      joints
      (
        {
          type Ry; //local coordinate system
        }
        {
          type Rx; //local coordinate system
        }
      );
    }
    patches      (ccell);
  }
}

restraints
{
  PTO
  {
    body        ccell;
    type        CCcoulombDamper;
    axis                (0 1 0);
    piston_attach       0.3;
    coulomb_damping     30000; //N
    friction_torque     500;
  }

```

```
    RollMechanism
    {
        body        ccell;
        type        linearAxialAngularSpring;
        axis        (1 0 0);
        stiffness     0;
        damping       0;
    }
}
```

TMA-NewWave Spectrum

To add this functionality to waves2Foam, the following two files must be added in a folder of the same name to the path waves2Foam/src/waves2FoamProcessing/preProcessing/setWaveProperties/irregular/waveSpectra/spectra.

TMA_NewWave.h

```
/*---------------------------------------------------------------------------*\
Class
    Foam::TMA_NewWave

Description
    A spectrum which takes the TMA transformation of the a specified spectrum at the
    given water depth. The spectrum is then scaled to provide the correct amplitudes
    for NewWave wave profile.

SourceFiles
    TMA_NewWave.C

\*---------------------------------------------------------------------------*/

#ifndef TMA_NewWave_H
#define TMA_NewWave_H

#include "stokesFirstProperties.H"
#include "waveSpectra.H"

namespace Foam
{

class TMA_NewWave
:
    public waveSpectra
{
private:

        scalarField spectralValue
        (
            const scalar&,
            const scalar&,
            const scalar&,
            const scalarField&,
            const scalar&,
            const vector&
        ) const;

        scalarField spectralValueTemp
        (
            const scalar&,
            const scalar&,
            const scalar&,
            const scalarField&
        ) const;

public:

```

```
48          //- Runtime type information
49          TypeName("TMA_NewWave");
50
51          TMA_NewWave
52          (
53              const Time&,
54              dictionary&,
55              scalarField&,
56              scalarField&,
57              scalarField&,
58              vectorField&
59          );
60
61          virtual void set(Ostream&);
62
63          virtual wordList list();
64  };
65
66  }
67
68  #endif
69
70  // ************************************************************************* //
```

TMA_NewWave.C

```
1   #include "TMA_NewWave.H"
2   #include "addToRunTimeSelectionTable.H"
3
4   // * * * * * * * * * * * * * * * * * * * * * * * * * * * * * * * * * * * * //
5
6   namespace Foam
7   {
8
9   // * * * * * * * * * * * * * * * * * * * * * * * * * * * * * * * * * * * * //
10
11  defineTypeNameAndDebug(TMA_NewWave, 0);
12  addToRunTimeSelectionTable(waveSpectra, TMA_NewWave, waveSpectra);
13
14  // * * * * * * * * * * * * * Private Member Functions  * * * * * * * * * * * * * //
15
16  scalarField TMA_NewWave::spectralValue
17  (
18      const scalar& Hs,
19      const scalar& Tp,
20      const scalar& gamma,
21      const scalarField& freq,
22      const scalar& depth,
23      const vector& direction
24  ) const
25  {
26      // Additional parameters
27      scalar fp = (1.0/Tp);
28      scalar alpha = 0.0624/(0.230 + 0.0336*gamma - 0.185/(1.9 + gamma));
29      scalar celerity_ratio, kmag;
30
31      scalarField sigma(freq.size(), 0.07), beta(freq.size(), 0.0), S_TMA(freq.size(),
         0.0);
32
33      forAll (sigma, ii)
34      {
35          if (freq[ii] >= fp)
36          {
37              sigma[ii] = 0.09;
38          }
39      }
40
41      beta = Foam::exp(- Foam::pow(freq - fp, 2.0)
42          /(2*Foam::pow(sigma, 2.0)*Foam::pow(fp, 2.0)));
43
44      // Compute spectrum
```

```
45      scalarField S = alpha*Foam::pow(Hs,2.0)*Foam::pow(fp,4.0)*Foam::pow(freq,-5.0)
46          *Foam::pow(gamma,beta)*Foam::exp(- 5.0/4.0*Foam::pow(fp/freq, 4.0));
47
48      forAll (sigma, ii)
49      {
50              kmag = Foam::mag(k_[ii] & direction);
51              celerity_ratio = 0.5 + kmag*depth/(Foam::sinh(2*kmag*depth));
52
53              S_TMA[ii] = S[ii]* Foam::pow(Foam::tanh(kmag*depth),2)/(2*celerity_ratio)
        ;
54      }
55
56      return S_TMA;
57  }
58
59
60  scalarField TMA_NewWave::spectralValueTemp
61  (
62      const scalar& Hs,
63      const scalar& Tp,
64      const scalar& gamma,
65      const scalarField& freq
66  ) const
67  {
68      // Additional parameters
69      scalar fp = (1.0/Tp);
70      scalar alpha = 0.0624/(0.230 + 0.0336*gamma - 0.185/(1.9 + gamma));
71
72      scalarField sigma(freq.size(), 0.07), beta(freq.size(), 0.0);
73
74      forAll (sigma, ii)
75      {
76          if (freq[ii] >= fp)
77          {
78              sigma[ii] = 0.09;
79          }
80      }
81
82      beta = Foam::exp(- Foam::pow(freq - fp, 2.0)
83          /(2*Foam::pow(sigma, 2.0)*Foam::pow(fp, 2.0)));
84
85      // Compute spectrum
86      scalarField S = alpha*Foam::pow(Hs,2.0)*Foam::pow(fp,4.0)*Foam::pow(freq,-5.0)
87          *Foam::pow(gamma,beta)*Foam::exp(- 5.0/4.0*Foam::pow(fp/freq, 4.0));
88
89      return S;
90  }
91
92  // * * * * * * * * * * * * * * * * * * Constructors  * * * * * * * * * * * * * * * * * //
93
94
95  TMA_NewWave::TMA_NewWave
96  (
97      const Time& rT,
98      dictionary& dict,
99      scalarField& amp,
100     scalarField& freq,
101     scalarField& phi,
102     vectorField& k
103 )
104 :
105     waveSpectra(rT, dict, amp, freq, phi, k)
106 {
107     Info << "\nConstructing: " << this->type() << endl;
108 }
109
110 // * * * * * * * * * * * * * * * * * * Member Functions  * * * * * * * * * * * * * * * * * //
111
112 wordList TMA_NewWave::list()
113 {
114     wordList res(5);
115
116     res[0] = "Hs";
117     res[1] = "Tp";
```

```
118     res[2] = "gamma";
119     res[3] = "depth";
120     res[4] = "direction";
121 
122     return res;
123 }
124 
125 void TMA_NewWave::set(Ostream& os)
126 {
127     // Get the input parameters
128 
129     scalar Hs(readScalar(dict_.lookup("Hs")));
130     scalar Tp(readScalar(dict_.lookup("Tp")));
131     scalar gamma(readScalar(dict_.lookup("gamma")));
132     scalar depth(readScalar(dict_.lookup("depth")));
133     vector direction(vector(dict_.lookup("direction")));
134     label N = readLabel(dict_.lookup("N"));
135     scalar inXwaves(readScalar(dict_.lookup("Maxin")));
136 
137     // Calculate the frequency axis
138 
139     autoPtr<Foam::frequencyAxis> fA = Foam::frequencyAxis::New(rT_, dict_);
140     scalarField nodeFrequency(N + 1, 0);
141 
142     // An intermediate step needed for certain discretisation types
143     // Placed in scopes such that the temporary variables to not 'survive'
144     {
145         equidistantFrequencyAxis equiFA(rT_, dict_);
146         scalarField tempFreqAxis = equiFA.freqAxis(10000);
147         scalarField tempSpectrum
148             = this->spectralValueTemp(Hs, Tp, gamma, tempFreqAxis);
149         nodeFrequency = fA->freqAxis(tempFreqAxis, tempSpectrum, N);
150     }
151 
152     // Prepare variables
153     freq_.setSize(N);
154     amp_.setSize(N);
155     phi_.setSize(N);
156     k_.setSize(N);
157 
158     // Prepare stokesFirst to compute wave numbers
159     Foam::stokesFirstProperties stp(rT_, dict_);
160 
161      for (int i = 1; i < N + 1; i++)
162     {
163         // The frequency is the mid-point between two nodes
164         freq_[i - 1] = 0.5*(nodeFrequency[i - 1] + nodeFrequency[i]);
165 
166          // Wave number based on linear wave theory
167         k_[i - 1] = direction*stp.linearWaveNumber(depth, freq_[i-1]);
168 
169                 // The phase is computed based on the phase-function
170         phi_[i - 1] = phases_->phase(freq_[i - 1], k_[i - 1]);
171     }
172 
173     // Calculate the spectrum
174     scalarField S_TMA = this->spectralValue(Hs, Tp, gamma, nodeFrequency, depth,
    direction);
175 
176     scalar zeroth_mom = 0;
177     for (int i = 1; i < N + 1; i++)
178     {
179         zeroth_mom += 0.5*(S_TMA[i-1] + S_TMA[i])*(nodeFrequency[i] - nodeFrequency[i
     - 1]);
180     }
181 
182   \\Calculate the scaling coefficient for the amplitudes to give NewWave.
183     scalar AmpScale = Foam::sqrt(2*zeroth_mom*Foam::log(inXwaves))/zeroth_mom;
184     Info << "\n zerothmom: " << zeroth_mom << endl;
185     Info << "\n AmpScale: " << AmpScale << endl;
186 
187     // Compute return variables
188     for (int i = 1; i < N + 1; i++)
189     {
```

```
        // Amplitude is the square root of the trapezoidal integral
        amp_[i - 1] = AmpScale*(S_TMA[i-1] + S_TMA[i])
                *(nodeFrequency[i] - nodeFrequency[i - 1]);
    }

    writeSpectrum(os, nodeFrequency, S_TMA);
}

// * * * * * * * * * * * * * * * * * * * * * * * * * * * * * * * * * * * * * * * * * * * * * * * * * * * * * * * * * * * * * * * * //

} // End namespace Foam

// ************************************************************************* //
```

TMA-NewWave Wave Properties Dict

```
// Wave type to be used at boundary "inlet" and in relaxation zone "inlet"
  waveType     irregular;

//Number of wave components
  N          100; //Number of frequency components
  Maxin        1000; // The largest wave in X.

//Define wave spectrum
  spectrum    TMA_NewWave;
  Hs                 4; //[m] Spectral wave height
  Tp                 9; //[s] Peak wave period
  gamma            3.3; // [-] Peak enhancement factor
  depth              5; // [m]
  direction      (1 0 0);
  Tsoft              0;   // Ramp time

//Define focal point for NewWave
  phaseMethod    focusingPhase;
  focusTime          15;
  focusPoint        (10 0 0);

//Define Frequency limits of components
  frequencyAxis
  {
    discretisation    equidistantFrequencyAxis;
    lowerFrequencyCutoff     0.01; //[Hz] Default = 1/(3Tp)
    upperFrequencyCutoff      0.4; //[Hz] Default = 3/Tp
    writeSpectrum          true; //[bool] Writes the target Spectrum (f,S)
  }
```